3-19-2019

Process Parameter Development of Additively Manufactured AF9628 Weapons Steel

Erin M. Hager

PROCESS PARAMETER DEVELOPMENT OF ADDITIVELY MANUFACTURED AF9628 WEAPONS STEEL

THESIS

Erin M. Hager, Captain, USAF

AFIT-ENY-MS-19-M-217

DEPARTMENT OF THE AIR FORCE
AIR UNIVERSITY

AIR FORCE INSTITUTE OF TECHNOLOGY

Wright-Patterson Air Force Base, Ohio

AFIT-ENY-MS-19-M-217

PROCESS PARAMETER DEVELOPMENT OF ADDITIVELY MANUFACTURED AF9628 WEAPONS STEEL

THESIS

Presented to the Faculty

Department of Aeronautical Engineering

Graduate School of Engineering and Management

Air Force Institute of Technology

Air University

Air Education and Training Command

in Partial Fulfillment of the Requirements for the

Degree of Master of Science in Aeronautical Engineering

Erin M. Hager, B.S.M.E.

Captain, USAF

March 19, 2019

AFIT-ENY-MS-19-M-217

PROCESS PARAMETER DEVELOPMENT OF ADDITIVELY MANUFACTURED AF9628 WEAPONS STEEL

Erin M. Hager, B.S.M.E.
Captain, USAF

Committee Membership:

Maj Ryan O'Hara, PhD
Chair

Dr. Philip Flater, PhD
Member

Dr. Eric Payton, PhD
Member

Maj Ryan Kemnitz, PhD
Member

Abstract

The manufacture of components in Additive Manufacturing processes is limited by the range of materials available. Qualification of materials for Additive Manufacturing is time intensive, and is often specific to a single type of machine. In this study, an approach to selecting power, speed, and hatch spacing values for a newly powderized material, AF9628 weapons steel, is described that results in highly dense (>99.9%) parts on an MLab 200R Cusing. Initial power and speed values used in a weld track study were selected based on a survey of parameters used on similar materials, with a focus on the energy density value known as laser fluence. Shape and penetration depth of the weld tracks were used to select the most promising parameters for generation of solid parts. Solid cylinders were printed with hatch spacing values of 90%, 80%, and 70% of the weld track widths and evaluated for porosity using sectioning and microscopy and CT scanning. Several parameter combinations resulted in parts with >99.9% density, with these parts occurring at a fluence value of between 200 and 300 J/mm^3, and a volumetric energy density (E_V) value of between 80 and 90 J/mm^3. Initial material characterization of the as-built material was conducted, with strength and hardness values that met or exceeded values taken from the original material patent. Weld track studies at various laser focal diameters were then conducted on the larger, more powerful M2 Cusing by sweeping along a 250 J/mm^3 line of fluence, and solid parts were successfully generated using hatch spacing values based on 80% of the weld track width. Additionally, the gas atomized AF9628 powder morphology and chemistry were evaluated in both the virgin and used-sieved conditions, with no change in print quality directly attributed to powder recycling.

Table of Contents

Page

Page

Page

List of Figures

List of Tables

List of Symbols

E_V	Volumetric Energy Density
E_f	Energy Density due to Laser Spot Size
F	Laser Fluence
I	Interaction Time of the Laser
P	Laser Power
P	Pearlite
V	Laser Scan Speed
α	Alpha Ferrite
α'	Martensite
α_b	Upper Bainite
α_{bl}	Lower Bainite
γ	Austenite, Gamma-Ferrite
θ	Cementite
f	Laser Focal Spot Diameter
h	Hatch Spacing
t	Powder Bed Thickness
μ**m**	Micrometers (microns)
Al	Aluminum
As	Arsenic
CE	Circle Equivalent Diameter
Cr	Chromium
Cu	Coper
C	Carbon
Fe	Iron
H	Hydrogen
J	Joules
MPa	Mega Pascal
Mn	Manganese
Mo	Molybdenum
Ni	Nickel
O	Oxygen
P	Phosphorus
Sb	Antimony
Si	Silicon
Sn	Tin
S	Sulfur
Ti	Titanium
V	Vanadium
W	Watts
cc	Cubic Centimeters
g	Grams
kip	1000 pounds, kilopound
ksi	Kips per Square Inch
mm	Millimeters
ppm	Parts Per Million
s	Seconds

PROCESS PARAMETER DEVELOPMENT OF ADDITIVELY MANUFACTURED AF9628 WEAPONS STEEL

I. INTRODUCTION

Steel, the world's most widely used metal, has been known to humanity since the Bronze Age, when its only source was fortuitously discovered meteorites [1]. The first true steel smelting process was invented in India around 400 BCE, and involved heating iron ingots and charcoal in a sealed crucible. While improvements in smelting were made over the next 2200 years, it was the 1856 discovery by Henry Bessemer that produced the first modern steel [1]. The Bessemer process was the first successful method of mass producing steel from molten pig iron, which provided the raw material for the Second Industrial Revolution and made large projects like skyscrapers, suspension bridges, transcontinental railroads, and oceanliners possible. Notable inventors such as Samuel Colt, Nickolaus Otto, and the Wright Brothers were able to create a reliable handheld revolver, the four-stroke internal combustion engine, and fittings for the Flyer I, respectively, with the new availability of inexpensive, high-quality steel [2, 3, 4].

1.1 Development of AF9628

In 1941, the United States congress passed the Berry Amendment to the Appropriations Act, requiring that items procured by the US military be preferentially obtained from domestic sources to protect the industrial base and prevent shortages during wartime [5]. However, many metals with military applications, such as Titanium and Tungsten, are not readily present in domestic deposits. The SR-71 spy

plane was built during the height of the Cold War, despite being designed with over 90% titanium. The ore to build the Blackbird was obtained with great difficulty by the CIA, working through several shell companies, from mines located deep within the Soviet Union [6].

Tungsten is noted for its extreme hardness, and is an important alloying element in many weapons steels because of its ability to increase the both the steel's hardness and toughness. In 2003, the Air Force announced that it had developed a new weapons steel that significantly reduced the nickel content of its preferred weapons alloy. This new alloy, designated Eglin Steel, was alloyed with 4% tungsten. While Nickel is an expensive alloying element that is also difficult to source domestically, it is far more terrestrially common than tungsten [7]. Additionally, the material cost of tungsten is significantly higher, and the primary source of tungsten deposits is China [8]. In 2010, section 1502 of the US Dodd Frank act was passed, which declared tin, tungsten, tantalum, and gold to be conflict minerals due to their influence on armed conflict in eastern Congo. This the passage of this law increased scrutiny of supplies of tungsten, further driving up costs [9].

In 2015, Air Force Research Laboratory (AFRL) engineer Rachel Abrahams took on the challenge of removing all conflict minerals from Eglin steel. Despite many peers asserting that a similar tungsten-free alloy would be inferior [10], she was able to develop a steel alloy that matched the strength and toughness of Eglin Steel while completely removing tungsten and further reducing the amount of nickel in the formula. The new alloy, designated AF9628 Weapons Steel (AF9628), also has the benefit of being easier and cheaper to manufacture, as it does not require the use of a vacuum furnace and is highly weldable [11]. The AF in the name indicates development by the Air Force, the 96 refers to the specific experiment number, and the 28 indicates 0.28% carbon by weight by American Iron and Steel Institute (AISI)/Society of Automo-

tive Engineers (SAE) convention. If AF9628 were named by AISI/SAE convention, its chromium-silicon-nickel-molybdenum composition would make it difficult to easily characterize, and it could be considered a 4XXX, 8XXX, or 9XXX-series steel [12].

This new formulation opens up new routes of innovation not possible before due to cost constraints. "...military applications of high strength, high performance steels include hard target penetrator warhead cases, missile components including frames, motors, and ordnance components including gun components, armor plating, military aircraft frame and landing gear components [7]." In particular, the weldable nature of the steel indicates that it could be a good candidate for the additive manufacture of warheads for small diameter bombs. Warheads that are optimized for penetrating hardened stone and concrete bunkers could lead to a reduction in strategic threats. While the first applications of this new alloy will doubtless be simple improvements of existing products, entirely new applications are bound to follow.

1.1.1 Future Applications

The penetration of hard buried targets using advanced weapons systems has been a focus area for the Air Force since before the start of the War on Terror in 2002 [13] due to the prevalence of abandoned Cold War bunkers in former Soviet Bloc countries. After the September 11th attacks, the strategic relevance of these bunkers became extremely important as the fear of terrorists building nuclear weapons in these sites grew. Nearly two decades later, the defeat of deeply buried targets is still of paramount importance, as rogue states are using underground centrifuges to refine uranium for nuclear weapons [14]. The ability to manufacture complex new penetrating warhead designs in state-of-the-art domestic alloys is vital to current and future national security.

1.2 Additive Manufacturing of Metals

The welding of metals using an electrical arc became popular in the mid-19th century [15], and lasers were developed in 1960 [16]. Powder metallurgy, or at least the concept of working with powderized metals to create a solid part, has been around since 3000 BCE, when both the Egyptians and Incas showed evidence of working with powdered iron [17]. However, it was not until 1971 that anyone attempted to combine these technologies. Frenchman Pierre Ciraud filed a patent for a manufacturing process whereby a metallic substrate was coated in a metallic powder and then welded with a laser beam [18]. Ciraud thought that his concept would allow for the manufacture of complex geometries without the need for casting molds; however, his invention was limited by the rudimentary lasers and computers of the day [18]. After some development in stereolithography and plastic powder sintering in the 1980's, the first commercial laser sintering machine was shipped by DTM Corporation of Austin, TX in December of 1992, followed quickly by a sintering machine from EOS GmbH of Munich, Germany in April of 1994. Each of these companies soon followed with proprietary metal sintering machines [18].

Today, additive manufacturing of metals through laser sintering has become commonplace, and companies like General Electric (GE) have entire facilities dedicated to production of additively manufactured parts. GE is using additive facilities to produce fuel nozzle injectors at full production rates for the commercially successful LEAP jet engine, and are additively producing 35% of all parts for the new Advanced Turboprop Engine; additive manufacturing has allowed GE to reduce 855 traditionally manufactured parts down to just a dozen [19].

Additive manufacturing of metals has opened up exciting new design opportunities and has the power to transform the aerospace and defense industries, among others. Designs that were previously impossible to manufacture with traditional

milling equipment are now possible in a range of metals, including titanium, inconel, aluminum, niobium, and stainless steels. Recent research in Laser Powder Bed Fusion (LPBF) parameter development of non-stainless steel alloy 4340 and 300 maraging steel indicates additive potential for other oxidation-prone high-strength steels [20]

1.3 Research Outline

1.3.1 Problem Statement

Currently, the uses of AF9628 have been limited to manufacturing bomb case and warhead designs using traditional forging fabrication methods. The relatively low cost and producibility of this material, however, has the potential to enable innovative design in other areas where steel is currently used. The ability to additively manufacture optimized bomb cases and warheads, something that has currently only been trialed with less tough and more expensive stainless steels, could provide a new warfighting edge for weapons of the future, such as the topology optimized, additively manufactured, penetrating warheads designed by previous AFIT students [21, 22]

1.3.2 Research Questions

Based on previous additive manufacturing demonstrations with weldable steel alloys [20], it is hypothesized that AF9628 is a good candidate for additive manufacturing by LPBF. This hypothesis will be guided by several research questions:

- Which process parameters on a 200 watt LPBF machine will result in conduction/penetration mode melting of additively manufactured AF9628?
- Can lines of constant fluence be used to scale to a more powerful 400 watt LPBF machine?

- Can volumetric energy density or fluence be used to select scan strategies for fully dense (>99%) additively manufactured AF9628 parts?
- Will the additive manufacturing process cause changes in the chemical composition of AF9628 during melting?
- How will the properties of additively manufactured AF9628 compare to those published in the patent?
- Will the heat treat process as described in the AF9628 patent create similar properties to forged specimens?

1.3.3 Scope and Methodology

This research will develop laser power, speed, and hatch spacing parameters to produce fully dense AF9628 parts in a LPBF machine. Additionally, it will compare the hardness and microstructure of the printed parts, both with and without the recommended heat treatment, to those published for the wrought material. The research will determine porosity using both Computed Tomography scanning and optical estimation techniques; microstructure will be examined with Scanning Electron Microscope (SEM)'s outfitted with Electron Backscatter Diffraction (EBSD) modules.

This research will follow an iterative experimental approach, in which a literature survey will be used to identify an initial parameter set and progress toward more complex experiments. Single weld tracks over bare and single-powder-layer covered build plates will guide the initial selection of conduction-mode melting parameters. Once a smaller pool of potential power and speed settings have been chosen, solid parts will be built at hatch spacings based on measured weld track widths. An optimal zone of parameters will be determined after evaluating for surface finish, discoloration, density, hardness, and microstructure analysis.

1.3.4 Assumptions

While there are myriad factors that affect the quality of an additively manufactured part, laser power, laser speed, powder bed depth, and hatch spacing have been accepted as the dominant variables [23]. As such, the likely variations in part quality due to build plate location, virgin vs. sieved powder, powder manufacturing techniques, or random variation between builds will be considered negligible over the course of this study. Additionally, for the purposes of rapid parameter development in the initial single weld track studies, all linearly interpolated points between two successful power and speed settings will be assumed to also produce good results. All experiments conducted on the MLab Cusing 200R will be assumed to be at the reported powder bed thickness of 30 μm and laser focus diameter of 50 μm. Experiments on the M2 Cusing will be assumed to be at the default powder bed thickness of 40 μm with a variable spot size of 50 to 350 μm.

1.3.5 Near-Term Impacts

Successful selection of laser power, speed, and hatch spacing parameters, along with comparison to published material values both with and without the proscribed heat treatment will open up research opportunities in penetrating weapons design. Previous work in optimized warheads has been limited to materials currently available in commercial additive manufacturing, but not necessarily well suited to penetrating weapons. The publication of print parameter values for a new alloy will lead to testing and comparison to all published material properties, such as Charpy V-notch impact toughness, ultimate and yield tensile strength, and fracture toughness and fatigue values.

II. BACKGROUND

2.1 Steel

Steel, an alloy of iron with carbon, is valued for its combined strength and ductility. In ancient times, steel was associated with legendary weapons such as the Viking Ulfberht and the Japanese Katana, which were able to outlast their soft, weak iron contemporaries and stand up to multiple impacts with armor [24]. The difficulty with steel is that the carbon concentration must be precise: between 0.05% and 2% [25]. Less than this, and the smith is left with elemental iron; more than this, and the smith has hard, brittle wrought iron. Manufacturing techniques developed at the dawn of the 20th century finally permitted the large-scale manufacturing of steel, and it is now the world's most prevalent engineering metal due to its relative abundance, strength, ductility, and ease of manufacturing. It can be combined with a wide array of elements beyond carbon to yield an incredible variety of alloys tailored to specific purposes, such as tensile strength or toughness [1]. Specific heating and cooling cycles cause crystalline changes that alter the microscopic and macroscopic properties of the steel, further tailoring the strength, hardness, toughness, and ductility [25]. Tailoring of modern steels involves a tradeoff of strength and hardness with ductility and toughness [26], so it is vital to fully understand the alloying and heat treating processes to successfully produce a steel that will maximize the desired properties.

2.1.1 Steel Metallurgy

Pure, room temperature iron at thermodynamic equilibrium is arranged in a Body-Centered Cubic (BCC) crystalline lattice, with iron atoms arranged in a cube with a fifth iron atom located in the center of the cubic body, for a total of two atoms per unit cell. This form of iron is called alpha iron [25]. When iron is heated above

its critical temperature, typically around 730 °C, it will change to a Face-Centered Cubic (FCC) crystal lattice, where iron atoms are still arranged in a cube, but with a fifth atom centered on each face instead of one centered in the body, causing an increase to four atoms per unit cell [26]. This form of iron is called gamma iron. The geometries of BCC and FCC unit cells are below in figure 2.1.

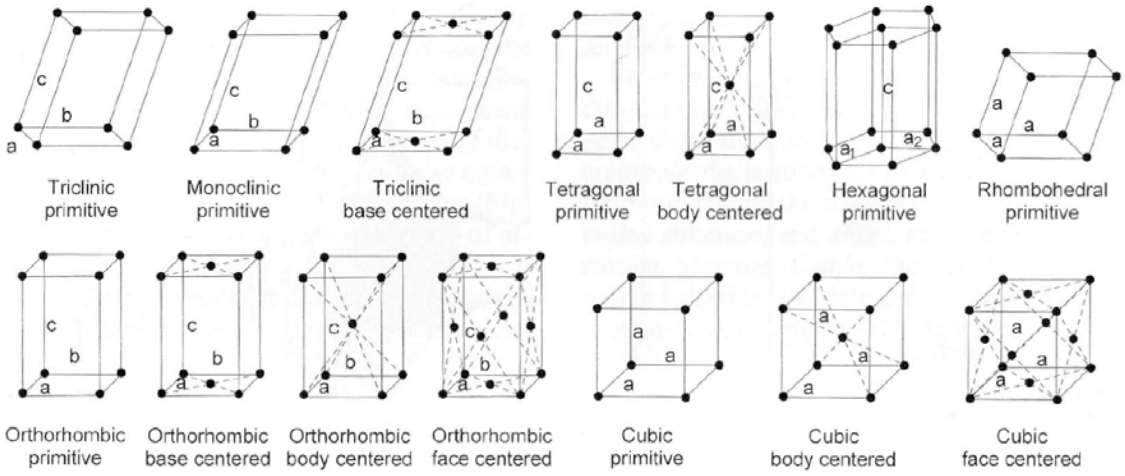

Figure 2.1. Schematics of the 14 Bravais crystal lattices [26]

The transition to FCC enlarges the interstitial voids between the iron atoms and allows other elements to diffuse through the solid steel. The maximum solubility of carbon in iron is 2.11% at 1148 °C [25]; higher concentrations of carbon are achieved above the iron liquidus temperature, 1650 °C. When carbon diffuses through the FCC iron in solid solution, this form of steel is called austenite, denoted γ [25]. The equilibrium phase diagram for plain carbon steel is shown in figure 2.2. When rapidly cooled, the steel reforms in BCC (ferrite) or Body-Centered Tetragonal (BCT) (martensite); since iron atoms are larger than the diameter of BCC and BCT interstitial voids, they cause a distortion in the lattice which prevents slipping along the close-packed plane, $< 111 >$ [25]. This distortion is what causes the increase in strength and ductility that distinguishes the behavior of steel from iron [26].

When a fully saturated steel FCC lattice is cooled, the maximum solubility of

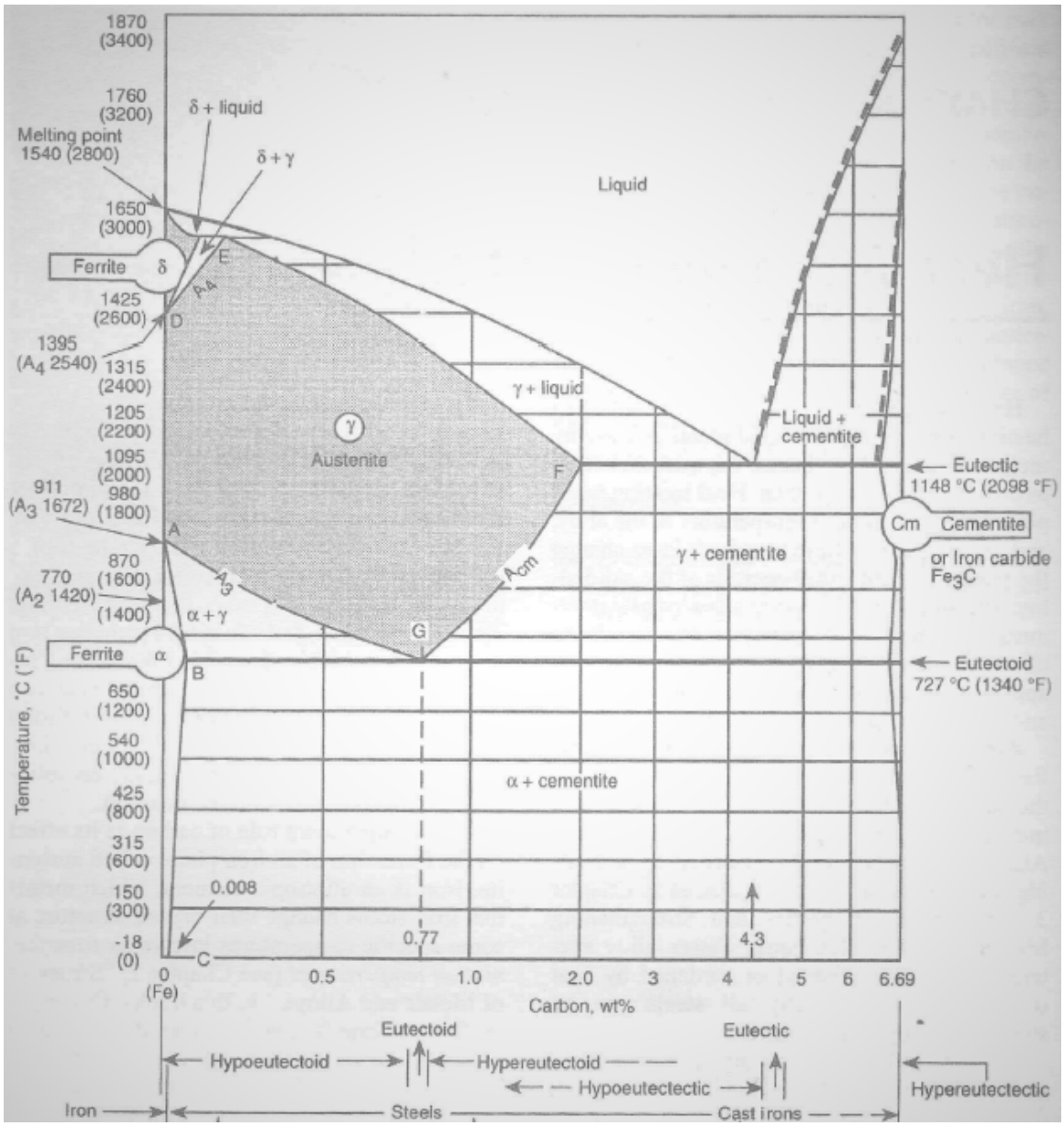

Figure 2.2. Equilibrium phase diagram of the iron-cementite system [26]

carbon in iron is exceeded, resulting in the supersaturated strained lattice. This phase of steel is called alpha ferrite (α) [25]. If the cooling rate is sufficiently slow, the interstitial solutes will precipitate out from the solid solution in a process called quench aging [25]. A similar phenomenon occurs in air furnaces during heat treatment, as the carbon at the surface of the material precipitates out in a process known as decarburization. At sufficiently low aging temperatures, typically between 100 and 250 °C, carbon will precipitate out as ϵ-carbides. These carbides precipitate along [100] planes, and minimum potential energy and the influence of strain energy force the ϵ-carbides to form in plate or rod shapes [25], as shown in Figure 2.3. Cementite, similar to ϵ-carbide, is formed by eutectoid decomposition of cooling austenite by diffusion of carbon. It will precipitate out when α is aged at above 200 °C [25]. Austenite that is rapidly quenched in oil, water, or brine experiences displacive transformation and becomes martensite, which is very hard and brittle due to the stressed lattice [25]. The lattice stress is due to a sudden transformation from FCC to BCT to accommodate the large carbon atoms, and is not associated with the equilibrium steel process; it is often aged or tempered to improve ductility [26].

2.1.1.1 Steel Microstructure

The six primary steel phases are: austenite (γ), ferrite (α), pearlite (P), upper and lower bainite (α_b and α_{bl}), martensite (α'), and cementite (θ), are typically identified by a combination of imaging techniques and knowledge of the material processing history. Austenite is the reference condition, as it is the only phase that is commonly present above the critical temperature and is considered the starting condition, though it is often present in room-temperature steels in some percentage as retained austenite. Reconstructive transformation, which results in several sub-categories of ferrite and pearlite, occurs primarily at higher temperatures (below

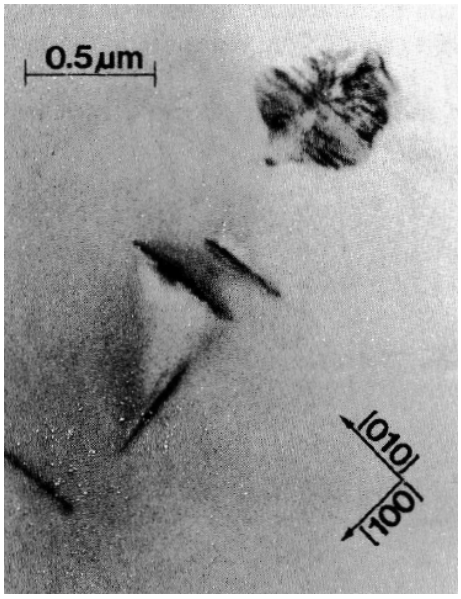

Figure 2.3. Metastable ϵ-carbide precipitates on [100] planes ([110] and [010] directions are crystallographically equivalent) in an Fe-0.013%C alloy quenched from 700°C and then aged 6 hours at 200°C

the eutectoid temperature), while displacive transformation, which results in several other sub-categories of ferrite, bainite, and martensite, occurs during non-equilibrium processes such as quenching. A time-temperature transformation diagram for plain carbon steel depicting the products from the different temperature regimes is in figure 2.4 below. Pearlite results from the cooperative growth of two phases, ferrite and cementite, and forms easily recognizable spherical colonies as shown in Figure 2.5b, provided the grains are coarse enough. Reconstructive transformation is so called because it 'reconstructs' the austenite grain boundaries, and the transformation phases can grow without regard for the austenite grains. Displacive transformation results from the displacement of the crystal structure, and the phases cannot grow beyond the discontinuities that are austenite grain boundaries. Thus, materials that depend on displacive transformation for hardening are subject to embrittlement due to any impurities that collect along the austenite or prior austenite grain boundaries [27, 28].

Austenite microstructures are generally large, with wrought materials exhibit-

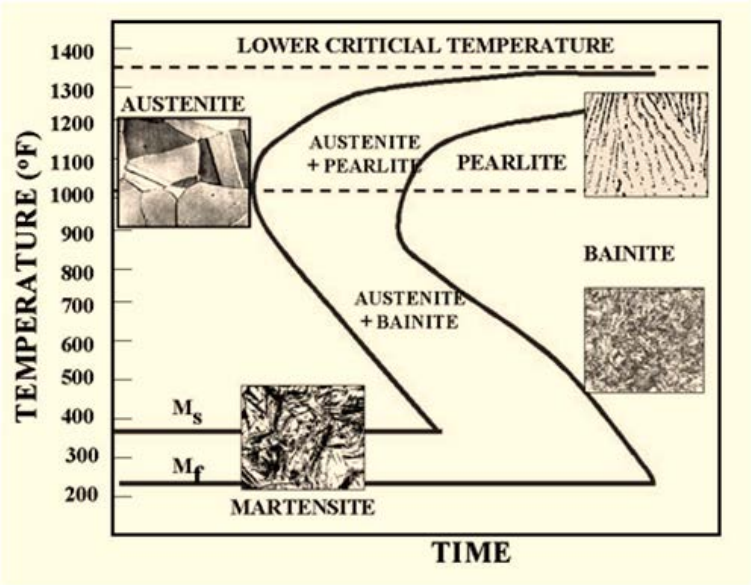

Figure 2.4. A nominal time-temperature transformation diagram for a plain carbon steel [29]

ing generally equiaxed grains with a unimodal size distribution, as demonstrated by the Prior-Austenite Grain Boundaries (PAGB)'s displayed in Figure 2.6. As the other phases will initiate either on or within the Austenite grains, the PAGB's are likely to be the largest microstructural features present. In Figure 2.5a, a reconstructive phase of ferrite has grown along the PAGB's while the remaining austenite has transformed into pearlite, which is recognizable by its characteristic iridescence when etched. Martensite, shown in Figure 2.7, is typically identified by its plate or lath structure and its white color when etched. Upper and lower bainite are distinguished by the location at which carbides precipitate; upper bainite forms at higher temperatures, and carbon precipitates only between the laths (Figure 2.8a); lower bainite forms at lower temperatures, where carbides precipitate within and below the laths (Figure 2.8b), and are generally smaller [27]. Figure 2.9 demonstrates the increasing complexity of identifying multi-phase mixtures of steel.

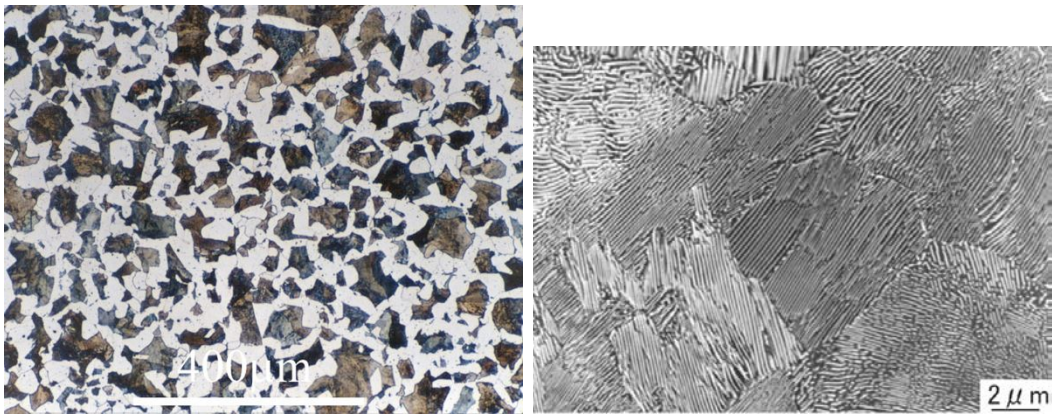

(a) (b)

Figure 2.5. Examples of etched and magnified pearlite [27]

Figure 2.6. Prior austenite grain boundaries outlined by cementite that grew on the austenite grain boundaries [30]

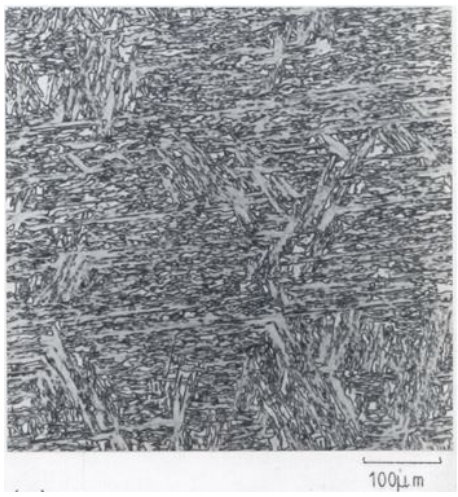

Figure 2.7. A low-alloy steel which has transformed almost completely to Martensite, exhibiting typical plates and laths [27].

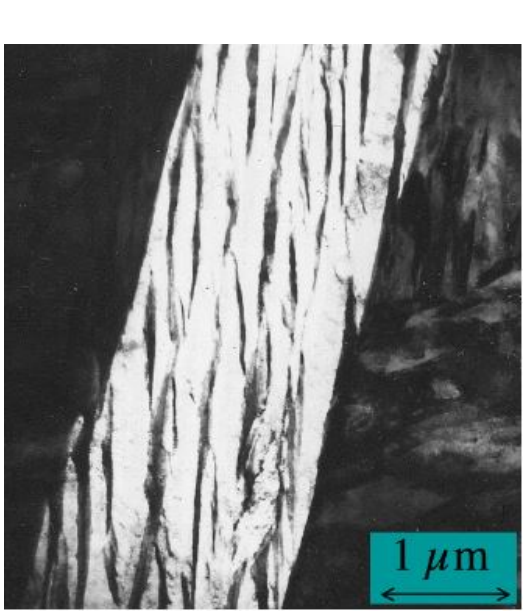

(a) Upper bainite, with cementite (dark) between the platelets

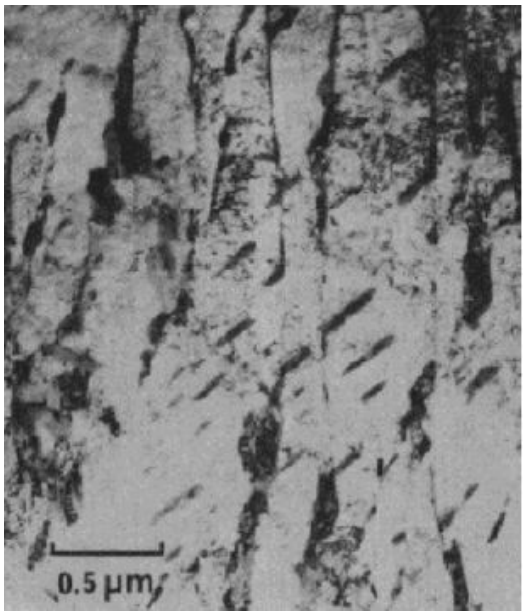

(b) Lower bainite, with cementite (dark) inside and between the platelets

Figure 2.8. Upper and lower bainite [27]

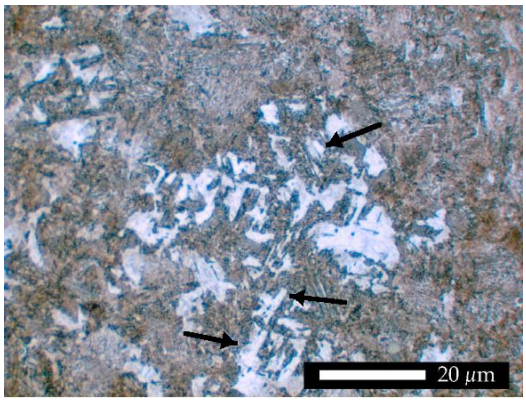

(a) Optical micrograph of a mixture of of bainite and martensite, etched with Nital; martensite etches white on a brown bainite matrix. Bainite forms on specific crystallographic planes of austenite, causing straight edges between the bainite and martensite. Perlite forms spherical colonies, and would not result in straight edges of martensite.

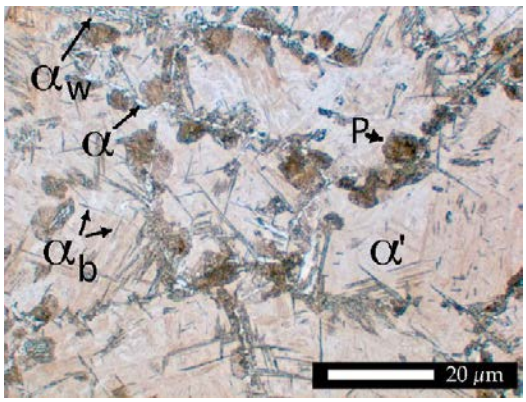

(b) Optical micrograph of the heat affected zone of a weld; the microstructure consists of retained austenite, bainite, a reconstructive ferrite, and pearlite in a martensitic matrix.

Figure 2.9. Examples of mixed microstructures [27]

2.1.1.2 Effects of Common Alloying Elements

There are thousands of distinct chemistries of steel alloys that provide specific advantages. In addition, the synergy of alloying elements and heat treatments produces a tremendous and complex variety of microstructures and properties [26]. It is difficult to predict the outcomes of complex alloying chemistries, so most alloy theory is based on the cumulative effect of the individual alloying element effects [26].

Manganese is present in nearly all commercial steels as it aids in manufacturing. It deoxidizes the melt, improves machinability, and improves hardenability and strength. Manganese will affect the phase transition temperatures by increasing the time needed to begin the transformation to pearlite or bainite. This increases the hardenability by increasing the time available to make the transition to martensite, but can also result in higher amounts of retained austenite [28]. It facilitates hot working by reducing separation along grain boundaries at elevated temperatures, which also helps prevent solidification cracking in welds [26]. The presence of manganese reduces the mobility of the interstitial solutes, reducing the effect of strain aging [25]. Silicon is also a primary deoxidizer [26], and benefits hardness and temper resistance [11].

Copper can serve to prevent corrosion, but is detrimental to hot working, welding, and surface quality [26]. Chromium is the preferred corrosion preventative, and stainless steels contain at least 10% Cr. It also aids in high temperature strength and hardness, especially when paired with cobalt. Nickel is also often added to prevent corrosion, but its main advantage is that it strengthens austenite without forming carbides, which gives it the rare skill of jointly improving strength and toughness [26]. The lower concentration of difficult to melt carbides also make nickel alloys easier to heat treat [25]. Nickel, like manganese, will shift the time-temperature transformation curve as shown in figure 2.10, increasing hardenability but potentially resulting in more retained austenite.

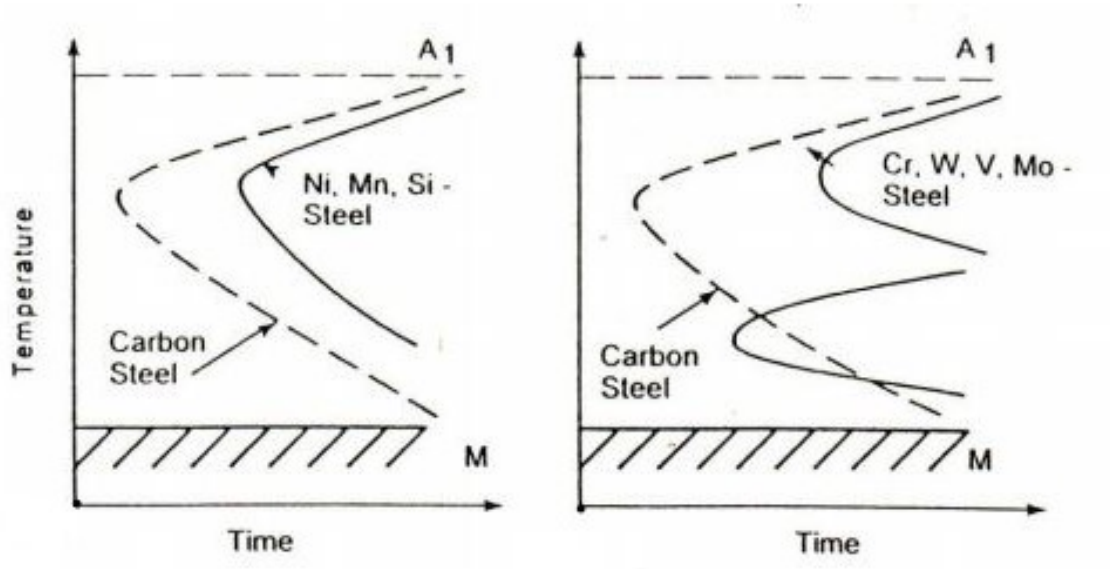

Figure 2.10. Time-temperature transformation diagrams comparing plain carbon steel with steel alloyed with non-carbide forming elements (left) and plain carbon steel with steel alloyed with carbide-forming elements (right). [31]

Molybdenum increases hardenability, high temperature tensile strength, and creep strength, and also improves fracture toughness [26]. Vanadium inhibits grain growth during heat treat, improving strength and toughness [26]. Niobium can increase yield and tensile strength, but will impair notch toughness; the first High-Strength, Low-Alloy (HSLA) steels were made with small additions of niobium [26].

Aluminum is a deoxidizer, and is also used to control grain size. Aluminum is the strongest nitride former of the common alloying elements and is commonly used in nitrided steels [26]. The low vapor pressure of aluminum means that it is prone to vaporization while welding in open atmosphere [32].

Tungsten is used extensively in high speed tool steels as it significantly improves hardness and toughness, especially at elevated temperatures [26]. Titanium increases strength and hardness by controlling grain size, and improves the hardening effect of Boron [26]. Zirconium is also used for deoxidizing, and will inhibit grain growth [26]. Calcium is a deoxidizer, and improves toughness in HSLA steels [26].

Some elements that are generally considered undesirable impurities include nitrogen, phosphorus, sulfur, and hydrogen. Nitrogen will increase strength, hardness, and machinability, but decreases ductility and toughness [26]. Phosphorus increases strength and hardness, but severely decreases toughness and ductility [26]. Sulfur can improve machinability, but will lower transverse ductility and toughness, decrease weldability, and degrade surface quality [26]. The effects of hydrogen are always negative, but it is very difficult to exclude during melting, casting, and welding [26]. Hydrogen embrittlement is a major problem in steel manufacturing, but can be mitigated by hydrogen bake-out procedures [33].

Many alloying attributes that are similar are overlaid to increase the overall effect, though often increasing alloy content above a certain point will degrade performance. Understanding where the maximum point is when multiple alloying elements are combined currently remains more of an art than a science, and getting the balance correct becomes more difficult as the number and weight percentage of alloying elements increase.

2.1.1.3 High-Strength, Low-Alloy (HSLA) Steels

High-strength steels are generally considered to have a yield strength above 300 MPa (44 ksi), and ultra-high strength steels are those with a yield strength above 780 MPa (113 ksi) [34]. High-Strength, high-alloy quenched and tempered steels have the best combination of strength and toughness, but are difficult to find in structural shapes as they are prone to warping during the quenching process. HSLA steels are comparatively inexpensive, easy to manufacture and machine, and easily weldable. The first developed HSLA steel was patented by the Union Carbide Corporation in 1936 and involved alloying plain carbon steel with a small amount of Niobium. At that time, however, the cost of Nb was very high, and there was little demand for

high performing steels. In the late 1950's, increased demand for strong, light, weldable pipelines, along with a sudden drop in the price of Nb, led to a resurgence of interest in HSLA steels [25]. Common strengthening methods employed for high-strength, low-alloy steels include grain refinement and precipitation hardening.

Grain refinement, the process of reducing the average grain size, strengthens materials because grain boundaries impede dislocation motion [35]. Grain size can be reduced by hot rolling [25], cold working, rapid thermal cycling, or a short period of annealing after sufficient plastic work. Refinement of AF9628 Weapons Steel (AF9628) was demonstrated through four thermal cycling steps by Payton and Sinha [36], as shown in Figure 2.11. Grain refinement is a preferred method of strengthening because it will increase strength while also initially increasing toughness [25], though repeated refinement will eventually cause embrittlement.

Precipitation hardening occurs when impurities that exist in solid solution precipitate out at grain boundaries as the material is cooled [35]. This process is outwardly similar to the process that creates carbides, but precipitation hardening refers to the interphase precipitation of alloying elements out of solution, not the formation and precipitation of carbon-rich structures within a single phase. Interphase precipitation occurs at the γ-α transus temperatures, but will only occur if the precipitate is crystallographically coherent with the matrix [25]. The yield strength of the base alloy may be increased substantially if the precipitate has a hard crystal structure that resists deformation; this effect is even more pronounced (for a given volume fraction) if the precipitate particles are relatively small and distributed uniformly [35].

2.1.1.4 High-Toughness Steels

Toughness is typically measured with a Charpy v-notch impact test (See Figure 2.12), and measures the energy absorbed by a notched material before fracture. This

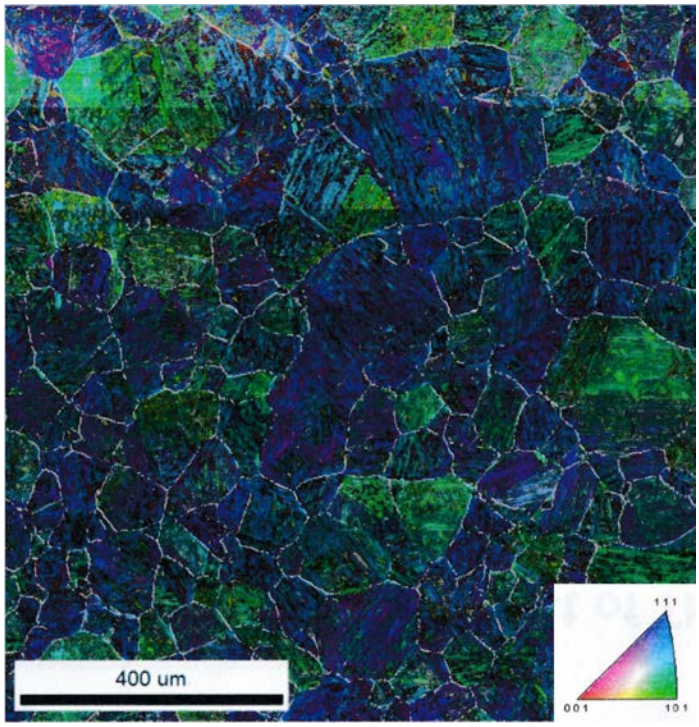

(a) AF9628 microstructure after typical heat treatment procedure, 51 μm mean lineal intercept grain size

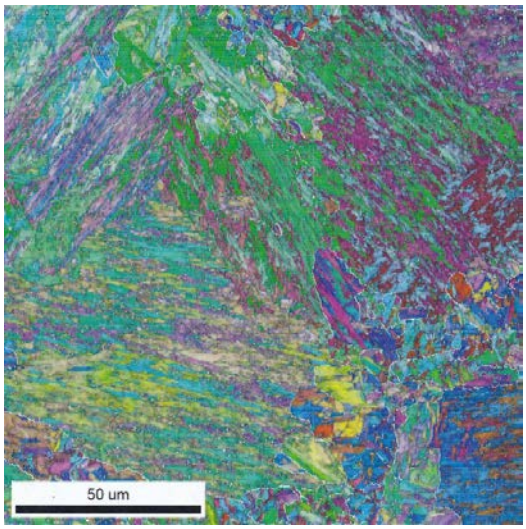

(b) AF9628 microstructure after one cycle (825^{o}C for 30 s, then quench)

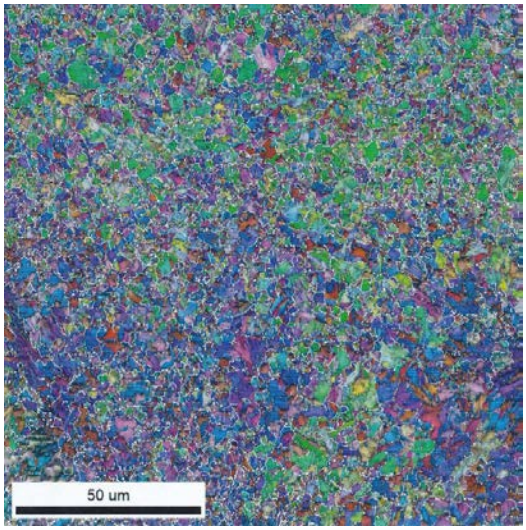

(c) AF9628 microstructure after four cycles (825^{o}C for 30 s, then quench)

Figure 2.11. Change in grain size of AF9628 after four thermal cycles, EBSD step size 0.5 μm, Inverse Pole Figure, Ferrite [36].

correlates to the ability of a material to resist sudden fracture. A material must be both strong and ductile to be considered tough; brittle materials with high strength such as cast iron and ceramics have a low toughness [26]. Without Charpy impact test values, the area under a material's stress-strain curve can be calculated to estimate its relative toughness, as shown by Figure 2.13 [37].

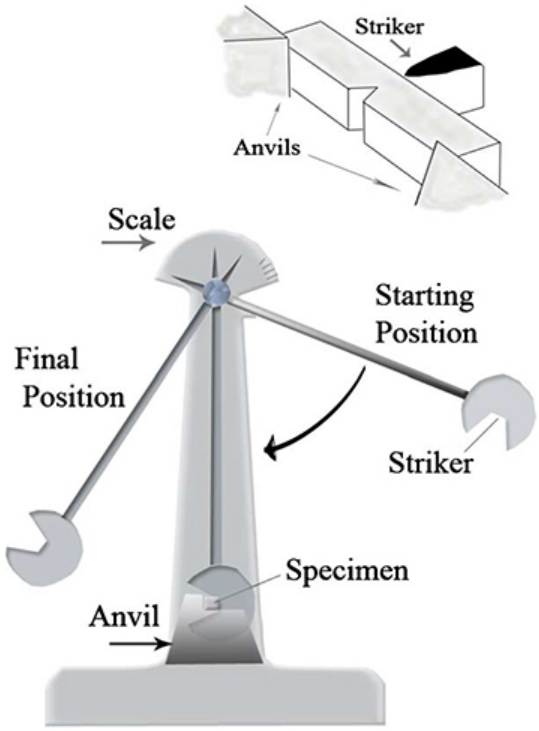

Figure 2.12. Diagram of the Charpy Impact apparatus and specimen [38]

There is a sharp drop in the toughness of most steels at the material's Ductile-Brittle Transition Temperature (DBTT). At this temperature, slip mechanisms of BCC crystals are restricted, leading to brittle fracture in ferritic steels. Austenitic steels and other FCC metals, such as aluminum, do not exhibit DBTT behavior because their close-packed structures and slip systems are maintained at all temperatures. The DBTT can be lowered in ferritic steels by refining the grain size. Martensite, with a BCT structure, has a higher toughness at low temperatures when tempered [26].

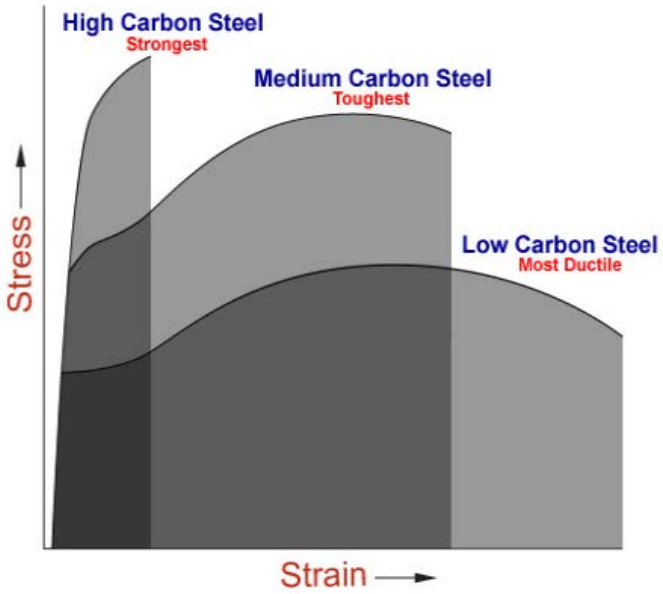

Figure 2.13. Relationship between the shape of the stress strain curves and toughness [37]

2.1.1.5 Heat Treatments

The manipulation of steel properties through the addition and removal of heat is one of the greatest tools that metallurgists possess. While alloying on its own is important, steel alloys are designed to reach their optimal properties only after quenching and tempering steps [25]. Steels are typically kept in the soft annealed condition during manufacturing to make shaping faster and easier; this section is concerned with the heating and cooling steps performed after parts have been formed into their near final geometries.

Finished parts destined for high-strength applications are typically heated to a critical temperature and rapidly quenched to form martensite. Martensite describes microstructures that are formed by an athermal phase transformation in which the parent (usually Austenite) and product phases have a specific crystallographic rela-

tionship [26]. Over 0.20% carbon, which is the primary concern of this work, the FCC austenite transforms into BCT martensite. While the martensite transition is considered athermal, some movement from interstitial sites will occur during quenching [28]. The size of the parent austenite grain boundaries strongly influences the strength and performance of the tempered martensite, though it is difficult to accurately determine the size of the grain boundaries of the previous crystallographic arrangement. Successful recipes for illuminating the PAGB's will vary between alloys, with varying degrees of success with etching and Electron Backscatter Diffraction (EBSD) [39].

Quenched carbon martensite is very hard and strong, but not ductile. A tempering step is added to increase ductility and toughness by allowing inclusions to precipitate out without providing enough freedom for a crystal transition [26]. Tempering mechanisms are segregation of carbon to lattice defects, precipitation of carbides, transformation of retained austenite, and recovery and recrystallization of the martensitic structure. When carbon martensite is tempered at 100°C, atoms cluster along the 100 plane prior to precipitation of ϵ-carbide. If martensite is tempered above 250°C, cementite (Fe_3C) will form along martensite lath boundaries [25]. Embrittlement during tempering can affect low-alloy steels that are tempered at between 250 and 350°C. Hardness will increase, but toughness will pass through a minimum. These embrittled steels fracture primarily along PAGBs, and are caused by the change in carbide structures from ϵ-carbide to cementite. The primary technique for avoiding tempering embrittlement is the reduction of phosphorus, antimony, tin, arsenic, and nitrogen impurities [25].

The hardenability of a material determines the depth and distribution of hardness induced by quenching, and is heavily dependent on the cooling rate. Steels have several potential quenched forms; in order of increasing cooling rate and hardenability, they are: ferrite, pearlite, upper bainite, lower bainite, and martensite [28]. Thinner

metal structures are able to be cooled more rapidly, and thus are more able to approach 100% martensite. A schematic of the transformation diagram for quenching and tempering is shown in figure 2.14. Quenchants can be (in order of severity) air, oil, water, and brine. Agitating the quenching fluid also increases the severity of the quench. Factors that affect the hardenability of steels are carbon content, alloy content, and austenite grain size [25].

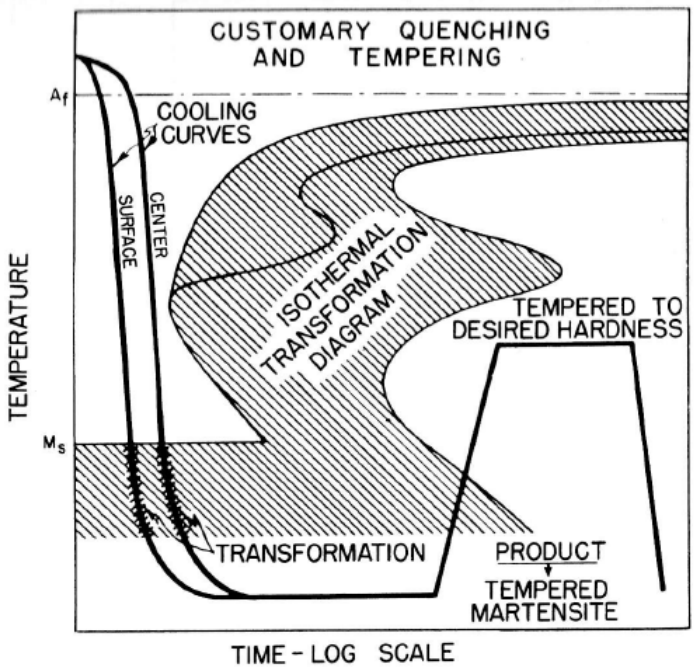

Figure 2.14. Schematic transformation diagram for quenching and tempering [25]

2.1.2 Steel Welds

In welding, the primary conflict is the need to provide adequate heat for fusion versus the detrimental effects of heating. These detrimental effects can include embrittlement, alloy vaporization, and residual stresses [33]. The liquidus temperature for steel is above 1650°C, which introduces very large thermal gradients in the area near the weld, typically called the Heat Affected Zone (HAZ). Near the HAZ the microstructure becomes austenite and coarsens the grain structure, making the area

more hardenable. Of course, this coarse austenite will produce coarse products once cooled, reducing toughness and increasing the risk of cracking [33]. Multiple weld passes can cause some recrystallization, resulting in a mix of coarse grains, refined grains, and inter-critical martensite/pearlite regions. This mix of products is caused by the the variable cooling rate, which is governed primarily by ambient temperature, size of the base metal, and size of the melt pool. The mechanical properties of the weld and HAZ can be modified by a post-weld heat treatment, but these heat treatments often cause distortion if not restrained in a jig throughout the heating and cooling cycle [33].

The composition of steels determine how weldable they are; in general, low-carbon steels are easiest to weld. Higher strength steels are more prone to cracking, as they are less ductile. High alloy steels have a high risk of hydrogen cracking, which is partially mitigated by preheating the main structure. Hydrogen cracking is the most common cause of problems when welding ferritic steel; the best way to control it is to reduce exposure of the melt pool to hydrogen [33].

Residual stresses result from welds when adjacent areas are at different temperatures from the HAZ. As it is not usually practical to weld red-hot steel, residual stresses are inevitable. When residual stresses build to above the yield stress, they will result in plastic deformation [33]. To combat this, welders will typically build up a piece in a carefully planned order, and some parts will be bolted to jigs [32]. As melt pools solidify, they shrink. This shrinking can result in solidification cracking, and can be worse when parts are restrained by jigs [33]. Inclusions can occur when alloying elements do not fully dissolve in the melt pool, and vaporization can occur when alloys melt more readily than the base metal. While post-weld heat treatments can cause distortion, especially if the part is unsupported, they can reduce residual stresses and soften the HAZ, which will increase toughness, reduce the risk of stress

corrosion cracking, and reduce the risk of in-service hydrogen cracking [33].

2.1.3 AF9628 Weapons Steel

In the preface to his 1981 text on steel metallurgy, Leslie [25] states that "...as the less abundant metals become more costly...it will be essential to achieve optimum properties with minimum use of alloying elements." While this statement may be nearly four decades old, the sentiment is as true as ever. AF9628 steel was developed in 2016 out of a desire to produce a less expensive, easier to manufacture steel for manufacturing bomb cases [11]. Dr. Rachel Abrahams of the Air Force Research Laboratory (AFRL)'s Munitions Directorate spent five months developing trying to improve the cost/performance ratio of Eglin Steel, an ultra-high strength, high toughness munitions steel developed with low cost in mind [7]. The goal was to improve ease of manufacturing and reduce total cost by 10%; instead, Dr. Abrahams and her team were able to create a new alloy that approached the high performance of Eglin Steel while realizing a cost savings of 50%. While this steel was developed with munitions in mind, the potential applications are boundless. It is even predicted that the high performance and low cost of this steel could inject new life into the domestic steel industry [40].

2.1.3.1 Alloy Composition

The chemical composition of AF9628 steel is free of both tungsten and cobalt, and has a relatively low percentage of nickel. Tungsten was removed from the alloy due to its high manufacturing cost; tungsten has a high melting point and high density, and creates stable tungsten carbides with even higher melting temperatures, making it difficult to melt in open furnaces [11]. A table comparing selected alloying elements of weapons steels is listed in table 2.1 below. The weapons steels prior to AF9628

were too cost prohibitive to manufacture on the scale needed for hardened target penetrating weapons, and additionally were difficult to process in thick sections [11].

AF9628 is classified as a mid-carbon steel, identified earlier (figure 2.13) as generally having a high toughness. The alloy contains chromium for hardenability, strength, and temper resistance [11]. Temper resistance is the ability of a material to resist reduction in yield strength and formation of carbides while relieving internal stresses due to the stressed lattice [25]. Molybdenum was added to increase solid solution strengthening, prevent embrittlement, and improve fracture toughness. Vanadium is present to increase strength and hardenability, and control grain growth at high temperatures [11]. Vanadium will contribute to a mechanism called Zener pinning that depends on finely divided vanadium carbides to inhibit austenite grain growth [25]. Manganese provides strength [11] and deoxidation, and nickel provides low-temperature toughness by replacing iron atoms in the crystal lattice [26]. Silicon aids in the hardenability and temper resistance of the alloy by reducing the coarsening of ϵ-carbide to cementite. By preserving the smaller, semi-coherent ϵ-carbides, silicon also enhances toughness. Copper is considered an undesirable inclusion in this alloy; if it is present above 0.20% by weight it will precipitate out and reduce fracture toughness [11].

Table 2.1. Comparison of alloy composition of several weapons steels

Alloy Name	**C**	**Ni**	**Cr**	**Mo**	**Co**	**Mn**	**V**	**W**	**Si**
AF1410 [41]	0.15	10	2	1	14	-	-	-	-
Aermet-100 [41]	0.24	11.5	3.1	1.2	13.5	-	-	-	-
HY-180 [42]	0.13	10	2	1	8	0.10	-	-	0.05
HP 9-4-30 [43]	0.30	7.5	1.0	1.0	4.5	0.30	0.10	-	0.10
Eglin Steel [7]	0.28	1.03	2.75	0.36	-	0.74	0.06	1.17	1.00
AF9628 [11]	0.28	0.95	2.52	0.91	-	0.62	0.064	-	0.96

2.1.3.2 Strengthening Mechanisms

AF9628 is believed to be strengthened by special meta-stable nano-carbide filamentous rods that are precipitated within a primarily martensitic matrix. Specifically, the combination of alloying elements and heat treatment would likely lead to the mixed precipitation of metastable ϵ-carbide and cementite. However, the actual presence of these ϵ-carbides has been difficult to confirm due to their extremely small size. The potential ϵ-carbides are nano-sized, iron-rich, metastable, and semi-coherent, which leads to increased strength and reduced loss of toughness [11]. AF9628 is typically void of tool-steel alloy carbides such as $M_{23}C_6$, M_2C, or M_6C. The matrix is intentionally kept to 90% martensite or greater, in contrast to most other high-strength Ni-Cr-Mo steels [11]. Values for strength, hardness, ductility, and toughness for AF9628 and five other munitions steels are provided for comparison in table 2.2.

The potential ϵ-carbides, shown in Figure 2.15 are 100nm to 150nm in length and 10nm in width. Their shapes are similar to feathery rods and fit within the matrix (semi-coherent), causing localized strain features. The configuration of ϵ-carbide is believed to be $Fe_{2/4}C$, hexagonal close packed. ϵ-carbide is thermally unstable, so tempering is performed at temperatures less than 260°C. The semi-coherent distribution, rather than at the grain boundaries, promotes the favorable combination

Table 2.2. Comparison of material properties of several weapons steels

Alloy Name	**Ultimate Tensile Strength** ksi	**Yield Strength** ksi	**Elongation to Failure** %	**Charpy Impact Toughness** ft-lb at -40C	**Hardness** Rockwell C
AF1410 [41]	235	215	12		
Aermet-100 [41]	280	235	8		
HY-180	190	175	12		
HP9-4-30	232	194	15	20	51
Eglin Steel [7]	260	230	17.5	20	46
AF9628 [11]	230	180	11	24	45

of strength and dynamic toughness [11]. AFRL/RX has attempted to confirm the presence of the ϵ-carbides with higher-resolution Transmission Electron Microscopy (TEM), but has not yet achieved success.

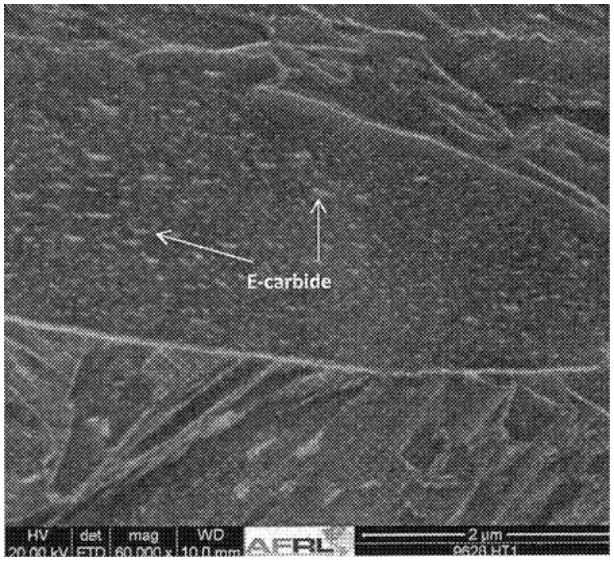

Figure 2.15. SEM image taken at 60,000x magnification showing what may be nanoscale ϵ-carbide within a primarily martensitic matrix grain structure [11]

2.1.3.3 Processing Characteristics

AF9628 may be significantly easier to process than other weapons steels, most notably in that it can be produced in an open ladle process. It is also easily welded and machined, especially in the annealed condition, as it does not contain a large number of carbides in that state [11]. The alloy can be cast or wrought, and shape casts can be further treated using a Hot Isostatic Press (HIP) process. The declared material processing characteristics of the six munitions steels of note are tabulated below (table 2.3 for comparison.

The suggested heat treating process begins with an austenitizing step, heating to above 954°C for 30 minutes per inch of thickness. The heating rate between 316 and 899°C should be maximized to prevent the formation of stable tool steel

Table 2.3. Comparison of manufacturing qualities of several weapons steels

Alloy Name	**Melt Process**	**Weldability**	**Machinability**	**Hardening Process**
AF1410 [41]	Double Vacuum Melted	Good, no pre-heat		Multiple heat and air quench steps, refrigeration, and aging
Aermet-100 [41, 44]	Double Vacuum Melted	Good, no pre-heat	More difficult than 4340	Crucial air or oil quench, refrigeration, and aging
HY-180	Double Vacuum Melted	Good		
HP 9-4-30 [43]	Consumable Electrode Vacuum Arc Re-melting	Good, helium shielded tig	Similar to 4340	Oil quench
Eglin Steel [7]	Electric Arc, Ladle Refined, Vacuum Treated	Excellent	Similar to 4340	water, oil, or gas quench, low heat temper
AF9628 [45]	Ladle	Excellent	Similar to 4340	water quench, low heat temper

carbides. The steel should then be rapidly quenched to below 66°C; the value of the Grossman H-value for quench intensity should be above 0.25. Sections over one inch thick should be quenched in water, as an oil quench will be too slow to prevent the formation of undesirable carbides. A tempering step performed between 177 and 260°C for a minimum of three hours (or one hour per inch of thickness) will improve toughness. The AF9628 patent recommends a sub-critical step to decrease the size of prior austenite grain boundaries, however, in work presented by Sinha at Materials Science & Technology (MS&T) 2018, the sub-critical anneal produced no measureble change in PAGB size.

2.2 Metal Powderization

Powderized metals are important for the creation of high-quality parts through pressing and sintering processes, and are used heavily in metal additive manufacturing. The powder type and fabrication influence the ease of compaction, sintering, flow, and welding. The initial interest in powder applications was due to low cost, but the industry has evolved to produce high quality parts with tightly controlled chemistry and microstructure. Pre-alloyed powders allow fabrication of parts below the melting temperature, eliminating casting defects [46].

2.2.1 History and Applications

Powder metallurgy is an ancient art, with powderized gold shaped into jewelry by the Inca and records of the Egyptians working with iron powder as far back as 3000 BCE. The pillar of Delhi, erected in 300 CE, was formed of over 6.5 tons of iron powder, and is remarkable in that it has no significant corrosion [46]. The discipline of powder metallurgy became prominent in the 1800's when there was a sudden increase in demand for platinum lab equipment. Platinum has a high melting

point, but sintering of metal powders does not require fully liquid metal. Powder production techniques were preferred for working with platinum, as they avoided very high temperature castings [46]. Thomas Edison's first successful light bulbs were made with carbon filaments, but they were dim and had a short life. The tungsten filament developed by Coolidge was made with sintered tungsten powder, and was the primary filament used in incandescent light bulbs until compact florescent (CFL) and LED bulbs took over the market nearly a century later. By the 1940's, powder metallurgy was being used for the fabrication of structural steel and high-melt refractory alloys [46]. Today, the majority of pressed and sintered structural parts are made from iron, and additive manufacturing has opened the way for development of many new powder materials.

2.2.2 Powder Fabrication - Atomization

The formation of powder involves the delivery of energy to create new surface area. This energy can be mechanical, thermal, or chemical. For high value applications such as aerospace and additive manufacturing that require high purity, atomization currently provides the highest quality powder [46]. While metal powders can be created through mechanical, electrolytic, or chemical techniques, they are beyond the scope of this work.

Atomization provides direct control of powder chemistry and shape, and is currently the primary method of metal powder production. Atomized powder is produced when a molten spray of metal is dispersed into droplets and rapidly cooled. Water atomization is typically used for metals that melt below 1600°C. Using water as the cooling fluid produces larger, less regular particles with high oxide content, but it is the most energy-efficient atomization process. Centrifugal atomization consists of a central beam melting incoming feedstock that is flung out into a rotating chamber.

This process produces near-perfect spheres, but production quantities are limited, it is difficult to produce powder sizes below 150μm, and it is very expensive [46]. A more recent technology, plasma atomization, produces extremely spherical powder in a size range of 0-200μm. In plasma atomization a plasma torch melts a wire that is fed in, then allowed to disperse and cool in a gravity-driven spray (see figure 2.16. While plasma atomization is a promising technology, it is currently too expensive to be the dominant powder production method, and will always be limited to metals that can be formed into a wire [47].

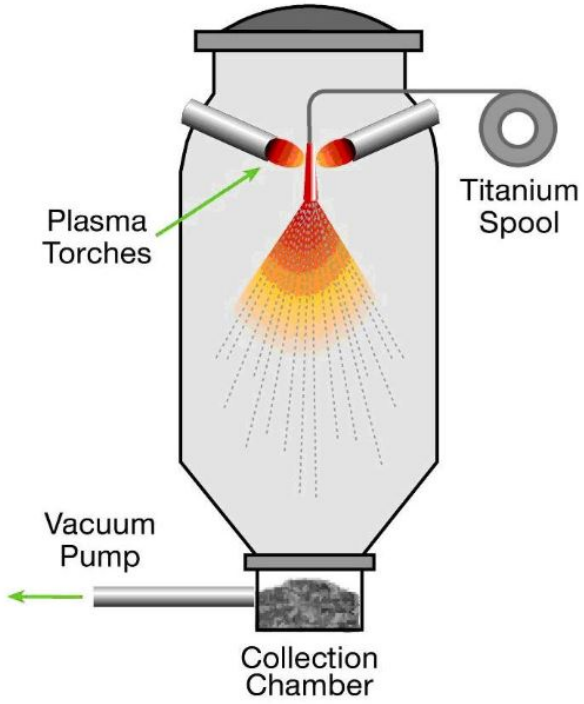

Figure 2.16. Diagram of the plasma atomization process [47]

2.2.2.1 Gas Atomization

The single most dominant metal powder production method is gas atomization as it provides a high quality product useful for a wide variety of applications at a moderate cost. Figure 2.17 is a schematic of the gas atomization equipment. Metal

feedstock is melted under air, inert gas, or vacuum and poured through a nozzle that mixes the molten metal with air or an inert gas such as nitrogen or argon and rapidly disperses it into a spray. A detail view of a generic nozzle is shown in figure 2.18. Spray solidifies as it falls through a contained chamber and forms mostly spherical particles with some asymmetry or satellites. To avoid back pressure in the chamber, a cyclone separator lets gas exit while removing suspended fines. The chamber size must be large enough that the particles will solidify before hitting the sides or bottom. An unchilled chamber is usually on the order of 10 meters tall; cooling with water or liquid nitrogen can reduce the required height, but this will force particles to solidify sooner, often at a larger size and/or more irregular shape [46].

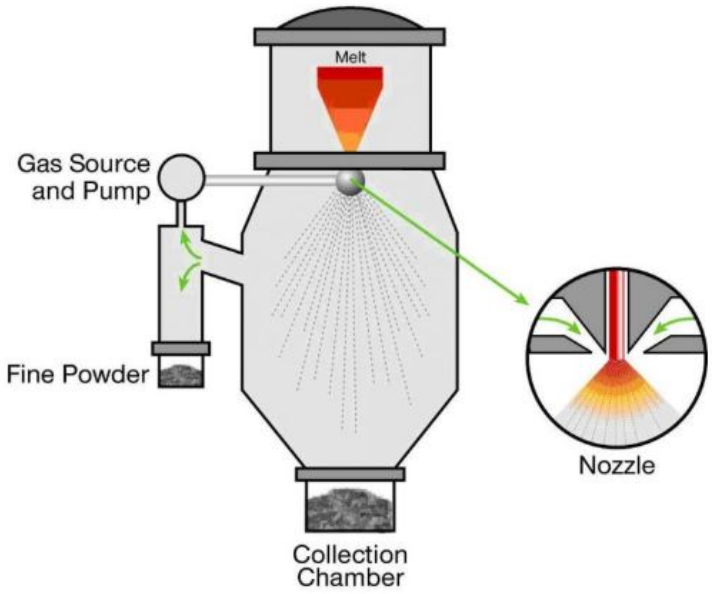

Figure 2.17. Diagram of the gas atomization process [47]

Gas atomization variables include gas type, melt temperature and viscosity in the nozzle, alloy type, feed rate, gas pressure, gas feed rate and velocity, nozzle geometry, and gas temperature. High quality powders from gas atomization require strong control of the variables, with different effects shown in figure 2.19. The greater the energy input, whether melt heat, gas pressure, or another variable, the smaller the

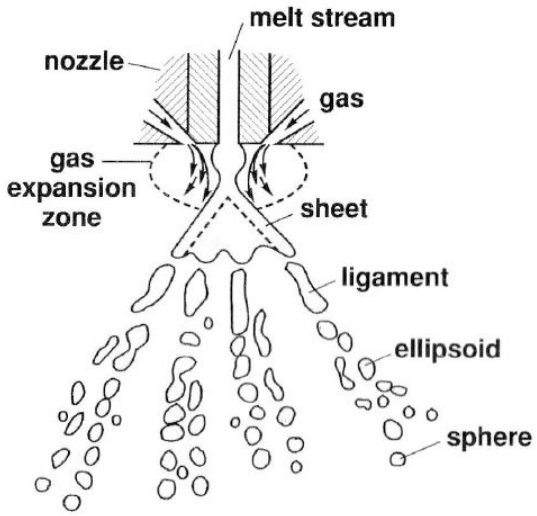

Figure 2.18. The formation of a metal powder by gas atomization involves the break-up of the liquid steram by the rapidly expanding gas. Because of a suction pressure in the gas expansion zone, the stream first forms into a thin hollow sheet, and subsequently forms ligaments, ellipsoids, and spheres. [46]

particle size [46].

After exiting the nozzle, the melt stream forms a hollow cone. Due to high surface shear, the cone breaks down into long ligaments, then continues to break down into smaller spheroid particles. A longer solidification time aids in particle spheroidization, enhanced by higher melt temperatures and lack of coolant. Turbulence and mixing cause fine particles suspended in the chamber gas to re-enter the solidification zone, resulting in agglomeration and satellites. The laser strobe images in figure 2.20 show the degree of turbulence around the nozzle. The final particle size is determined by the initial ligament diameter d_L, which depends on cone sheet thickness W, gas velocity V, melt density ρ_m, and surface energy γ. The equation relating these variables is $d_l = 3[(3\pi\gamma W)/(\rho_m V^2)]^{1/2}$. By the Rayleigh Instability, which dictates that system energy cannot increase and volume is constant, final particle size will be 1.5 times the ligament diameter [46].

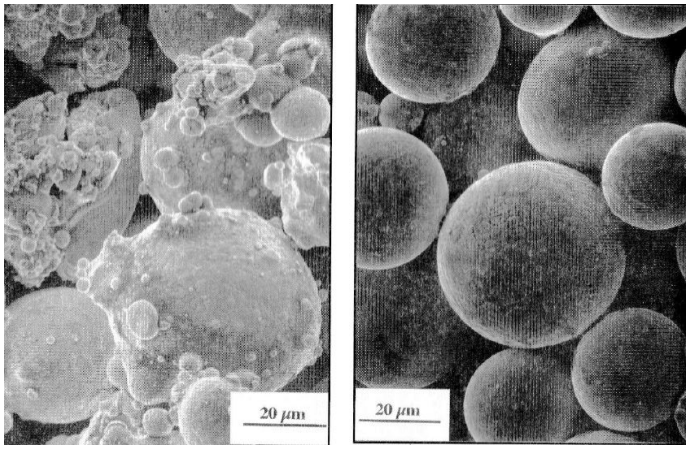

Figure 2.19. SEM images of inert gas atomized powders show the dramatic difference in particle agglomeration and satellite formation associated with control of turbulence and particle reentry into the atomization zone. The powder on the left exhibits poor control and shows splats, agglomerates, and satellites; in contrast, the powder on the right was formed under controlled flow conditions and is free of satellites. [46]

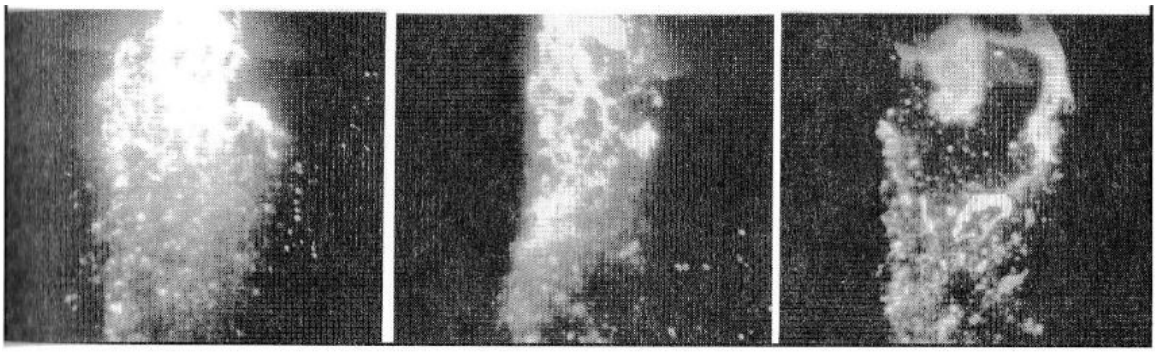

Figure 2.20. These three high speed laser strobe video pictures show the turbulent events during gas atomization of stainless steel, taken 0.033 seconds apart. [46]

2.2.3 Powder Characterization

Powder can be described by its size and distribution, shape and shape variation with particle size, surface area, inter-particle friction, flow and packing, internal particle structure, and composition homogeneity and contamination.

2.2.3.1 Sampling

Collecting a representative sample of powder can pose a challenge when the production lot size is often several tons and the typical sample size is less than a gram. The best samples are blends of several small samples taken from moving streams of powder. When static sampling is necessary, many small samples must be taken from random locations to avoid bias [48]. If the powder has been shipped before sampling it has likely settled and should be remixed to even out the distribution of particle sizes [46].

2.2.3.2 Morphology

Typical methods of determining size and shape involve screening/sieving and microscopy. Particle size measurement depends on the measurement technique as well as particle shape and orientation, and can encompass surface area, projected area, maximum dimension, minimum cross sectional area, or volume. Most instruments will assume a spherical shape and report a diameter, though this measurement becomes less accurate as particles become more irregular. Consequentially, more spherical powders will report data with higher confidence. Particle size is reported as a distribution or histogram; unsieved powder will typically follow a log-normal distribution [49].

Particle shape influences packing, flow, and compressibility, and can provide a qualitative measure of ease of fabrication and processing. Some typical powder shapes

are shown in figure 2.21. The simplest quantitative particle descriptor is aspect ratio; more spherical particles approach unity [46].

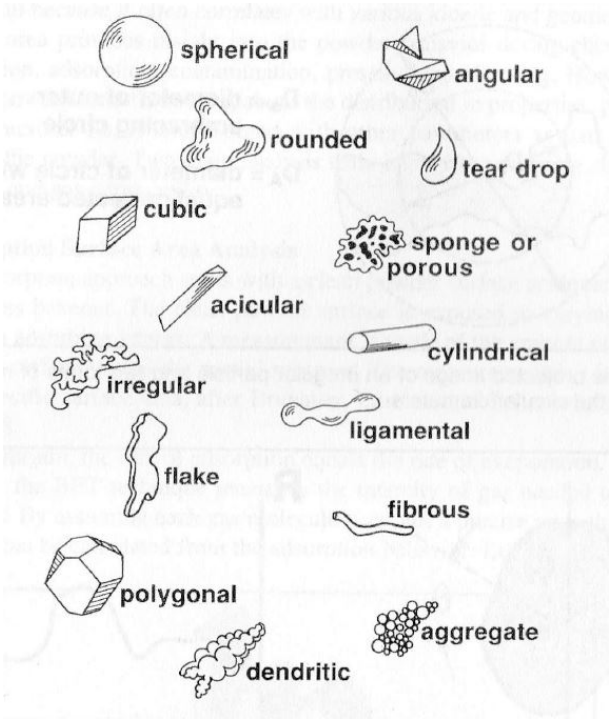

Figure 2.21. A collection of possible particle shapes and the suggested qualitative descriptors [46]

Most metal powders are cohesive due to their small size and are not easily dispersed. Fines, small particles typically below 10 μm in diameter, will agglomerate together due to small amounts of adsorbed moisture and can create a falsely high particle size measurement. Removing moisture can actually increase capillary action and increase the strength of agglomerates, so if agglomerates are a problem they can be dispersed by adding in polar molecules such as OH^- and agitating [46].

2.2.3.3 Inter-Particle Friction

Inter-particle friction determines how the powder will flow and pack. The friction is dominated by surface area, surface roughness, and surface chemistry. As surface area increases, friction increases, and particles pack and flow less efficiently. Spherical

particles have the the lowest surface area to volume ratio and are the ideal shape for packing and flowing [46].

Tap density refers to the highest density that can be achieved by vibration of a powder without external compression. The ratio of tap to apparent (un-vibrated) densities is called the Hausner ratio and is a signature characteristic of the inter-particle friction. The Hausner ratio of smooth, spherical powders will approach unity [50].

The angle of repose is a simple measure of inter-particle friction; it is defined as the angle a free cone of powder makes with a normal surface when poured through a funnel. Unfortunately, the angle varies significantly with the method of measurement. The most common techniques are to pour the powder through a funnel at a set height and measure the diameter of the cone once the cone is as tall as the funnel, or to pour the powder through a funnel until it completely fills a ring under the cone, then measure the height of the cone [50].

Powder flow rate is often measured with a Hall flowmeter, diagrammed in figure 2.22. The flowmeter measures the flow rate as the time required for 50g of powder to flow through a standard funnel [50]. The specifications and procedures for the Hall flowmeter can be found in American Society for Testing and Materials (ASTM) B212. Some Hall flowmeter times are listed in figure 2.23.

2.2.3.4 Chemical Composition

Metal powders can be produced from blended elemental stock, or by powderizing a pre-alloyed material. Bulk chemical compositions can be verified from wet analysis, flame spectroscopy, atomic absorption, x-ray diffraction, x-ray florescence, or neutron activation [46]. It is easy to contaminate powders during production, and essential to confirm that the powder produced match the specification.

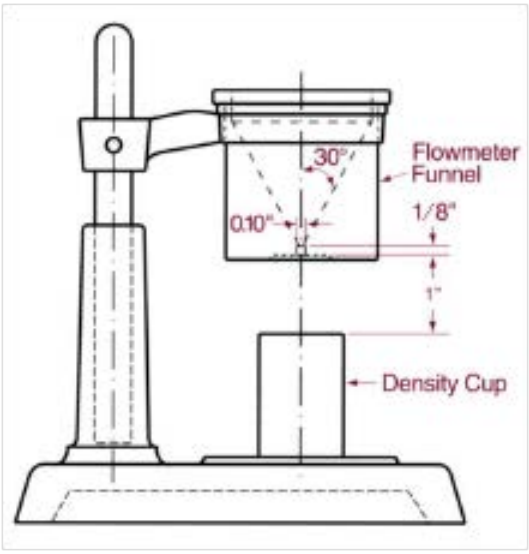

Figure 2.22. Diagram of the Hall Flowmeter [51]

Metal powder		Lubricant		Apparent density, g/cm³	Flow rate of 50 g (2 oz) powder, s		Flow rate of 25 cm³ (1.5 in.³) powder through Hall funnel, s	Weight of 25 cm³ (1.5 in.³) powder used in volumetric flow rate study		Calculated flow rate for 50 g (2 oz) powder based on volumetric flow rates, s
Material	Grade	Type	Additions, wt %		Hall funnel	Carney funnel		g	oz	
Iron	MP-35HD	Zinc stearate	None	2.81	25.77	4.62	37.74	70.27	2.46	26.86
		Zinc stearate	0.25	3.12	23.37	4.16	...	...	...	...
		Zinc stearate	0.50	3.05	25.93	4.30	...	...	...	...
		Zinc stearate	0.75	3.02	26.80	4.41	...	...	...	...
		Zinc stearate	1.00	3.00	27.57	4.59	40.55	74.52	2.61	27.21
Iron	MH-100	Zinc stearate	None	2.48	30.14	5.26	38.61	62.06	2.17	31.11
		Zinc stearate	0.25	2.97	23.23	4.14	...	...	...	...
		Zinc stearate	0.50	2.93	26.39	4.47	...	...	...	...
		Zinc stearate	0.75	2.86	28.97	4.80	...	...	...	...
		Zinc stearate	1.00	2.87	30.42	5.12	42.20	71.31	2.50	29.59
Iron	A-Met 1000	Zinc stearate	None	2.94	26.24	4.34	39.16	73.91	2.59	26.49
		Zinc stearate	0.25	3.27	23.89	4.04	...	...	...	...
		Zinc stearate	0.50	2.98	28.30	4.55	...	...	...	...
		Zinc stearate	0.75	3.18	25.46	4.41	...	...	...	...
		Zinc stearate	1.00	3.18	25.58	4.45	41.70	79.57	2.78	26.20
Stainless steel	304-L	Lithium stearate	None	2.61	30.62	4.92	39.65	65.45	2.29	30.29
		Lithium stearate	0.50	3.08	29.43	4.80	...	...	...	...
		Lithium stearate	0.75	3.01	33.20	5.42	...	...	...	...
		Lithium stearate	1.00	3.02	37.51	6.13	59.89	75.54	2.64	39.64
Premix bronze (90% Cu–10% Sn)	5099	Stearic acid	None	2.96	21.68	3.99	32.69	74.92	2.62	21.82
		Stearic acid	0.25	3.54	24.01	5.17	...	...	...	...
		Stearic acid	0.50	3.54	24.66	5.38	...	...	...	...
		Stearic acid	0.75	3.42	27.91	5.24	49.84	85.68	3.0	29.08
		Stearic acid	1.00	3.38	34.75	7.20	...	...	...	...
Brass	B-126	Lithium stearate	None	2.89	33.26	5.51	48.56	72.67	2.54	33.41
		Lithium stearate	0.25	3.06	33.52	5.77	...	...	...	...
		Lithium stearate	0.50	3.14	38.70	6.38	64.01	78.25	2.74	40.90
Aluminum	...	None	...	1.19	66.43	...	39.23	29.73	1.04	65.97

Figure 2.23. Flow rate of metal powders through Hall and Carney funnels [50]

2.2.4 Microstructure Control

The microstructure of metal powders will affect how they melt and sinter. Amorphous microstructures are easier to melt than crystal lattices, which require additional energy to break down. Powders with sufficient time to form dendrites on the surface will be rougher, increasing particle friction [46]. It is therefore important to understand the different potential microstructures and their driving processes.

2.2.4.1 Microstructure of Powder

Due to their small size, powders are rapidly solidified and can contain amorphous structures, smaller microstructures than those of wrought or cast material, and nonequilibrium compositions. Generally, powder microstructures are very homogeneous. The cooling rate of powders tend to be on the order of $10^3 - 10^4$°C/s vs a maximum of 10^3°C/s in castings, and with coolants the rates can be as high as 10^8°C/s. If cooling rates are on the slower side, powders will form with a very small dendrite microstructure, with small 'arms' caused by segregation. The dendrite crystals in each particle will have a higher melting point vs. the interdendritic regions. When cooling rates increase, dendrites will decrease in size until there is a shift to fully equiaxed grains. The extreme case of rapid cooling will produce a powder that is fully amorphous, retaining the random atomic arrangement corresponding to the liquid phase. Figure 2.24 compares dendrite and equixed surface grains. Internal powder microstructure is typically evaluated by mounting a sample in resin or polymer, polishing, and etching [46].

2.2.4.2 Kinetics of Solidification

Homogeneous transformations of liquids to crystalline solids start with spontaneous nucleation by the organization of atoms into a solid structure withing the

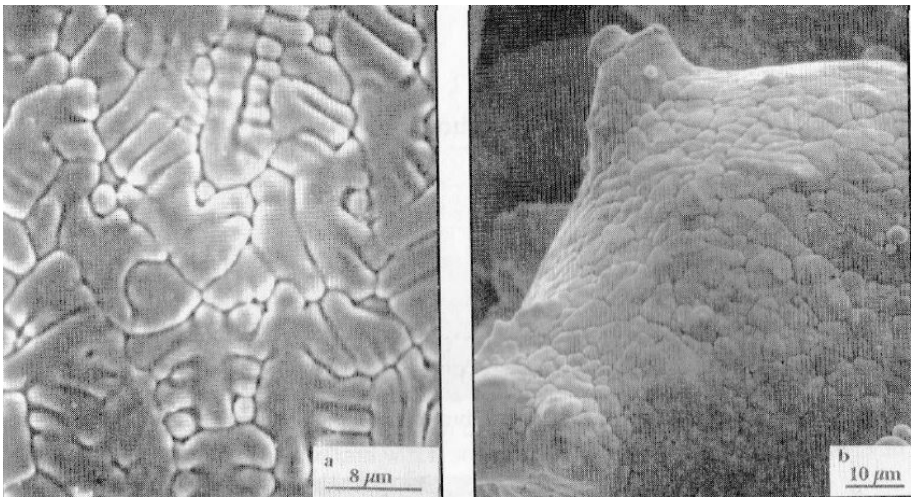

Figure 2.24. A microstructural comparison of steel powders of the same alloy: (a) centrifugal atomization produces a dendritic microstructure due to slower cooling and (b) the faster cooling of inert gas atomization produces an equiaxed microstructure [46]

liquid. Once a solid nucleus exists, other atoms will join it and reduce the system energy, creating a crystalline solid. Nucleation is a process that requires energy, as it implies the creation of an interface at the boundaries of a new phase; at high temperatures, the driving force for nucleation is low, the required nucleation size is high, and nucleation is impeded. If a nucleus does not form, especially at high temperatures, the liquid will simply become so viscous that it cannot transform, becoming a glassy amorphous solid. The nucleation frequency in solidifying particles follows a Poisson distribution; consequently, there is a probability for any given particle size that some of the particles will solidify without crystallization [52].

Far more commonly, solidification occurs heterogeneously, when a defect or small particle initiates solidification. This can be caused by small particles in the gas atomization chamber impacting liquid droplets and providing an initiation site for solidification, as shown in figure 2.25. If the goal is an amorphous solid to aid in melting, it is beneficial to increase melt temperature, reduce turbulence at the nozzle, and reduce airborne fines. At the high solidification rates typical of gas atomization, the solidification front can move faster than the rate of atomic diffusion in the liquid,

preventing dendritic segregation and increasing homogeneity [46].

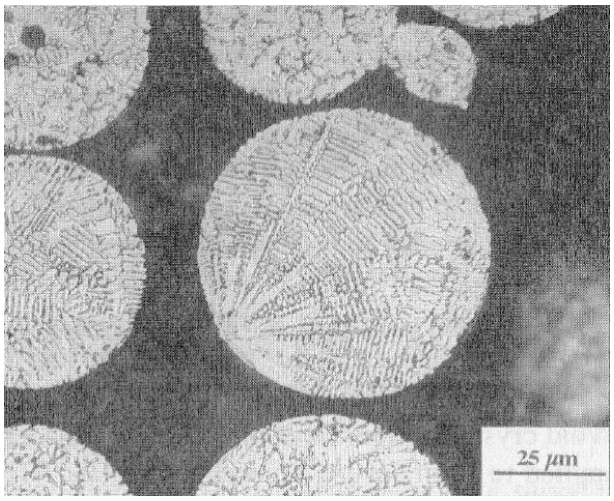

Figure 2.25. Optical micrograph of an atomized Pd-Cu-Au particle showing the radial dendrite structure originating from a surface nucleation site, most likely induced by contact of the molten droplet with a solidified satellite. [46]

2.2.5 Powder Tailoring

Once powders have been produced, it is possible to modify them so that they better fit the requirements of the end user. Powders can be selected for size, smoothed, combined to aid in packing, annealed, and work hardened. Powders are sometimes blended to form new compositions because prealloyed powders, though more chemically pure, have higher hardness, higher melting temperatures, make coarser powders, and are more prone to work hardening [46].

2.2.5.1 Handling and Safety

When working with metal powders it is important to avoid inhaling the smallest particles, which can reach the lungs and be dissolved. Particles between 0.01 and 10μm in diameter can bypass the mucous membranes and be dissolved. Masks or respirators should be worn when working with powder, and Positive Air Pressure Respirator (PAPR) systems should be used with toxic or reactive powders [53]. The

maximum toxic air exposure for metals such as arsenic and lead is around 10^{-4}g/m^3. Metal dust is an explosion hazard, especially reactives such as aluminum, magnesium, zirconium, and titanium. Fortunately, the danger associated with normal handling of common metals like copper, iron, or steel is low [46].

2.2.5.2 Shape Modification

The highest density parts are made from smooth, spherical particles with hard surfaces. Tumbling powder smooths rough surfaces and cold works the powder, adding strain energy that decreases melt temperature. Powder impurities are often segregated to particle surfaces, and can be removed with chemical or ultrasonic treatments. Oxidation on the surface of metal powders leads to an unexpected result: a decrease in inter-particle friction. Once the powder has been sieved to a specified size, it will sometimes be annealed to further homogenize microstructure and decrease surface roughness [46].

2.2.5.3 Packing

Powders are classified using sieves or screens, then combined to aid in packing. Most powders will pack randomly, with typical spherical powder tap density at 65% of the theoretical maximum. Bimodal particle blends will pack to higher densities than monosized particles. Smaller particles are selected to fit the interstices of the large particles without forcing them apart; there is an optimal ratio of large particles to small particles for every particle diameter ratio, as shown in figure 2.26. Generally, the ratio of large particle diameter to small particle diameter should be between seven and ten. Trimodal powder mixtures will also work, but returns diminish while complexity increases. The ideal case for packing density assumes spherical particles; actual optimal points will vary with shape [46].

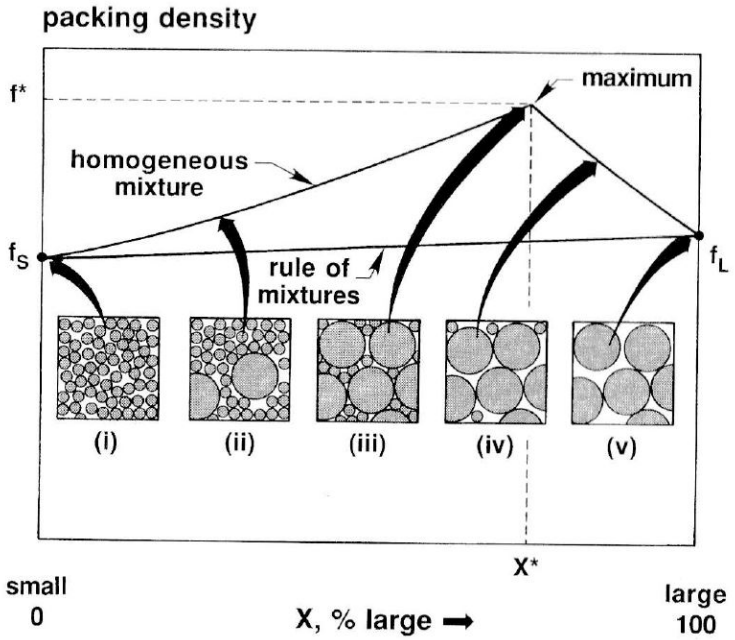

Figure 2.26. A plot of fractional packing density versus composition for bimodal mixtures of large and small spheres. The sketches show how the density improves up to the critical point where the large particles are closely packed and the small particles fill the interstitial voids. [46]

2.2.5.4 Mixing

Vibration during powder transportation will cause segregation, as large particles will 'float'. Powders must be re-mixed, which is typically accomplished through rotating drums, similar to concrete mixers. In additive manufacturing shops without access to mixing drums, powders should be sieved on arrival to redistribute the particle sizes. Metallic particles will work harden with prolonged agitation, so if this is undesirable for the application, mixing should be minimized [48].

2.3 Additive Manufacturing of Metals

Additive manufacturing (AM) is defined as an incremental layer-by-layer build up to create solid parts, in contrast to traditional subtractive manufacturing methods where material is removed from a large block. Most AM technologies use powder

or wire as feedstock that is then selectively melted by a localized heat source. The technology has proven to be a way to bypass traditional supply lines, enable rapid prototyping, and massively increase design flexibility, though its applications in metals were limited until 2006, when machines were able to reliably produce high density, high quality parts [54]. As AM transforms from rapid prototyping to rapid manufacturing it is required that we fully understand the process, its variables, the effect they have on part microstructure, and consequently the performance of the AM parts.

2.3.1 Printing Technologies

There are currently three dominant technologies used to produce dense metal parts with high surface quality: Laser Beam Melting (LBM), Electron Beam Melting (EBM), and Laser Metal Deposition (LMD). The various AM processes share the same basic approach: a 3D model is created on a computer, the model is virtually sliced into layers corresponding to the AM process layer thickness, and this data is read into a machine that directs the process through the deposition of the individual layers [54].

LMD is similar to traditional welding; a melt pool is created under argon or helium and feedstock in the form of powder or wire is fed in. The system is typically set up with a head that moves around on a five-axis gantry while the part is open to the atmosphere. LMD is faster than powder bed technologies, and the build volume can be much larger. However, part quality is not as high, as surface finishes are coarse (see figure 2.27) and large pores between tracks are common [54]. New hybrid systems where LMD is coupled with a Computer Numerical Control (CNC) mill show promise [55].

LBM, also called Laser Powder Bed Fusion (LPBF), is a powder bed process: powder is spread or dispersed at a predetermined layer thickness over a build chamber

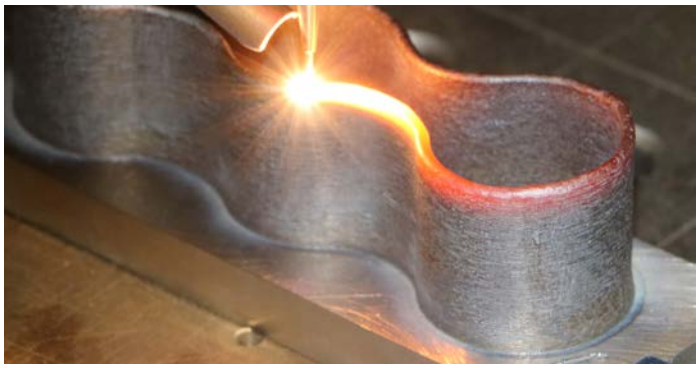

Figure 2.27. An example of the surface finish typical of a wire-LMD part [55]

area. The build chamber is enclosed and filled with a constant flow of an inert gas such as argon or nitrogen. The powder is melted by a laser in a predetermined pattern based on the 3D model slicing. Certain LBM machines have the ability to preheat the build area, reducing part deformation. EBM is similar to LBM, except that the heat source for melting powder is an electron beam generated by an electron gun. The build environment is vacuum, as opposed to an inert gas. Before melting a layer, the electron beam will unfocus and preheat the powder bed, though this can cause some sintering of powder prior to melting, potentially making parts more difficult to clean and roughening the finished surfaces [54]. The powder bed preheating produces parts with more uniform microstructures and less residual stresses due to reduced thermal gradients, though the magnetic lensing of the electron beam limits the process to non-magnetic alloys [56].

2.3.2 Laser Beam Melting

Most LBM machines use a metal or polymer coater blade to scrape a thin layer of powder off of a main working pile and over the build area. The powder storage bin, called the dosing chamber, has a motor underneath that raises a predetermined level for every layer of the part, supplying a new layer of powder for the coater. Likewise, the the build area has a motor underneath that will drop the part the preset depth

of the powder bed thickness for every layer of the part. As the part grows in size, the build chamber lowers and the dosing chamber raises [57], as shown in Figure 2.28. To ensure that the entire build area is evenly coated in powder, more powder than would be necessary to perfectly cover the surface should be used. If the powder is not overdosed, the region of the build area furthest from the powder chamber may be thin, or parts on closer to the dosing chamber may block powder from reaching the far side of the plate [53].

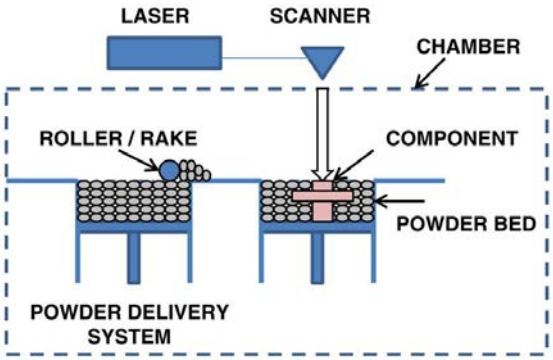

Figure 2.28. Generic illustration of an AM powder bed system [57]

Laser beam sources commonly used in LBM are single mode fiber lasers in continuous wave mode that emit in the near infrared, typically 1060 to 1080 nm. Spot diameters on the focal plane are typically 50 - 180 μm; laser scan speeds are typically between 15 mm/s and 15 m/s. The laser must provide enough heat to exceed the material melt temperature and create a melt pool [54], otherwise the part is only sintered. Sintered parts are weak and porous, and require additional processing steps to become useful [46]. The melt pool follows the movement of the laser and creates weld tracks; the pattern of the weld tracks and the degree to which they overlap is called the scan strategy. A sample scan strategy is shown in Figure 2.29. The distance between weld tracks is called hatch spacing [57].

The commonly used volumetric energy density (W/mm^3) calculated from hatch

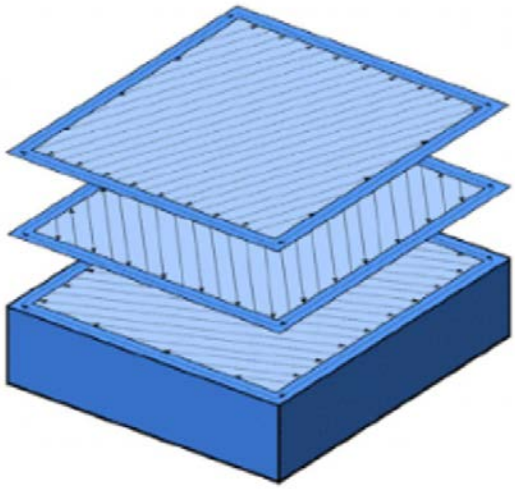

Figure 2.29. A sample scan strategy with skin contours and parallel meander core infill. Note that the angle of the infill track changes with each layer [58].

spacing h, powder bed thickness t, laser power P, and laser scan speed V is [54]:

$$E_V = \frac{P}{Vht} \tag{2.1}$$

Another form of energy density that is used in the literature is a surface area measure based on laser focal spot diameter f rather than hatch spacing and laser speed[59]:

$$E_f = \frac{P}{\pi t \frac{f^2}{4}} \tag{2.2}$$

The energy density due to laser spot size, E_f, can be multiplied by the interaction time I, defined as the spot size diameter divided by the scan speed, to produce the laser fluence [59]:

$$LaserFluence = E_f * I = \frac{4P}{\pi f t V} \tag{2.3}$$

Laser Fluence is less commonly used, as it does not capture the influence of hatch spacing and weld overlap, but it is very useful in initial scaling during single weld track trials, and can be more descriptive for thin walled structures. E_V is simpler

to calculate from others' work and use for scaling, as power, speed, powder bed depth, and hatch spacing are nearly always reported; laser beam diameter is less often reported. While neither E_V or Fluence fully captures the physics of the process, they are still useful for comparison and initial scaling [60].

Powder bed fusion requires a substrate to build upon and provide a heat sink. LMD processes use a heavy build plate that is clamped or bolted to the machine to provide a rigid substrate and resist warping [32]. The build plate material should complement the powder alloy to minimize differences in thermal stresses and enhance weld fusion - ideally, the build plate and powder are identical materials. When building in a machine without a preheated build plate, the first layer of the part is usually burned in by the laser, or exposed, multiple times to locally heat the plate and provide better fusion [53]. High thermal gradients between the part and plate can cause cracking and warping if the thermal path is inadequate, as shown in figure 2.30.

Figure 2.30. Warped and cracked AM parts due to inadequate thermal bridging

When the powder is melted by the laser, some powder will burn off and produce soot. This soot and any excess powder are collected in in the overflow area. The inert gas in the system progresses over the build chamber in such a way to blow airborne soot towards the overflow. To prevent the soot from contaminating the powder bed, the laser exposure sequence should begin on the 'downwind' side, nearest the overflow [53].

2.3.3 Relation of Additive Manufacturing to Welding

The technologies used in additive manufacturing (AM) and welding are nearly identical, the difference being that welding joins two semi-finished parts into a more complex part, and AM builds complete parts layer-by-layer. Because of the similarities, the experience gained from a century of welding can be used to make informed decisions in AM.

The small physical dimensions possible with powder bed parts require low power (<400 W), small spot sizes (<100 μm), and must be moved rapidly (1 m/s) to avoid keyholing. In welding, keyholing is sometimes desirable when making a very thick weld, as the heat of fusion will penetrate narrowly through a thick section. While the extreme heat needed does penetrate through the part, it will also vaporize some of the metal and leave gas pores trapped in the weld [32]. In powder bed processes, the weld thickness is small, so the porosity introduced by keyholing is undesirable. Ideal welds are created in the conduction regime of melting, where the power density is not great enough to cause boiling, as happens in the keyhole regime. A pictorial comparison of the conduction vs keyhole regimes is shown in Figure 2.31. The power and speed must be balanced so that the weld penetrates deeply enough for the application without crossing into the keyhole regime.

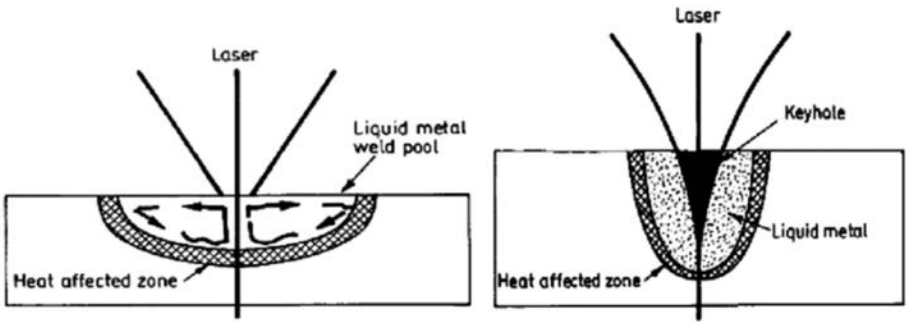

Figure 2.31. keyhole and conduction mode welds [61]

As the deposition rate of a weld process increases, so does surface flatness and

roughness, which scale with layer or bead height. Similarly, the surface finish of AM parts degrades as the powder bed thickness increases. Higher quality surface finishes can be achieved at lower and slower power and feed settings. A surface roughness feature unique to powder bed processes is a fine sandpaper-like roughness due to satellites, especially on lateral and overhanging surfaces. Smoother parts can be manufactured by starting with finer powders, as LPBF surfaces will never be better than the mean particle powder size [32]. Ideally, LPBF parts would be used in the as built or simple heat treated condition, but the surface roughness often needs to be removed. Due to the complex nature of additive geometries, it is often difficult or impossible to reach some areas for smoothing [57].

Welding and AM both require a localized heat source to create a small melt pool. The leading area of the melt pool is liquid, while the rear is a cooled fusion zone. The area in the region immediately surrounding the melt pool is the HAZ, which is caused by the steep thermal gradients. The regions of the melt pool are diagrammed in Figure 2.32. The thermal conditions of the melt pool control the cooling rate, which determines the micro and macrostructures of the final product. The size and shape of the melt pool are affected primarily by scan speed, which can be orders of magnitude higher for AM processes vs. traditional welds. Faster speeds reduce melt pool size and cause them to become more elongated [32].

The mechanical properties of a weld will depend on solidification rate and severity of the thermal gradient. The preferred crystal growth direction is parallel to the temperature gradient, creating columnar grains. In welds, the columns will radiate from the weld into the main structure. In AM parts, the columns will point from the melt pool to the largest local heat sink, usually down in solid parts. Texture describes the macroscopic orientation of grains that have grown into each other after multiple layers have been melted. Weld texture is similar to AM texture: columnar

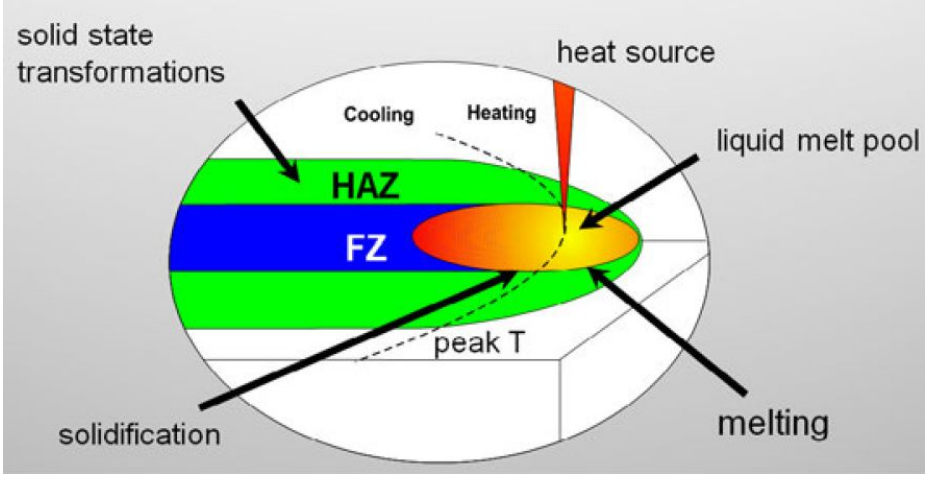

Figure 2.32. Illustration of a localized melt pool used for welding. Melting takes place on the front side of the pool, while solidification and solid state cooling trnasformations take place on the back side of the weld pool to create a fusion zone and heat affected zone around unaffected base metal [32]

grains that follow the thermal gradients, but no explicit preference in grain crystal orientation. The primary method used for interpreting grain texture is EBSD, as it will highlight grain size, orientation, crystal structure, and crystal orientation [32]. Figure 2.33 compares EBSD maps of a welded and additively manufactured material.

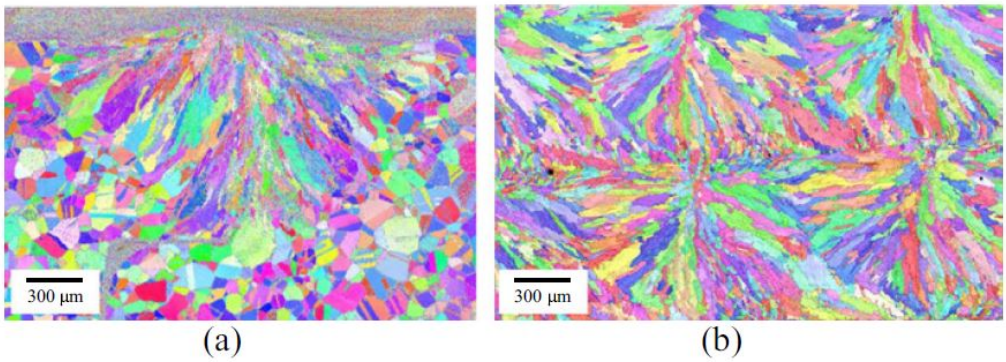

Figure 2.33. Similarities between the grain structures formed by (a) a single pass computer controlled electron beam weld in 21-6-9 stainless steel [62] and (b) a DED multilayer build in 304L stainless steel [63]

The localized heat source and thermal gradients cause plastic deformation around the melt pool. The deformation causes stresses that can cause solidification cracking or distortion. Distortion profiles common to welding, shown in figure 2.34, are often

seen in AM. Welders will commonly plan out build sequences to reduce distortion, and AM parts can be made with specific scan strategies to reduce warping [33, 32].

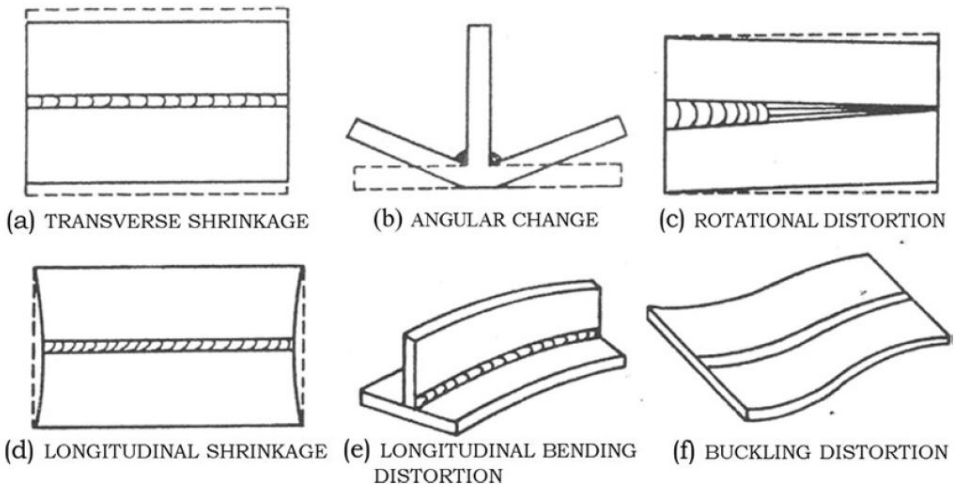

Figure 2.34. Six types of distrotion that occur during welding as a reult of the localized heat [64]

AM parts are built on a substrate that introduces mechanical restraint; thicker build plates decrease distortion, but also introduce higher residual stresses. Welders see this same issue if they build parts in jigs and do not heat treat before removing the part from the jig. If a large AM part is cut off of its build plate before stress relieving in a furnace, the part is likely to warp [32].

2.3.4 Limitations

As with any technology, AM powder bed processes have limitations. Faults common to welded parts, anisotropy of the microstructure, and specific difficulties of geometry are currently limiting the applicability of the technology. Details of these faults are laid out below.

2.3.4.1 Anisotropy

AM parts are subject to mechanical anisotropy due to the microstructural texture. The alignment of coarse columnar grains causes the development of preferential directions, which is detrimental to applications involving multidirectional stresses [32]. In small, solid, vertical parts built directly under the laser, the anisotropy of the parts can be considered orthotropy, and there has been some interest in exploiting this for the manufacture of nickel superalloy turbine blades, but parts with simple geometries are more economical to manufacture using traditional methods [65]. In parts built nearer the edges of the build plate, the laser will not be at a normal incidence angle, changing the angle of the thermal gradients. The columnar grains can be equiaxed by specific heat treatments, significantly reducing the anisotropy, though the heat treatments are not necessarily the same processes that work for other manufacturing methods due to the different microstructures induced by casting, forging, or sintering [66].

2.3.4.2 Porosity

Solidification texture and inherent defects (porosity and lack of fusion) are unavoidable in layer-by-layer AM processes. Additionally, defects in AM parts can link together more easily in plane and form at much more regular intervals. When AM processes are performed at high power density, melting is likely to occur in the keyhole regime, resulting in entrapped vapor which forms spherical voids. To ensure proper interlayer bonding, the penetration of the weld into previous layers only needs to be a small fraction of the layer height, so staying well within the conduction mode and avoiding keyholing is not difficult when the primary concern is only avoiding delamination [32]. A generic view of the processing zone in terms of speed and power of the laser is shown in Figure 2.35.

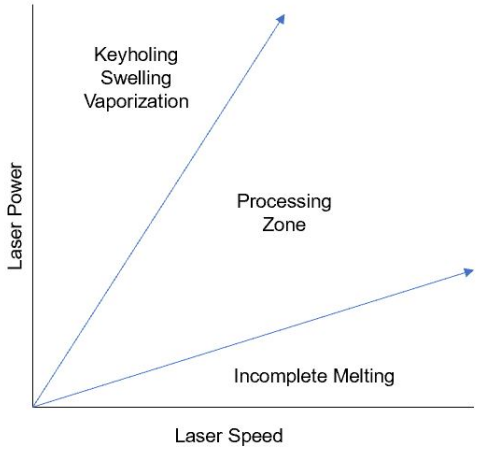

Figure 2.35. A generic illustration of the parameter cone seen when plotting speed vs power

If the power density is insufficient, lack of fusion pores can form between weld tracks; these pores will be irregularly shaped. Porosity can also come from gas that is entrapped in powder during gas atomization, or get trapped in the melt pool during solidification. The noble gasses will not dissolve in liquid metals, so to reduce porosity some metals are manufactured under nitrogen, which can dissolve into the liquid metal before solidification. This is only possible if the nitrogen requirement for the material will not be exceeded [32]. Images comparing the different types of pores are in figure 2.36.

It is important to reduce the porosity of AM components to below 0.5% to increase their fatigue life, fracture toughness, and service life [54]. Until a material can be reliably produced with low porosity, it will not be possible to manufacture structural parts from that material. Porosity can be measured in a variety of different ways. The Archimedes method, in which part porosity is estimated from density is nondestructive and inexpensive, but its accuracy is low as it does not account for partially melted powder. Optical microscopy is widely used, but it is a destructive technique and can only evaluate a 2D plane; shape effects are not accounted for. CT scanning

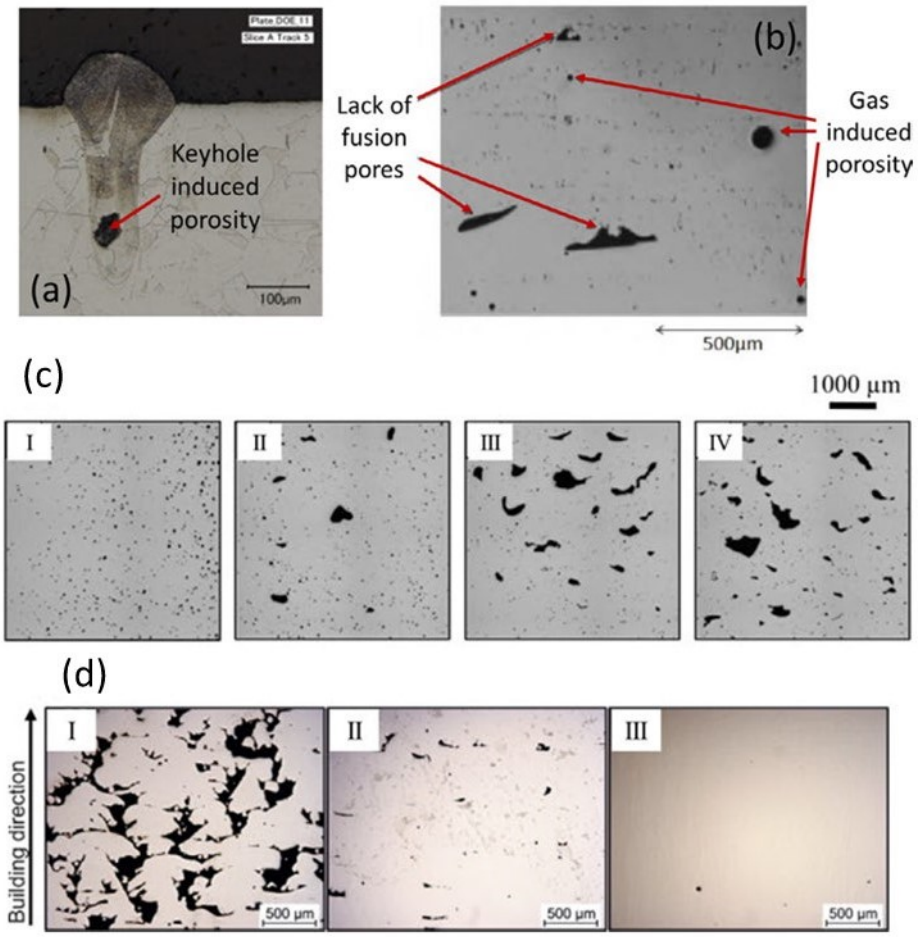

Figure 2.36. (a) keyhole porosity [67], (b) lack of fusion pores and gas induced porosity [68], (c) effect of scanning speed on porosity (I) 250 (II) 500 (III) 750 and (IV) 1000 mm/s [69], (d) effect of laser power on porosity (I) 90 (II) 120 and (III)180 W [70]

and Synchroton Radiation micro-Tomography (SRμT) are very accurate above their noise floors and account for all 3-dimensional effects, but the initial equipment cost is very high and they require highly trained personnel [32].

Pores can be closed with HIP treatment, but closing pores becomes more difficult as part thickness increases. Additionally, HIP cannot close surface cracks, is expensive, and adds additional processing time [32].

2.3.4.3 Chemical Vaporization

As in welding, the high temperatures in the melt pool can cause some of the metal to vaporize. Some elements, like aluminum, are more volatile than others and can cause changes to the composition of the alloy, causing changes in material properties [33]. Because the entire part must be built up by the melt pool, changes to the alloy chemistry are fairly homogeneous and can result in the entire part not meeting its requirements. It should be noted that though vaporizing elements escape through the surface of the melt pool, there is enough mixing within the melt pool to ensure that the losses are even throughout the melt pool depth. When working with a new alloy or process parameter settings, it is essential to track chemistry both before and after the build process; this is most commonly done with Energy Dispersive X-Ray Spectroscopy (EDS) or destructive flame mass spectroscopy [32].

2.3.4.4 Surface Quality

AM parts will have rough surface finishes, and the roughness increases with layer thickness. High roughness at the surface of a part will reduce part strength and fatigue life, so it is vital to achieve a smooth surface on structural parts. Some AM parts can be machined, peened, or etched, but these steps are often not practical when applied to multiple areas of a part [54]. Building parts with high surface finishes requires thin layers, low power, and low speed, which cumulatively increase processing time. Print settings will often run at higher power and speed in the center of a solid part to decrease print time, but the surface contours will be run at a quality setting to achieve a higher surface finish. Another technique is to only expose the center of the part at very high power every other layer to drastically decrease print times; this is typically only used in parts where the quality setting requires a very thin layer [53].

Rough surfaces can also be created from improper melting and balling. Improper

melting occurs when not enough energy is applied to melt the power particles. Balling occurs at high scan speeds when the melt pool becomes elongated and breaks into small islands due to the Rayleigh Instability. The surface tension of the liquid metal pulls the balls to the edges of the weld [32]. Images of surface defects are shown in Figure 2.37.

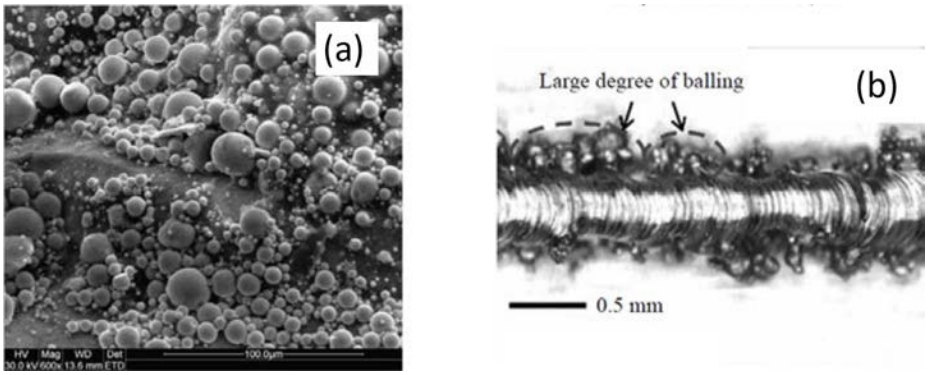

Figure 2.37. (a) SEM image of solid powders on build surface [71], (b) balling effect [72]

2.3.4.5 Cracking

There are three main types of cracking present in AM: solidification cracking, liquation cracking, and delamination. Solidification cracking in AM is similar to what is seen in welding, with cracking occurring along grain boundaries. Solidification cracking occurs when the melt pool shrinks as it cools; it occurs most often at the top center of the weld beads. Liquation cracking occurs in the partially melted zone when grain boundary precipitates melt below the alloy liquidus temperature. Delamination is the separation of consecutive layers caused by residual stresses in excess of yield and the incomplete fusion of layers [32]. Any cracking is cause for part rejection and must be eliminated.

2.3.4.6 Geometric Constraints

Geometric constraints, other than the obvious maximum dimensions of the build chamber, refer to geometries that cannot be printed reliably and with sufficient quality. Overhanging features, typically at angles over 45^o, are prone to warping, especially upward, and interfering with the powder coating blade [73]. Every material will have a minimum sized structure that it can successfully print; some materials, such as inconel, are capable of being printed as single-laser-width lattices [74], while others, such as aluminum, need several passes of the laser to successfully bond [75]. Even if a material can be successfully printed at a single laser-width pass, if the part exceeds a certain size it will begin to warp, as the thin sheet does not provide an adequate thermal bridge. Parts built using a scan strategy of interrupted laser passes can cause powder denudation, where powder is blown off a part by the melt pool vapors, especially at the end of a laser pass. It is easier to produce a high-quality part if the laser path is continuous, as powder denudation will be minimized and consistent [76].

2.3.5 Additive Manufacturing of Steel

Steel, the world's most common engineering metal, has several alloys that have been proven in powder bed manufacturing techniques. The most commonly used steel is 300M maraging steel, treated within the AM community as a tool steel. Maraging steels are low carbon steels that were developed in the aerospace industry for missile and rocket motor casings, recoil springs, landing gear, and high performance shafts, gear, and fasteners. Maraging steels can be used in the as-built condition, though their strength improves with aging [77].

Stainless steels are also popular, as they can resist oxidation to the high surface area powder. Two precipitate hardened alloys, 17-4PH and 15-5PH, are successfully

used in AM, and offer high strength and good toughness, though their corrosion resistance is decreased when additively manufactured. Printed precipitate hardened steel parts can be used in the as-built condition, but they are most often heat treated to cause the precipitate hardening they are named for. Austenitic stainless steels, especially 316L, are popular in AM. Austenitic stainless steels are single phase, indicating that they are not heat-treatable, but AM parts built from 300 series stainless have been shown to achieve higher strengths than their wrought counterparts. Unlike with precipitate hardened steels, printed austenitic stainless steels maintain their high corrosion resistance [77].

Recent work has been done to develop printing parameters for two high value nickel-chrome-molybdenum alloys, 4340 and 4140. Initial results indicated that parameters could be selected that produced high-density parts with strengths similar to that of wrought 4340 and 4140. However, cracks formed during heat treatment, and more must be done before these alloys can be used for production AM parts [20].

2.4 Process Parameter Theory

The initial work for additively manufacturing a newly powderized material must always begin with establishing the primary process zone that will create high-density parts. The primary variables manipulated during this initial development are laser power and speed, followed by weld track hatch spacing, though powder bed depth and laser focal point size can also be manipulated if the machine has variable capabilities [32]. For a new material to be used in production, understand and control of all of the process variables, listed in table 2.4, must be established.

Table 2.4. List of the primary processing parameters of LPBF [32]

Variable	Units
Beam Power	W
Energy Density	J/mm^3
Beam focal offset, spot size	
Hatch spacing (line offset)	μm
Scan speed	mm/s
Scan strategy	
Powder, density, morphology	
Powder bed thickness	μm
Powder moisture level	
Deposit layer, Z step	μm
Build plate preheat	°C
Chamber gas, ppm O_2, H_2O	

2.4.1 Parameter Development

Typically, printability is determined by a series of experiments that explore a parameter space, holding all but a few variables constant. This parameter space is usually laser power and speed, beginning with weld tracks and moving solid parts. Initial weld track experiments look for areas where successful material deposition is obtained. Such studies produce process maps such as the one shown in Figure 2.38 and use successful combinations to evaluate optimal hatch spacing. Successful results allow progress in manufacturing without explicitly understanding the complex relationship between the thermal, mechanical, and chemical/metallurgical processes. Heuristic approaches can be developed [78] to limit the parameter range, but are generally more time consuming and expensive than experimentation [32].

Despite the difficulty of using any mathematical processes to predict parameter success, printability can be broadly predicted using laser Fluence or E_V. Ranges of Fluence and E_V that resulted in high quality parts of the same or similar metals to be printed can be used to extrapolate potential regions of process parameters that will produce high quality parts. Fluence is ideal for initial weld track studies,

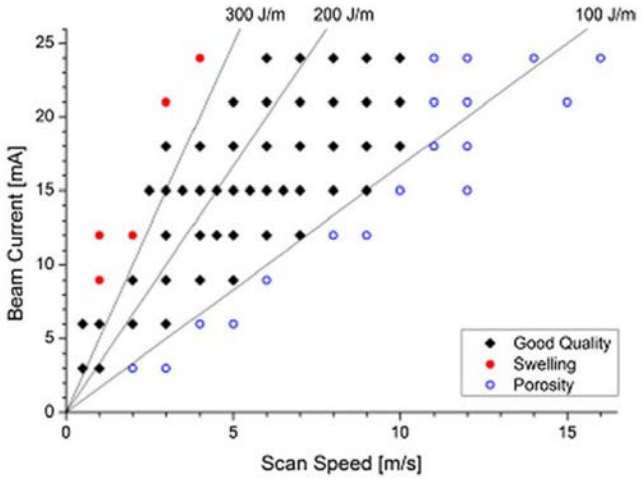

Figure 2.38. Process map for the electron beam melting of Ti-6Al-4V for achieving optimal build quality [79]

as it calculates an energy density independent of hatch spacing. If an ideal line of Fluence is identified for a particular material, additional high quality laser power and speed combinations on the same or similar machines can be chosen along that line of Fluence. Once an ideal level of Fluence has been identified, E_V can be used to compare differences in hatch spacing studies when creating solid parts.

2.4.2 Limitations of Theory

Volumetric energy density or heat input is often used to compare studies, though it is not good to directly compare energy density between different lasers without accounting for differences in laser absorptivity. The successful parameter space is typically shaped as a cone, with the lower bound of power input appearing as a shallowly sloped line defining the transition to incomplete melt porosity, and the upper bound of power input appearing as a steeply sloped line defining the transition to keyholing, swelling, and vaporization (see figure 2.35). The transition from successful parameter space to incomplete melt or keyholing is not purely linear, but the space can be approximated by the cone [32].

Process simulation using data derived from limited empirical observations is typically insufficient due to the complexity of AM material-process parameter interactions. For this reason, researchers will most often focus on a single alloy and run a large variety of experiments. There are standard processes in place to determine weldability of engineering alloys and filler wires; for AM to mature as a technology, similar standardized test procedures for determining printability of new alloys must be developed [32].

2.4.3 Previous Methods in New Parameter Development

The transformative potential of AM initiated a surge of interest in both government and industry, leading to large investments in researchers in AM. Most researchers will follow the same development path as listed above in the section introduction: selection of initial parameter range, trials of initial speed, power, and bed thickness settings to find a suitable range of settings for fusion, followed by trials to determine optimal hatch spacing, and finishing with solid part builds and maximizing density.

2.4.3.1 Initial Parameter Selection

In the early days of LPBF, parameters were selected in a purely random manner. Now that there is a large data base from which to draw, parameter selection in a new range can be projected from previous studies of the same material, and parameter selection for a new material can be hypothesized from successful values of similar materials. Researchers who were able to extrapolate previous work on a material to a larger, more powerful machine include Kamath et al. [80], Yasa [81], Wang et al. [82], and Sadowski et al. [83] . Researchers who used similar materials to choose initial parameter values include Jelis [84], Dzogbewu et al. [85], and Shahzad et al. [86].

In a study at Lawrence Livermore National Laboratory, Kamath et al. were able to scale process parameters for 316L steel from a 200W machine to a 400W machine. Their work began with an Eager-Tsai simulation to compute the temperature distribution of the surface of the melt pool, as well as the longitudinal melt pool cross-section for several parameters, including laser power, speed, and spot size. The Eager-Tsai simulation uses a simple model of a Gaussian beam on flat plate to describe conduction mode laser melting in the absence of powder. While the study did identify an initial parameter range, it was also able to determine which parameters were most important in governing melt pool depth, length, and width. Their results indicated that laser speed and power were most important in determining melt pool width and depth, while laser power and absorptivity determined melt pool length, while beam size had little impact on the melt pool size [80]. This study confirms that laser power and laser speed should be the primary parameters varied in an initial experiment.

2.4.3.2 Weld Track Studies

Weld track studies are used to confirm parameter settings, and can be used to identify the keyholing region, whether the melt pool has penetrated for sufficient fusion, and weld bead quality. The general process for weld track experiments is described in Yadroitsev et al. (2010) [87]. Bare base plate material is exposed at the proposed settings to determine if the heat is sufficient to fuse the powder to the base plate, and single track trials are run at the same settings, then compared to the no-powder results. The primary finding of Yadriotsev is that there is a considerable negative correlation between the thermal conductivity of the powder and the range of optimal scanning speed for LMD processes. Considering that the thermal conductivity of steel is an order of magnitude greater than that of Inconel and Titanium [88],

two metals commonly used in AM, it is likely that there is a large range of optimal speeds for AM of steel.

Etched cross sections of weld tracks will identify the depth and shape of the melt pool, and the effect that different powers and speeds will have on them, as shown in Figure 2.39. Studies of this sort have been undertaken by Dzogbewu et al. [85], Kamath et al. [80], Yeuling et al. [89], Wang et al. [82], Yadroitsev et al. [90], and many others, and their processes will be followed in this research.

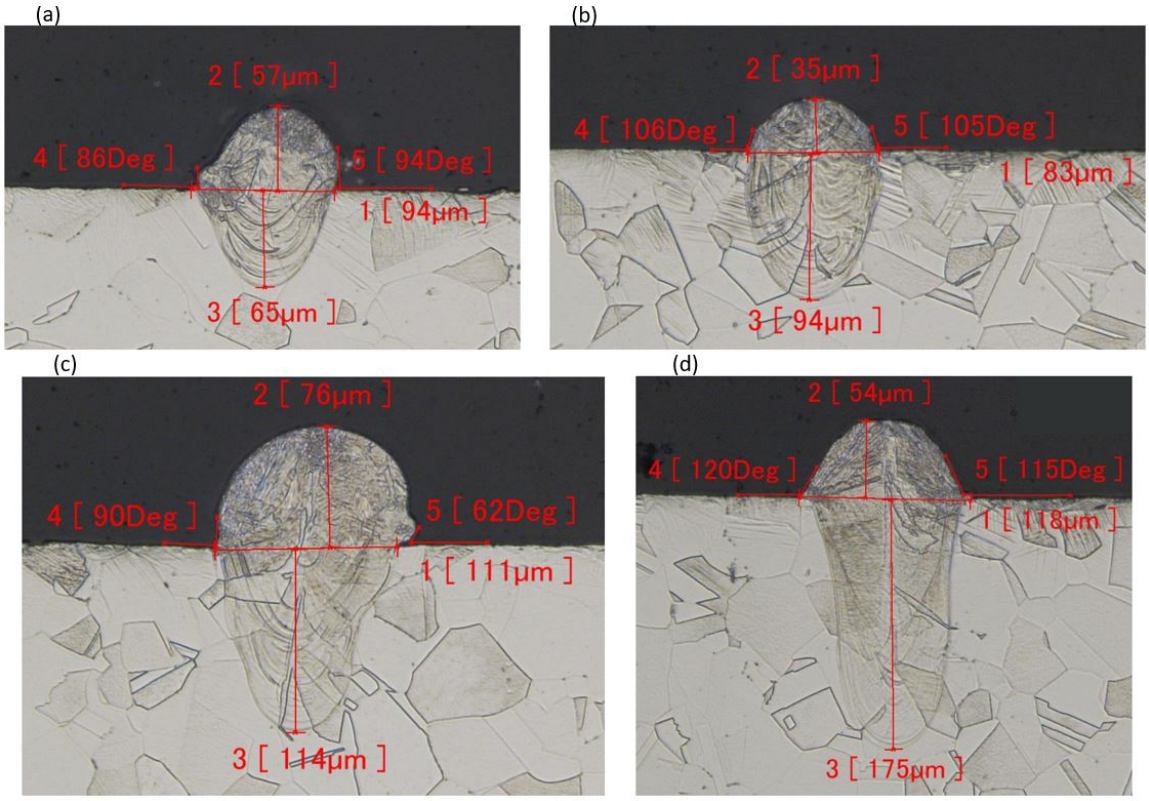

Figure 2.39. The melt pool width, height, and depth for (a) 300 W and 1800 mm/s, (b) 300 W and 1500 mm/s, (c) 300 W and 1200 mm/s and (d) 300 W and 800 mm/s. The weld in figure (b) is the best quality of the four, with conduction regime melting, penetration 2-3 times the powder bed depth, and a symmetric profile [80]

2.4.3.3 Porosity Studies

The establishment of an optimum hatch spacing is almost exclusively a trial and error process. It can be accomplished similarly to weld track studies, by cross sec-

tioning a single weld layer perpendicular to the weld direction and evaluating gaps between weld beads [85], or, more often, by printing small solid objects and sectioning in multiple directions [91, 69, 92]. Hatch spacing can also be evaluated to some extent by a surface finish and topology analysis [59]. Once a hatch spacing has been selected to minimize lack of fusion defects, power and speed selections can be modified to account for any further remaining porosity, improve surface finish, or optimize for a specific microstructural phenomena [93].

2.5 Summary

This research will cover the parameter selection and optimization process of AF9628 steel, a high-strength, high-toughness martensitic alloy that is entirely devoid of tungsten. The powder, produced using gas atomization, will be evaluated for chemistry, morphology, and flowability, and its microstructure will be examined to gain insight into the process control and make generalizations about microstructure post-weld. Initial LPBF parameters will be selected for printing on a 200W machine with a 50 μm laser spot size by comparison to similar alloys, and adjusted based on successful weld track trials. Once successful weld tracks are completed, solid parts will be built and parameters adjusted to maximize density. It is expected that the rapid cooling inherent to LPBF will produce primarily martensitic AF9628 with very small columnar grains. This as-built AF9628 will likely not have the required strength and toughness to meet the material specifications, and will need heat treatment to reach the desired values. This chapter has reviewed all of the theory and background needed to complete the experiments and analysis.

III. Powder Characterization

3.1 Overview

In powder bed process additive manufacturing, consistent powder characteristics are important for ensuring repeatability in the manufacture of metal parts. In general, powders that are essentially spherical and have a particle size distribution that facilitates dense packing have been shown to result in final manufactured parts with high densities and good mechanical properties [94]. In addition to sphericity and particle size distribution, morphology, density, chemistry, flowability, and thermal properties will contribute to the performance of the powder. Characterizing these properties in both virgin and recycled powder is essential to establishing a data pool from which to create thresholds that correlate powder properties with mechanical properties of finished parts [94]. This chapter presents a discussion of several methods used to characterize the morphology, particle size, internal porosity, and chemistry, as well as an evaluation of the overall quality of the gas atomized AF9628 Weapons Steel (AF9628) powder produced by Powder Alloy Corporation (PAC). A summary of the measurands used for AF9628 powder characterization in this thesis is presented in Table 3.1.

Table 3.1. Metrology methods used for powder characterization in this thesis and their associated measurands

Measurand	Metrology Method	Equipment Used
Powder Appearance	Scanning Electron Microscopy	Tescan Maia3
Particle Size Distribution	Optical Microscopy	Morphologi 4
Particle Morphology	Optical Microscopy	Morphologi 4
Particle Porosity	Optical Microscopy	Zeiss Observer
Powder Chemistry	Energy Dispersive Spectroscopy	EDAX Octane Elect

3.2 Methodology

3.2.1 Manufacturing Data

Production of the AF9628 powder was contracted to PAC in Cincinnati, a company with experience creating small batches of custom powders. The powder was created by combining individual elemental powders, using argon gas atomization, for a lot of 288 lbs, and would adhere to the specifications listed in Table 3.2. The powder was delivered at the end of November, approximately three months after the contract was awarded, at a cost of $66 per pound.

Table 3.2. Powder Contract Specifications and Reported Values, by % Weight

Element	**Specified Amount (Min/Max)**	**Reported Value**
Carbon	0.26/0.29	0.28
Manganese	0.5/0.8	0.7
Silicon	0.9/1.1	0.9
Chromium	2.5/2.8	2.8
Nickel	0.9/1.2	1.1
Copper	0/0.2	<0.1
Vanadium	0.05/0.15	0.12
Molybdenum	0.85/1.05	1.00
Phosphorus	0/0.10	<0.010
Sulfur	0/0.005	<0.005
Aluminum	0/0.015	0.009
Titanium	0/0.006	0.004
Oxygen	0/300 ppm	280 ppm
P+Sn+As+Sb	0/0.035	<0.035
Hydrogen	0/2 ppm	2 ppm
Hall Cup Time	-	19.6 s/50 g
Apparent Density	-	4.4 g/cc

The powder was delivered with a report of its chemistry, size distribution, apparent density, and Hall Flowmeter time. Reported values were determined by independent laboratories that are GE, SAFRAN, NADCAP, and ISO17025 approved, and tests were performed per ASTM's B214, B822, B212, and B213. The testing indicated that

the powder lot met all specifications, with values listed in Table 3.2. The full report delivered with the powder is available in Appendix A.

3.2.2 Sampling

Static powder sampling was conducted in accordance with the procedures found in ASTM B215-15. A representative virgin powder sample was collected from the top of five of the 10 lb containers delivered with the powder lot, after the containers had been inverted twice to account for settling during transport. A representative recycled powder sample was collected from two separate sieving batches, after multiple builds of dense parts produced with virgin powder.

3.2.3 Appearance and Morphology

Initial powder testing involved characterizing the powder's appearance, confirming particle sizes and distribution, and evaluating the powder's circularity and aspect ratio. To determine appearance, pieces of conductive double-sided carbon tape were dipped into the representative powder samples and placed in a Tescan Maia3 Scanning Electron Microscope (SEM). SEM images are valuable for surface visualization, which can provide insight into the quality of the powder manufacturing process. To confirm the reported particle size and distribution, 3 mm^3 samples of powder were dispersed in a Malvern Morphologi 4, an optical instrument that measures particle size. Access to this equipment was provided by the University of Dayton Research Institute (UDRI). The Morphologi 4 measurements are comparable to X-Ray Diffraction (XRD), with dimensions accurate to ± 4 μm [95]. After the powder samples were dispersed in the Morphologi 4, images were taken to confirm an even dispersion of powder particles (Figure 3.1). The raw data was filtered to remove any lint or dust particles that would skew the data. The Morphologi 4 also calculated the average particle circularity and

aspect ratio, which provide a quantitative evaluation of particle quality.

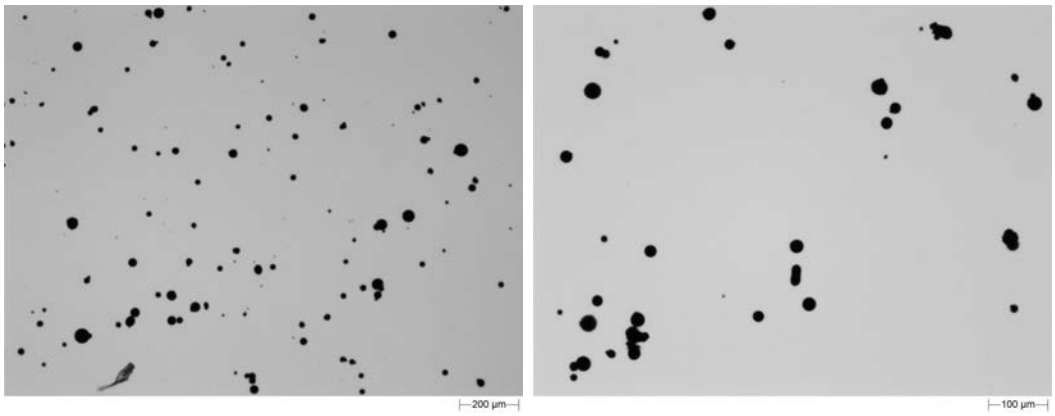

(a) Virgin powder dispersion **(b)** Sieved powder dispersion

Figure 3.1. Dispersion pattern of powder samples in the Morphologi 4.

3.2.4 Porosity

Entrapped gas within the powder can contribute to porosity of the finished parts, and large pores in particular can contribute to low density. To evaluate internal porosity, powder must first be mounted in a binder so that it can be held for sectioning. Powder samples of 0.25 cm^3 were placed in 1.25 mm cylindrical plastic molds, which were then placed under vacuum. Approximately 20 mL of thinset two-part epoxy, mixed by weight, was siphoned into the molds. The molds were then removed from the vacuum and allowed to cure for 24 hours. After curing, the resin pucks were removed from the molds and wet ground by hand on a succession of silicon carbide grinding disks. Polishing with diamond slurry and a polishing wheel was attempted, but resulted in powder being ripped out of the resin matrix. The best finish was achieved through wet sanding by hand on a 1200 grit grinding disk, then buffing with a dry cotton pad, though this did leave numerous scratches in the surface. Sputter coating with 5 nm of iridium was attempted for imaging in an SEM, but this obscured most features. Final images of the sectioned powder were obtained on an optical Zeiss Observer equipped with an Axiocam 503 mono camera and extended depth of field

z-stack image stitching software.

3.2.5 Chemistry

The primary objective of the chemical analysis was to characterize differences between virgin and recycled powder, not to confirm the detailed elemental analysis delivered with the powder. An initial powder chemistry characterization was conducted via an EDAX Energy Dispersive X-Ray Spectroscopy (EDS) unit, which is useful for determining which elements are present in a material and their relative concentrations, though it cannot identify compounds formed by those elements. EDS uses the characteristic x-rays released by elements upon excitement by an electron gun to generate a spectrum of wavelength peaks. Several elements have similar characteristic x-ray wavelengths, and the user should be careful to avoid misidentification of the peaks. The virgin and soot samples used for appearance characterization in the SEM were compared for differences in composition and relative changes in concentration. The chemistry data was compiled from six points within each viewing window, with an excitation voltage of 10 kV. Powder chemistry was again evaluated using X-Ray Fluorescence (XRF) courtesy of Dr. Flater, AFRL/RWMW, Eglin AFB. The theory behind XRF is similar to that of EDS; a sample is bombarded with x-rays, and it releases an electron. This causes electrons to move between shells, which by conservation of energy causes the release of a secondary x-ray at a characteristic wavelength. XRF data can identify chemical compounds, and can also be used to determine the relative quantities of elements present, excluding light and heavy elements that are difficult to detect. These two similar characterization techniques will be compared to confirm the repeatability of the results.

3.3 Results

3.3.1 Appearance

The images of virgin powder indicate that the PAC process produces primarily spherical powder with some bonded particles and satellites, and a grain structure produced during solidification. Elongated particles (ligaments) and accretionary particles are present, but not common. Some shattering of particles appears to have occurred, with some containing large pores. The overall quality of the powder indicates that the manufacturer's gas atomization is well-controlled, but cannot approach the quality of plasma atomized powder. Very few particles had a smooth surface texture and most show evidence of dendrite arms, indicating that the particles had time to crystallize during solidification and may require a higher energy density to fully melt. Examples of the different features observed in the virgin powder sample are shown in Figure 3.2.

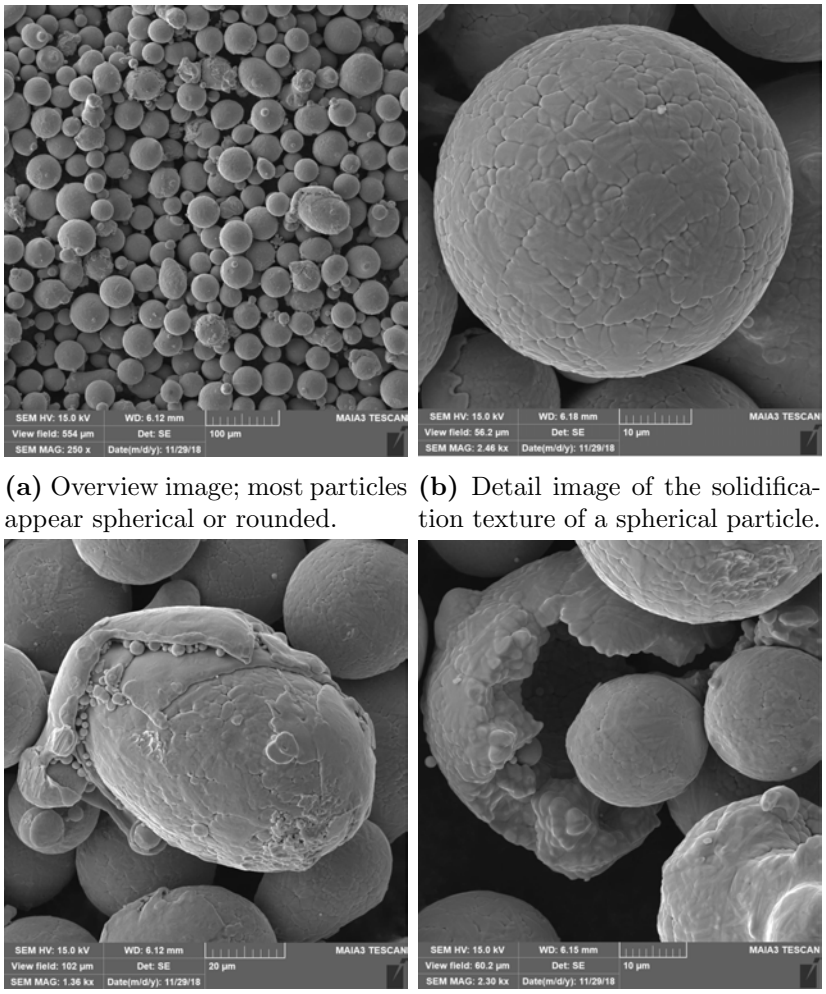

(a) Overview image; most particles appear spherical or rounded.

(b) Detail image of the solidification texture of a spherical particle.

(c) Detail image of an elongated particle that appears to have solidified before being partially covered by a molten particle.

(d) Detail image of a hollow particle; most likely the particle shattered during formation, as the entrapped gas made the particle weak.

Figure 3.2. Scanning electron micrographs of different virgin powder features.

Repeating the imaging with recycled powder yielded similar results in terms of the overall appearance. However, there was an addition of clearly identifiable partially melted particles, examples of which are shown in Figure 3.3. The partially melted powder creates agglomerates which will eventually decrease the overall smoothness and sphericity, leading to a decrease in powder flowability. To ensure that the sieve was removing most of the soot, soot samples were swabbed from inside the MLab at

the end of a large part build and examined with an SEM. The soot, visually deep black in appearance, was revealed to be composed primarily of powder, with large agglomerated soot particles and very fine sub-micron individual soot particles mixed in. Examples of the different features observed in the dirty powder sample are listed in Figure 3.3, and pictures of the soot are shown in Figure 3.4.

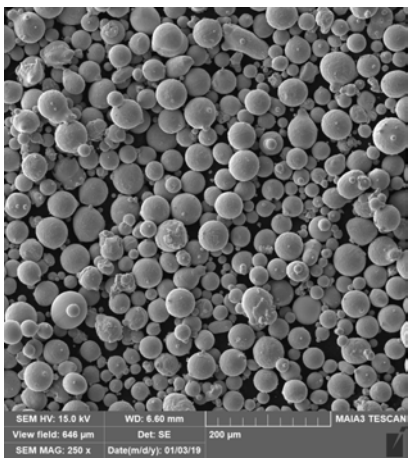

(a) Overview image; most particles appear spherical or rounded, with a slight increase in the number of agglomerates.

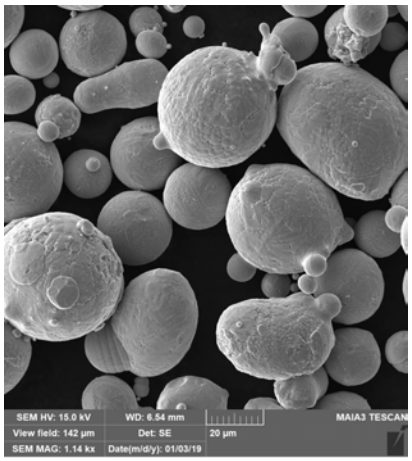

(b) Detail image of agglomerates created during processing.

(c) Detail image showing powder with smooth, partially melted patches joining larger particles into agglomerates.

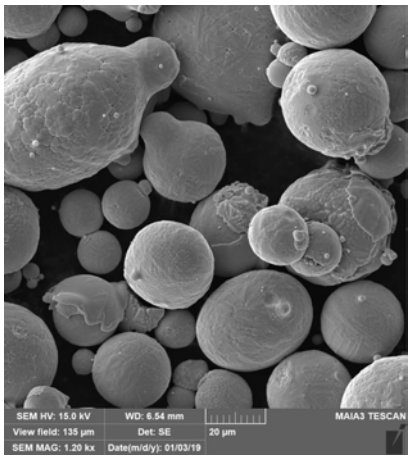

(d) Detail image of additional partially melted regions.

Figure 3.3. Scanning electron micrographs of different sieved powder features.

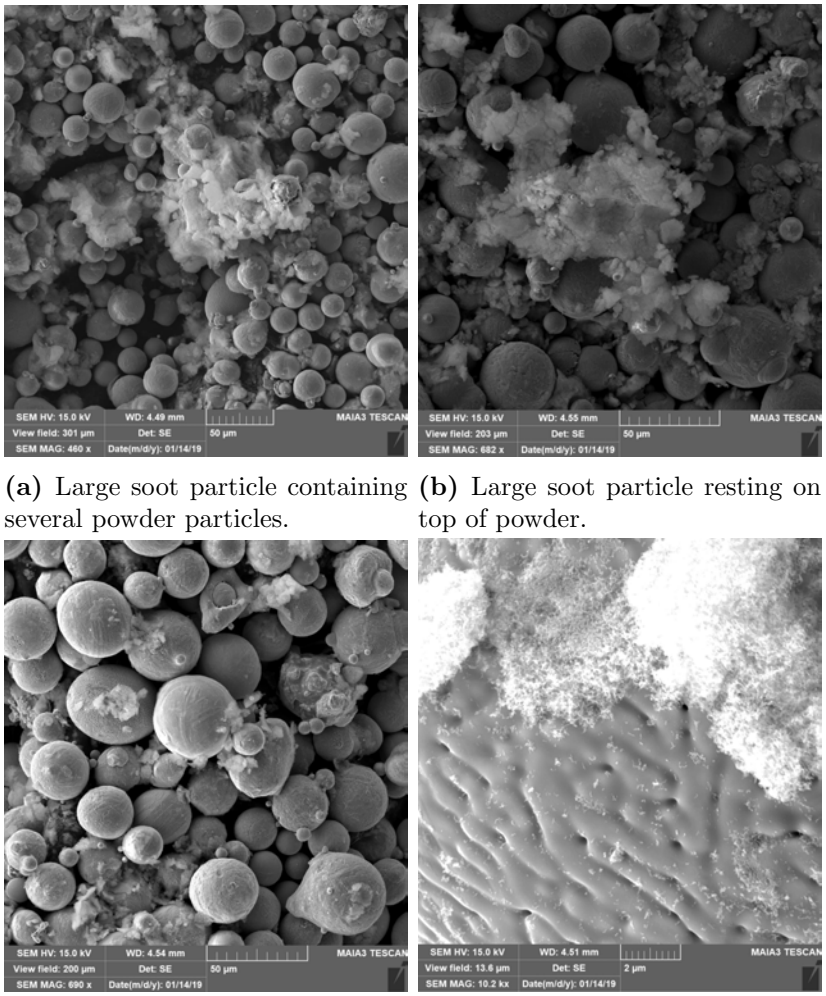

(a) Large soot particle containing several powder particles.

(b) Large soot particle resting on top of powder.

(c) Small particles of soot intermixed with used powder.

(d) Detail image of the very fine soot particles present, which are unlikely to be removed in the sieve.

Figure 3.4. Scanning electron micrographs of soot mixed in with used, unsieved powder.

As the SEM images cannot provide any information on color, top-light images from the Morphologi 4 were taken which captured particle coloration. The virgin powder reflected white light, while the recycled powder reflected white, yellow, or blue light. These images indicate that the recycled powder was receiving enough heat to change its microstructure due to thermal cycling. The image taken of the recycled powder in the Morphologi 4 is displayed below in figure 3.5.

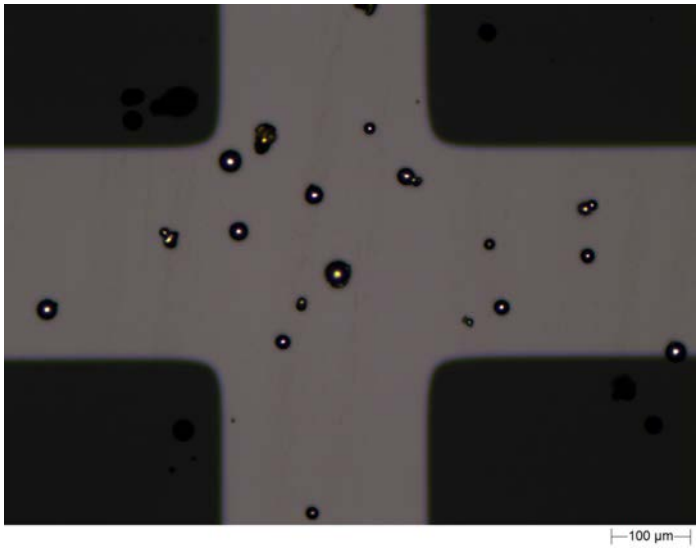

Figure 3.5. Toplight image of sieved powder reflecting some iridescence typical of exposure to heat, taken in the Morphologi 4.

3.3.2 Size and Morphology

The data produced by the Morphologi 4 indicates that the virgin powder is highly circular, with a circularity of around 0.95 and an aspect ratio of around 0.90. The drop in part circularity and aspect ratio, and increase in elongation and diameter with powder reuse indicate that powder agglomeration during processing will affect the flowability and evenness of the powder bed. However, some anecdotal evidence from UDRI researchers indicates that powders with a circularity of above 0.8 will flow well, and can be used without any loss of part quality. The metrics generated by the Morphologi 4 (see Table 3.3) indicate that the reuse of AF9628 powder should not have any detrimental affect on powder flowability.

The particle size distribution delivered with the powder indicates that the powder follows a classic log-normal distribution, with a mean diameter of 38 microns (see Figure 3.6). The Morphologi 4 samples, however, indicate that the powder size is bimodal, with a small peak at a 4 microns, and a second peak at 20 - 40 microns. This may be because the manufacturer removed all size data of below 10 microns, as

Table 3.3. Powder metrics from Morphologi 4

Metric	Virgin Powder		Recycled Powder	
	Unfiltered	Filtered	Unfiltered	Filtered
Number of Particles	38512	38207	26132	25396
CE Diameter Mean (μm)	15.46	15.46	20.24	20.51
HS Circularity Mean	0.946	0.953	0.920	0.936
Aspect Ratio Mean	0.901	0.907	0.873	0.8877
Elongation Mean	0.099	0.093	0.127	0.113
Convexity Mean	0.994	0.991	0.982	0.986

particles this size approach the noise floor of XRD and the Morphologi 4. Inspection of the individual particles measured at this size by the Morphologi 4, however, indicate that there are a large number of small, spherical, dense particles present in the powder. The Morphologi 4 data also shows a shift in particle size after processing and sieving, which is likely due to the agglomeration of particles during processing. There is no evidence of an increase in the number of particles larger than 100 μm, indicating that the Concept Laser mechanical sieve used is effective at removing larger sintered particles. The volume transformation data, which is comparable to the raw volume measurement calculated by XRD, is displayed in Figure 3.7.

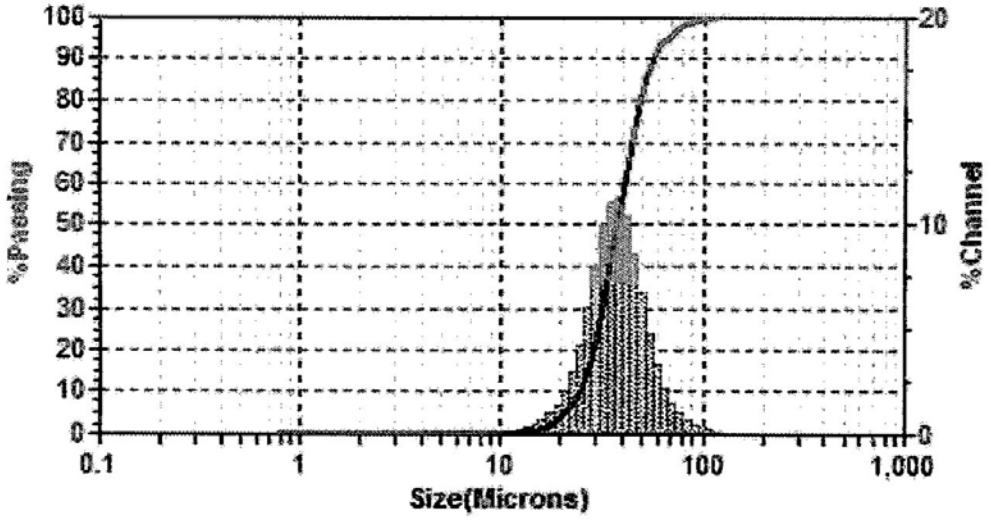

(a) Particle size distribution, as reported by the manufacturer.

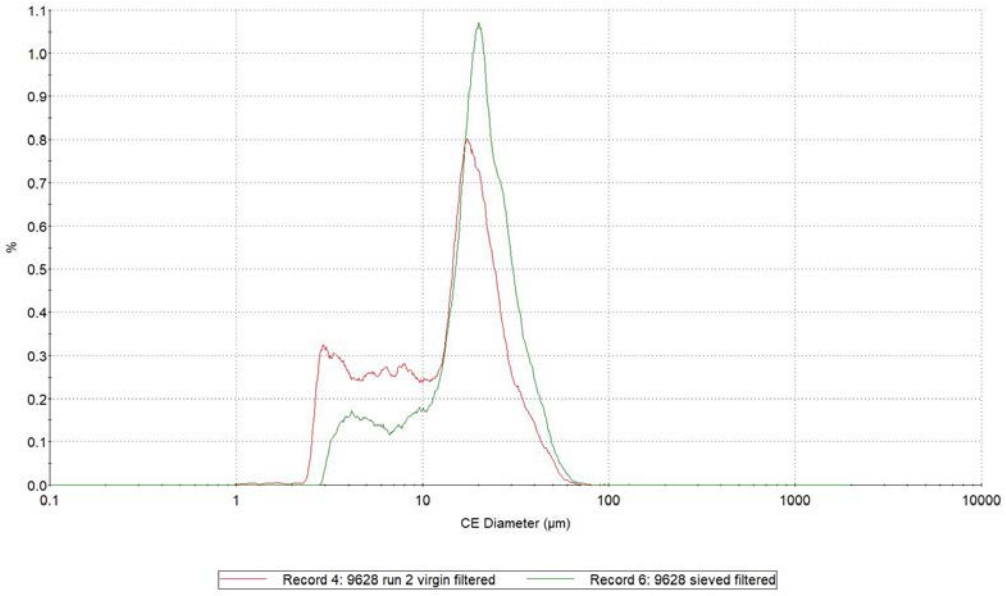

(b) Particle size distribution, as measured by the Morphologi 4, virgin vs sieved.

Figure 3.6. Comparison of the as-reported size dist vs the size distribution calculated by the Morphologi 4.

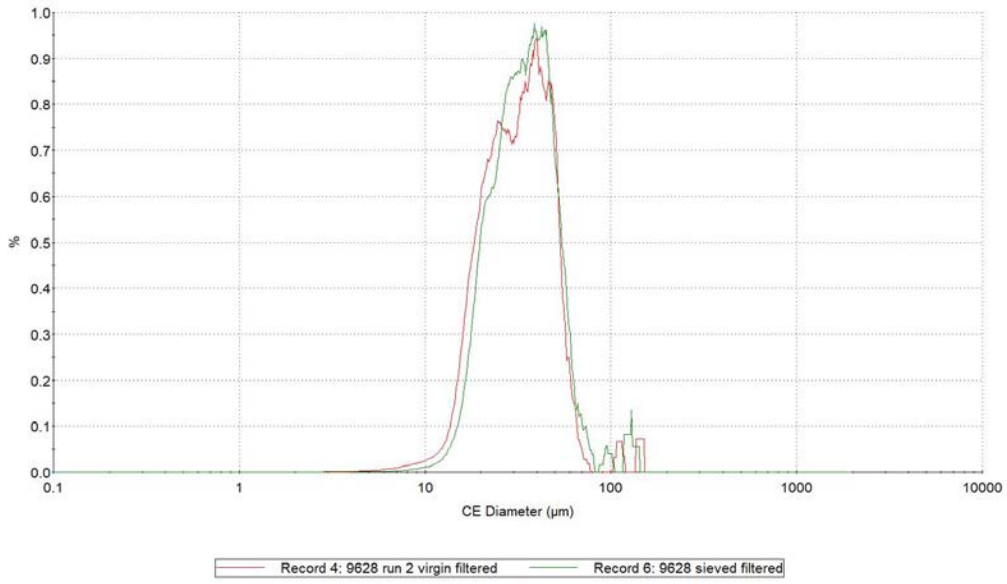

Figure 3.7. Volume Transformation size data from Morphologi 4 of virgin and sieved powders.

3.3.3 Porosity

Images of the internal features of the powder, shown in Figures 3.8 and 3.9, indicate that the gas atomization process leaves several small, 1 - 3 micron pores in most powder particles, in addition to rarer large pores. It is likely that during processing, the smaller entrapped gas pores are not able to escape the melt pool as easily as larger, more buoyant pores, especially at higher processing speeds, and that finished parts will contain these small pores. Finished parts should be investigated at high magnification for evidence of these 1 - 3 micron pores. No significant change in internal pore quantity or size was noted between the virgin and sieved samples.

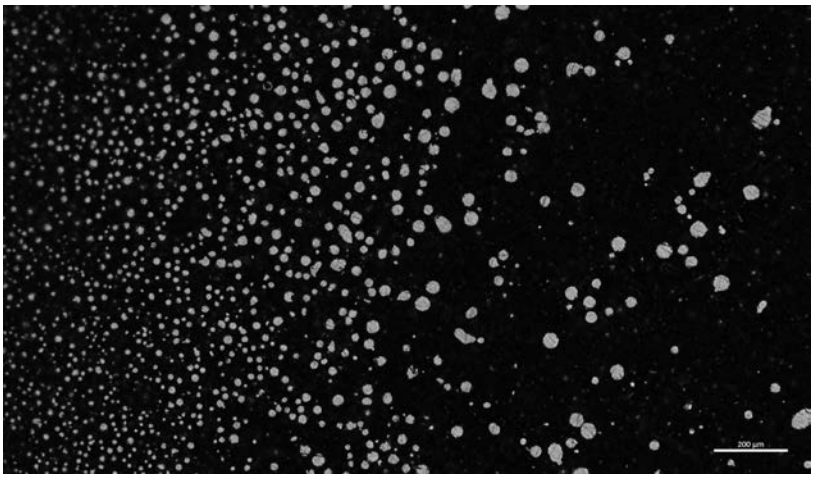

(a) Overview

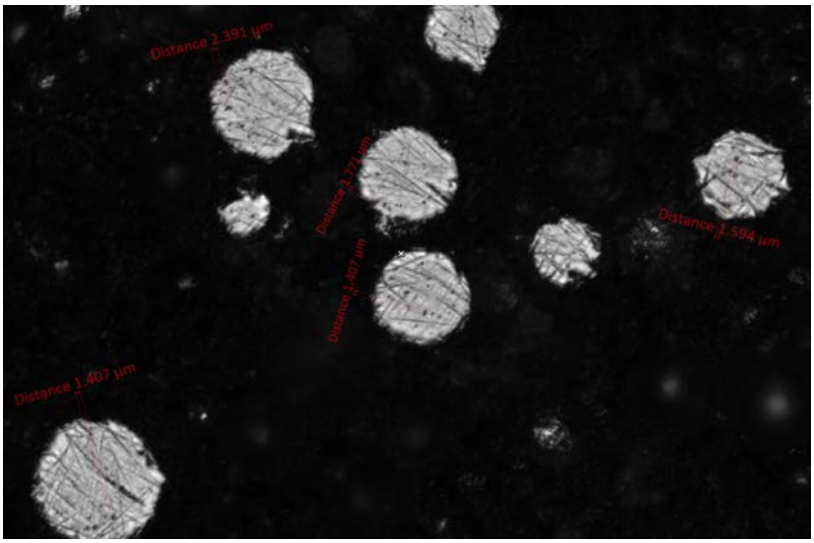

(b) Detail

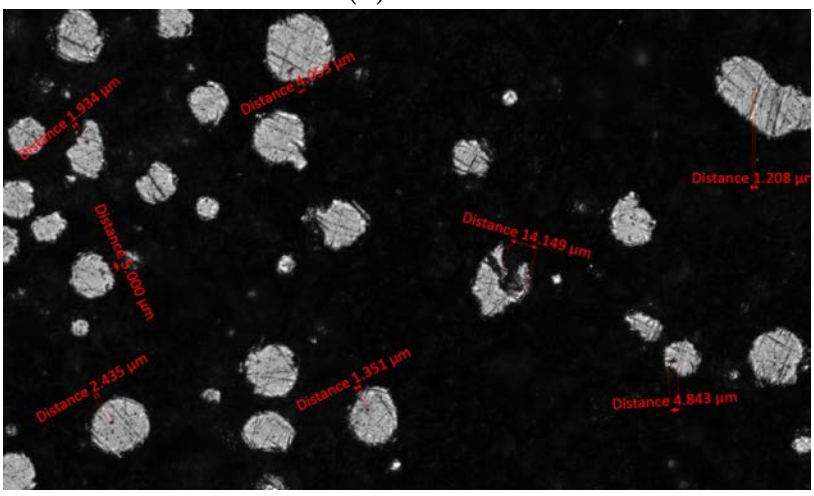

(c) Detail

Figure 3.8. Optical micrograph of sectioned powder, virgin.

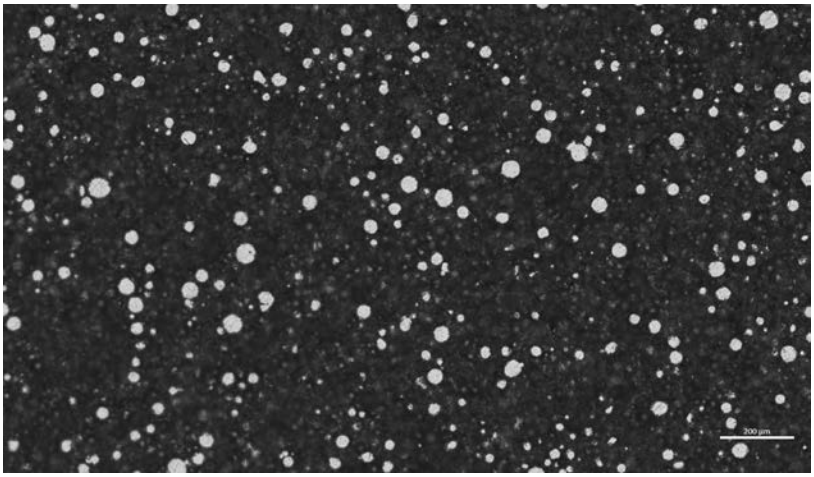

(a) Overview

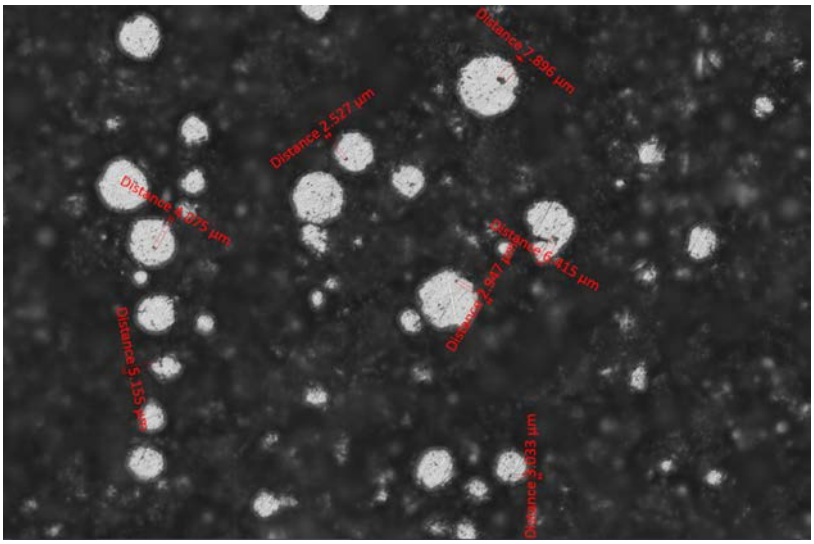

(b) Detail

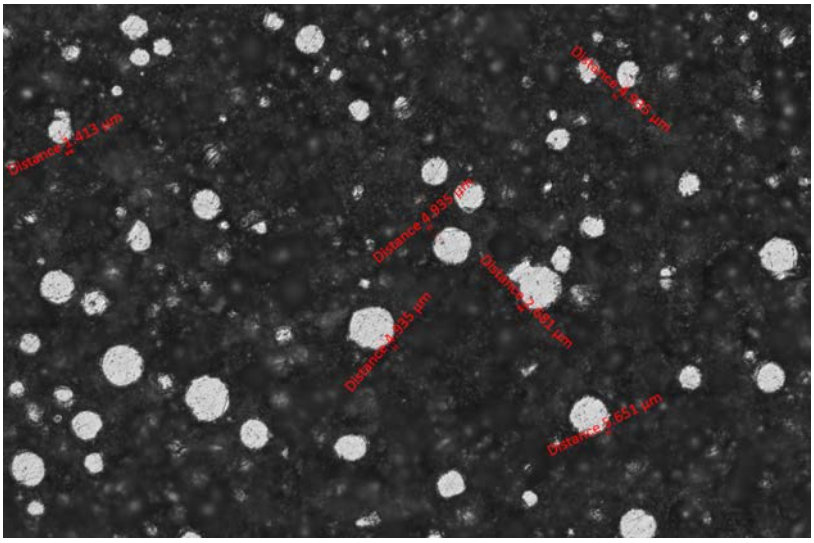

(c) Detail

Figure 3.9. Optical micrograph of sectioned powder, sieved.

3.3.4 Chemistry

EDS characterization of the virgin powder sample was consistent with the chemical composition of AF9628, with all primary alloying elements except manganese appearing in the spectrum. No additional elements were detected, including copper, aluminum, sulfur, or oxygen, indicating that the powder chemistry is very low in impurities and does not oxidize quickly. Similar evaluation of the sample of seived powder produced an identical spectrum, also lacking manganese. This indicates that there is very little chemical difference between the virgin and sieved powder. The lack of Mn is more likely due to the limited sample size than an actual lack of Mn in the alloy.

Evaluation of the soot by SEM EDS analysis revealed that the soot is primarily oxygen. Though the oxygen content of the powder in the process chamber is less than 0.5%, oxygen is necessary for the visible burning occurring during laser exposure, and is a necessary component of combustion products. No carbon was detected, which is interesting, as the combustion reaction requires a fuel to react with the oxygen, and carbon is a likely source. Changes is carbon content can strongly influence the properties of the finished steel, and being able to determine carbon content is important for further development of the material. The color of the sparks produced during the melt process were orange to red-orange, which is consistent with iron and carbon, or the sparks produced when grinding steel [96]. This indicates that the laser is not preferentially burning chromium or nickel, which burn white, or molybdenum or manganese, which burn yellow-green. When iron is heated in the presence of oxygen, it will produce magnetite, Fe_3O_4, which is black [97]. This is consistent with the presence of black soot in the build chamber. The weight percentage of iron and oxygen in the soot estimated with are 85% and 15%, versus an expected weight percentage of Fe_3O_4 of 71% and 29%. This is not within the 10% error expected

of EDS weight percentages. It is likely that the primary composition of the soot is Fe_3O_4, and the difference could attributed to more complex oxides occurring as a result of the very low oxygen content. The EDS spectra are displayed in figures 3.10 and 3.11.

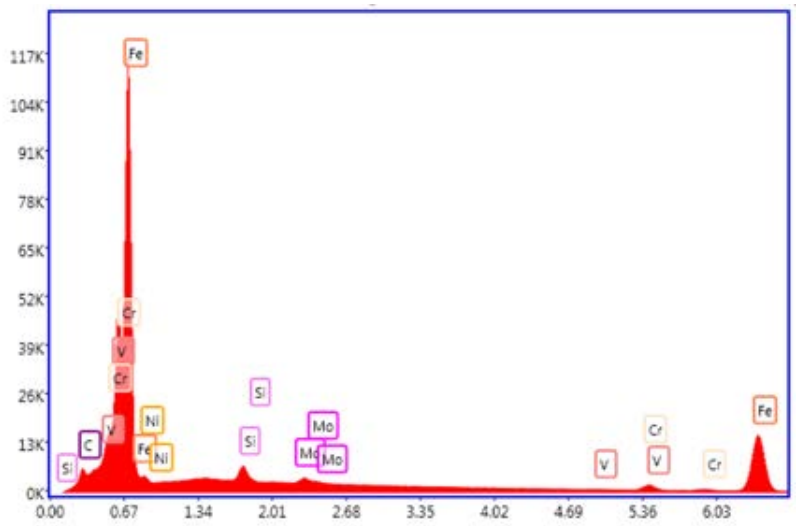

(a)

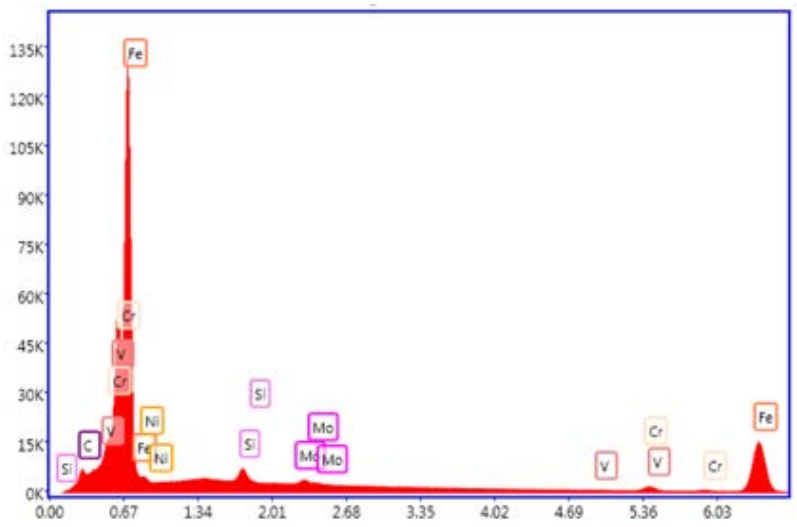

(b)

Figure 3.10. Characteristic X-ray spectrum peaks of virgin (a) and sieved (b) powder samples. No difference in elemental composition was detected in the powder with EDS

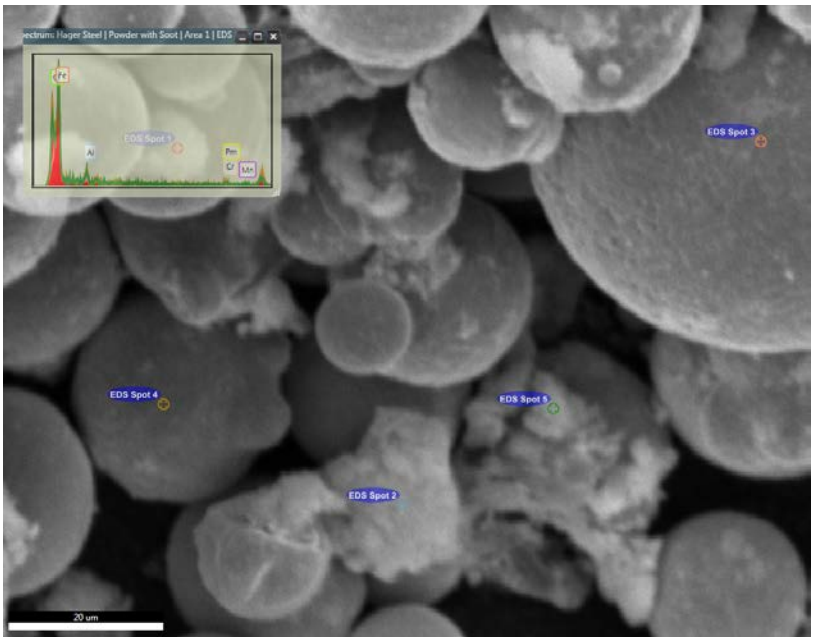

(a)

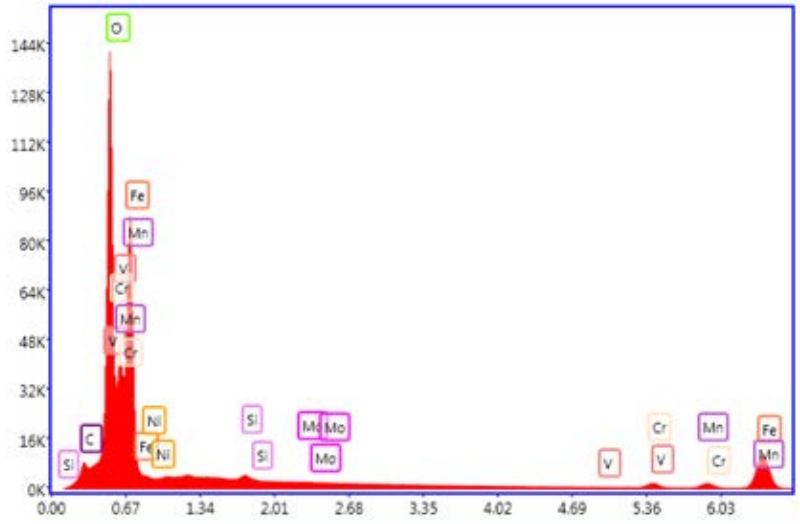

(b)

Figure 3.11. EDS selection points (a) and identified characteristic x-ray spectrum peaks of a spot 2, which is centered on the largest soot particle (b).

3.4 Summary

The gas atomized powder produced by PAC is consistent with other gas atomized metallic powders. The powder is highly spherical, with some small satellites and a small number of elongated particles. The morphological data is consistent with this assessment, and the powder is not showing significant detrimental changes after processing and sieving. There are a number of small pores present within the powder, and finished parts should be sectioned to determine if these pores are destroyed or retained during processing. The combustion products of additive manufacturing appear to be oxygen-rich, and chemical characterization of sieved powder should be conducted to determine if the oxygen is removed during sieving. Additional chemical characterization to determine the element that is providing the fuel for the combustion reaction would be useful, as carbon is the most likely element in AF9628 to burn. As steel is highly sensitive to changes in carbon content, this is a particularly important point of investigation. Overall, this powder's quality is consistent with other metallic powders used to create high quality additively manufactured parts, and any flaws in finished parts are more likely to be due to processing errors than powder flaws.

IV. MLab Weld Tracks

4.1 Overview

Parameter development, whether for a new machine or with a new material, will almost always begin with weld track analysis. Weld tracks allow the rapid testing of a large number of laser (or electron beam) power and speed combinations to narrow a near infinite set of variables to a more promising region. The process typically involves the selection of a grid of power and speed combinations that are evaluated for weld consistency and penetration. Welds that are too 'hot' will result in burnt regions and sputtering, while welds that are too 'cold' will not have a defined melt pool, or will be very tall and round if they fail to penetrate into the base plate. After sectioning and etching, minimal penetration into the base material is also indicative of a 'cold' setting, and excessive penetration that results in keyhole pores indicates a 'hot' setting. Eliminating parameter combinations based on these observable flaws will most often result in a cone shape that can be approximately defined by lines of fluence. In lieu of exclusively choosing power and speed points on a grid, this research will also use lines of fluence to survey the initial test region, as recently demonstrated by Cacace in her doctoral research [98]. To facilitate rapid analysis, a puck and insert system was used, which also prevented the destruction of build plates.

4.2 Methodology

4.2.1 Concept Laser MLab Cusing

Primary parameter analysis was conducted on a GE Additive/Concept Laser MLab 200R Cusing(R), an Laser Powder Bed Fusion (LPBF) instrument capable of printing reactive alloys (Figure 4.1. The MLab is equipped with a 100mm x 100mm x 120mm build volume and a Nd:Yag 200W continuous fiber laser with a 50 μm spot

size and a maximum speed of 7000 mm/s. The machine will accept nitrogen or argon as the inert gas, and is connected to an argon supply in the AFIT additive manufacturing laboratory. The Mlab is designed for a powder bed thickness of 15 - 30 μm, though different file formats allow more flexibility in layer thickness.

Figure 4.1. GE Additive/Concept Laser MLab 200R Cusing and glove box [99].

4.2.2 *P-V* Process Maps

The primary input parameters for additive manufacturing, other than material feedstock, are laser power, laser speed, powder bed depth, scan path hatch spacing, and laser focus spot diameter. As powder bed depth and laser focal diameter for the MLab are fixed, parameter development was focused on power, speed, and hatch spacing. To narrow the initial field of test points, current additive manufacturing literature was surveyed for power, speed, powder bed depth, hatch spacing, and laser focus spot diameter values used on ferrous materials and reported to produce high

density parts. The power and speed values are plotted in Figure 4.2 over lines of constant fluence; and the full table can be found in Appendix B. The fluence values for each parameter set with a published laser focus size was calculated and compared between different materials; this comparison is shown in Figure 4.2.

Once successful process parameter sets were identified, the maximum power was limited to 200 W, and a primary area of interest was identified using lines of fluence. In general, it appeared that mild steels required a higher energy density than stainless steels to achieve low porosity. A minimum fluence bound of 100 J/mm^3 and a maximum fluence bound of 660 100 J/mm^3 were set, and six speeds were chosen at approximately 100 J/mm^3 intervals with powers set at 80W, 100 W, and 200 W. After later deciding that eight sets of weld track speeds could be run at each power level without increasing processing time, two additional test points were chosen at each of these power levels. Since using fluence as a method for selecting processing parameters is an untested concept and filling in power and speed combinations along a grid is more common, eight speeds from 200 mm/s to 1600 mm/s were tested at 140 W at 170 W. The power, speed, and fluence values of the weld track process parameters are listed in Table 4.1. These values are plotted over the initial survey values, and separately over isolines of fluence in Figure 4.3.

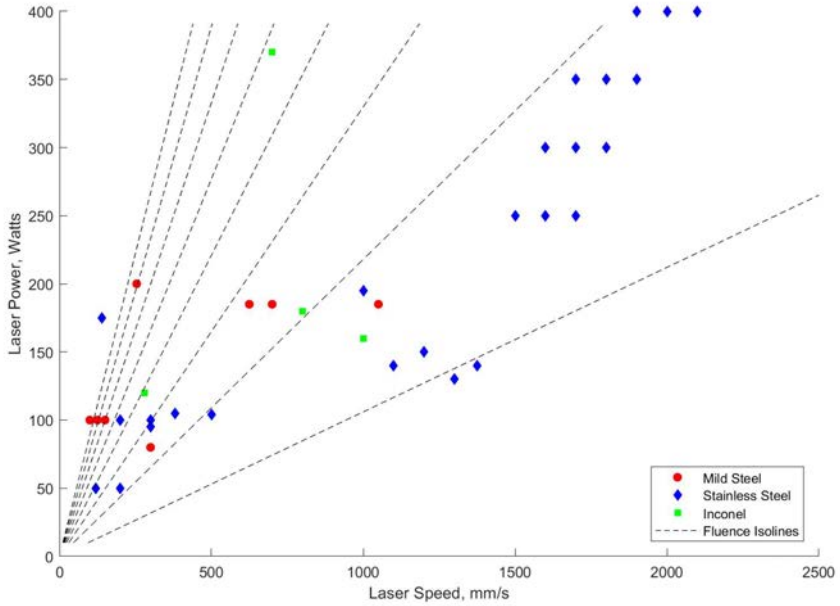

(a) Survey of power and speed settings used in LPBF on other ferrous materials

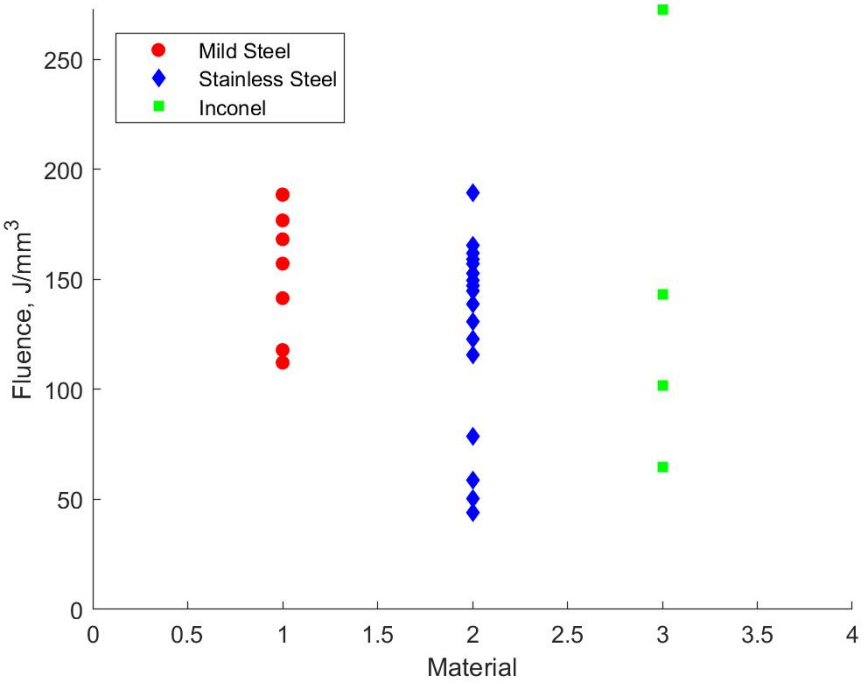

(b) Fluence values of the power and speed combinations for ferrous materials which also reported laser spot size.

Figure 4.2. A survey of published process parameters used to additively manufacture dense parts out of ferrous powders. Data points and references are available in Appendix B.

Table 4.1. Power, Speed, and Fluence values evaluated in initial weld track trials, powder depth and laser focus diameter are set at 30 μm and 50 μm, respectively.

Power W	**Speed** mm/s	**Fluence** J/mm^3	**Power** W	**Speed** mm/s	**Fluence** J/mm^3
80	630	108	140	800	149
80	500	136	140	600	198
80	420	162	140	400	297
80	350	194	140	200	594
80	300	226	170	1600	90
80	250	272	170	1400	103
80	170	399	170	1200	120
80	125	543	170	1000	144
100	640	133	170	800	180
100	430	197	170	600	241
100	320	265	170	400	361
100	212	400	170	200	722
100	180	472	200	1280	133
100	160	531	200	900	189
100	130	653	200	640	265
100	100	849	200	425	399
140	1600	74	200	370	459
140	1400	85	200	320	531
140	1200	99	200	255	666
140	1000	119	200	200	849

4.2.3 Rapid Analysis with Build Plate Inserts

To increase the speed of the weld track analysis and reduce the single-use destruction of build plates, a puck insert system was used. Circular holes with a 30 mm diameter and a 10 mm flat mere machined 0.25" deep in a 316 stainless steel build plate at the center and at $\pm$25 mm from the center. Pucks with a matching indexing flat were machined to fit into the build plate with a sliding fit tolerance. In case of puck expansion due to heating, 0.25" diameter holes were added to the bottom of the build plate insert holes so that pucks could be hammered out; the machined build plate is shown in Figure 4.4. The pucks were made from A36 plain carbon structural

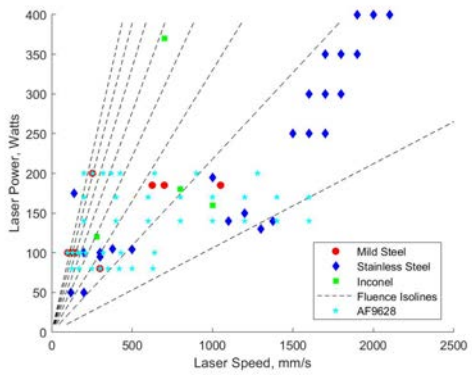

(a) Power and speed combinations for AF9628 Weapons Steel (AF9628) weld tracks superimposed over the $P - V$ survey.

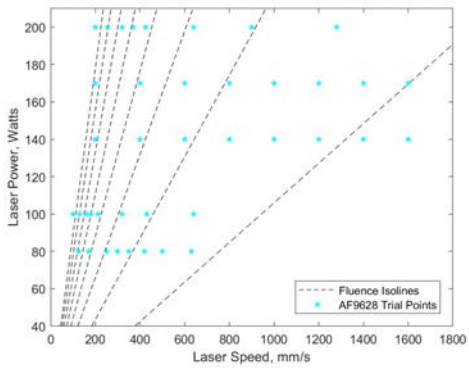

(b) Power and speed combinations for AF9628 weld tracks.

Figure 4.3. Plots of the power and speed combinations used for weld track experiments for AF9628.

steel, which should mimic the melt characteristics of AF9628, which was not readily available as plate. This puck design also enabled later rapid analysis of solid parts, as the puck would fit into 1.25" mounting press for sectioning and polishing, eliminating the time needed to cut parts off of and then resurface a build plate.

Figure 4.4. Image of the MLab build plate with five insert holes milled in for rapid build turnover.

The weld tracks were designed as a 2 mm by 8 mm box with four internal, non-contacting lines, and was built in nTopology's implicit modeling software Turbo. The weld boxes were fit eight to a puck so that each would contain all points for a single

laser power. The welds were first run on bare steel, without a powder layer, to ensure that the parameter sets used were capable of melting the base steel, and providing a control reference. During trials with powder, small differences in puck insert height would cause one puck to protrude above the others. To avoid differences in powder bed layer thickness, the powder bed was leveled to 40 μm on the tallest puck, and the welds sets were exposed one at a time, as shown in Figure 4.5. Uneven or streaky powder beds caused noticeable streaks in the welds tracks, as shown in Figure 4.6. This uneven coverage of the first layer was common on the MLab, though it was especially pronounced with the puck insert build plate. All reported weld data in this document is from pucks that had even coverage and resulted in continuous welds.

Figure 4.5. Image of the MLab insert build plate in use in the machine, covered with a typical uneven 40 μm first powder layer. The insert in the back left corner received an even 40 μm layer and was used for a weld track exposure.

4.2.4 Weld Evaluation

After a single exposure at the selected power and speed settings, the pucks were imaged with a Zeiss Observer equipped with an Axiocam 103 to examine surface quality. Defects such as solidification cracking, balling, and uneven welds were used to exclude the parameter from further use. Pucks were then cut orthogonal to the weld tracks, to examine weld penetration and melt zone regime. The cut pucks were polished using diamond slurry in a succession of 9, 3, and 1 μm, then etched in a

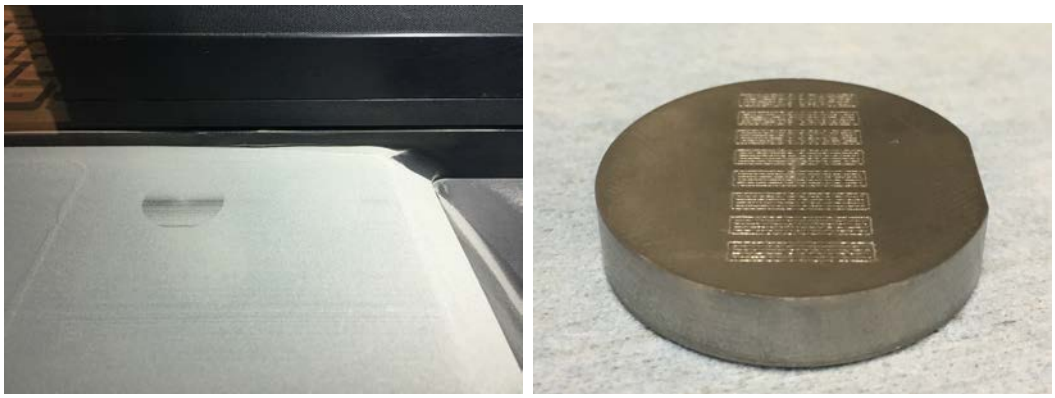

(a) Uneven powder layer on the rear left puck prior to weld track exposure.

(b) Clearly visible streaks in weld tracks attempted on unevenly covered pucks.

Figure 4.6. Image of a poorly set up powder layer, and the resulting inconsistent weld tracks.

solution of 20 mL of nitric acid in 180 mL of methanol (Nital) for 12 seconds, or until the surface visibly dulled. The pucks were then neutralized in a sodium bicarbonate solution, rinsed in deionized water, rinsed in acetone, and dried in a jet of Nitrogen. Etched specimens were imaged under a Keyence light microscope at 500x as quickly as possible, as rust appeared on the cut surface in as little as one hour after etching. The depth and width of the weld tracks was measured using the native Keyence software. Due to the limited viewing window of the microscope at 500x, dots of black ink were applied with a permanent marker between parameter weld track sets in order to avoid mix-up. This resulted in a few of the individual weld tracks being obscured, but prevented data mislabeling. The weld penetration was then classified as shallow, conduction, penetration, or keyhole; shallow and keyhole welds were excluded from further use.

4.3 Results

4.3.1 Weld Appearance

The weld tracks were first evaluated from above using a Zeiss Observer optical microscope equipped with an Axiocam HRc camera. The welds were categorized by visual quality, with balling and the lack of a melt pool used to completely exclude settings, while elongation and inconsistencies in the appearance did not fully exclude settings from further contention. Examples of welds in these categories are shown in Figures 4.7 and 4.8. The weld track widths were measured in the Zeiss AxioVision software and later compared to the weld penetration width and used to calculate hatch spacing. Several weld tracks at 80 W and 100 W looked very similar to a classic 'stacked-coin' Tungsten Inert Gas (TIG) weld, while welds at higher laser powers and speeds had highly elongated tails typical of automated laser welding procedures. Weld inconsistencies were far more prevalent in welds generated with powder, which may indicate that the inconsistency is due more to small differences in powder bed thickness than actual process flaws.

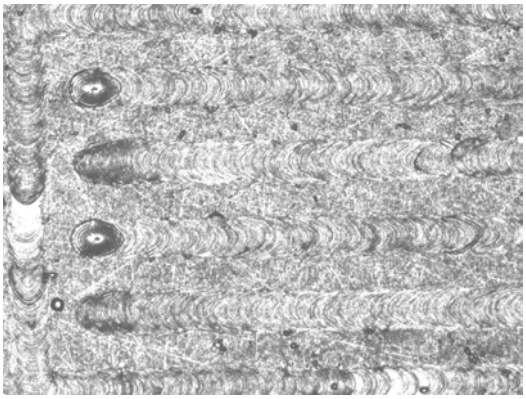

Figure 4.7. Top view of an acceptable weld.

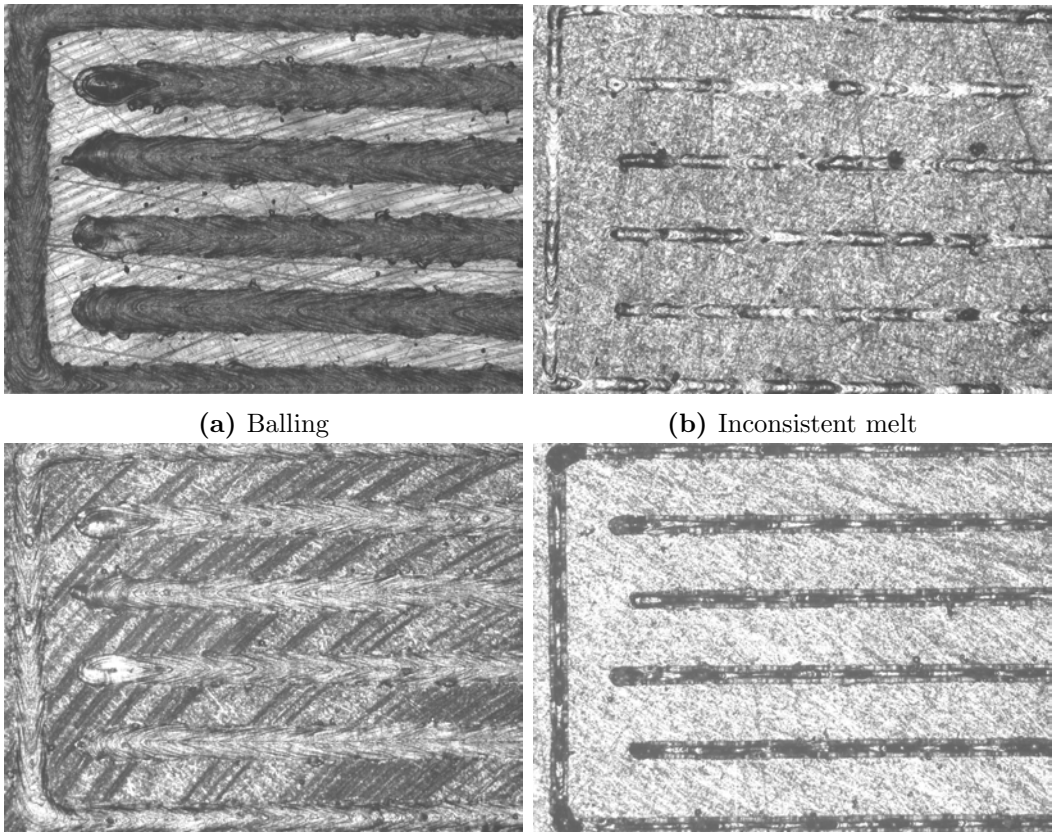

(a) Balling **(b)** Inconsistent melt

(c) Elongated **(d)** No melt pool

Figure 4.8. Representative images of different weld track surface quality flaws used to exclude settings.

4.3.2 Weld Penetration

After surface evaluation, the weld track pucks were sectioned, mounted, and etched with Nital before being examined on a Keyence VH-Z250R optical microscope. The welds were categorized by penetration depth as conduction/penetration, shallow, or keyhole. Some welds exhibited significant undercutting, which is generally attributed to an overly rapid processing speed in traditional welding. Representative images of these categories are displayed in Figure 4.9. Weld width and depth were measured in the native Keyence software, with width being used for hatch spacing calculation and depth used to exclude shallow welds or preferentially select for layer remelting. Top surface weld quality did not immediately appear to directly result in conduction

zone welds, as the 'stacked-coin' welds were very shallow, and elongated welds more typically resulting in penetration depths adequate to prevent layer delamination.

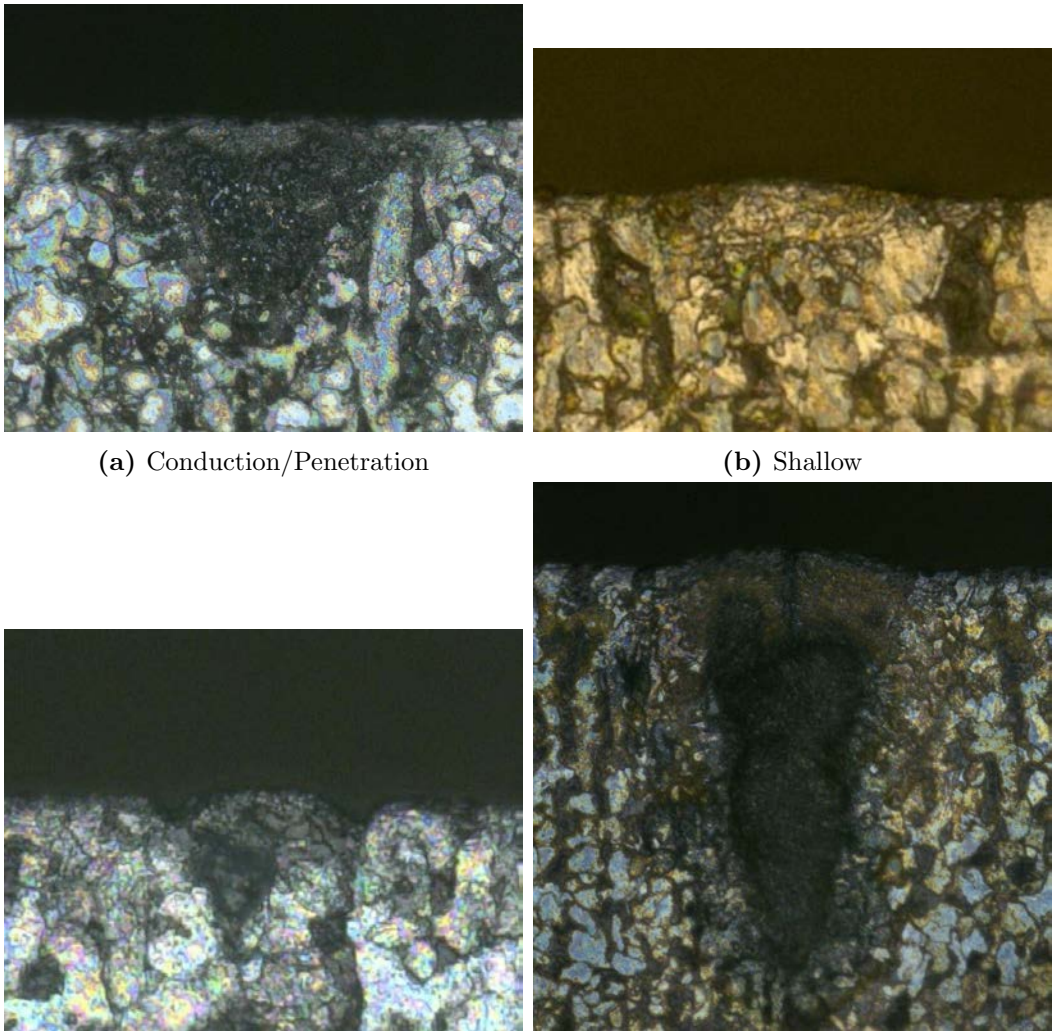

(a) Conduction/Penetration **(b)** Shallow

(c) Undercut **(d)** Keyhole

Figure 4.9. Representative images of different weld track depth descriptors.

4.3.3 P-V Process Maps

Weld track quality evaluations were applied to the Power-Velocity ($P - V$) process maps to define a cone of viable processing parameters. In the welds without powder, the best visual quality welds were produced at 80 W and 100 W settings, with inconsistencies and elongation prevalent at 140 W and 170 W settings, and

positive identification of the balling phenomenon at high fluence values. When the weld width, measured from the top, was compared to fluence, there appeared to be a positive linear correlation, with the narrowest weld for each value of fluence generally appearing as the highest quality. Plots of the surface evaluation of the no-powder welds are shown in Figure 4.10.

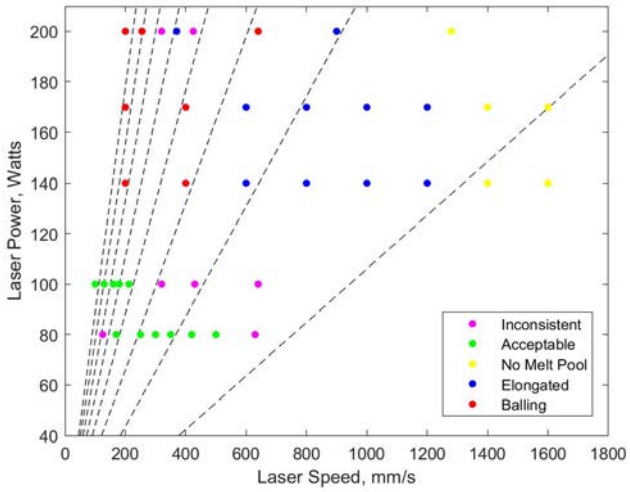

(a) $P - V$ map of welds without powder, sorted by top surface quality.

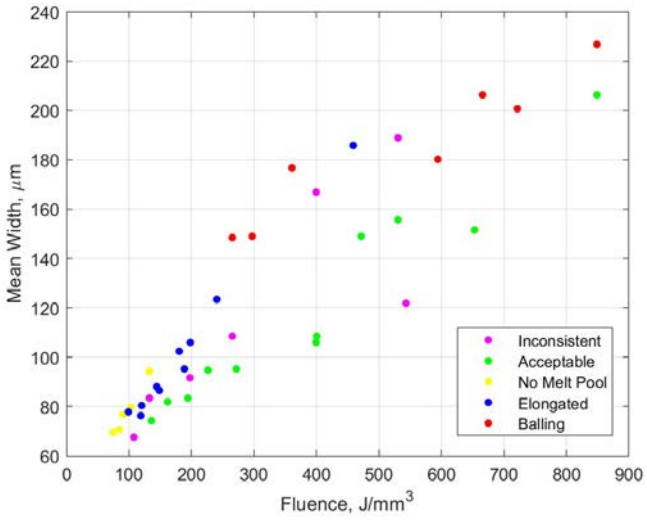

(b) Weld track width vs fluence, sorted by top surface quality.

Figure 4.10. $P - V$ **map and width vs fluence plots of weld tracks run without powder, top surface evaluation only.**

The surface quality of the weld tracks with powder was similar to that of the weld tracks without powder, with the best looking welds occurring at lower powers, elongation appearing at higher powers and balling occurring at high-power, high-fluence parameter sets. The highest quality welds were again the narrowest for each value of fluence, though the addition of powder actually appeared to make this relationship more linear. Plots of the surface evaluation of the with-powder welds are shown in Figure 4.11. The weld track experiments indicate that a decision to carry parameters forward solely on top surface quality would be limited to laser powers of 100 W or less, and there would be no clear values of fluence to use as a bounding cone.

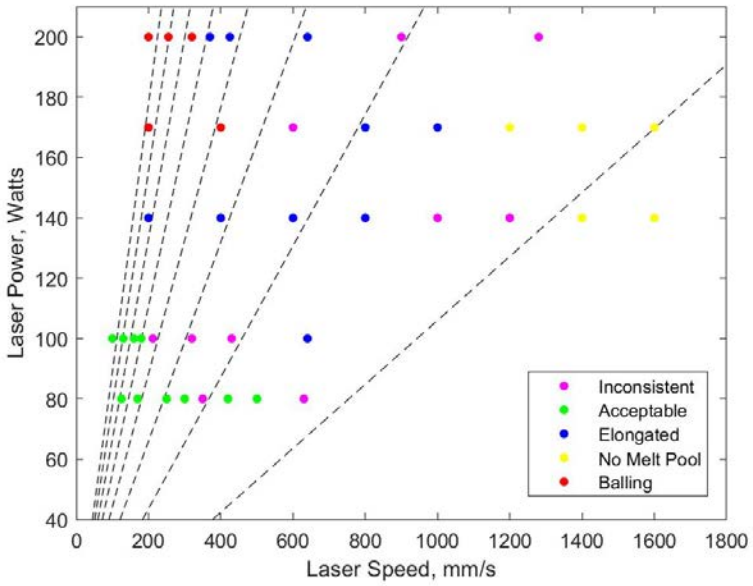

(a) $P - V$ map of welds with powder, sorted by top surface quality.

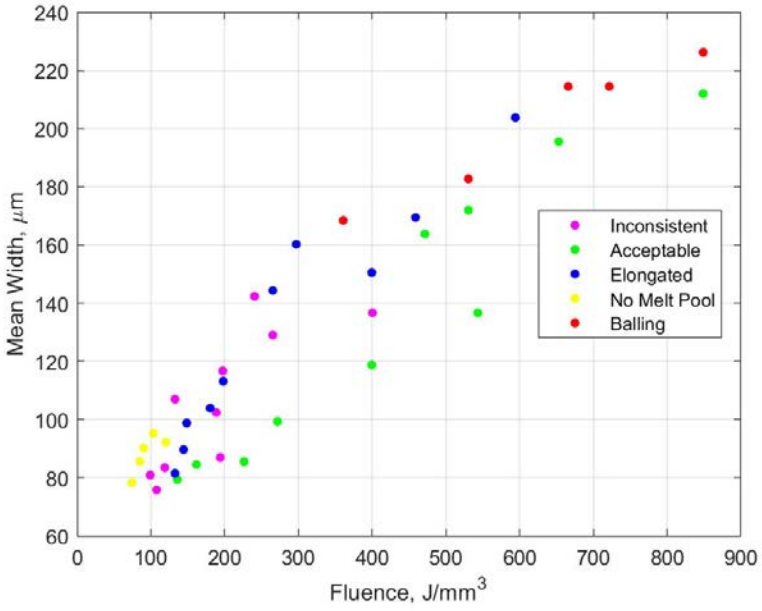

(b) Weld track width vs fluence, sorted by top surface quality.

Figure 4.11. $P - V$ **map and width vs fluence plots of weld tracks run with powder, top surface evaluation only.**

Analysis of the weld tracks sections indicated that the weld surface quality was not a reliable indicator of weld melt quality. While welds that were excellent in appearance

did in fact result in conduction mode penetration, the depth of penetration indicated that they would not remelt multiple previous layers, which is known to increase part density. Symmetric, penetrating weld profiles that are ideal for creating high density parts were associated with elongated welds. Tracks that did not have a clearly identifiable melt pool structure were those that resulted in undercutting around the sides of welds. High-power, high-fluence parameter sets that resulted in balling, as well as some of the elongated welds, were associated with keyhole mode welds. The $P - V$ map produced for weld sections, displayed in Figure 4.12, positively identified a cone-shaped region for further development. Unlike the previous weld width vs fluence plots, the weld sections did not exhibit a linear quality relationship. The welds instead seemed to indicate that there was a fluence region of between 200 J/mm^3 and 500 J/mm^3 in which the parameters would produce the weld profiles needed for well-bonded, crack-free parts.

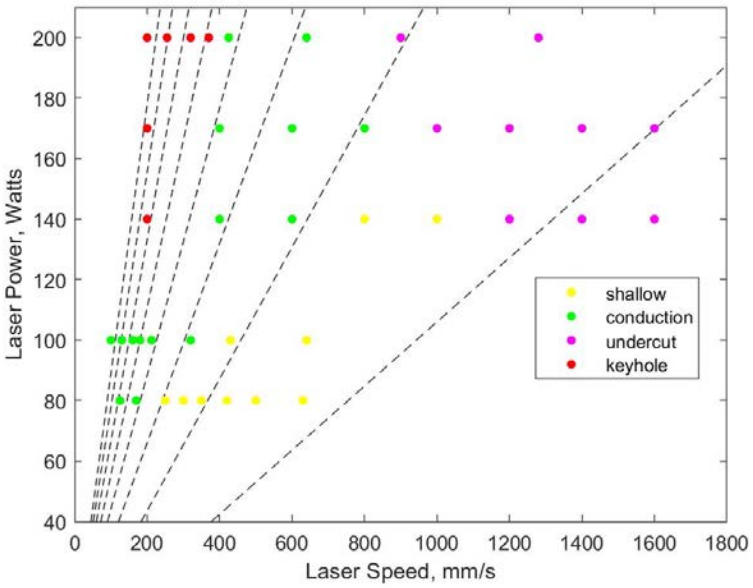

(a) $P-V$ map of sectioned welds with powder, sorted by top surface quality

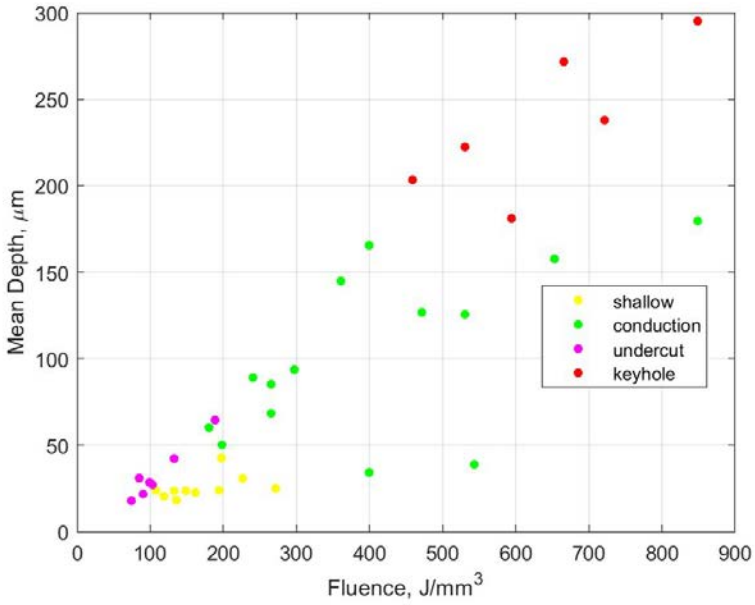

(b) Weld track width vs fluence, sorted by melt penetration mode.

Figure 4.12. $P-V$ **map and width vs fluence plots of sectioned weld tracks, with powder case.**

4.3.4 Parameter Selection

After evaluating the weld tracks, a set of ten initial power and speed combinations were chosen for the generation of solid parts, shown in Figure 4.13. Parameter sets that did not achieve conduction mode melting were eliminated, and two points were chosen at each power level based on the top surface evaluation. Top surface evaluations of acceptable were chosen preferentially, with elongated welds chosen when no other options were available. The fluence values of these initial points ranged from 180 J/mm^3 to 550 J/mm^3.

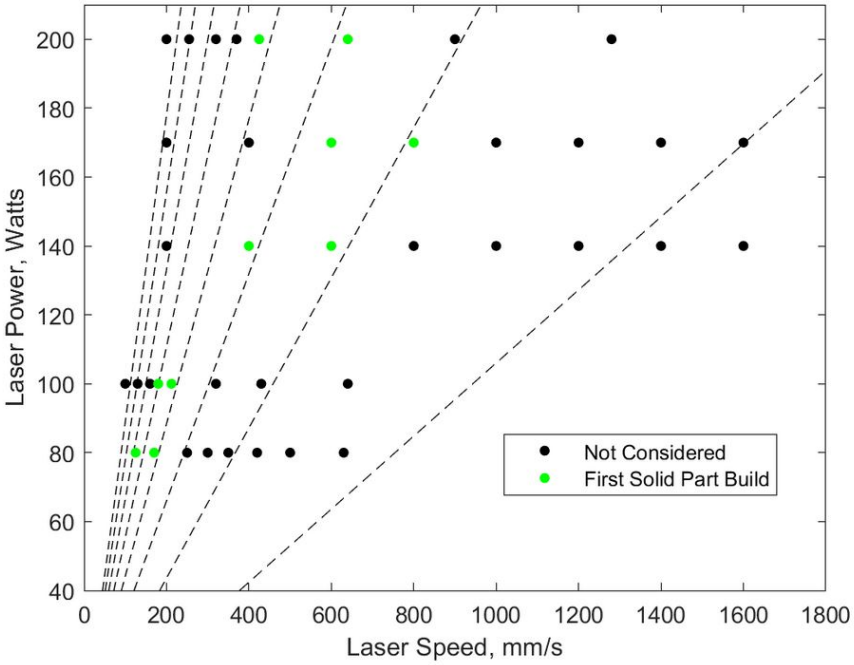

Figure 4.13. The initial ten points chosen with weld track sectioning results for evaluation as solid cylinders, vs the set of 40 parameters tested as weld tracks.

4.4 Summary

The weld track experiments conducted on the MLab 200R resulted in potential settings for high density parts at each of the four power levels surveyed. The welds that had the appearance of classic TIG welds and those that appeared as smoothly

elongated versions of those welds were most likely to result in conduction or penetration mode processes. Welds that exhibited balling are likely to generate keyhole pores, and welds without a discernable melt pool are likely to be too shallow to adequately melt powder layers. Using a survey of power and speed settings used on similar materials successfully resulted in welds that are promising for further development as additive manufacturing settings, but no conclusions can yet be made on the use of fluence as a selection parameter.

V. Material Characterization

5.1 Overview

The weld track experiments covered in Chapter 4 resulted in the selection of ten power and speed settings that would be carried forward for solid part generation and porosity analysis. Following testing of these initial ten settings, additional test points were chosen based on fluence to test its viability as a scaling parameter. The solid parts generated were subjected to porosity analysis consisting of both sectioning and optical microscopy, and CT scanning. Preliminary tests were promising, with multiple parts exhibiting densities of greater than greater than 99.9%. This early success with high density parts led to extensive material characterization, including surface roughness, hardness, microstructure, chemistry, and tensile and impact strength.

5.2 Methodology

5.2.1 Hatch Spacing Selection

An initial set of ten power and speed combinations were chosen based on the weld track quality. The weld track widths measured from the top view and across the etched section were averaged and multiplied by factors of 0.9, 0.8, and 0.7 to attempt to find the ideal overlap ratio. Other studies indicated that a 10% overlap on each side of the weld track was ideal for fully melting all powder while avoiding overheating and reducing total build time [100]. These first ten settings were printed on steel pucks as 7 mm by 7 mm cylinders with a triangular directional indicator and a surface spiral that would indicate sectioning depth. The part files were built in nTopology's implicit modeling and slicing software, Turbo. The three overlap settings for each power and speed combination were printed three to a puck as shown in Figure 5.1 to facilitate rapid processing.

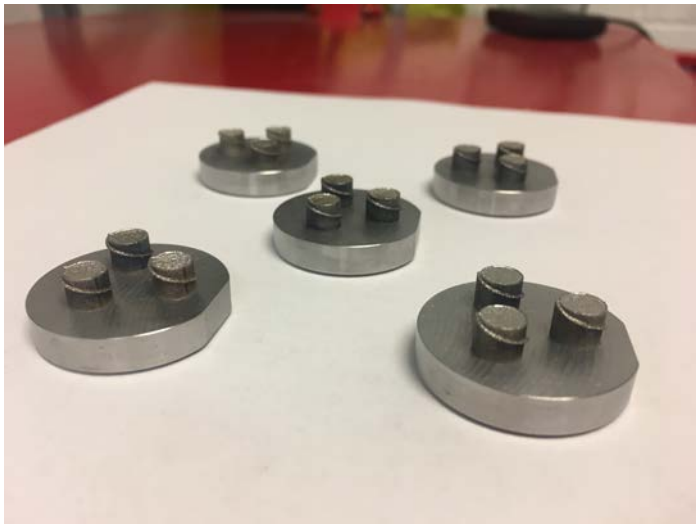

Figure 5.1. Image of the 7 mm cylinders wrapped with depth-key helixes used to evaluate the first 10 power and speed points.

To increase the quality of the data, larger cylinders with a diameter of 10 mm and a height of 15 mm for use in AFIT's new Nikon CT scanning machine (Figure 5.2) were prepared. The cylinders were again printed three to a puck, with hatch spacing calculated at 0.90, 0.80, and 0.70 of the weld track widths. This created an extremely high density build, as shown in Figure 5.3, and the powder dosing factor was increased to 300% to maintain even powder coverage. The initial ten settings were re-printed, followed by five additional power and speed combinations from the original set of weld track experiments that fit within a fluence cone of 200 - 400 J/mm^3. These fluence values were chosen based on results from 2-D sectioning of the 7 mm cylinders. Parts were evaluated for discoloration, as well as flaws observed during printing such as excessive lippage. Consistent part quality was observed along the 250 J/mm^3 line of fluence, so additional test points along this line were created, with weld track widths interpolated from the weld track data. The twenty power and speed settings evaluated as solid parts, for a total of sixty power, speed, and hatch spacing settings, are plotted below in Figure 5.4.

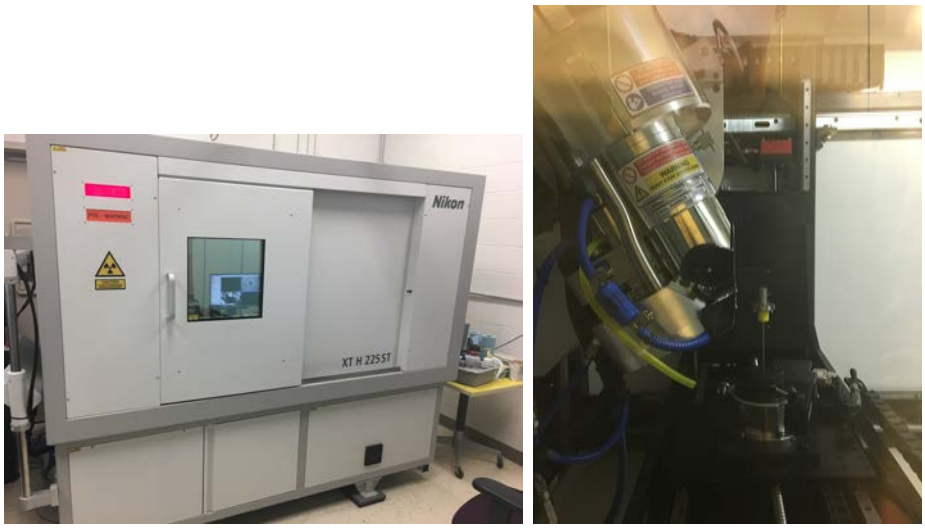

(a) AFIT's Nikon XT H 225 ST computerized tomography scanner

(b) AF9628 Weapons Steel (AF9628) part mounted in the CT scanner

Figure 5.2. Images of AFIT's CT scanner and a AF9628 part during scanning.

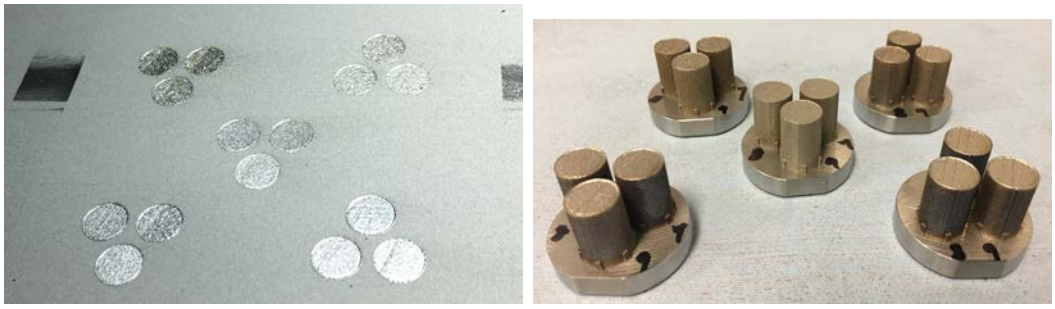

(a) **(b)**

Figure 5.3. Images of densely packed parts generated for CT analysis at different hatch spacing settings.

5.2.2 Porosity Evaluation

The 7 mm cylinders were given a visual evaluation, with classification as clean, yellowed, or blued to characterize any overheating, then mounted in conductive resin and ground and polished according to the procedures in Appendix C.3. After polishing, the pucks were placed under 10x magnification on a Zeiss Observer equipped with an Axiocam HRc, and an overview image was taken using the Mosaic stitching function. The overview image was then read into the Matlab script in Appendix C, which converts black and white images to binary and calculates the ratio of white to

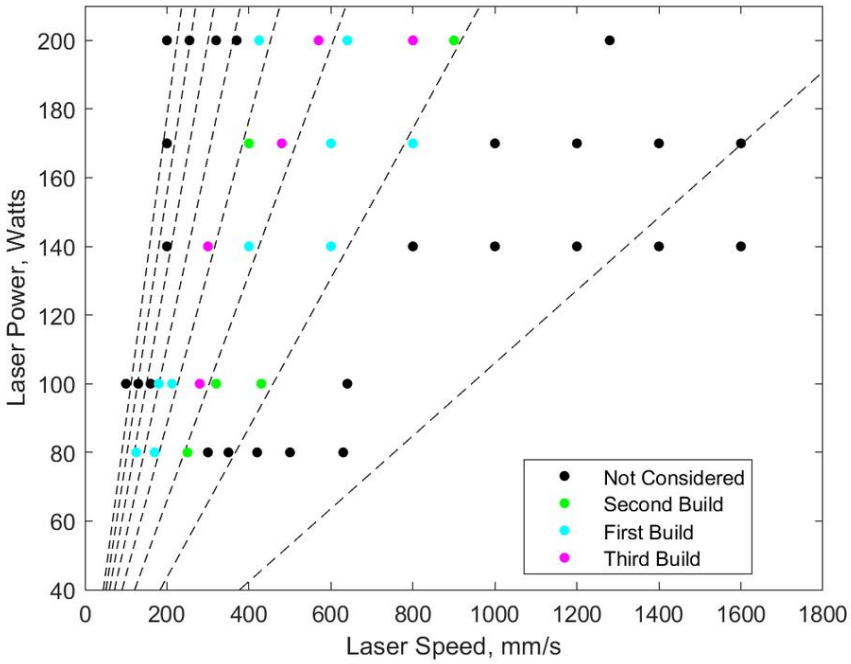

Figure 5.4. Plot of power and speed points tested as solid parts, color coded by batch, over lines of fluence

total pixels. This ratio is used to calculate a percent density value for that power, speed, and hatch spacing combination. The density calculated by this script was later confirmed by Fiji (ImageJ) [101].

The Nikon XT H 225 ST CT scanner is capable of reliably detecting pores in metals down to a minimum volume of approximately $0.4{\cdot}10^{-5}$ mm. Unfortunately, CT scanning of the 10mm cylinders proved to be more difficult than expected, as scanning multiple dense parts at once created a large amount of noise where parts overlapped. Due to time constraints, a selection of eight of the sixty parts was made based on fluence, E_V, previous 2-D sectioning of 7 mm parts, and lack of discoloration. The raw CT scan data was reconstructed and read into VolumeGraphics software. After scanning, the eight parts were cut in half, mounted, and polished according to the procedures in Appendix C.3 to confirm the existence of detected pores. The sectioned parts were again imaged with an optical microscope, a Zeiss Observer equipped with

an Axiocam 503 at both 5x and 20x to determine bulk porosity and concentration of small, sub-8 μm pores.

5.2.3 Surface Quality

In general, a smoother finish in an additively manufactured part is considered more desirable, as it indicates the part will have greater fatigue, fracture, and corrosion resistance. A Zeiss laser scanning microscope was used to quantify the surface roughness of finished parts, with scans run at both 5x and 20x magnification. The eight parts scanned in the CT machine and later sectioned for porosity evaluation were all evaluated for top and side roughness, and the side scans were fitted to a cylindrical surface for flattening. As the calculated surface roughness values of the 5x and 20x scans were not similar, the values were normalized by the surface roughness values of the part with the largest top roughness at 5x and compared for relative roughness.

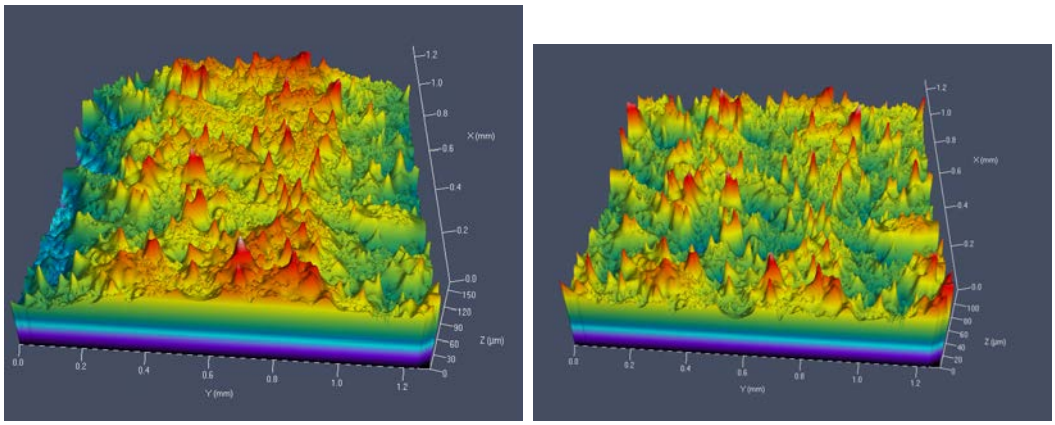

Figure 5.5. LSM scan of the side of a cylindrical part, before and after fitting to a cylinder.

5.2.4 Heat Treat Schedule

Since it is unlikely that the as-built parts are likely to be optimal for end use, a heat treatment used previously for AF9628 was applied to evaluate the ability of

printed AF9628 to be tailored in post-processing. The heat treat schedule is outlined in Table 5.1 below. Parts were created for as-built and heat-treated analysis at two parameter settings proven to create high density parts without discoloration or excessive surface roughness. The heat treatment was accomplished by AFRL/RX and utilized a series of furnaces accurate at high, moderate, and low temperatures. The furnace temperatures were confirmed by a thermocouple embedded in a small block of Inconel 600. Parts receiving heat treatment that would have 1 mm or less of material removed from each face during machining were encapsulated in small sealed pipes purged with Argon to prevent decarburization.

Table 5.1. Heat treat schedule used for AF9628

Process Step	**Temperature** °C (°F)	**Time** hours	**Cooling**
Solution Anneal	1010 (1850)	1	Air cool to room temp
Subcritical Anneal	677 (1250)	4	Air cool to room temp
Hardening	1010 (1850)	1	Water quench to room temp
Temper	205 (400)	4	Air cool to room temp

5.2.5 Hardness

To evaluate microstructure and hardness, 1 cm tall cylinders with 1 cm diameters were printed as test coupons to evaluate hardness and microstructure at each phase of the heat treatment. Each cylinder was mounted and polished according to the standard procedures in Appendix C.3 prior to Vickers hardness testing. A Vickers indenter, also referred to as a microhardness tester, presses a small pyramidal diamond tip into the material at a set load and time. The diagonals of the resulting indent are measured and used to calculate the Vickers Hardness in kilogram-force (kgf) or gram-force (gf). Isotropic materials will have indent diagonals of similar lengths and consistent indent sizes in all planes. The Vickers indenter is a reliable method of

measuring hardness in metals and ceramics, except for tests using very low forces (below 25 gf) or for indentations with diagonals smaller than about 25 μm. To determine bulk hardness, several values of microhardness measured across a sample can be averaged [102]. Hardness values can also be used to predict material ultimate and yield strength in metals. Vickers indenters measure hardness differently than other hardness testers, but the values can be easily converted between the different measurment systems.

5.2.6 Microstructure

After the 1 mm cylinders were evaluated for hardness, the specimens were sectioned so that microstructure in the Z plane could be evaluated. The specimens were remounted and polished according to the standard procedures in Appendix C.3 before being placed in a vibratory polisher filled with a mixture of colloidal alumina and colloida silica for 17 hours. The polished samples were then evaluated in an Scanning Electron Microscope (SEM) equipped with an EDAX Pegasus Electron Backscatter Diffraction (EBSD) unit at a step size of 1 μm.

The cylinders in the as-built and tempered conditions were etched with the procedure developed by AFRL for revealing Prior-Austenite Grain Boundaries (PAGB)'s in AF9628 steel [103]. The polished samples were swab etched with a solution of 100 mL of saturated aqueous picric acid and 0.5 g sodium dodecyl benzene sulfonate before being neutralized in a solution of sodium bicarbonate. A range of swab times were trialed at between 30 seconds and 10 minutes, with no etching noted at below 2.5 minutes. Additionally, initial as-built cylinders produced for porosity analysis were submersion etched with Nital to confirm the lath Martensite microstructure.

5.2.7 Tensile Testing

As an initial evaluation of material strength, cylindrical tensile blanks were printed in the vertical direction for tensile strength determination. Nine cylinders with diameters of 18 mm and heights of 100 mm were printed on the MLab 200R Cusing using the successful parameter combination of 140 W, 600 mm/s, and 86 μm. The nine parts were located at points on a 3 x 3 grid rotated 20° by the rotation matrix script in Appendix C; the parts are displayed in Figure 5.6. To maintain an even powder bed over such a densely packed build plate, the powder dosing was increased to 270%. The densely packed, dense parts generated a large amount of soot, and a second build failed after the argon ventilation was unable to maintain proper flow speed due to filter saturation. Subsequent builds of tensile bars were then generated on a Concept Laser M2 Cusing using the parameter set previously built on the MLab, as well as a second successful parameter combination of 170 W, 600 mm/s, and 110 μm. The number of parts built, along with the machine and parameters used, are summarized in Table 5.2. The laser focus diameter of 50 μm and powder bed thickness of 30 μm were maintained, though the dosing was able to be reduced to the standard 200%. On each M2 build, ten tensile bars with dimensions of 18 mm diameter and 105 mm height were generated. The ten parts were located at points on a 3 x 3 grid rotated -20° by the rotation matrix script in Appendix C, plus a tenth location in the top center of the plate; these parts are displayed in Figure 5.7. A signifianct amount of discoloration was noted on the M2 parts, and is attributed to the increase in soot within the build chamber, as the discoloration only occurs on the 'upstream' side of bars that are downwind in the argon flow from other parts. With ten tensile blanks manufactured for each parameter set, five of each were set aside for heat treatment for evaluation in the as-built and standard heat-treated conditions. The original nine parts printed on the MLab were divided for heat treat and machined to evaluate

machine-to-machine variation.

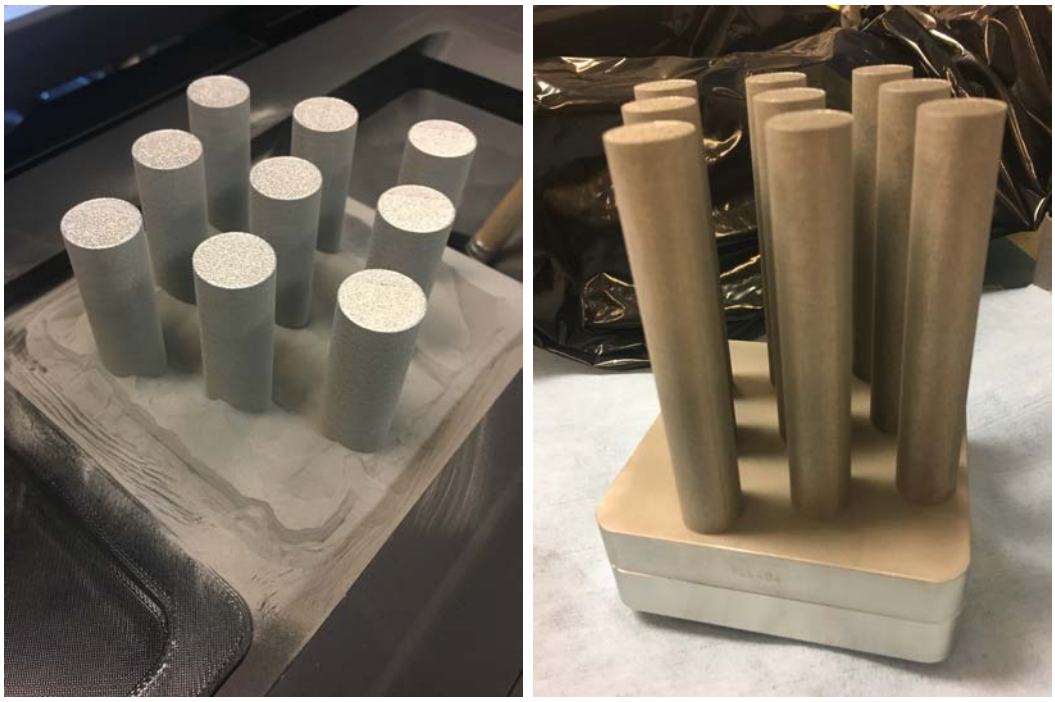

(a) **(b)**

Figure 5.6. Densely packed tensile bars printed in MLab at maximum build height, dosing factor 270%.

Table 5.2. Summary of the tensile and charpy machining blanks built for mechanical testing.

Part Type	Build Parameters	Machine Used	As-Built	Heat Treated
Tensile Round	140-600-86	MLab	4	4
Tensile Round	140-600-86	M2	5	4
Tensile Round	170-600-110	M2	5	4
Charpy V-Notch	140-600-86	MLab	5	4
Charpy V-Notch	170-600-110	MLab	5	4

After heat treatment, the blanks were turned into round bar tensile specimens by the AFIT model shop. The specimens complied to ASTM E8 with test section diameters of 6 mm. The finished bars, as-built and heat treated, were tested in the AFIT mechanical testing laboratory on a 100 kip hydraulic Hillburn Biaxial machine. This machine is ideal for biaxial tension-torsion tests of round bar specimens, not

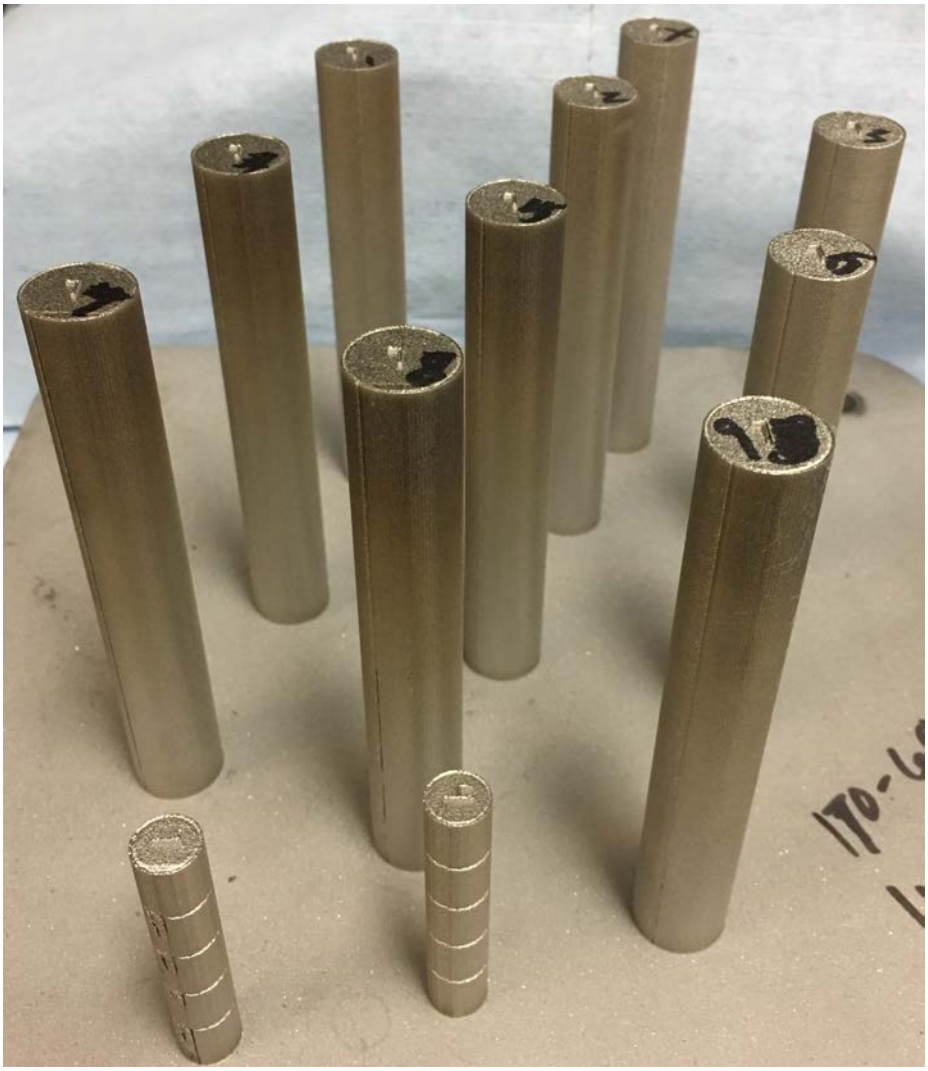

Figure 5.7. Tensile bars as printed on the M2, dosing factor 200%.

pure axial tension, but was the only machine available in the lab with round grips. Prior to testing, the torsion load was set to zero; controls within the machine held the torsion load to approximately 5 Nm or less. The initial elastic response was captured with an MTS extensometer. In image of the specimen loaded in the machine with extensometer installed in shown in Figure 5.8. The initial test was completed in load control, 0.5 kN/min, which was too fast to examine the plastic response, and the extensometer knives slipped several times during the initial elastic loading. Yield and modulus data was discarded, though the ultimate strength was retained. The control

mode was then changed to displacement, 0.025 mm/s, and smaller rubber bands were located for the extensometer. Grip pressure during testing was 9000 psi.

Figure 5.8. A 6mm diameter round bar specimen loaded in the Hillburn Biaxial machine with extensometer installed.

5.2.8 Charpy Testing

As AF9628 is a weapons steel, its primary purpose is to penetrate targets. While hardness and tensile strength contribute to the effectiveness of a weapons steel, it must be able to resist shattering on impact. The most basic experiment for testing impact strength is the Charpy impact test. Since Air Force weapons are dropped from high-altitude weapons bays, they must be able to withstand impact while cooled to cryogenic temperatures. To evaluate the impact strength of additively manufactured AF9628, the two parameter sets used to produce tensile specimens were also used to produce Charpy specimen blanks. Rectangular bars 58 mm tall with a 12 x 12

mm square cross section were printed on the MLab at the same locations used for the previous tensile build and a dosing factor of 230%, as displayed in Figure 5.9. A tenth blank for each parameter was printed in a third and final build. Half of the Charpy blanks were heat treated before the batch of 20 specimens were machined to the dimensions of full-sized v-notch specimens as outlined by ASTM E23-12c. Impact testing is planned at Eglin AFB on the same equipment used to characterize the original wrought specimens, however, the parts were not heat treated and manufactured soon enough to be reported in this document.

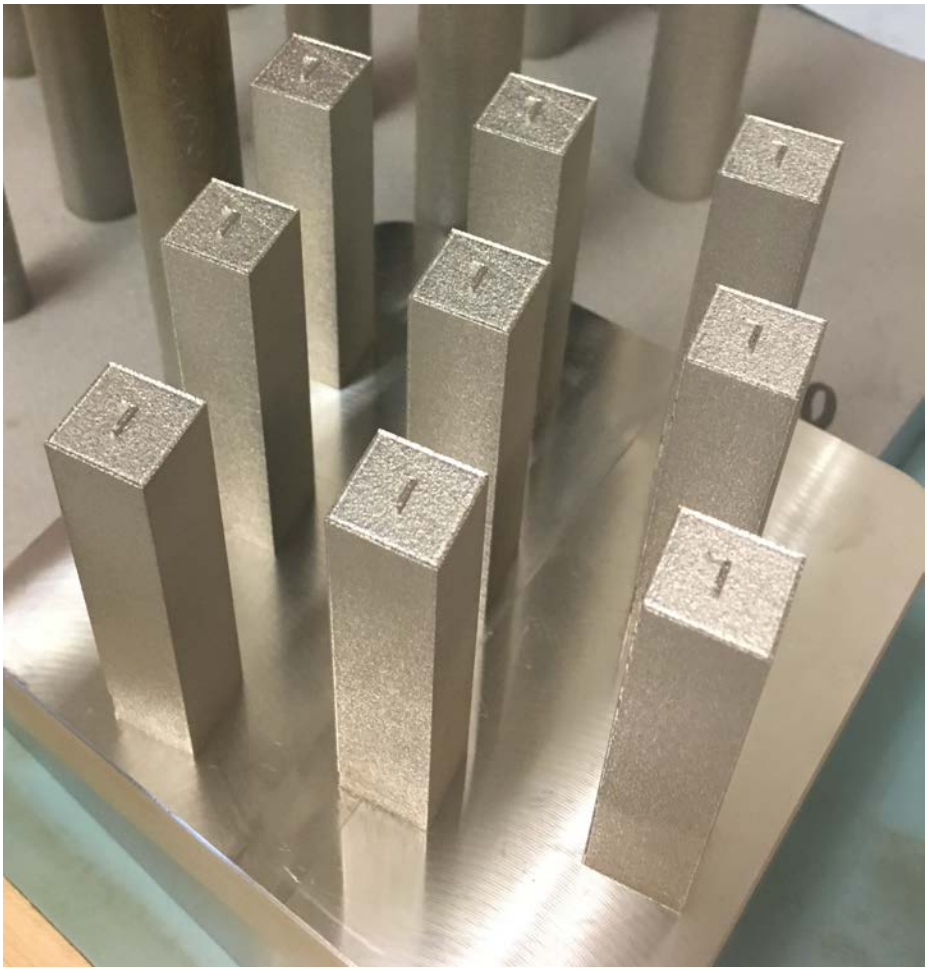

Figure 5.9. Charpy Impact specimens as printed on the MLab, 58 mm tall, dosing factor 230%.

5.3 Results

5.3.1 Porosity

5.3.1.1 Initial 2-D Porosity

The initial 7mm cylinders were remarkably successful, with eleven of the thirty parts exhibiting greater than 99.9% density. Images of the sectioned 7 mm parts are presented in Figure 5.10, and their processing conditions, fluence, volumetric energy density, part density, and coloration are summarized in Table 5.3. The two parameter sets tested at 80 W showed high porosity, and all overlap settings resulted in parts with significant blue discoloration from overheating. Because of this evidence of overheating, as well as the highly rounded shape, the pores present in the six 80 W parts are likely to be from keyholing during remelting, not a lack of fusion between powder layers and hatches. The six parts generated at 100 W settings achieved higher densities, though they were also discolored blue. The parts printed at 80 and 100 W were generated with the highest fluence levels tested, indicating that better print quality and less overheating could be achieved at a lower fluence value at those same power levels. The parts created at 140 W exhibited high densities, though the pores noted at 400 mm/s were rounded, indicating keyhole pores. The cylinders produced at 140 W and 600 mm/s achieved high densities without any discoloration, and the 86 μm hatch spacing setting was considered for further development. At 170 W, there was some success at 800 mm/s, but parts generated at 600 mm/s achieved consistently high densities without discoloration. The highest density was achieved at 170 W, 600 mm/s, and 110 μm hatch spacing, and this parameter set was selected for further development. At 200 W, the 426 mm/s parts exhibited clear keyholing and discoloration, but the 640 mm/s parts achieved extremely high densities when the large pore near the edge was excluded. This pore was observed during processing, and

is due to lipping along the contour scans of the cylinders that caused the rubber coater blade to jump and fail to deposit powder in that location. Despite the high densities observed at 200 W and 640 mm/s, these settings were cautiously excluded from immediate development due to some part discoloration and the consistent creation of the large pore near the edge.

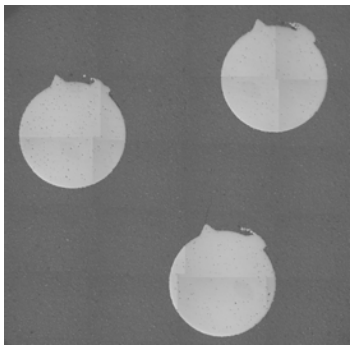

(a) 80 W, 125 mm/s

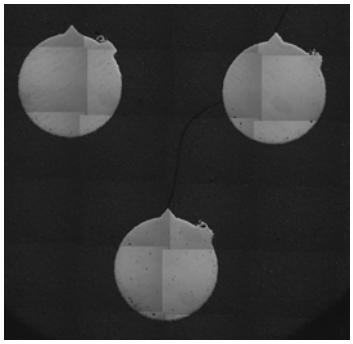

(b) 80 W, 170 mm/s

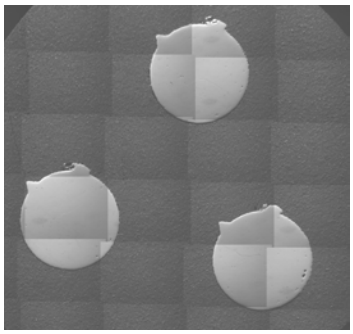

(c) 100 W, 180 mm/s

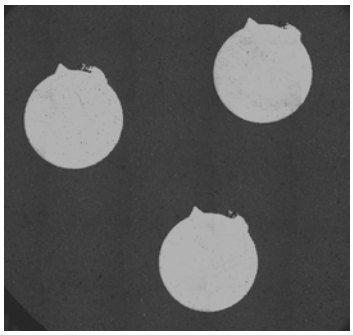

(d) 100 W, 212 mm/s

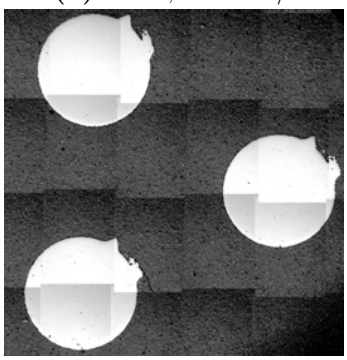

(e) 140 W, 400 mm/s

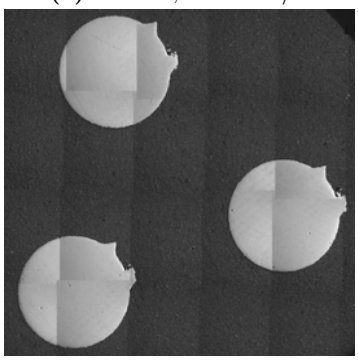

(f) 140 W, 600 mm/s

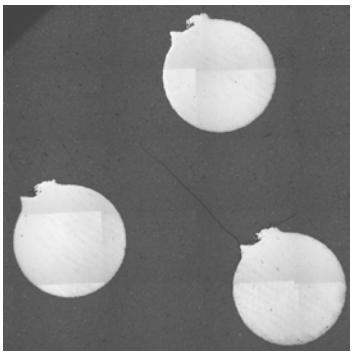

(g) 170 W, 600 mm/s

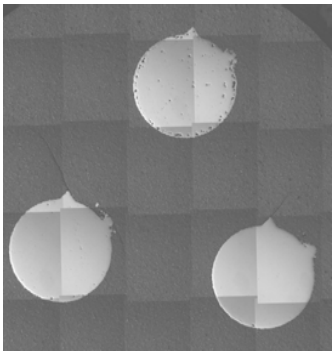

(h) 170 w, 800 mm/s

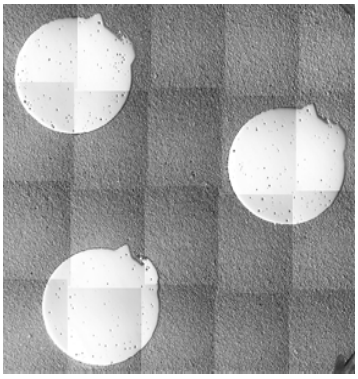

(i) 200 W, 425 mm/s

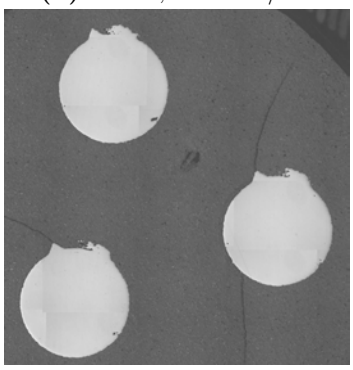

(j) 400 W, 640 mm/s

Figure 5.10. Images of sectioned and polished first 10 settings as 7mm cylinders. Hatch spacing is 90%, 80%, and 70% of measured weld track widths, clockwise from bottom-right most cylinder when triangular indexing marks are facing up.

Table 5.3. Porosity and discoloration of 7 mm cylinders, printed on the MLab at 30 μm powder bed thickness and 50 μm laser spot size.

Power W	**Speed** mm/s	**Hatch Spacing** μm	**Fluence** J/mm^3	E_V J/mm^3	**Density** %	**Coloration**
80	170	103	399	152	99.0411	Blue
80	170	91	399	171	99.8042	Blue
80	170	80	399	196	99.6914	Blue
80	125	119	543	179	99.4332	Blue
80	125	105	543	203	99.2676	Blue
80	125	92	543	232	99.725	Blue
100	212	107	400	147	99.702	Brown
100	212	96	400	164	99.4544	Blue
100	212	84	400	187	99.7341	Blue
100	180	144	472	129	99.701	Blue
100	180	128	472	145	99.8177	Blue
100	180	112	472	165	**99.9459**	Blue
140	600	97	198	80	**99.9068**	None
140	600	86	198	90	**99.9445**	None
140	600	76	198	102	**99.9305**	None
140	400	133	297	88	99.8349	Brown
140	400	119	297	98	**99.9411**	None
140	400	104	297	112	99.8859	None
170	800	90	180	79	99.8955	None
170	800	80	180	89	99.8380	None
170	800	70	180	101	97.6442	None
170	600	123	241	77	**99.9023**	None
170	600	110	241	86	**99.9805**	None
170	600	96	241	98	**99.9756**	None
200	640	119	265	88	**99.9698**	Brown
200	640	106	265	98	**99.9767**	Yellow
200	640	93	265	112	**99.9871**	Yellow
200	425	145	399	108	99.7454	Brown
200	425	129	399	122	99.4512	Brown
200	425	113	399	139	99.5504	Brown

As the parts tested now included hatch spacing as a parameter, fluence is no longer adequate to describe the amount of energy input into the volume of each part. The power, speed, and E_V of each part were read into a three-dimensional scatter plot, with individual points colored according to their densities, the density threshold at

99.8% (Figure 5.11. The intent of this plot was to highlight a potential relationship between the three axes, potentially a surface that could be described mathematically. However, the region of highest density appeared to cluster around a particular value of E_V, with some linear variation along power and speed. As the only values changing in fluence for these parts were the power and speed, this plot was re-interpreted as fluence vs E_V (Figure 5.12). Comparing fluence and E_V revealed that the highest density parts were clustered around a fluence of around 250 J/mm^3 and an E_V of around 85 J/mm^3.

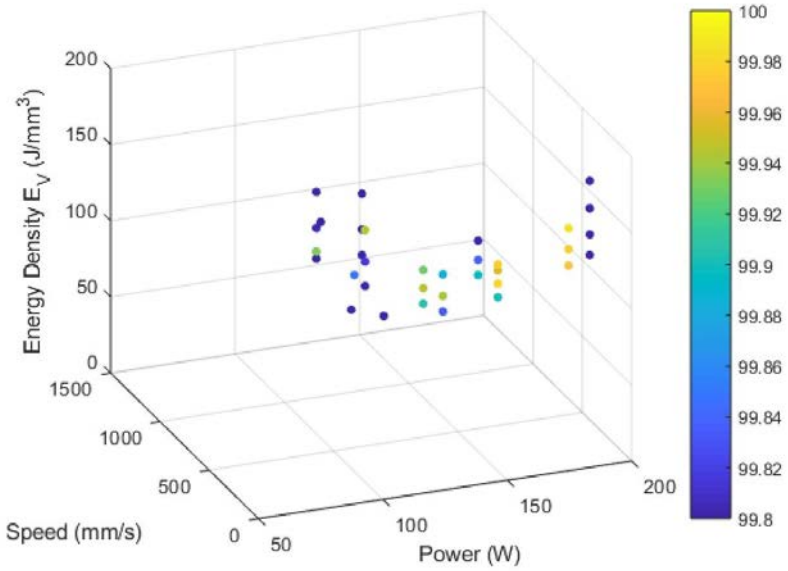

Figure 5.11. Plot of power, speed, E_V, and density of the first 30 parts generated for porosity analysis.

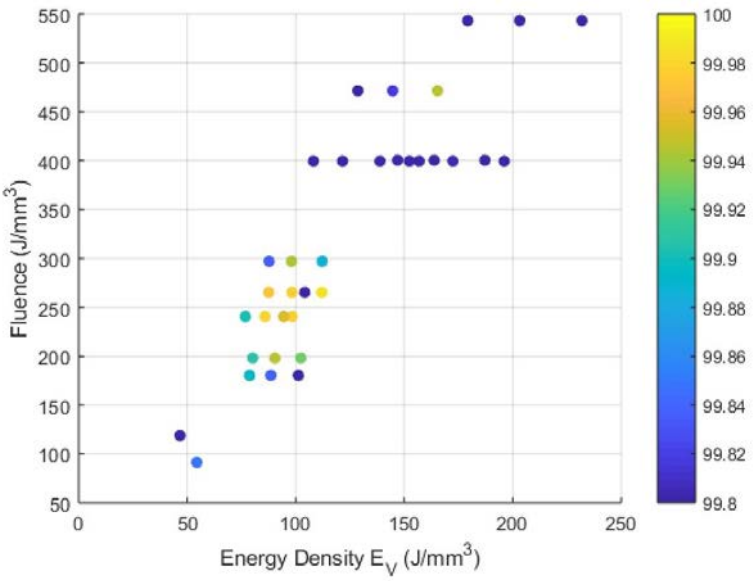

Figure 5.12. Plot of E_V vs Fluence, with points colored by density.

5.3.1.2 CT Scanning of Selected Parts

As the CT scanner was not able to scan through the 60 parts created for it in a reasonable amount of time, a selection of eight of the sixty party was made based on the high density intersection of fluence and E_V noted in the previous section. The processing parameters of these parts are are noted in Table 5.4. While an exact match to the intersection was not always possible, values were matched as closely as possible given the options. The selection was also biased toward power levels of greater than 100 W due to the decreased time to build.

The images output by the VolumeGraphics analysis of the CT scans are presented in Figure 5.13, 5.14, and 5.15 below. The raw scans of the steel parts generated a large amount of what appeared to be noise, which was then filtered out. The porosity/inclusion analysis was run with an Only threshold algorithm in Void analysis. The threshold was interpolated at a factor of 0.85, with minimum and maximum thresholds set at 8 voxels (volume) and 10 mm (diameter), respectively. An adaptive gauss

Table 5.4. 7 mm vs CT vs Sectioned porosity

Power W	**Speed** mm/s	**Hatch Spacing** μm	**Fluence** J/mm^3	E_V J/mm^3
80	250	81	272	132
100	430	85	197	91
140	400	119	297	98
140	600	86	198	90
170	480	137	301	86
170	600	110	241	86
200	640	93	265	112
200	800	94	212	89

smoothing function was used, with a smoothing factor of 1.500 and an edge threshold of 0.100. All data filtering was performed by Greg Cobb, Research Assistant, who had specialized training for the CT scanner and associated data analysis.

The parts generated at 80 W and 100 W again exhibited high porosity, though a large number were concentrated at the interface between the skin and core scans, which implies the scan strategy was a factor in the overall porosity. The parts created at 140 W and 170 W displayed low porosity consistent with that previously observed in the 7 mm cylinders. The parts generated at 200 W settings exhibited extraordinarily low porosity, though the 800 mm/s setting included a larger than usual amount of noise before filtering. The actual densities of the parts as calculated by VolumeGraphics are discussed later in section 5.3.1.3. As the CT scanner is not capable of detecting pores with diameters of less than 8 μm, the scanned parts were then sectioned and polished to confirm their high densities.

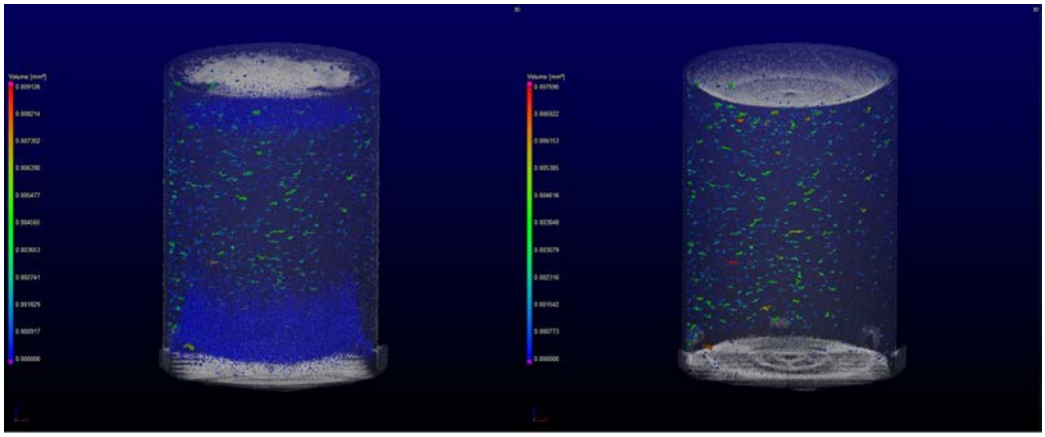

(a) 80 W, 250 mm/s, 81 μm

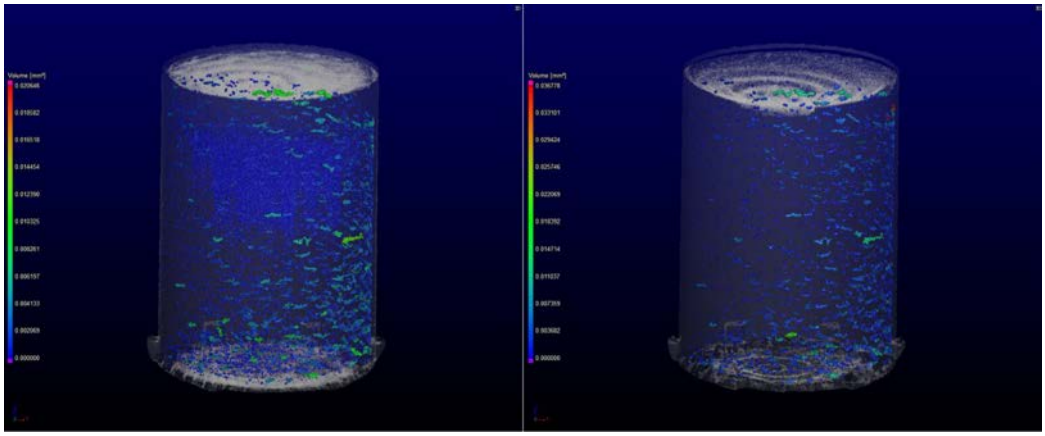

(b) 100 W, 430 mm/s, 85 μm

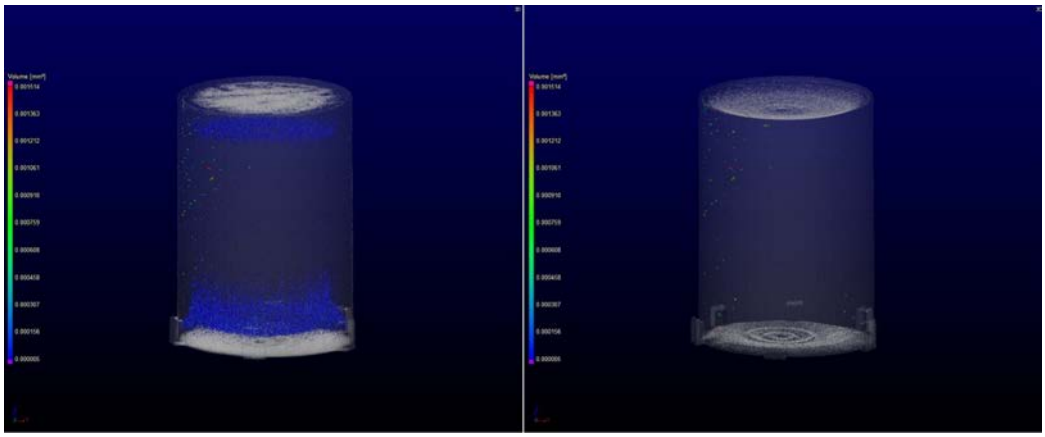

(c) 140 W, 400 mm/s, 119 μm

Figure 5.13. VolumeGraphics output of three CT scanned cylinders

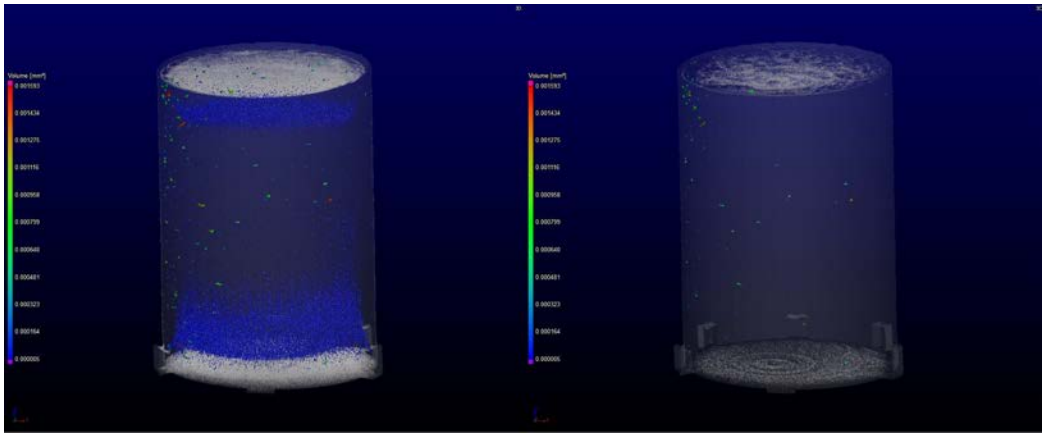

(a) 140 W, 600 mm/s, 86 μm

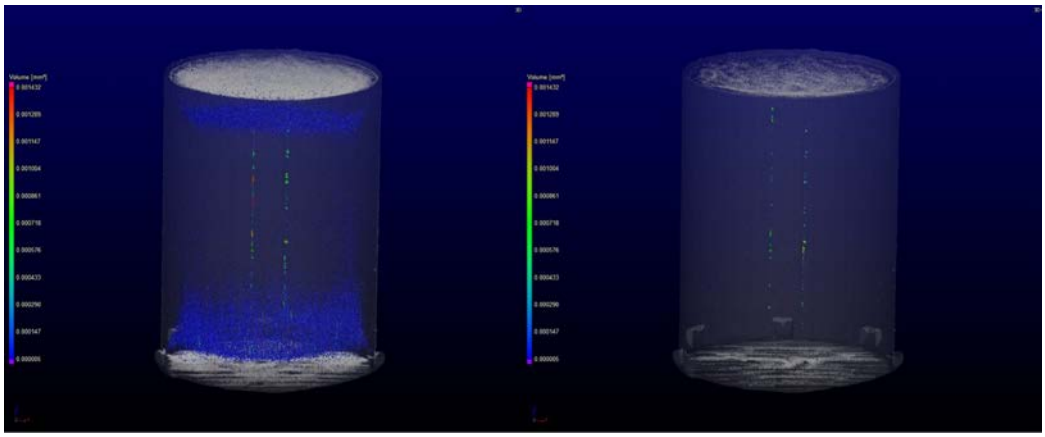

(b) 170 W, 480 mm/s, 137 μm

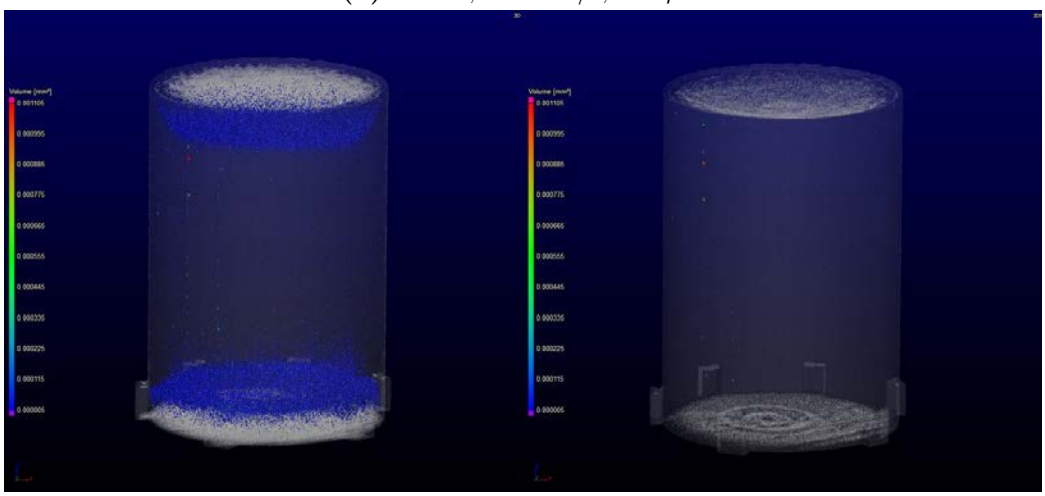

(c) 170 W, 600 mm/s, 110 μm

Figure 5.14. VolumeGraphics output of three CT scanned cylinders

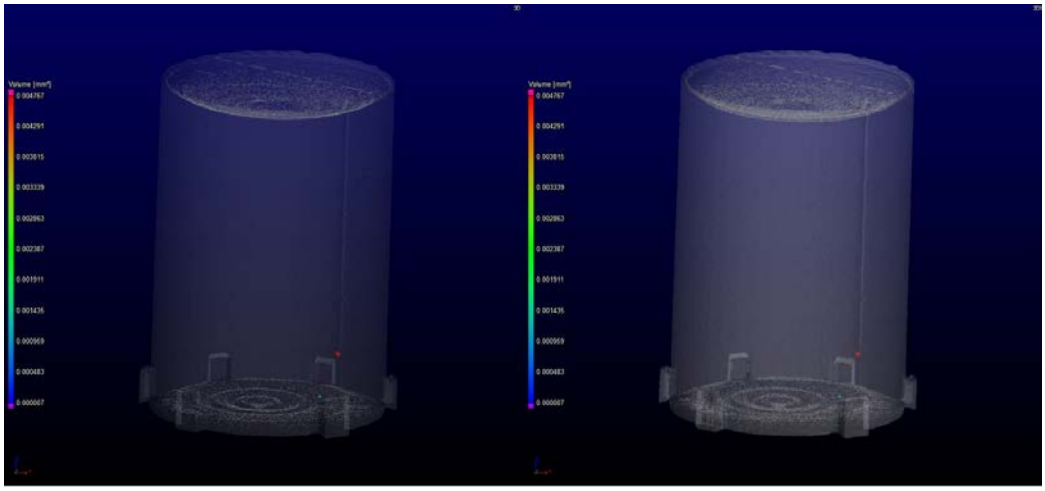

(a) 200 W, 640 mm/s, 93 μm

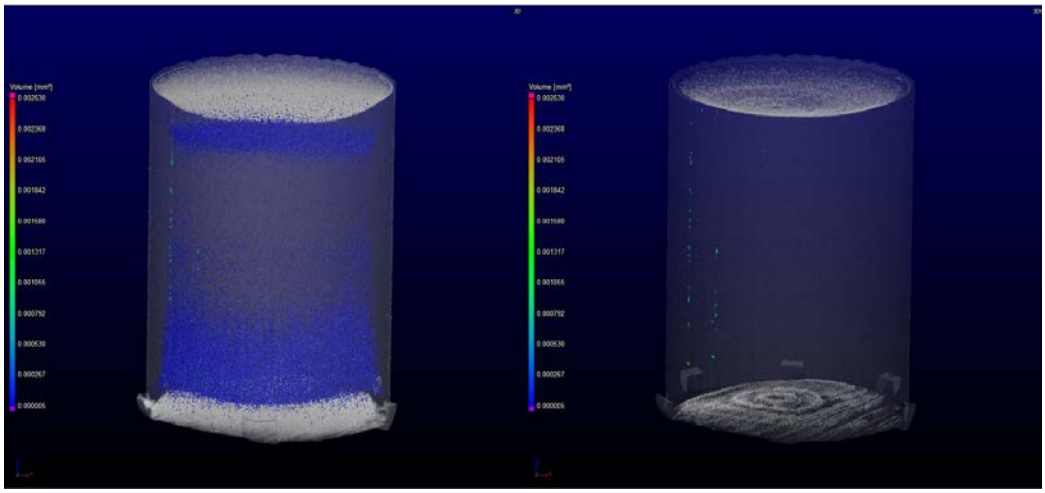

(b) 200 W, 800 mm/s, 94 μm

Figure 5.15. VolumeGraphics output of two CT scanned cylinders

5.3.1.3 2-D Porosity of CT Scanned Parts

The sectioned parts, pictures of which are displayed in Figures 5.16, 5.17, and 5.18, tended to confirm the CT findings. The parts generated at the 80 and 100 W settings had high numbers of pores, and most were large enough to be detected by the CT scanner. At 140 W, the part created at 400 mm/s appeared to have fewer pores than the part created at 600 mm/s, and the pores present in the 600 mm/s part are consistently smaller than the noise floor of the CT scanner. The decrease in

part density between the original 7 mm sectioned part and this larger 10 mm cylinder could be attributed to the use of reused powder, though this increase is not evident in any of the other parts, which were also build from recycled powder. The placement of each part on the build plate was consistent for each parameter set, and position is unlikely to be a cause of increased porosity. The 170 W parts exhibit densities similar to what has been observed previously, with the 600 mm/s part displaying few larger pores, with a scattering of small, sub-micron diameter pores. The 200 W parts, especially at 640 mm/s, display high densities consistent with their CT scans. The 200 W, 640 mm/s again repeats the high density first measured with the 7 mm cylinders, but the large pore at the bottom right hand corner of the surface is again present, indicating that this may be a good core parameter, but is not the best choice for generating part contours or skins. The density of the eight parts calculated with each technique used is summarized in Table 5.5, along with the relative build rates of each process parameter set. In general, the increase in the number of pores vs. the 7 mm cylinders can be attributed to the increase in size and density of the build, which will increase both the amount of soot and the amount of area that can be negatively affected.

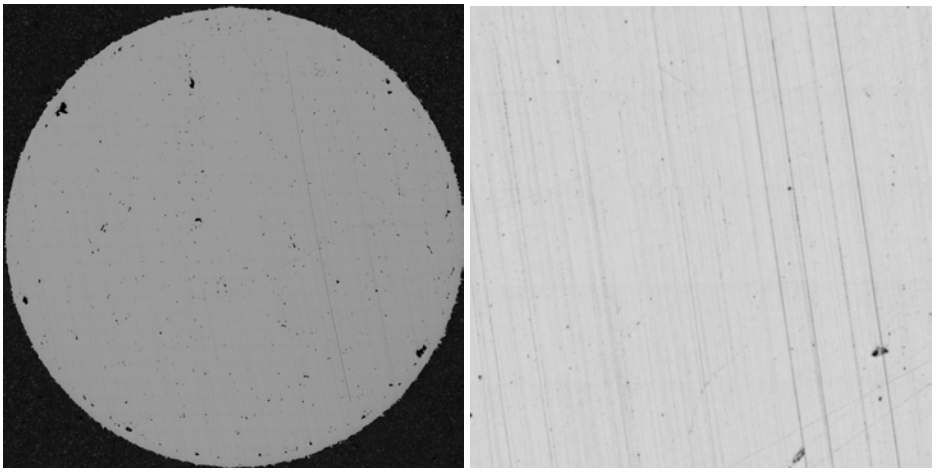

(a) 80 W 250 mm/s 81 μm

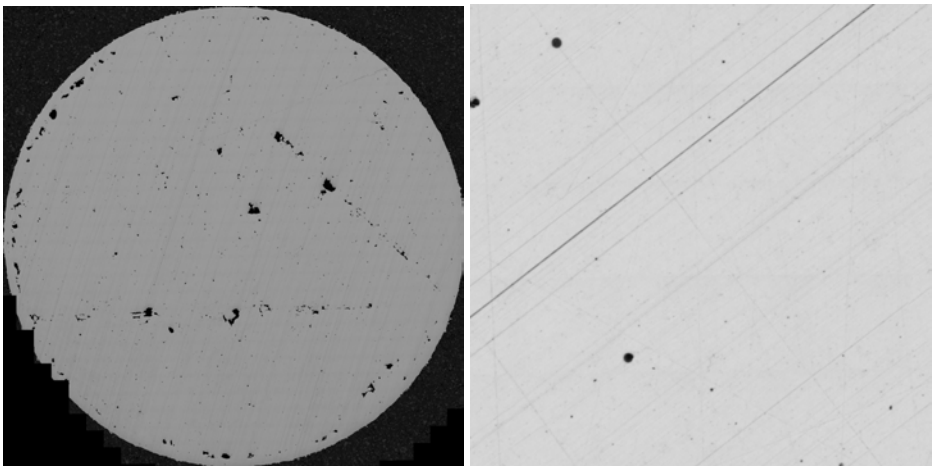

(b) 100 W 430 mm/s 85 μm

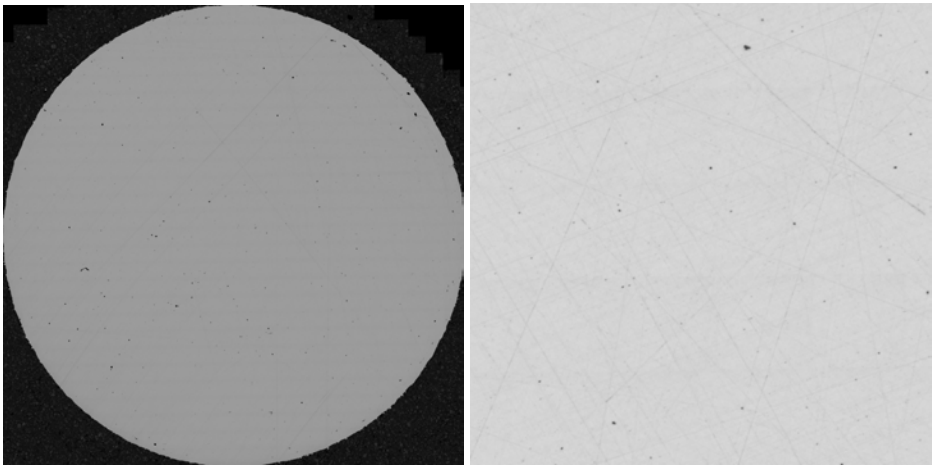

(c) 140 W 400 mm/s 119 μm

Figure 5.16. Optical micrographs of the internal porosity of the CT scanned cylinders at 5x and 20x magnification.

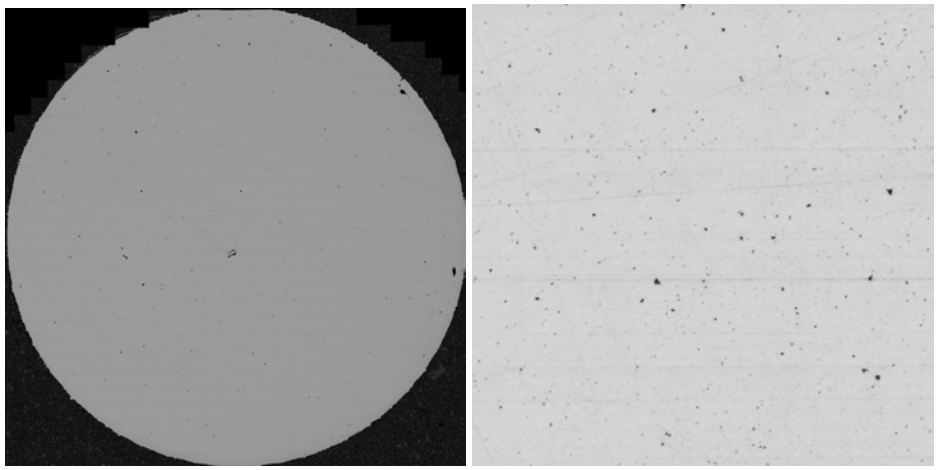

(a) 140 W 600 mm/s 86 μm

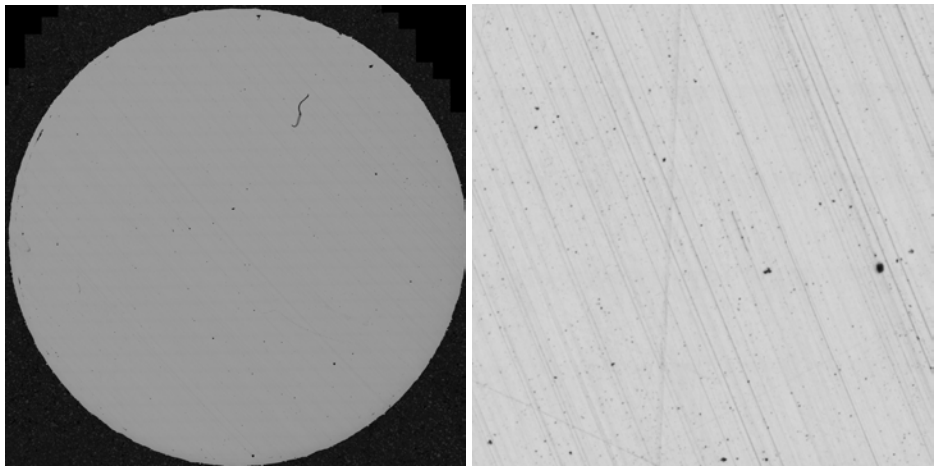

(b) 170 W 480 mm/s 137 μm

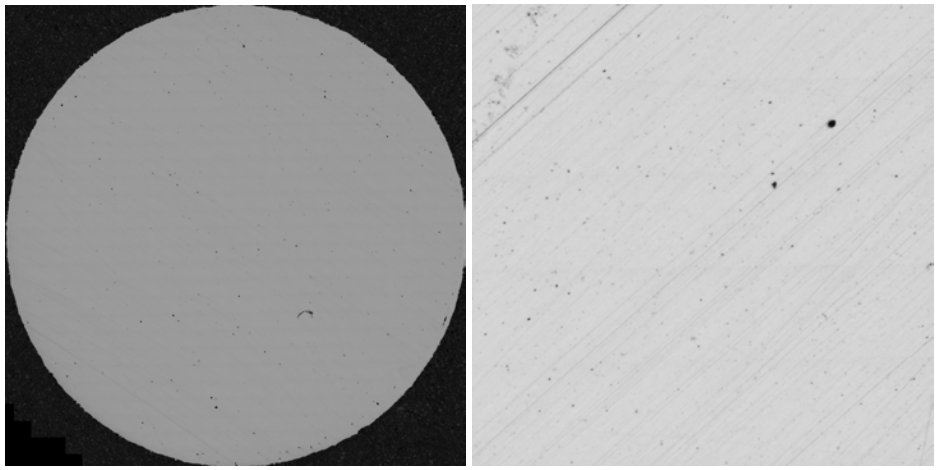

(c) 170 W 600 mm/s 110 μm

Figure 5.17. Optical micrographs of the internal porosity of the CT scanned cylinders at 5x and 20x magnification.

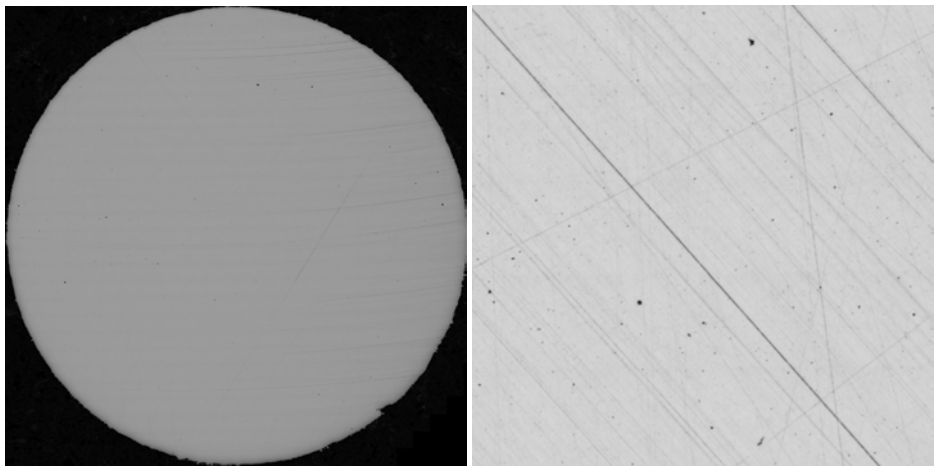

(a) 200 W 640 mm/s 93 μm

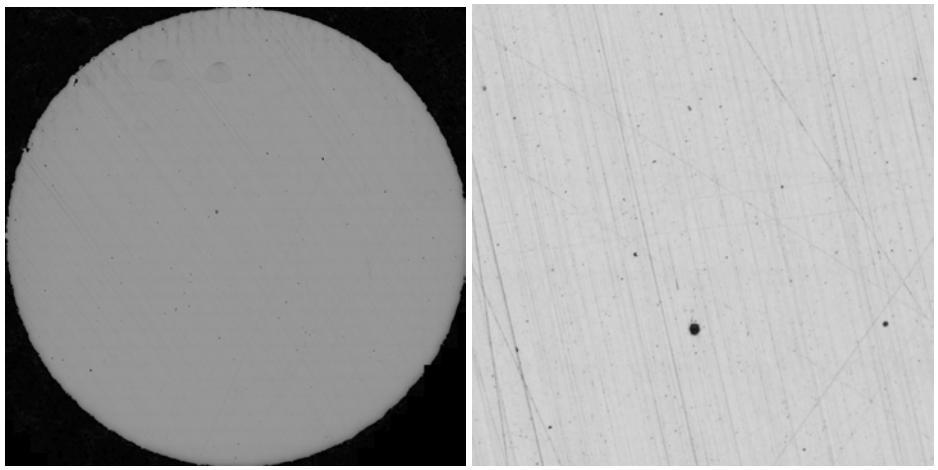

(b) 200 W 800 mm/s 94 μm

Figure 5.18. Optical micrographs of the internal porosity of the CT scanned cylinders at 5x and 20x magnification.

5.3.2 Surface Roughness

The laser scanning of the topology of the eight parts evaluated in the CT scanner revealed two distinctive topological profiles for the tops and sides of the additively manufactured parts. The top surfaces were consistent with the appearance of the weld tracks, with a ripple-like appearance due to the hatch spacing overlap. The largest features were the undulations over the weld stripes, with spikes where powder particles partially melted or sintered to the molten surface. The sides of the cylinders displayed

Table 5.5. A summary of the densities of the eight parts selected for CT scanning, evaluated as 2-D sections and CT scans, along with their relative build rates.

Process Parameters W - mm/s - μm	**7 mm Porosity** %	**CT Porosity** Unfiltered %	Filtered %	**Sectioned CT Porosity** %	**Time to Build 1 cm^2** s
80-250-81	-	99.7114	99.8772	99.5238	49.4
100-430-85	-	99.6251	99.7963	99.0803	27.4
140-400-119	99.9411	99.8948	99.9963	99.9080	21.0
140-600-86	99.9445	99.8434	99.9964	99.9055	19.4
170-480-137	-	99.8652	99.9982	99.9096	15.2
170-600-110	99.9805	99.7892	99.9987	99.9270	15.2
200-640-93	99.9871	99.9994	99.9994	99.9688	16.8
200-800-94	-	99.4203	99.9952	99.9485	13.3

a characteristically pockmarked appearance, with most of the features caused by partially sintered powder adhering to the heated parts while surrounded by loose powder during processing. The side scans did not reveal any noticeable features at the 30 μm layer spacing, indicating that the laser was fully remelting previous layers and the parts would not be prone to delamination. Similarly, there was no evidence of solidification cracking on the top surface, and the welds appeared to smoothly melt together. Representative images of top and side scans of the images are displayed in Figures 5.19 and 5.20. Scans of all eight parts are located in Appendix E. The surface roughness values of each part at both 5x and 20x magnification is tabulated in Table 5.6 and normalized and plotted in Figure 5.21. The normalized data does not indicate any clear trends in surface roughness, other than a relatively high roughness at the 80 W and 100 W parameter sets.

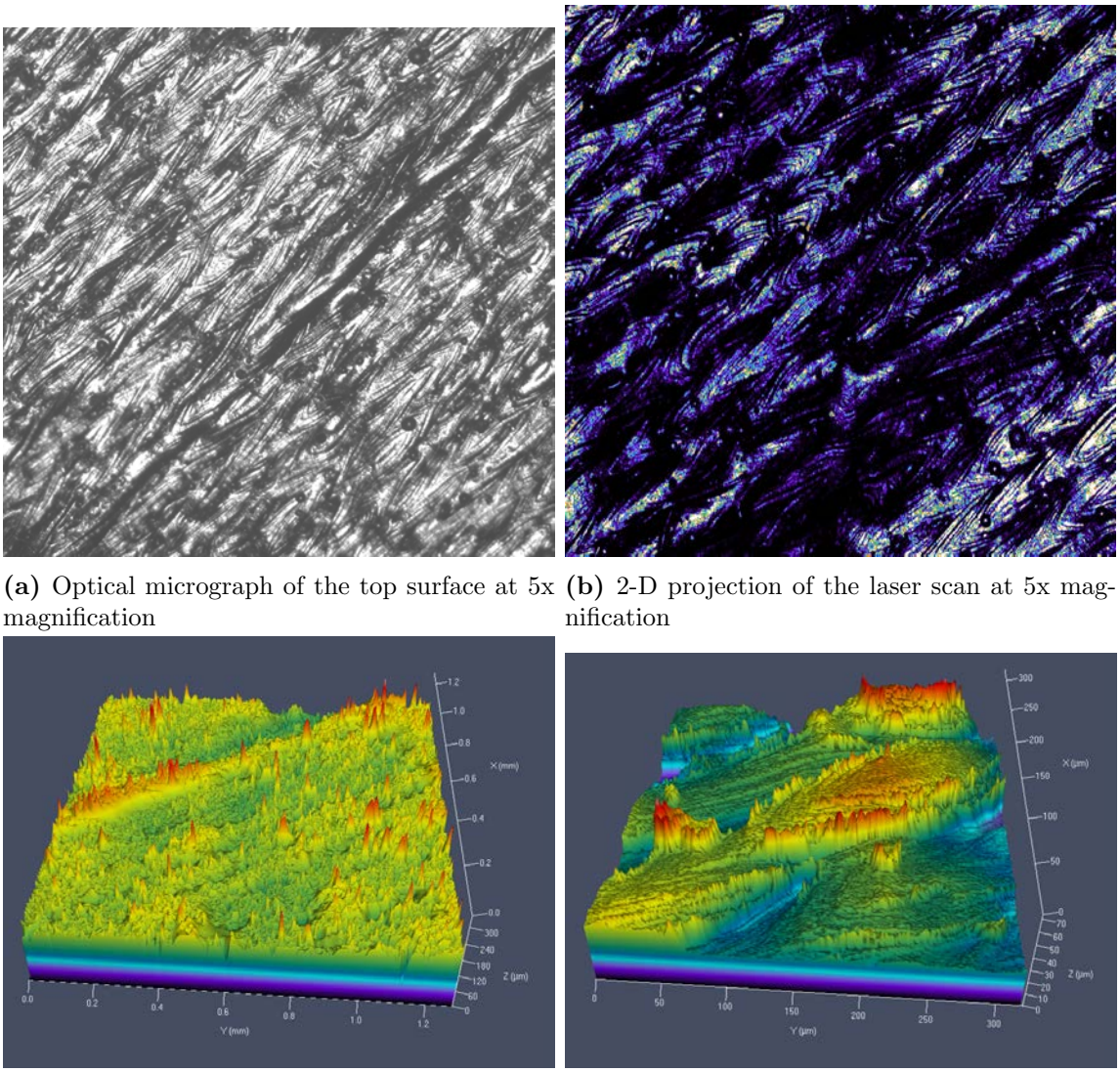

(a) Optical micrograph of the top surface at 5x magnification

(b) 2-D projection of the laser scan at 5x magnification

(c) Topographical map at 5x magnification

(d) Topographical map at 20x magnification

Figure 5.19. Representative images of the surface roughness of the top of an additively manufactured AF9628 cylinder

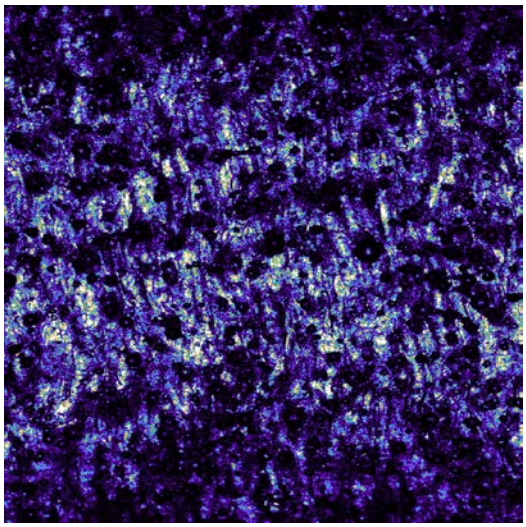

(a) 2-D projection of the laser scan at 5x magnification

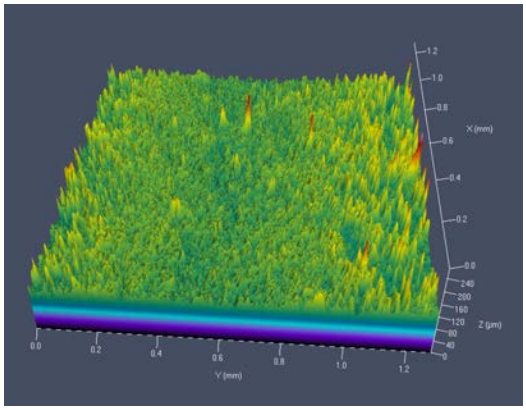

(b) Topographical map at 5x magnification

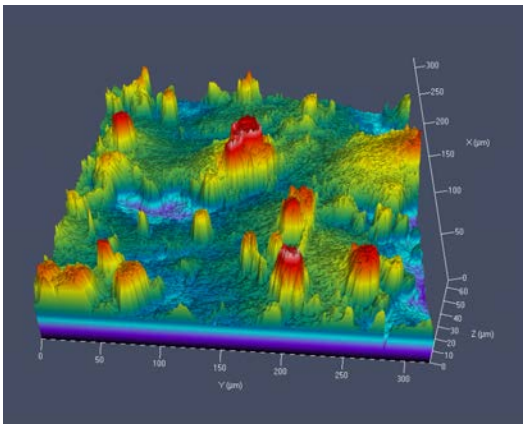

(c) Topographical map at 20x magnification

Figure 5.20. Representative images of the surface roughness of the side of an additively manufactured AF9628 cylinder

Table 5.6. Surface Roughness Values on top and side, 5x and 20x

Process Parameters	Side Sa		Top Sa	
W - mm/s - μm	5x	20x	5x	20x
80-250-8	18.885	13.579	24.855	17.899
100-430-8	17.038	9.419	24.118	8.903
140-400-8	7.613	6.379	12.539	7.310
140-600-86	13.019	5.054	17.032	8.696
170-480-9	6.669	5.249	12.989	7.629
170-600-110	10.643	6.827	16.760	7.532
200-640-7	9.704	8.877	6.704	4.963
200-800-8	10.868	7.529	9.997	5.408

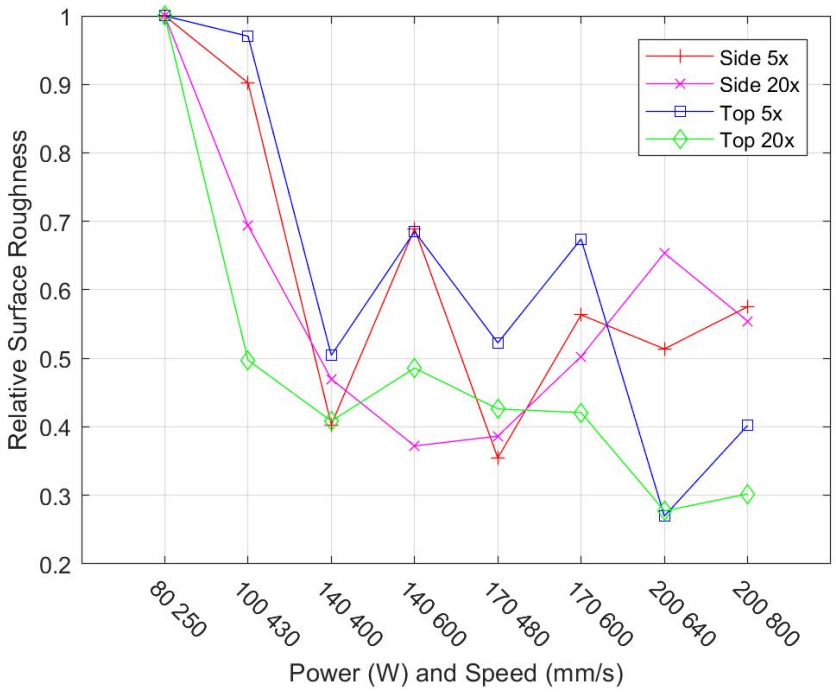

Figure 5.21. Normalized surface roughnesses of the tops and surfaces of additively manufactured cylinders produced at eight process parameter combinations.

5.3.3 Hardness

The material microhardness measured in the as-built condition is very similar for both of the process parameters evaluated, with both near 450 Vickers, as shown in Table 5.7. When converted to the Rockwell C scale, this results in hardnesses of 45.5

and 45.0. As the published Rockwell C hardness of wrought AF9628 steel is greater than or equal to 45, this indicates that the as-built parts may have similar martensitic microstructures to the original quenched and tempered steel. This suggests that the elevated temperatures and long build times of additively manufactured steel parts may result in in-process tempering. The fact that the parts produced at 140 W and 198 J/mm^3 of fluence are slightly harder than the parts produced at 170 W and 241 J/mm^3 of fluence support this conclusion, as the increased energy density would increase the build volume temperature, therefore increasing the softening effect of the in-process temper. The diagonals produced by the Vickers indenter were of similar lengths, which suggests that in the case of these axisymmetric, vertical parts, there is some orthotropy present in the Z direction.

Table 5.7. Vickers hardness measurements and computed values, 500g and 13s, conversion via table provided by Non-Destructive Testing Educational Center [104]

Process Parameters	**Diagonal A**	**Diagonal B**	**Hardness**	
W - mm/s - μm	μm	(μm)	Vickers	Rockwell C
140-600-86	44.5	44.2	471.3	47.0
140-600-86	44.8	45.4	455.8	46.0
140-600-86	47.1	45.5	432.5	43.6
140-600-86	45.9	46.4	435.3	44.0
140-600-86	44.5	44.4	469.2	46.8
170-600-110	44.8	44.5	465.0	46.5
170-600-110	43.0	43.3	447.8	45.1
170-600-110	45.1	45.9	447.8	45.1
170-600-110	46.2	47.5	422.4	42.9
170-600-110	45.7	44.9	451.8	45.5

5.3.4 Microstructure

5.3.4.1 Etching

The 2% Nital etch of an early sample of additively manufactured AF9628 shown in Figure 5.22 indicates that the melting and solidification in the heat affected zone

results in a martensitic microstructure, as is typical in welds. The martensitic plates appear to be on the order of 20 - 30 μ in length, as compared to the plates present in wrought AF9628, which are more regular and on the order of 30 - 40 μm. Evaluation of the Nital etched sample in an SEM (Figure 5.23) revealed equiaxed dendritic cells associated with a vertical build. If a part sectioned in the transverse direction was etched with Nital and similarly evaluated in an SEM, we would expect to see the elongated, lamellar dendrites associated with columnar grains. Swab etching with saturated aqueous picric acid for times up to 2.5 minutes produced no change, so the time was increased to five minutes. The fivue minute etch produced a blued over-etched surface, but low magnification in an optical microscope produced what are believed to be PAGB's. The features produced by the etch were long, rounded, and present in perfectly aligned groups, indicating that they are following the shape of the laser scan path. They looked remarkably similar to the light colored features observed in the top right corner of Figure 5.22a. The etching time will need to be fine-tuned before imaging, and this work will be presented in later papers.

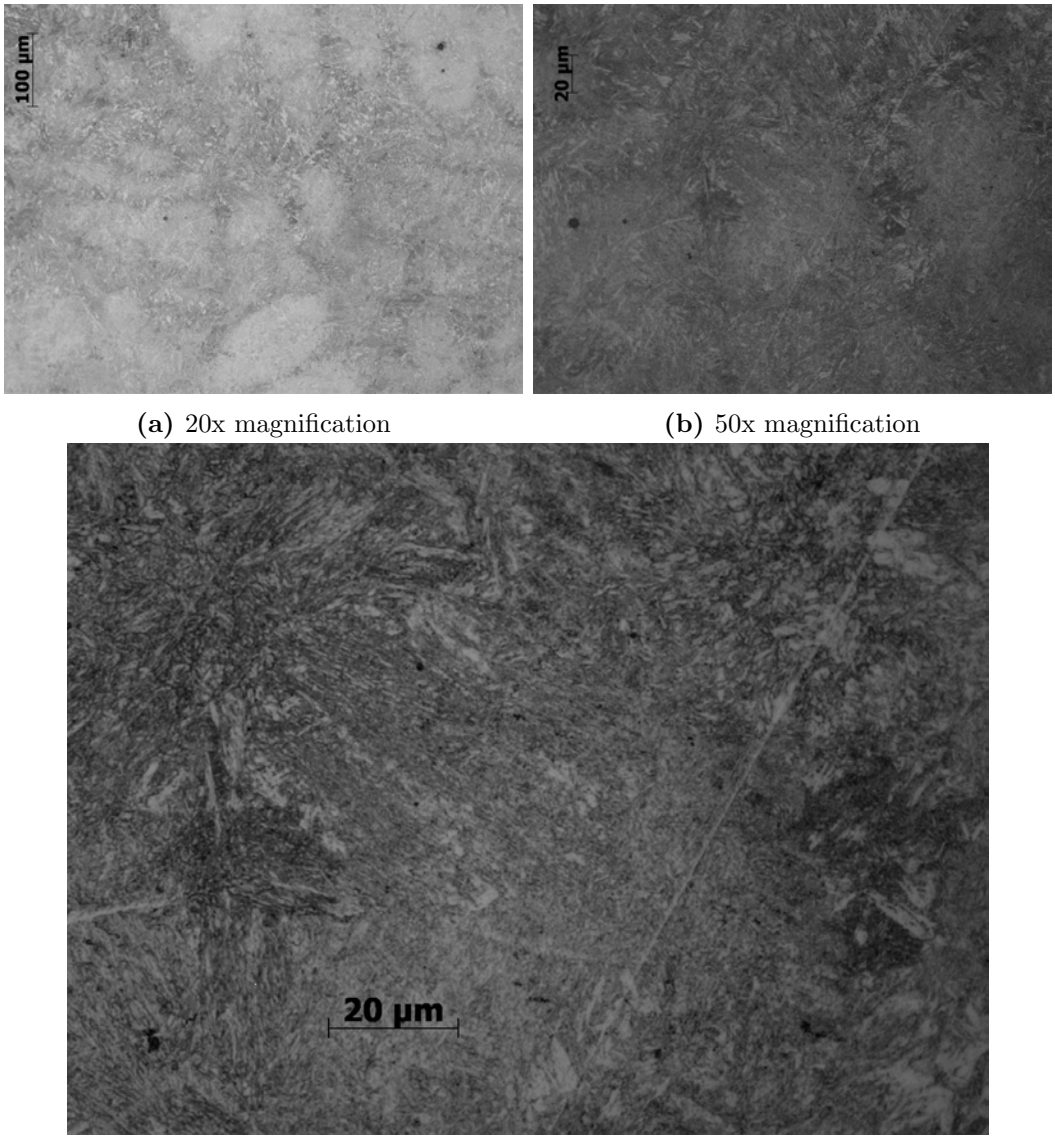

(a) 20x magnification **(b)** 50x magnification

(c) 100x magnification

Figure 5.22. Optical micrographs of a Nital etched sample of additively manufactured AF9628 steel, printed at 100 W.

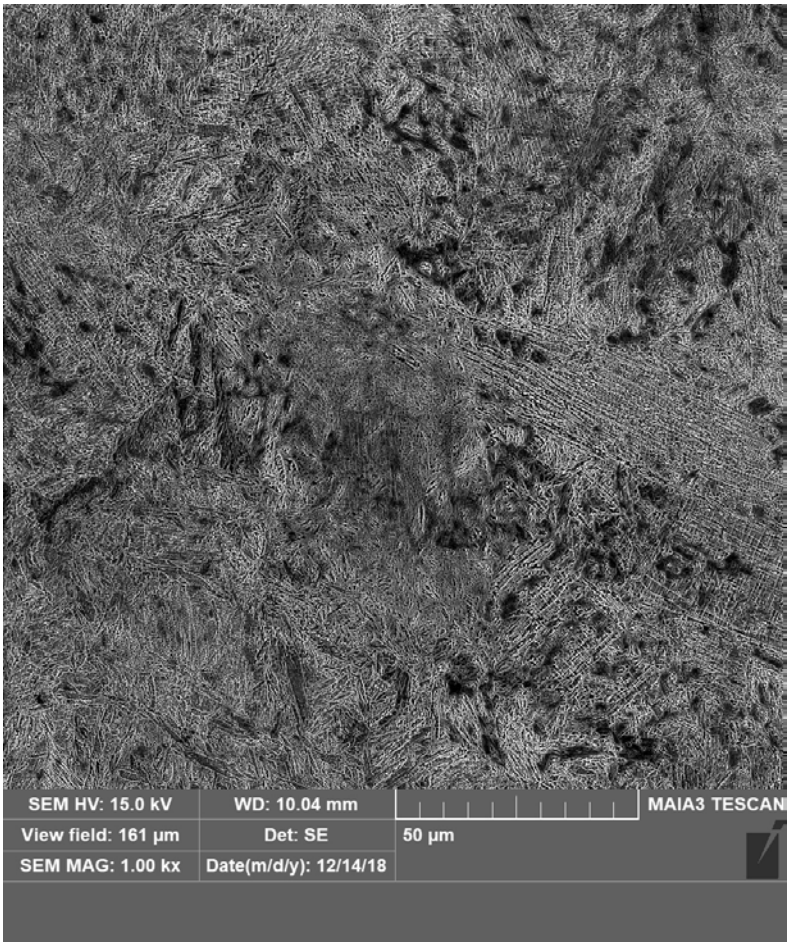

(a) 1000x magnification

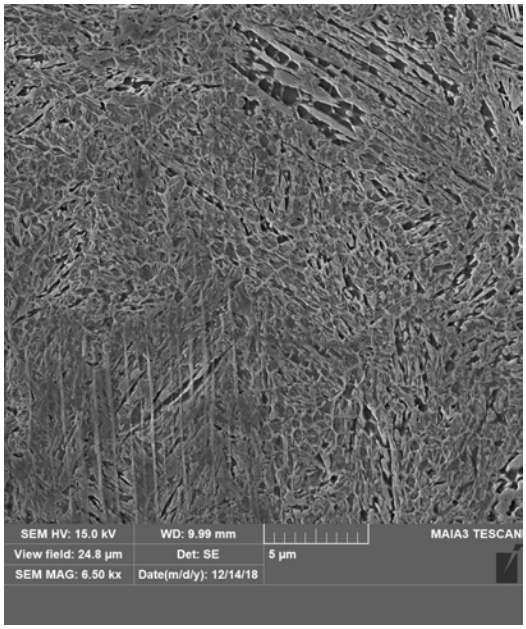

(b) 6500x magnification

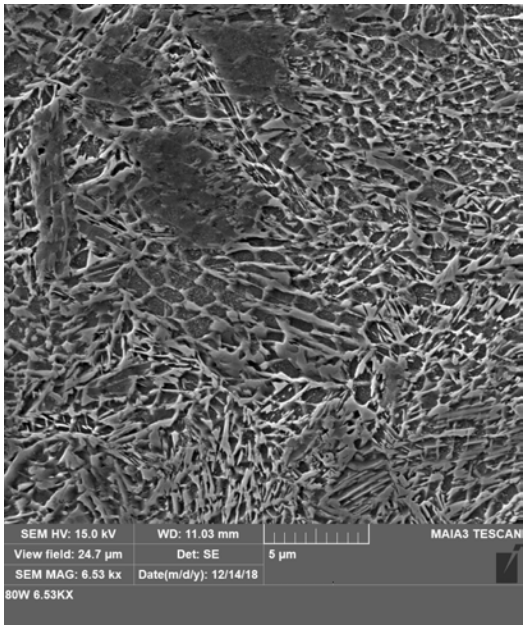

(c) 6530x magnification

Figure 5.23. Scanning electron micrographs of a Nital etched sample of additively manfactured AF9628 steel, printed at 100 W.

5.3.4.2 Electron Backscatter Diffraction

An intial EBSD scan of the Z plane (Figure 5.24) conducted at AFRL/RX displays microstructures demonstrating the fine martensitic grain structure consistent with growth with the vertical build direction of additively manufactured parts. The scan was indexed with ferrite, which is nearly crystallographically identical to martensite, and there appears to be very little retained austenite. Further scans will need to be conducted at smaller step sizes to improve the resolution and detection of PAGB's.

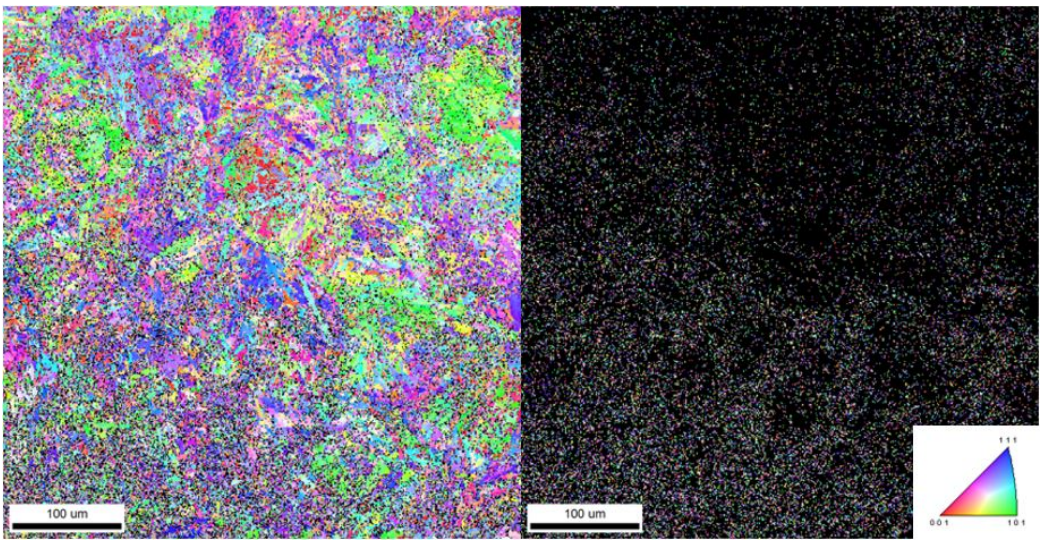

(a) Raw EBSD Inverse Pole Figure, indexed with Ferrite (left) and Austenite (right).

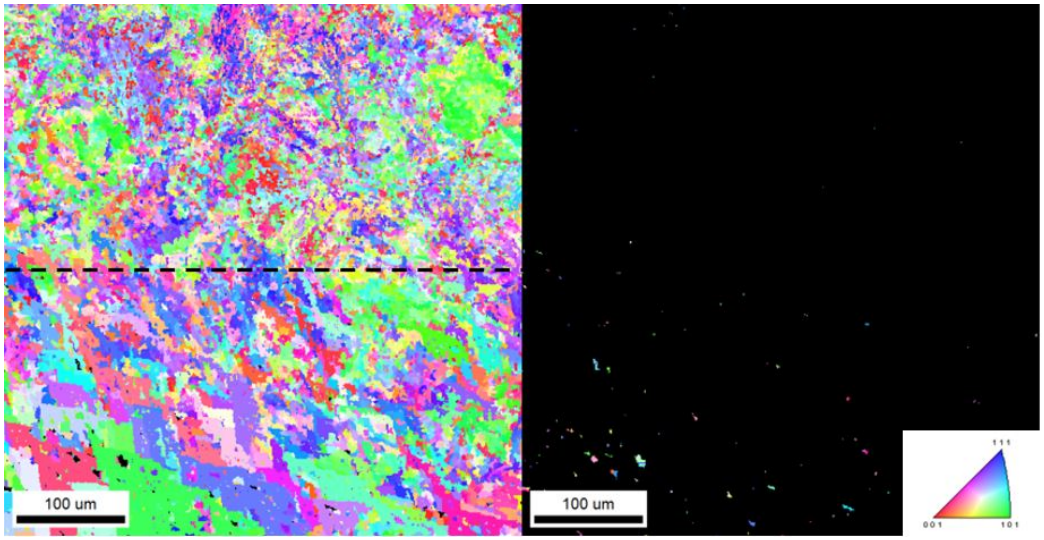

(b) EBSD Inverse Pole Figure after cleanup, indexed with Ferrite (left) and Austenite (right). Microstructure above the dashed line is most likely to be the best actual representation of the microstructural texture.

Figure 5.24. Z-plane EBSD scans of AF9628 steel printed on the MLab at 100 W, X mm/s, and 100 μm hatch spacing. The sample was final polished with a vibratory polisher filled with a mixture of SiO_2 and AlO_3 for 17 hours, and the scan step size was 1 μm. EBSD scans are provided courtesy of Mike Velez and Dr. Vikas Sinha, AFRL/RX.

5.3.5 Mechanical Testing

5.3.5.1 Tensile Bars

The four bars from the batch printed at 140 W on the MLab tested in the as-built condition consistently broke in a brittle manner, and examination of the fracture surface revealed evenly spaced, full-chord-with lack of fusion pores (Figure 5.25. Due to the regularity of the pores, the source was attributed to the scan strategy, not a buildup of soot that would have caused a more random distribution of porosity. Since the parameters used were developed on the MLab and proven to produce a high-density part, these defects are attributed to an intermediate software update from nTopology that was not tracked. The shape of these pores is also consistent with artifacts visible on the top surface of the cylindrical parts printed for CT scanning.

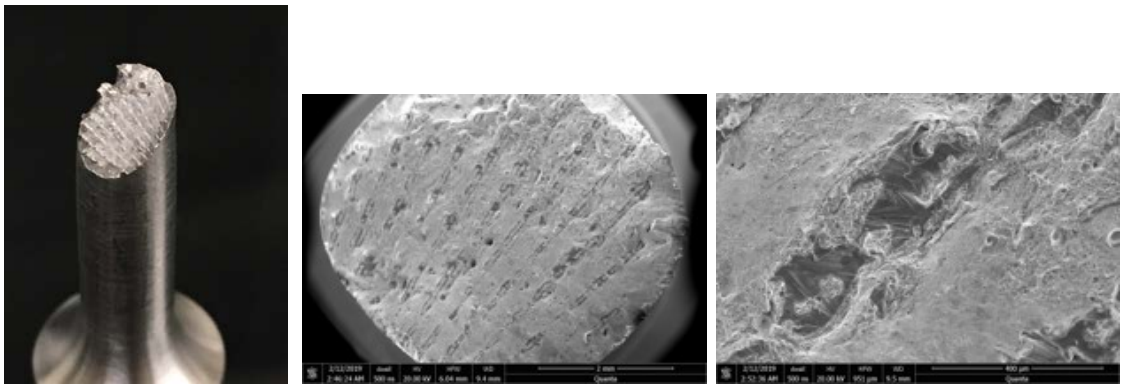

(a) Shape and appearance of the 140 W MLab fracture surface, with little to no necking noted, fracture along a 45 degree brittle shear plane, and visible lines of porosity.

(b) Shape and appearance of the 140 W MLab fracture surface, with regularly spaced lines of porosity, likely to be a scan strategy flaw

(c) Detail image of a large pore from the 140 W MLab fracture surface; the bottom of the pore looks similar to the top surface of an AM part, indicating that the pore is greater than one layer deep.

Figure 5.25. Images of the fracture surface of a representative tensile bar from the group of four as-built bars printed on the MLab at 140 W, 600 mm/s and 86 μm hatch spacing.

Three bars from the batch printed at 140 W on the M2 tested in the as-built condition broke in a ductile manner, with significant necking followed by a classic

cup-and-cone fracture (Figure 5.26). The slicing software received an update before these parts were built, eliminating the pores seen in the MLab build. A fourth bar broke in a brittle manner along a 45 degree shear plane, but reached a higher UTS and showed similar elongation and did not have any noticeably large pores. This bar was built in the top center position of the 3x3 grid, and should not have seen a larger than average amount of soot on its powder bed, so the brittle fracture is unlikely to be attributed to build plate location. The fifth bar was temporarily misplaced by the AFIT Model Shop during machining, and will be tested later.

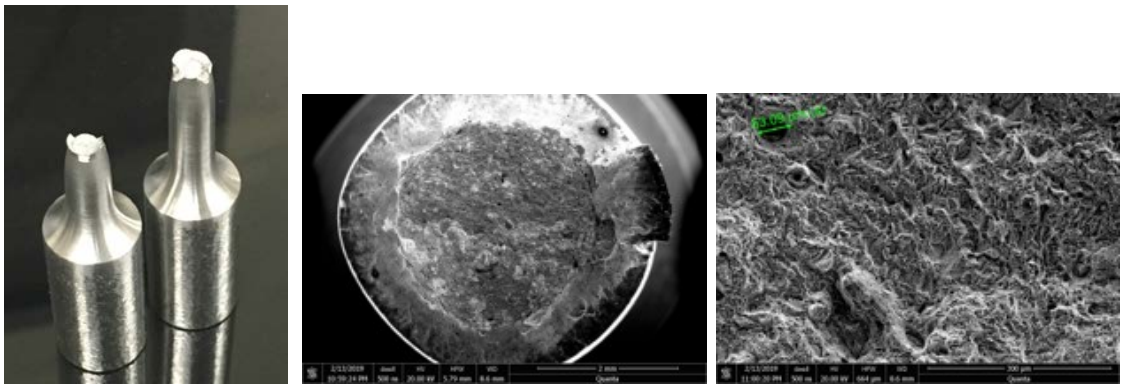

(a) Shape and appearance of the 140 W M2 fracture surface, with significant necking observed and classic cup-and-cone ductile fracture

(b) Shape and appearance of the 140 W M2 fracture surface

(c) Detail image of the ductile fracture region from the 140 W M2 fracture surface

Figure 5.26. Images of the fracture surface of a representative tensile bar from the group of five as-built bars printed on the M2 at 140 W, 600 mm/s and 86 μm hatch spacing.

Four bars from the batch printed at 170 W on the M2 tested in the as-built condition broke in a ductile manner, with significant necking followed by a classic cup-and-cone fracture (Figure 5.27). The fifth bar broke in a brittle manner along a flat 0 degree plane after only 3% elongation vs 16% from the other four, though it reached a similar UTS value. Examination of this fracture surface showed a few randomly located lack of fusion pores. This bar was printed at the top right location of

the 3x3 grid on the build plate, and this location makes soot contamination from the other bars unlikely. However, it is likely that soot caused weakness at this particular layer of fracture.

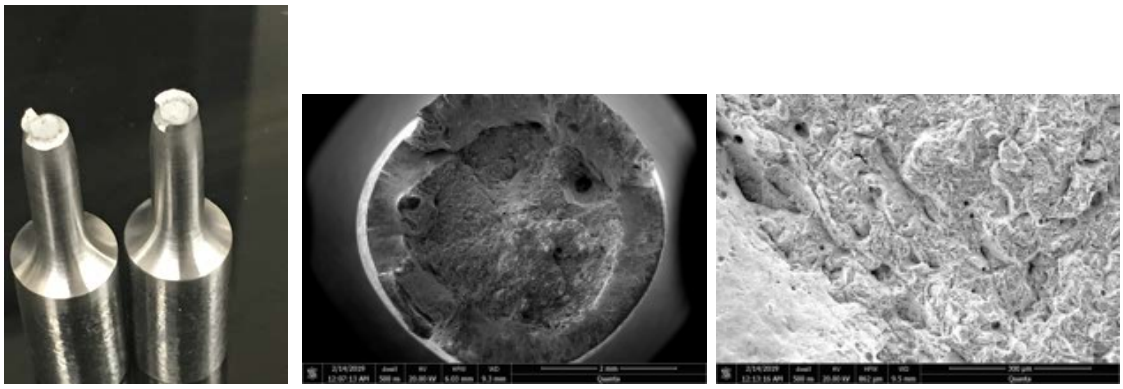

(a) Shape and appearance of the 170 W M2 fracture surface, with significant necking observed and classic cup-and-cone ductile fracture

(b) Shape and appearance of the 170 W M2 fracture surface

(c) Detail image of the ductile fracture region from the 170 W M2 fracture surface

Figure 5.27. Images of the fracture surface of a representative tensile bar from the group of five as-built bars printed on the M2 at 170 W, 600 mm/s and 110 μm hatch spacing.

The stress-strain curves for the tensile data shown in Figure 5.28 are plotted against a tensile curve for a 200°C temper of AF9628 provided by AFRL/RWMW. Since the UTS and elongation values of this curve did not match the values published in the patent, the curve was also scaled to fit the published parameters as an estimated reference line. The high porosity tensile bars printed on the MLab are similar to the patent data, but inconsistent, as expected with high porosity. The line with very little strain with break on the MLab plot is from the first test, where loading rates were too high and the extensometer slipped several times. The tensile curves of the parts printed at 140 W on the M2 appear to exceed the UTS, YTS, and elongation of the tempered curve. The modulus of elasticity for all curves appears to match. The tensile curves of the parts printed at 170 W on the M2 appear to also exceed the UTS,

YTS, and elongation of the tempered curve. In general, the 170 W setting appears to have decreased the tensile strength slightly while increasing elongation vs the 140 W setting. This substantiates the prediction of in-process tempering made after harness testing, and indicates that fluence may be used to alter the degree of tempering. The UTS, YTS, modulus, and % elongation values from the as-built tensile tests are summarized in Table 5.8.

Table 5.8

	140 W build MLab	**140 W build M2**	**170 W build M2**	**Patent**
UTS (ksi)	247 ± 25	328 ± 22	291 ± 7	230
YTS (ksi)	143 ± 22	196 ± 15	183 ± 9	180
Modulus, E (ksi)	151 ± 21	203 ± 15	190 ± 9	-
% Elongation	11 ± 1	12 ± 3	14 ± 6	11

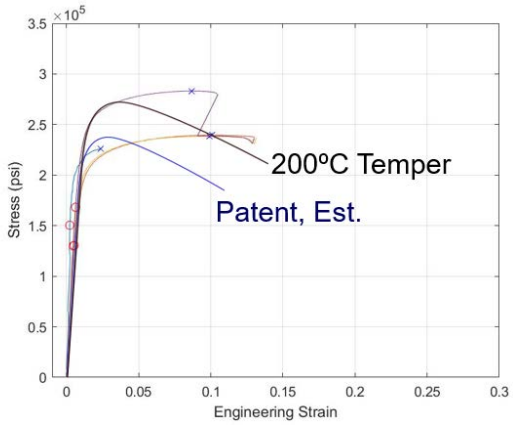

(a) Plots from bars built on the MLab at 140 W

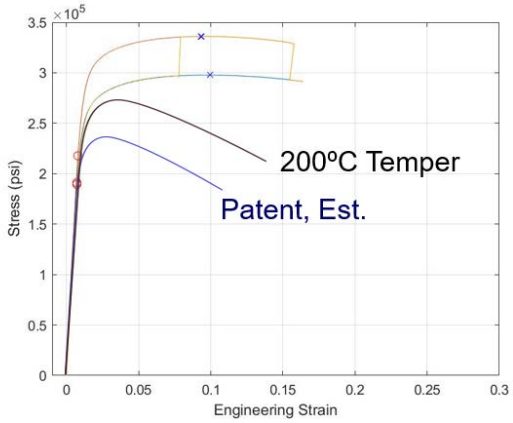

(b) Plots from bars built on the M2 at 140 W

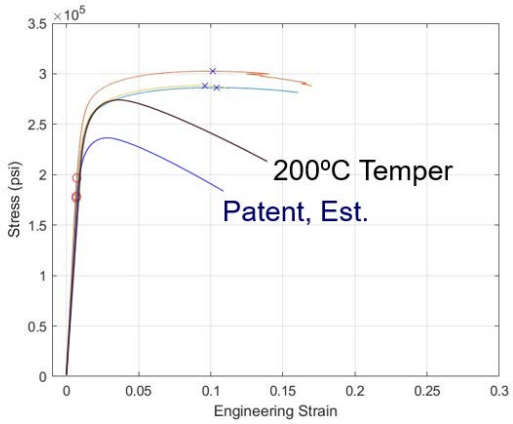

(c) Plots from bars built on the M2 at 170 W

Figure 5.28. Stress-strain curves from the as-built tensile bars, plotted with a curve from wrought material after a 200°C temper (provided by AFRL/RWMW), and the same curve scaled to meet the UTS and elongation values published in the patent.

5.4 Summary

Process parameter development of AF9628 steel successfully resulted in the generation of high density parts after an initial parameter space selection using weld tracks. Hatch spacing trials of these parts were generated based on 90%, 80%, and 70% of the average weld track widths. The porosity of the parts was evaluated with 2-sectioning and polishing, on newly generated parts with CT scanning, and again with sectioning of the CT scanned parts. Parts produced at parameter combinations believed to result in high density parts were selected from a larger pool for CT scanning based on a combination of energy density parameters. Several parameter combinations resulted in parts with less than 0.05% porosity, and two parameter sets were selected for evaluation of the hardness, tensile strength, and impact strength in the as-built and heat treated conditions. The hardness of the as-built material matched up with the published values of wrought AF9628 nearly exactly, and initial tensile tests indicate that the tensile strength is comparable or greater than that of the wrought material. Estimating toughness as area under the stress-strain curve, the toughness of the as-built material is likely to meet or exceed the toughness of traditionally manufactured AF9628. The surface roughness of the printed parts was characterized with a laser scanning microscope, and initial microstructural evaluations were conducted with both Nital etchant and EBSD. The success of the process parameters for this weapons steel indicate that it can be successfully used to produce penetrating warheads with complex optimized internal topologies. A test build of a warhead designed by a prior AFIT student was produced at a known successful parameter combination for initial demonstration purposes (Figure 5.29). The success of this research and the applicablility to future Air Force needs will no doubt propel future research in the additive manufacturing of AF9628 weapons steel.

Figure 5.29. Topology optimized warheads, as designed by Capt Thompson 'Digger' Graves [22], AFIT 2015, printed in AF9628 weapons steel.

VI. M2 Scaling Study

6.1 Overview

Due to the need to complete the tensile bar builds in a reasonable time frame, AF9628 Weapons Steel (AF9628) powder was loaded into a Concept Laser M2 Cusing, which afforded the opportunity to test additional parameter sets with a higher powered laser. Additionally, the parameters used to print the tensile bars resulted in long build times, which decreases the economic viability of 3-D printed AF9628. To reduce build times, parameters capable of melting thicker powder bed layers, such as the M2's default of 40 μm vs the MLab's default of 30μm, were investigated. A common tactic in the Additive Manufacturing industry, and one present in the M2's Inconel parameters, is to use a lower powered skin contour setting to produce a high quality surface finish, and use a higher powered core setting at an expanded spot size to melt the part interior every other layer. Identifying parameters that increase the build height produced for every powder layer while significantly reducing the working time of the laser will significantly reduce the time required to print AF9628 parts.

6.2 Methodology

6.2.1 Concept Laser M2 Cusing

The Concept Laser M2 Cusing is an Laser Powder Bed Fusion (LPBF) machine purchased in 2016 and equipped with a 400 W continuous fiber Nd:YAG laser with a variable spot size. The M2 has a maximum build volume of 250 mm x 250 mm x 350 mm, or over 18 times greater than that of the MLab. The M2 features separated build and process chambers for safe handling of reactive materials. The optimal powder bed thickness of the M2 is 40 μm, which allows it to produce parts at maximum

speed. The M2 also has a large filter, with over 2 m^2 of area, which greatly reduces the potential of a failed build due to filter saturation.

6.2.2 Energy Density Scaling

Parameter sets tested on the MLab that resulted in a high part density were consistently occurring near a fluence value of 250 J/mm^3 and a volumetric energy density (E_V) of 85 J/mm^3. Due to this success, parameter scaling for M2 weld track analysis was conducted along the 250 J/mm^3 line of fluence. The laser power was varied between 200 W and 400 W, and the MLab's laser spot focal diameter of 50 μm was maintained. A puck insert build plate was machined for the M2, with pucks located on a 40 mm grid, as shown in Figure 6.1. The build plate was then filled with A36 steel pucks and a thin, even layer of powder of approximately 80 μm thickness was applied. The nine parameter sets used for the first set of weld tracks are listed in Table 6.1, experiment set one. The scan paths were generated with the same scan path file used for the MLab weld tracks, with a 2 mm by 8 mm box filled with four straight lines. Due to the difficulty in previously encountered with differentiating parameter sets after sectioning, a maximum of five parameter sets were tested on each puck to increase spacing between groups of weld tracks.

After examining the shape of the weld beads with an optical microscope, it was determined that the 50 μm laser diameter would not produce a viable weld at a fluence value of 250 J/mm^3. Investigation of the Inconel settings for the M2 revealed that the parameter used for melting every other layer used a laser power of 370 W with a 130 μm diameter. A second set of parameters along the 250 J/mm^3 line of fluence were chosen with spot sizes of 100 μm, 120 μm, 140 μm, and 160 μm; the powder bed thickness was maintained at 80 μm. The 20 parameter sets used for the second set of weld tracks are listed in Table 6.1, experiment set two. These weld beads

Figure 6.1. M2 Puck build plate

were evaluated for appearance using optical microscopy, then mounted, polished in accordance with the procedures in Appendix C.3, and etched in 2% Nital before being examined with a Zeiss Observer optical microscope. The weld melt regime was then categorized as shallow, conduction/penetration, or keyhole. As the goal of this experiment was to develop process parameters capable of melting 80 μm powder bed layers, and remelting of previous layers generally contributes to increased density, only welds with a total depth of greater than 160 μm were considered for further development.

6.2.3 Solid Part Generation

Once weld track parameters with the potential to smoothly melt through an 80 μm powder bed were identified, cylindrical parts were designed in nTopology's implicit modeling and slicing software to evaluate laser melting at every other layer. An outer ring was designed so that three passes of the laser at a contour setting would contain the inner powder bed. An inner cylinder was designed with a layer thickness of twice the outer ring and a diameter that would overlap the outer ring by 15 μm

to prevent the lack of fusion pores observed in previous CT scanned specimens. The hatch spacing for the inner, every other layer cylinder was calculated at 80% of the weld track top width and cross section width.

Instead of using weld tracks to create a skin contour setting, the two parameter sets used to print dense specimens at 30 μm layer thickness were trialed at 40 μm. The part produced at 140 W, 600 mm/s, 86 μm hatch spacing, and 40 μm powder bed thickness exhibited large intermal pores due to lack of fusion between layers, but the outer ring of the cylinder appeared to fuse well and no discontinuities were observed. The part produced at 170 W, 600 mm/s, 110 μm hatch spacing, and 40 μm powder bed thickness achieved a high density and exhibited no discoloration. The parts were evaluated for porosity by scanning with a Nikon CT scanner; representative slices are displayed below in Figure 6.2. Both settings were considered acceptable for an outer contour, though the 140 W setting was preferred for its reduced required skin thickness, despite the measured internal porosity.

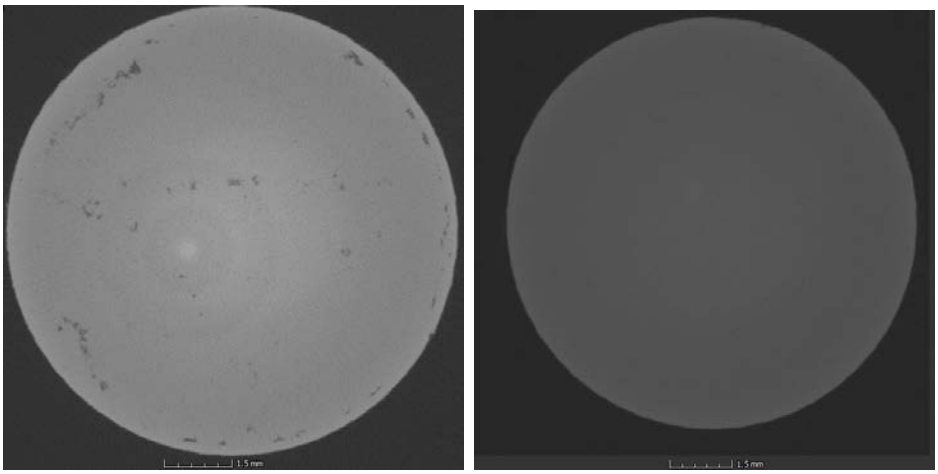

(a) 140 W slice **(b)** 170 W slice

Figure 6.2. Representative CT slices of parts created with 170 W and 140 W settings for contour evaluation at 40 μm layer depth.

To evaluate the potential of the contour settings for the creation of geometrically complex all-contour parts, two cylinders were generated in Turbo that were filled with

a Triply Periodic Minimal Surface (TPMS) geometry; a cross section of the model is displayed in Figure 6.3. TPMS parts include thin walls, overhangs, and surface finishes at a large range of angles and can be used to quickly evaluate the potential of a parameter setting to produce high-quality parts with complex geometries. The parameter sets used to generate parts at double powder bed depth and for contour evaluation are listed in Table 6.2. All parts, solid and TPMS, were printed singly on pucks for rapid CT analysis.

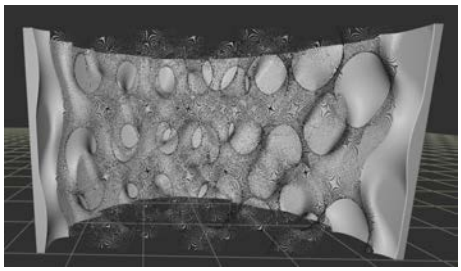

Figure 6.3. Image of the TPMS cylinder geometry generated in Turbo.

Table 6.1. Power, Speed, and Laser Focus Diameter values used in M2 weld track study. The powder bed thickness for all tests was approximately 80 μm, and all speeds were calculated to maintain a constant fluence of 250 J/mm^3.

Set	Laser Power Watts	Laser Speed mm/s	Spot Size μm
1	200	510	50
1	225	575	50
1	250	640	50
1	275	700	50
1	300	765	50
1	325	830	50
1	350	890	50
1	375	955	50
1	400	1020	50
2	275	175	100
2	300	190	100
2	325	210	100
2	350	225	100
2	375	240	100
2	275	145	120
2	300	160	120
2	325	170	120
2	350	185	120
2	375	200	120
2	275	125	140
2	300	135	140
2	325	150	140
2	350	160	140
2	375	170	140
2	275	110	160
2	300	120	160
2	325	130	160
2	350	140	160
2	375	150	160

Table 6.2. Process parameters used for solid part generation on the Concept Laser M2 Cusing, both every-other-layer exposure and contour-only.

Power	**Speed**	**Spot Size**	**Bed Thickness**	**Fluence**	**Hatch Spacing**	**E_V**	**Time to Build 1 mm^2**
W	mm/s	μm	J/mm^3	μm	μm	J/mm^3	s
375	240	100	80	250	265	74	15.7
325	170	120	80	250	272	88	21.6
300	160	120	80	250	265	88	23.6
375	170	140	80	250	276	100	21.3
325	150	140	80	250	282	96	23.6
325	130	160	80	250	323	97	23.8
140	600	50	40	149	25	233	19.4
170	600	50	40	180	25	283	15.2

6.3 Results

6.3.1 Weld Track Study

6.3.1.1 Weld Appearance

The welds produced at a fluence of 250 J/mm^3 at a range of spot sizes were remarkably consistent, with nearly all receiving categorization as acceptable or elongated. As moderately elongated welds resulted in highly dense parts when processed on the MLab, this indicated that most of the parameter combinations trialed with the M2 could result in highly dense parts. In particular, the welds produced at a laser spot size of 140 μm appeared very symmetrical, and resembled typical Tungsten Inert Gas (TIG) welds. There was an increase in the amount of sintered powder particles attached to the tops and sides of the welds compared to the MLab, but this was expected considering the increased powder layer thickness and laser power. Representative images of the M2 weld tracks are shown in Figure 6.4.

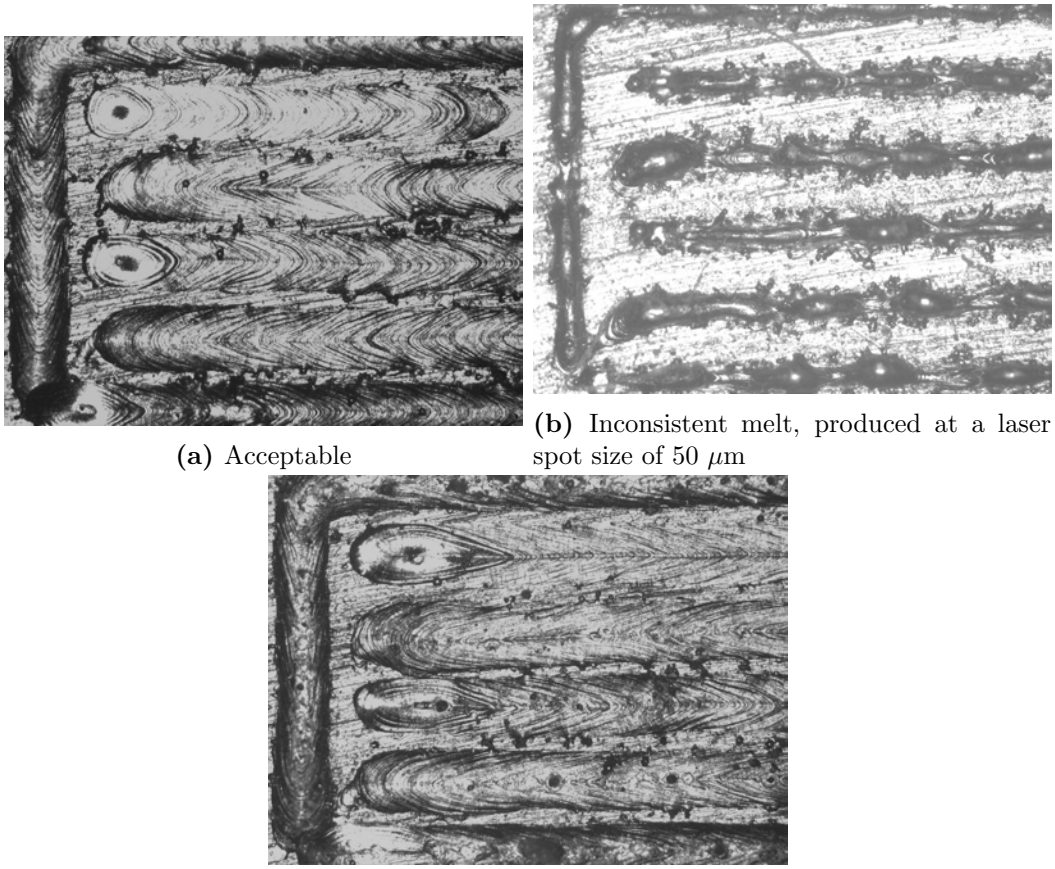

(a) Acceptable

(b) Inconsistent melt, produced at a laser spot size of 50 μm

(c) Elongated

Figure 6.4. Representative images of different M2 weld track surface quality descriptors.

6.3.1.2 Weld Penetration

The sectioned weld tracks were again consistent with the phenomena observed in the MLab weld tracks. Smoother, TIG-syle resulted in shallow, conduction mode welds, while the elongated weld tracks produced greater penetration. Some potential keyholing was observed, but no profiles approached the aspect ratios seen in the MLab tracks. Representative images of the M2 melt regimes observed are shown in Figure 6.5. The parameter sets tested in the second set of weld tracks, along with their qualitative appearance and melt descriptors, are summarized in Table 6.3. The six parameter sets chosen were based on a combination of the surface and section

observations.

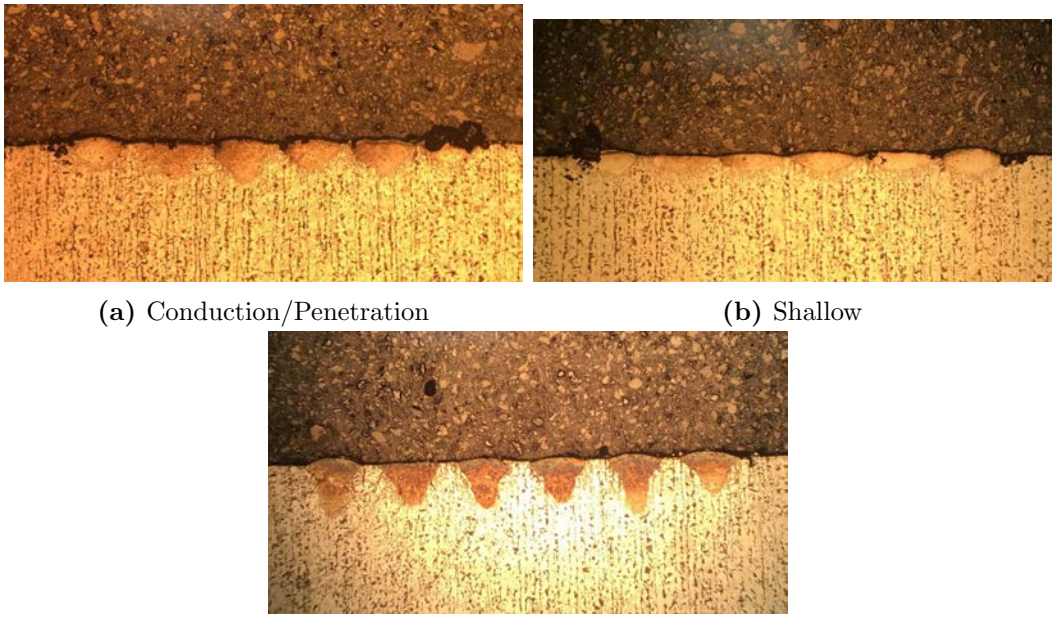

(a) Conduction/Penetration **(b)** Shallow

(c) Keyhole

Figure 6.5. Representative images of different weld track depth descriptors.

6.3.2 Solid Parts, Core Exposure Every Other Layer

The six parameter sets selected for further evaluation were printed at a double 80 μm powder bed thickness to decrease the total build time for solid parts. The six parts were printed successfully with no delamination due to the increased powder bed thickness. The spark plume generated during processing was more than twice the size of that observed with the 200 W and below parameter settings, though the amount of soot produced appeared to be similar. The parts finished on a contour-only layer, so the top surface is slightly sunken below the skin, as shown in Figure 6.6. The only notable difference between the cylinders produced at an 80 μm powder bed thickness and those produced at 40 μm is the increase in raised surface features on the top layer. These initial observations indicate that fluence can be successfully used to scale parameters, provided the laser and processing conditions remain similar.

Table 6.3. Qualitative descriptions for each of the process parameter combinations tested in the second set of M2 weld track experiments.

Laser Power Watts	**Laser Speed** mm/s	**Spot Size** μm	**Top Quality**	**Melt Regime**
275	175	100	acceptable	keyhole
300	190	100	elongated	conduction
325	210	100	elongated	conduction
350	225	100	elongated	conduction
375	240	100	acceptable	conduction
275	145	120	inconsistent	conduction
300	160	120	elongated	conduction
325	170	120	acceptable	conduction
350	185	120	acceptable	conduction
375	200	120	acceptable	conduction
275	125	140	acceptable	shallow
300	135	140	acceptable	shallow
325	150	140	acceptable	shallow
350	160	140	acceptable	shallow
375	170	140	acceptable	shallow
275	110	160	elongated	conduction
300	120	160	elongated	conduction
325	130	160	acceptable	conduction
350	140	160	acceptable	conduction
375	150	160	acceptable	conduction

The parts will later be evaluated in the CT scanner for internal pores; parts with densities of over 99.9% will receive further evaluation of mechanical, chemical, and microstructural properties.

6.3.3 Triply Periodic Minimal Surface Part Generation

Highly complex TPMS parts were generated in conjunction with the M2 scaling study. The cylindrical parts depicted in Figure 6.7 were created using the settings previously evaluated for skin contour suitability of the 80 μm layer cylinders. Both contour settings successfully generated TPMS parts, with only small amounts of blow-through at the fully overhanging regions of the surface. This blow-through is a

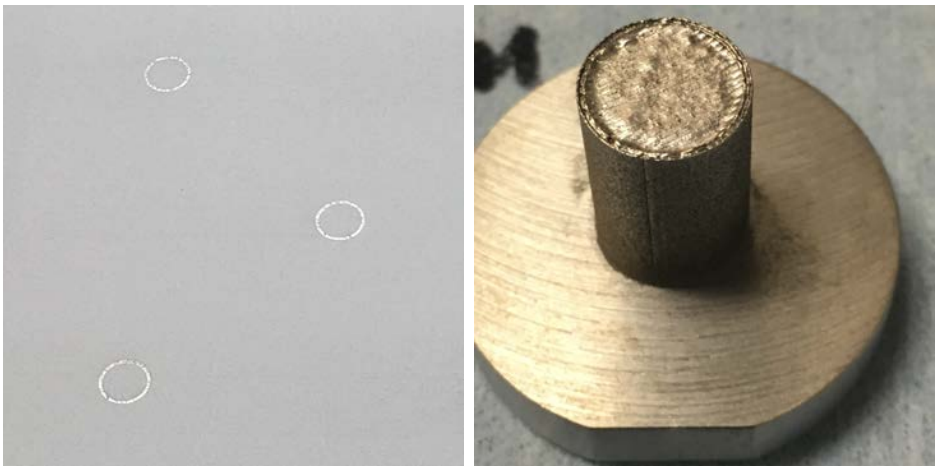

(a) Parts as finished in the processing chamber; the final layer was skin only, so top surface is slightly sunken.

(b) Single part

Figure 6.6. Parts generated for CT porosity analysis at every other layer infill parameters.

phenomenon observed in all additively manufactured materials produced with a full overhang. On close inspection, the higher powered 170 W setting resulted in slightly larger holes on overhanging surfaces. Complex geometries of this type can be adapted for use in high-strength applications where weight savings are beneficial.

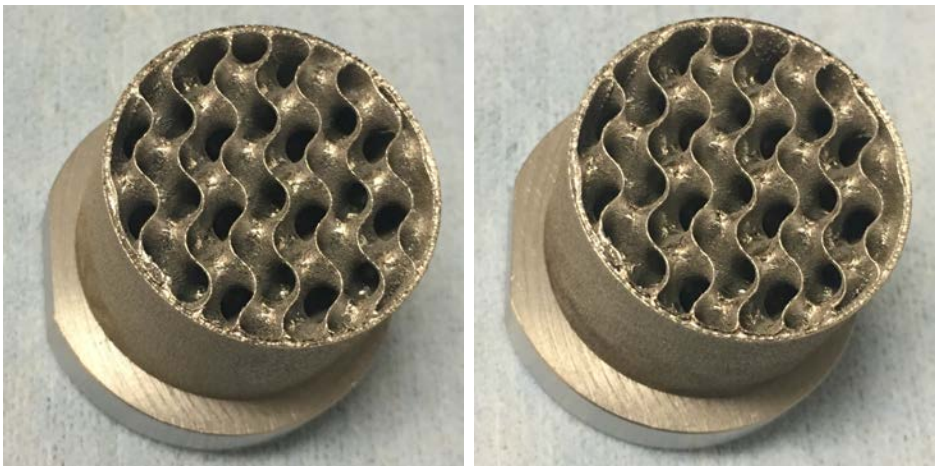

(a) 140 W, 600 mm/s, 25 μm hatch spacing, 40 μm powder bed thickness, 50 μm laser spot size

(b) 170 W, 600 mm/s, 25 μm hatch spacing, 40 μm powder bed thickness, 50 μm laser spot size

Figure 6.7. TPMS parts generated for contour evaluation

6.4 Summary

Initial results of a scaling study between the ConceptLaser MLab and ConceptLaser M2 indicate that fluence can be used to quickly scale successful parameter sets to higher powers. This method is not infallible, as too small of a laser spot size can produce a highly irregular weld unsuitable for creation of solid parts. This scaling method has not been tested on machines using different types of lasers, or in a different inert gas, such as Nitrogen. Further research could also explore using fluence to scale between similar machines produced by different companies, as this scaling only addressed ConceptLaser machines. The use of CT scanning to evaluate parameters for contour suitability appears to have been successful, as geometrically complex TPMS parts were quickly produced with a quality equivalent to identical geometries produced in different materials.

VII. Conclusions and Recommendations

7.1 Conclusions

This research has covered the characterization of a newly powderized material, AF9628 Weapons Steel (AF9628), described a process for developing processing parameters using weld track experiments, the confirmation that the process parameters have produced highly dense parts, and the process of scaling from a 200 W to 400 W Laser Powder Bed Fusion (LPBF) machine. The gas atomized powder purchased for this study appears to be of a quality consistent with other gas atomized powders used for additives manufacturing. The highly spherical nature of the powder contributed to its flowability, with consistently even powder bed layers contributing to the high densities of observed printed parts. An initial chemical characterization of the powder and parts was completed, but further characterization should be completed to determine if any alloying elements are being burnt off, or if oxygen present in the sieved powder due to soot content is being retained within the finished parts. As soot was observed to build up in the processing chamber and contribute to a gradient discoloration of the the finished parts, studies should be conducted to determine if chemical content changes with build height.

The weld track experiments conducted on the MLab were able to successfully lead into the selection of process parameters that resulted in highly dense parts. Welds with an observable elongation of the melt pool were shown to consistently outperform welds that more closely resembled traditional Tungsten Inert Gas (TIG) welds, with the elongated welds producing melt profiles with deeper penetration that contributed to remelting of previous layers, which has been shown to increase part density. Severely elongated welds, as well as those that exhibited the balling phenomenon, did not produce conduction mode welds appropriate for use in additive manufacturing.

Process parameters that resulted in high density parts were confirmed with a combination of optical imaging and CT scanning. Initial optical imaging of small 7 mm cylinders revealed pores consistent with keyholing, incomplete melting between layers, and localized pores due to processing flaws. Larger 10 mm parts were built for CT scanning, and scans of a selection of eight parts confirmed densities previously measured in the smaller cylinders. To ensure that the CT scanner was adequately characterizing the porosity of the printed parts, the scanned cylinders were sectioned and evaluated. The sectioned parts displayed a larger number of small pores than previously observed in the small 7 mm cylinders, which is most likely due to the use of recycled vs virgin powder. The highest density parts appeared to come from parameters at the intersection of a fluence of 250 J/mm^3 and an E_V of 70 J/mm^3. This value of fluence was the factor used to scale up to the larger M2, where weld tracks were again used to select a limited range of potential processing parameters. The observations made earlier on the MLab weld tracks were consistent with those made on the welds generated on the M2, and solid parts were generated successfully. Material characterization of the as-built material printed with two separate settings (Table 7.1) focused on hardness and microstructure, with parts also produced for tensile and impact testing of the as-built and standard heat treated conditions.

Processing parameters were also developed for the creation of geometrically complex parts (Table 7.1), with a focus on Triply Periodic Minimal Surface (TPMS) parts, as well as potential every-other-layer settings for reduced build times. The thin structures were able to achieve a part quality consistent with those made from commonly used additive manufacturing materials such as inconel. These contour settings were used to generate the skin of solid cylinders printed at a double layer height with the scaled high-power parameters. The ability to produce complex structures validates the applicability of this material for use in additive vs traditional manufacturing.

Table 7.1. Summary of the process parameters used to generate high density parts for material testing on the MLab and smooth TPMS surfaces on the M2

Part Type	**Power** W	**Speed** mm/s	**Spot Size** μm	**Bed Depth** J/mm^3	**Fluence** μm	**Hatch Spacing** μm	**E$_V$** J/mm^3	**Time to Build 1 cm^3** s
Solid	140	600	50	30	198	86	90	646
Solid	170	600	50	30	241	110	86	505
Solid	170	600	50	40	180	110	64	379
TPMS	140	600	50	40	149	25	233	1667
TPMS	170	600	50	40	180	25	283	1667

This research has succeeded in answering the three primary research questions: process parameters on a 200 W LPBF machine were developed that resulted in conduction mode melting of AF9628; lines of fluence were used to select scan strategies for fully dense parts; and a line of fluence was used to scale the successful parameters to a larger, more powerful machine. The question of whether the processing parameters caused any changes to the steel chemistry is being answered with ongoing work, as is the question of how the AF9628 heat treat process affects the material properties of additively manufactured AF9628. Initial testing has shown that additively manufactured AF9628 will result in a martensitic steel of similar hardness and similar or greater strength to tempered, traditionally manufactured steel. It remains to be seen if the toughness will also approach that of the reference condition.

7.2 Future Work

As this work was performed on a new material using a relatively new manufacturing technology, the potential for follow-on work is nearly boundless. Following mechanical testing of vertically printed parts, other build orientations should be considered. To be rigorous, these parts could be generated with both virgin and sieved powder to characterize any loss in part strength with recycled powder. Additional

mechanical testing, including split-Hopkinson pressure bar testing to evaluate the material's high strain response, can be conducted in preparation for use in weapons applications. The topology optimized warhead designs developed by previous AFIT students can be built in-house and evaluated in an actual weapons steel, instead of having to settle for steels that are not necessarily suited for penetrating warheads. Microstructures at a range of processing conditions should be studied, both in and out of the build plane, to explore options for microstructural tailoring of parts. chemistry variation with build height due to soot buildup could be investigated, as well as chemistry changes with fluence. There are thousands of options for continuing research of this material and its applications.

Acronyms

AF9628 AF9628 Weapons Steel

AFRL Air Force Research Laboratory

AISI American Iron and Steel Institute

ASTM American Society for Testing and Materials

BCC Body-Centered Cubic

BCT Body-Centered Tetragonal

CNC Computer Numerical Control

DBTT Ductile-Brittle Transition Temperature

EBM Electron Beam Melting

EBSD Electron Backscatter Diffraction

EDS Energy Dispersive X-Ray Spectroscopy

FCC Face-Centered Cubic

HAZ Heat Affected Zone

HIP Hot Isostatic Press

HSLA High-Strength, Low-Alloy

LBM Laser Beam Melting

LMD Laser Metal Deposition

LPBF Laser Powder Bed Fusion

PAC Powder Alloy Corporation

PAGB Prior-Austenite Grain Boundaries

PAPR Positive Air Pressure Respirator

SAE Society of Automotive Engineers

SEM Scanning Electron Microscope

SRμT Synchroton Radiation micro-Tomography

TIG Tungsten Inert Gas

TPMS Triply Periodic Minimal Surface

XRD X-Ray Diffraction

XRF X-Ray Fluorescence

Appendix A. Powder Data, As Delivered

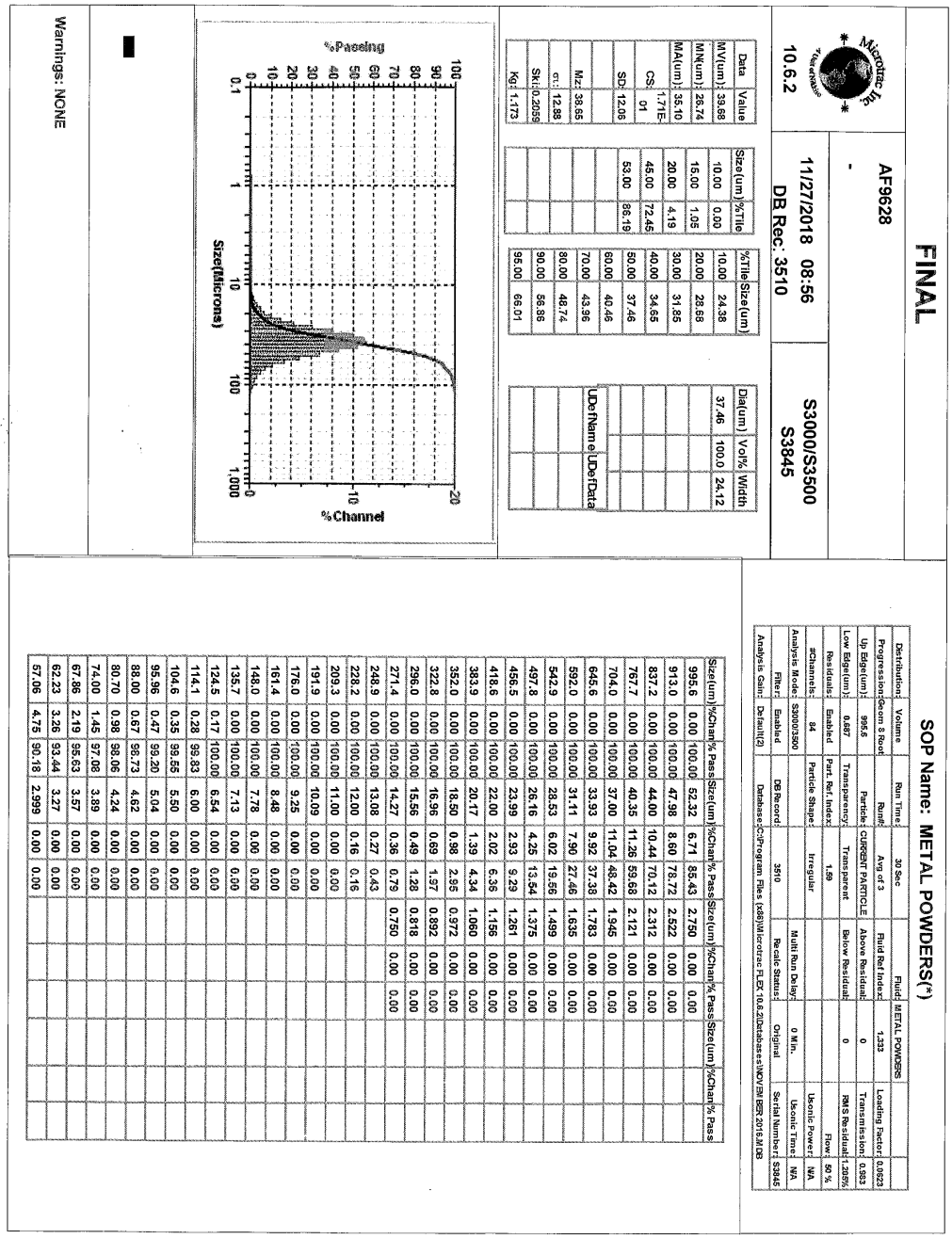

Figure A.1. Powder Alloy Corp AF9628 Distribution Profile

PAC
Powder Alloy Corporation

Certified Materials Report

To: Wright Patterson AFB
Air Force Institute of Technology
3060 Q Street Building 644
Wright Patterson AFB OH 45434

PO No: D 98063318
Quantity: 288 lbs
Date: 11/27/18
Packing List No.: 17214

Part No.: AMP AF9628 Revision A Description: Gas Atomized Steel Powder Lot: AMPAF96281001
Specification(s): FAR 52.225-1, FAR 52.225-5, & DFARS 252.225-7001

Chemical Analysis

Element	Results	Specification Min.	Specification Max
C	0.28	0.26	0.29
Mn	0.7	0.5	0.8
Si	0.9	0.9	1.1
Cr	2.8	2.5	2.8
Ni	1.1	0.9	1.2
Cu	<0.1		0.2
V	0.12	0.05	0.15
Mo	1.00	0.85	1.05
P	<0.010		0.010
S	<0.005		0.005
Al	0.009		0.015
Ti	0.004		0.006
O	280 ppm		300 ppm
P+Sn+As+Sb	<0.035		0.035
H	2 ppm		2 ppm
Fe	Balance	Balance	

Test Lab: Element Materials, Huntington Beach (GE Source Code T4707, No AQPS 538, NADCAP, & ISO17025)

Material Characteristics

Measurement	Results	Specification Min.	Specification Max
+230	0		0
+270	3		3
-22µm	6		10
-15µm	1		1
Apparent Density	4.4 g/cc	Report	
Hall Flow	19.6 s/50g	Report	

Test Lab: PAC (GE S-400 AIXS Source Code 59348 & SNECMA AQPS N° FAL 534)
Sieve test performed per ASTM B214, Microtrac test performed per ASTM B822, Apparent Density test performed per ASTM B212, & Hall Flow test performed per ASTM B213

Signature:		Date:	27-Nov-18

Material Melted & Manufactured in the U.S.A

PAC Quality System conforms to AS9100 & GE S-1000
All test labs are GE, SAFRAN, NADCAP, and ISO17025 approved
101 Northeast Drive • Loveland, OH USA 45140 • T: (513) 984-4016 • F: (513) 984-4017
PAC Certifies that the above material meets all requirements of the Purchase Order and Material Specifications
Page 1 of 1

Figure A.2. Powder Alloy Corp AF9628 Chemical Profile

Appendix B. Experimental Test Points

Laser power	Scan Speed	Thickness	Spot Size	Fluence	NoPow	Weld Quality	Weld Width				With Powder	Weld Quality	Weld Width			Quality	Weld Depth					
Watts	mm/s	micro m	um	J/mm^3			micro m	micro m	micro m	micro m			micro m	micro m	micro m		micro m	micro m	micro m	micro m	micro m	micro m
80	630	30	50	108		Inconsistent	65.52	69.62	69.62	65.52		Inconsistent	75.76	77.81	79.96	69.62 shallow	35.43	21.69	26.28	22.51	18.36	18.76
80	500	30	50	136		Acceptable	75.76	77.81	69.62	73.71		Acceptable	75.79	83.95	75.79	81.9 shallow	28.36	16.68	23.34	9.67	14.59	16.7
80	420	30	50	162		Acceptable	88.05	81.9	79.86	77.81		Acceptable	86.02	77.81	88.05	86.22 shallow	24.18	21.68	22.94	24.18	22.11	20.43
80	350	30	50	194		Acceptable	83.95	86	83.95	79.86		Inconsistent	75.56	90.12	88.05	94.19 shallow	25.03	27.52	20.43	20.43	24.63	25.46
80	300	30	50	226		Acceptable	96.24	92.14	94.28	96.24		Acceptable	81.9	88.05	88.05	83.95 shallow	25.43	27.53	45.02	34.6	27.96	24.65
80	250	30	50	272		Acceptable	94.19	98.29	90.1	98.29		Acceptable	90.12	108.52	100.33	98.29 shallow	22.93	25.43	22.99	26.28	26.76	25.86
80	170	30	50	399		Acceptable	108.54	106.48	100.33	108.52		Acceptable	139.19	110.57	120.8	104.45 conduction	29.18	26.27	30.43	37.53	50.9	30.85
80	125	30	50	543		Inconsistent	122.86	122.86	114.67	126.95		Acceptable	151.54	141.29	129	124.9 conduction	42.52	42.52	37.12	39.61	37.97	33.37
100	640	30	50	133		Inconsistent	88.05	83.95	83.95	77.81		Elongated	76.01	79.86	88.05	81.9 shallow	27.12	22.55	25.43	23.76	22.1	20.08
100	430	30	50	197		Inconsistent	88.07	94.19	90.1	94.21		Inconsistent	112.62	122.86	110.57	120.81 shallow	27.1	31.69	55.87	40.02	55.03	45.86
100	320	30	50	265		Inconsistent	116.71	100.33	108.52	108.52		Inconsistent	147.43	114.67	126.95	126.97 conduction	39.6	77.95	72.53	71.7	62.54	85.92
100	212	30	50	400		Acceptable	102.38	108.54	116.71	106.48		Inconsistent	124.9	139.24	145.38	137.21 conduction	65.94	42.94				
100	180	30	50	472		Acceptable	153.57	159.71	139.24	143.33		Acceptable	167.92	161.76	159.71	165.86 conduction	140.09	108.8	144.24	139.65	139.26	88.38
100	160	30	50	531		Acceptable	161.76	165.86	147.43	147.67		Acceptable	163.82	178.1	169.95	176.1 conduction	117.56	137.57	131.73	121.72	120.06	125.11
100	130	30	50	653		Acceptable	161.76	161.76	139.24	143.33		Acceptable	194.52	200.67	186.33	200.67 conduction	147.99	164.66	158.9	167.6	144.66	162.19
100	100	30	50	849		Acceptable	212.95	208.86	206.81	196.58		Acceptable	198.63	227.37	210.99	210.9 conduction	128.4	188.43	200.12	184.28	199.75	176.75
140	1600	30	50	74		No Melt Pool	69.62	73.71	65.52	69.62		No Melt Pool	81.9	75.79	81.9	73.71 undercut	17.92	18.36	11.26	20.85	18.38	20.49
140	1400	30	50	85		No Melt Pool	69.62	69.62	73.71	69.62		No Melt Pool	88.05	88.05	75.76	90.3 undercut	20.86	37.11	29.67	23.4	40.87	34.18
140	1200	30	50	99		Elongated	79.86	73.71	79.86	77.81		Inconsistent	79.86	83.95	81.93	77.81 undercut	34.21	36.28	35.49	26.73	22.11	15.85
140	1000	30	50	119		Elongated	88.07	73.74	73.71	69.65		Inconsistent	83.95	77.81	90.12	81.9 shallow	17.51	17.51	20.03	30.43	20.88	16.28
140	800	30	50	149		Elongated	88.05	83.95	90.1	83.95		Elongated	98.29	108.52	88.07	100.33 shallow	17.53	22.96	23.79	27.51	13.81	36.29
140	600	30	50	198		Elongated	112.62	108.52	106.48	96.24		Elongated	112.62	106.48	120.83	112.62 conduction	21.71	49.61	50.04	53.78	58.43	67.96
140	400	30	50	297		Balling	151.52	139.24	151.52	153.59		Elongated	163.8	151.5	157.67	167.9 conduction	44.19	107.57	108.8	102.55	99.64	99.22
140	200	30	50	594		Balling	178.14	184.29	172	186.33		Elongated	208.86	208.86	190.43	206.81 keyhole	192.17	206.79	206.35	155.97	152.16	173.01
170	1600	30	50	90		No Melt Pool	83.95	77.81	77.81	67.57		No Melt Pool	86.02	88.05	92.14	94.19 undercut	19.22	26.73	22.51	20.01	22.99	19.18
170	1400	30	50	103		No Melt Pool	79.86	83.95	79.86	75.56		No Melt Pool	92.17	100.33	94.19	94.19 undercut	25.48	26.68	28.35	28.78	27.56	25.88
170	1200	30	50	120		Elongated	80.05	79.86	88.05	73.71		No Melt Pool	88.05	83.95	96.24	100.33 undercut	35.91	40.44	35.44	33.35	33.77	
170	1000	30	50	144		Elongated	88.05	88.05	92.14	83.95		Elongated	88.14	90.12	90.12	90.1 undercut	47.12	48.36	45.44	42.94	46.27	
170	800	30	50	180		Elongated	90.1	106.48	108.52	104.43		Elongated	114.62	110.57	92.14	98.29 conduction	57.53	62.11	61.7	63.83	56.28	59.62
170	600	30	50	241		Elongated	135.14	114.67	129	114.68		Inconsistent	137.21	129	143.35	159.71 conduction	84.23	89.64	85.51	95.46	85.06	94.63
170	400	30	50	361		Balling	167.9	188.38	167.1	183.38		Balling	172	165.86	159.73	176.1 conduction	130.9	146.73	159.67	152.16	139.24	140.49
170	200	30	50	722		Balling	190.43	208.87	206.81	196.57		Balling	194.53	212.96	241.62	208.86 keyhole	210.93	245.55	233.03	266.37	254.29	217.22
200	1280	30	50	133		No Melt Pool	90.1	94.19	94.19	98.29		Inconsistent	112.64	106.48	106.48	102.38 undercut	45.86	47.52	44.62	42.94	42.52	30.01
200	900	30	50	189		Elongated	98.29	98.29	94.19	90.1		Inconsistent	92.14	102.38	108.54	106.5 undercut	50.45	67.98	61.7	73.79	68.81	64.61
200	640	30	50	265		Balling	157.67	133.1	157.68	145.38		Elongated	141.29	137.19	153.57	145.38 conduction	79.62	58.36	88.38	98.38	93.42	93.01
200	425	30	50	399		Inconsistent	184.29	169.95	143.33	169.95		Elongated	143.33	145.38	143.33	169.95 conduction	162.99	169.66	160.49	145.49	184.68	169.72
200	370	30	50	459		Elongated	208.86	212.95	157.67	163.81		Elongated	161.76	176.1	163.82	176.1 keyhole	120.89	243.03	223.03	225.11	215.11	193.04
200	320	30	50	531		Inconsistent	196.57	206.81	174.05	178.14		Balling	176.1	169.95	184.29	200.67 keyhole	184.26	236.36	231.8	235.95	209.69	236.36
200	255	30	50	666		Balling	196.57	217.05	206.81	204.76		Balling	233.43	212.96	194.52	217.05 keyhole	252.2	278.47	284.3	265.15	275.99	274.37
200	200	30	50	849		Balling	227.29	241.62	210.9	227.29		Balling	225.25	229.33	221.14	229.33 keyhole	176.77	343.07	338.08	327.66	323.51	262.22

Figure B.1. Test points and width data of MLab weld tracks.

Power	Speed	Hatch	Energy Density	Fluence	Quality	Density	Density	Time to Print 1cm^3
W	mm/s	um	J/mm3	J/mm3		cross section	Volumetric	s
80	250	92	87	272				43.5
80	250	81	99	272			99.8772	49.4
80	250	71	113	272				56.3
80	170	103	114	399	Overheating	99.0411		57.1
80	170	100	118	399	Overheating	99.9319		58.8
80	170	91	129	399	Overheating	99.8042		64.6
80	170	80	147	399	Overheating	99.6914		73.5
80	125	119	134	543	Overheating	99.4332		67.2
80	125	105	152	543	Overheating	99.2676		76.2
80	125	92	174	543	Overheating	99.725		87.0
100	430	96	61	197				24.2
100	430	85	68	197			99.7963	27.4
100	430	75	78	197				31.0
100	320	113	69	265				27.7
100	320	100	78	265				31.3
100	320	88	89	265				35.5
100	320	100	78	265	Overheating	98.2705		31.3
100	280	110	81	303				32.5
100	280	98	91	303				36.4
100	280	86	104	303				41.5
100	212	107	110	400	Overheating	99.702		44.1
100	212	96	123	400	Overheating	99.4544		49.1
100	212	84	140	400	Overheating	99.7341		56.2
100	180	144	96	472	Overheating	99.701		38.6
100	180	128	109	472	Overheating	99.8177		43.4
100	180	112	124	472	Overheating	99.9459		49.6
140	1000	100	35	119	Incomplete Melt	95.8244		10.0
140	1300	66	41	91	Incomplete Melt	99.8491		11.7
140	600	97	60	198		99.9068		17.2
140	600	86	68	198		99.9445	99.9964	19.4
140	600	76	77	198		99.9305		21.9
140	400	133	66	297		99.8349		18.8
140	400	119	74	297		99.9411	99.9963	21.0
140	400	104	84	297		99.8859		24.0
140	300	153	76	396				21.8
140	300	136	86	396				24.5
140	300	119	98	396				28.0
170	800	90	59	180		99.8955		13.9
170	800	80	66	180		99.838		15.6
170	800	70	76	180		97.6442		17.9
170	600	123	58	241		99.9023		13.6
170	600	110	64	241		99.9805	99.9987	15.2

Figure B.2. Every hatch spacing combination tested on the MLab, with measured porosity values

Laser power	Watts	275	300	325	350	375			275	300	325	350	375			275	300	325	350	375			275	300	325	350	375		
Spot Size	um	100	100	100	100	100			120	120	120	120	120			140	140	140	140	140			160	160	160	160	160		
Actual Scan speed	mm/s	175	190	210	225	240			145	160	170	185	200			125	135	150	160	170			110	120	130	140	150		
Fluence	J/mm3	250	250	250	250	250			250	250	250	250	250			250	250	250	250	250			250	250	250	250	250		
Surface Quality		acceptable	elongated	elongated	elongated	acceptable			inconsistent	Elongated	Acceptable	Acceptable	Acceptable			Acceptable	Acceptable	Acceptable	Acceptable	Acceptable			Elongated	Elongated	Acceptable	Acceptable	Acceptable		
Width, top		307	301	276	282	290			313	337	321	313	294			313	282	323	327	346			374	397	372	376	335		
		350	325	327	284	294			317	341	339	317	292			352	335	352	313	341			372	391	374	382	339		
		319	337	337	360	319			364	372	346	350	339			378	341	376	344	354			391	419	442	405	376		
		321	333	315	309	313			358	346	346	311	303			331	356	358	319	323			405	393	401	380	348		
		333	307	317	317	288			393	350	350	362	323			352	335	354	382	340			421	436	428	387	339		
Width Average		**326**	**320.6**	**314.4**	**310.4**	**300.8**			**349**	**349.2**	**340.4**	**330.6**	**310.2**			**345.2**	**329.8**	**352.6**	**337**	**340.8**			**392.6**	**407.2**	**403.4**	**386**	**347.4**		
Section Quality		keyhole	conduction	conduction	conduction	conduction			conduction	conduction	conduction	conduction	conduction			shallow	shallow	shallow	shallow	shallow			conduction	conduction	conduction	conduction	conduction		

Figure B.3. Test points and width data of M2 weld tracks.

Material	Reference	Density	Laser power	Scan Speed	Bed Thickness	Hatch Spacing	Spot Size	Ev	Fluence
		%	Watts	mm/s	micro m	micro m	um	J/mm^3	J/mm^3
316L	7		95	300	40	118	200	67.09039548	50.39906531
316L	8		104	500	30	130	200	53.33333333	44.13897088
316L	9		100	300	30	100	180	111.1111111	78.59503363
316L	10		50	120	40	120	70	86.80555556	189.4701703
316L	11		105	380	30	125	200	73.68421053	58.63603167
316L	12		100	200	60	126	180	66.13756614	58.94627522
316L	13		105	380		125	200		
316L	14		100	300	30	118	180	94.16195857	78.59503363
316L	15		50	200	50	80	40	78.125	159.1549431
316L	16		175	140	100	50		250	
316L	1		250	1500	30	150	54	37.03703704	130.9917227
316L	1		250	1600	30	150	54	34.72222222	122.80474
316L	1		250	1700	30	150	54	32.67973856	115.5809318
316L	1		300	1600	30	150	54	41.66666667	147.365688
316L	1		300	1700	30	150	54	39.21568627	138.6971182
316L	1		300	1800	30	150	54	37.03703704	130.9917227
316L	1		350	1700	30	150	54	45.75163399	161.8133045
316L	1		350	1800	30	150	54	43.20987654	152.8236765
316L	1		350	1900	30	150	54	40.93567251	144.7803251
316L	1		400	1900	30	150	54	46.78362573	165.4632287
316L	1		400	2000	30	150	54	44.44444444	157.1900673
316L	1		400	2100	30	150	54	42.32804233	149.704826
316L	1		250	1500	30	150	54	37.03703704	130.9917227
316L	1		300	1600	30	150	54	41.66666667	147.365688
316L	1		300	1700	30	150	54	39.21568627	138.6971182
316L	1		300	1800	30	150	54	37.03703704	130.9917227
316L	1		350	1700	30	150	54	45.75163399	161.8133045
316L	1		350	1800	30	150	54	43.20987654	152.8236765
316L	1		350	1900	30	150	54	40.93567251	144.7803251
316L	1		400	1900	30	150	54	46.78362573	165.4632287
316L	1		400	2000	30	150	54	44.44444444	157.1900673
316L	1		400	2100	30	150	54	42.32804233	149.704826
316L	2		200		50				
17-4	3		195	1000	40	100		48.75	
17-4	5		150	1200	40	50		62.5	
1.4404 (GE)	4		140	1100	40	100	100	31.81818182	
1.4404 (GE)	4		140	1375	40	100	100	25.45454545	
1.4404 (GE)	4		130	1300	40	100	100	25	
4340	3		185	1050	20	70	100	125.8503401	112.1663408
4340	3		185	625	20	120	100	123.3333333	188.4394526
4340	3		185	700	20	100	100	132.1428571	168.2495113
18Ni300 Mara	6		100	100	30	112	180	297.6190476	235.7851009
18Ni300 Mara	6		100	100	40	112	180	223.2142857	176.8388257
18Ni300 Mara	6		100	100	50	112	180	178.5714286	141.4710605
18Ni300 Mara	6		100	125	30	112	180	238.0952381	188.6280807
18Ni300 Mara	6		100	125	40	112	180	178.5714286	141.4710605
18Ni300 Mara	6		100	150	30	112	180	198.4126984	157.1900673
18Ni300 Mara	6		100	150	40	112	180	148.8095238	117.8925504
718	4		180	800	40	105	50	53.57142857	143.2394488
718	4		370	700	80	130	130	50.82417582	64.71135049
718	4		120	280	40	100	50	107.1428571	272.8370453
718	4		160	1000	40	100	50	40	101.8591636

Figure B.4. Data points used for initial survey of process parameters of ferrous materials

1	Kamath, 2013 (LLNL-TR-648000)
2	King, 2014
3	Jelis, 2017
4	AFIT Machines, ConceptLaser
5	3D System ProX 300 at AFRL/RWMW
6	Kempen, 2011
7	Yasa et al 2009
8	Spierings and Levy 2009
9	Yasa et al 2010
10	Yadroitsev and Smurov 2010
11	Kruth 2010a
12	Kruth 2010b
13	Yasa et al 2011
14	Yasa 2011
15	Lie et al 2011
16	Laohaprapanon et al 2012

Figure B.5. References for data points of initial process parameter survey [80, 67, 20, 105, 106, 87, 107, 108, 109, 110, 111, 112, 113, 114]

Appendix C. Matlab Code

C.1 Porosity Processing

```
%Choose File
% User Picks File to Convert
[FileName,PathName] = uigetfile('*.jpg*','Select the image file');
% [FileName,PathName] = uigetfile('*.tif*','Select the image file');
File = FileName(1:findstr(FileName,'.')-1);
Ext = FileName((findstr(FileName,'.')+1):length(FileName));

%Read and Display File
addpath(PathName);
IM = imread(FileName);
%IM = Tiff(FileName,'r');
%IM = read(IM);
GI = IM; %use for .jpg
%imshow(IM) %view image in case of issues

%Convert to Grayscale and Save
%always the chance it's not already grayscale format
[~,~, numberOfColorChannels] = size(IM);
if numberOfColorChannels > 1 %if non-grayscale (z-stack)
    GI = rgb2gray(IM);
else %if already grayscale
    GI = IM;
end
%imshow(GI) %view image in case of issues
%imwrite(GI, [PathName File ' gray.tif']); %if needed

%Threshold Gray Value
```

```
28 threshold = graythresh(IM);
29 BW = imbinarize(GI,threshold);
30 % default binarize seems to eliminate a lot of small spots from ...
       scratches
31 %BW = imbinarize(GI);
32 %imshow(BW)
33
34 %Select Region of Interest, Centroid, depth calculation
35 % Crop rectangular region, including depth keys
36 %message = sprintf('Draw box to select helix of interest; double ...
       click to exit');
37 %uiwait(msgbox(message));
38 %select = imcrop(BW);
39 % select = BW;
40 % imshow(select)
41 % hold on
42 % % automatically identify circles & data
43 % cc = bwconncomp(select);
44 % stats = regionprops(cc, 'Centroid', 'Eccentricity', 'EquivDiameter');
45 %
46 % % filters out the small circles
47 % idx = find([stats.EquivDiameter] > 100);
48 % BW2 = ismember(labelmatrix(cc), idx);  %create new image that just ...
       recognizes larger diameter circles
49 % stats = regionprops(BW2, 'Centroid', 'Eccentricity', 'EquivDiameter');
50 %
51 %
52 % % visual check of circle and centroid
53 % centers = stats.Centroid;
54 % diameters = stats.EquivDiameter;
55 % radii = diameters/2;
56 % viscircles(centers, radii, 'EdgeColor','b');
```

```
57 % plot(centers(1),centers(2),'b*')
58 %
59 % % select two points (double click second), and calculate angle ...
       from centroid
60 % message = sprintf('Select one point on each depth key to define ...
       angles; right click outside image to exit');
61 % uiwait(msgbox(message));
62 % [x,y] = getpts;
63 % plot(x(1),y(1),'r*')
64 % plot(x(2),y(2),'r*')
65 %
66 % %%Depth Calculation
67 % %Define vectors between selected points and centroid
68 % L1 = [(centers(1) - x(1)), (centers(2) - y(1))];
69 % L2 = [(centers(1) - x(2)), (centers(2) - y(2))];
70 % %plot([L1(1) L2(1)] , [L1(2) L2(2)], 'g*') %visual check of ...
       calculated vectors (not working)
71 % hold off
72 %
73 % %Calculate angle between vectors
74 % angle_deg = (atan(L1(2)/L1(1)) - atan(L2(2)/L2(1))) * 180/pi; ...
       %depends on accurate centroid and point selection
75 % Build_height_mm = 10 - 5*angle_deg/180 %drilling down from the ...
       top, uses proportions
76
77 %Select Region of Interest, porosity calcuation
78 imshow(select);
79 %set(gcf, 'Position', get(0,'Screensize')); % Maximize figure.
80 message = sprintf('Click and drag to define ellipse; double click to ...
       exit');
81 uiwait(msgbox(message));
```

```
hFH = imellipse(gca,[]); % % once images are standard, define size ...
    of ellipse; documentation Create a Binary Mask
wait(hFH);
% Create a binary image ("mask") from the ROI object.
binaryImage = hFH.createMask();
xy = hFH.getPosition;
% Mask the image outside the mask, and display it.
% Will keep only the part of the image that's inside the mask, zero ...
    outside mask.
blackMaskedImage = select;
blackMaskedImage(~binaryImage) = 0;
%imshow(blackMaskedImage);
% Get coordinates of the boundary of the freehand drawn region.
structBoundaries = bwboundaries(binaryImage);
xy=structBoundaries{1}; % Get n by 2 array of x,y coordinates.
x = xy(:, 2); % Columns.
y = xy(:, 1); % Rows.
% Now crop the image.
leftColumn = min(x);
rightColumn = max(x);
topLine = min(y);
bottomLine = max(y);
width = rightColumn - leftColumn + 1;
height = bottomLine - topLine + 1;
croppedImage = imcrop(blackMaskedImage, [leftColumn, topLine, width, ...
    height]);
imshow(croppedImage);


%%Calculate Porosity
%crop the binary image, define size of black and white mask
croppedMask = imcrop(binaryImage, [leftColumn, topLine, width, height]);
```

```
111 %imshow(croppedMask)
112 areaofellipse = nnz(croppedMask); % number of white elements in mask
113 areaoutsidemask = nnz(~croppedMask); %number of black elements in mask
114
115 % calculate ratio of black white space to black
116 proportionBlack = (nnz(~croppedImage)-areaoutsidemask) / areaofellipse;
117 Relative_Density = 100-proportionBlack*100
```

C.2 Rotation Matrix

```
1  close all;
2  clear; clc;
3  format bank
4
5  %Point space scaling
6  s = 30; %MLab
7  %s = 50; %M2
8
9  %Nine by nine grid centered at zero
10 a = s*[-1 1]; b = s*[0 1]; c = s*[1 1]; d = s*[-1 0]; f = s*[0 0]; g ...
       = s*[1 0]; h = s*[-1 -1]; k = s*[0 -1]; m = s*[1 -1];
11
12 %rotation matrix
13 theta = 20; %degrees, MLab
14 %theta = -20; %degrees, M2
15 R = [cosd(theta) -sind(theta); sind(theta) cosd(theta)];
16
17 %rotate points by theta
18 a = R*a'
19 b = R*b'
20 c = R*c'
```

```
d = R*d'
f = R*f'
g = R*g'
h = R*h'
k = R*k'
m = R*m'

figure %check size & alignment
x = [a(1),b(1),c(1),d(1),f(1),g(1),h(1),k(1),m(1)];
y = [a(2),b(2),c(2),d(2),f(2),g(2),h(2),k(2),m(2)];
scatter(x,y,180,'k','filled')
xlim([-120,120]);
ylim([-120,120]);
```

C.3 .cli Layer Height Modifier

```
%% User Picks File to Convert
[FileName,PathName] = uigetfile('*.cli*','Select the cli file');
File = FileName(1:findstr(FileName,'.')-1);
Ext = FileName((findstr(FileName,'.')+1):length(FileName));

%% Simple Read and Find

layerHeight=0.030; % Mlab Setup Layer Height

% Naming for Text Files
fid=fopen([PathName FileName],'r');
fidMod=fopen([PathName File 'Mod.cli'],'w');

% Indexing Initialization
layerValueIdx=1;
```

```
16 layerValue = 1;
17 lineIdx=1;
18
19 % Read and Copy File - see if thens for when to modify.
20 while ~feof(fid)
21 %    for n=1:120
22         tline = fgetl(fid);
23
24         % Check for Layer Value
25         if findstr(tline,'$$LAYER/') == 1
26             % Store Layer Value
27             layerValue(layerValueIdx)=str2num(tline(9:end));
28
29             if layerValueIdx == 1
30                 layerValue = 1;
31             else
32                 layerValue=(layerValueIdx-1)*layerHeight*1000;
33             end
34             % Print Modified Layer Value
35             fprintf(fidMod,['$$LAYER/' num2str(layerValue) '\n']);
36
37             % Increment layer Index
38             layerValueIdx=layerValueIdx+1;
39         else
40             fprintf(fidMod,[tline '\n']);
41         end
42         lineIdx=lineIdx+1;
43     end
44
45 fclose(fid);
46 fclose(fidMod);
47
```

```
48 %% Show Completed
49 fprintf( ['Read - ' FileName '\n' 'Modified - ' File 'Mod.cli\n']);
```

Appendix D. Standard Sample Preparation Procedures

William “Tommy” Cissel

Cobalt- and Nickel-based Superalloy sample preparation.

The procedures list are a combination of generic steps for the preparation of Cobalt- and Nickel-based Superalloys.

Sectioning:

The use of a high speed saw with an Aluminum Oxide Rubber Bonded blade at 3000 rpms, a feed rate 0.05” /min with a low force was used in the sectioning process.

Options are below:

Low speed Saw: HC Diamond Blade. Range 150 – 300 RPM (Speed range and force is dependent on size, thickness and density).

High Speed Saw: Aluminum Oxide Rubber Bonded. Range 2800 – 3000 RPM, 0.05”/min, low force.

Mounting:

The use of a conductive phenolic resin was used for various SEM analysis procedures. Currently, Struars PolyFast is used and cured with a hot mounting press. If light microscopy is the only unit used for analysis, a non-conductive phenolic, Buehler EpoMet, should be used.

	Resin Type	Heating Temp	Heating Pressure	Heating Time	Cooling Time	Cooling Rate
1	PolyFast	180°C	4800 psi	3.5	1.5	High
1	EpoMet	180°C	4800 psi	3.5	1.5	High

Grinding/Polishing:

Silicon Carbide papers, Buehler Apex DGD and TriDent cloths were used for the preparation of the specimens. The use of colloidal silica (SiO_2) is labeled for final polish; however, depending of the alloy, a combination of SiO_2 and alumina (Al_2O_3) can be used to chemically polish and etch the surface, revealing the macrostructure. Though, SiO_2 / Al_2O_3 should not be used if performing EBSD analysis.

A Buehler EcoMet 250 was used to grind and polish the samples. The settings used for each step can be found in Table 1.

Cleaning was performed before each step. After each grinding step, the samples were rinsed with water. After each polishing step, the samples were rinsed with isopropanol and water and hand washed to remove any colloidal particles from the surface.

After the 1 µm Diamond polishing step, the samples were cleaned as stated above, then rinsed with ethanol and dried with hot air. The samples were then mounted in a weighted holder, labeled, and polished in the Vibromet containing 0.05 µm SiO_2 solution overnight.

The following techniques show the parameter for a semi-auto unit, though could be modified to support “hand” grinding and polishing by eliminating the specifics of “Head Speed” and “Pressure” if desired.

Post-Vibromet Treatment:

After the sample was allowed to be polished in the vibromet using 0.05 µm SiO_2 solution, the sample was immediately rinsed with water. The sample was then immersed in a beaker containing acetone and sonicated for 5-10 minutes. The sample was then moved to a beaker containing isopropanol, where it was again sonicated for 5-10 minutes. It was then rinsed with distilled water, coated with ethanol or isopropanol, and dried.

	Surface	**Grit Size**	**Time** (Estimated)	**Spin Type**	**Base Speed**	**Head Speed**	**Pressure**
1	SiC Paper	240	5 min to start, Repeat until planar	Complimentary	300 rpm	50 rpm	5 lbs
2	SiC Paper	320	4 min	Complimentary	300 rpm	50 rpm	5 lbs
3	SiC Paper	400	3 min	Complimentary	150 rpm	50 rpm	5 lbs
4	SiC Paper	600	3 min	Complimentary	150 rpm	50 rpm	5 lbs
5*	Gold Label	9 µm Diamond	3 min	Contra	150 rpm	50 rpm	4 lbs
6	TriDent	3 µm Diamond	2 min	Complimentary	150 rpm	50 rpm	4 lbs
7	TriDent	1 µm Diamond	2 min	Complimentary	150 rpm	50 rpm	4 lbs

Table 1: Grinding/Polishing steps using a semi-automatic grinder polisher. *Note: The water should not be on during the polishing steps, and samples should be rinsed with ethanol to remove additional diamond suspension grit.

Appendix E. Additional Images of Interest

E.1 MLab Weld Tracks, Top

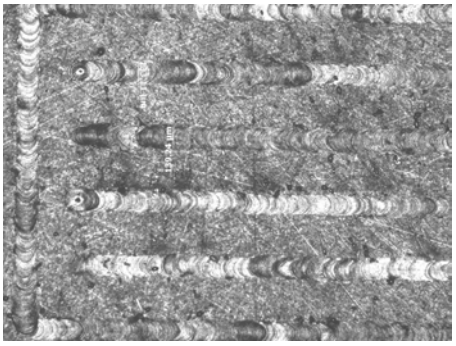

80W 125mm/s

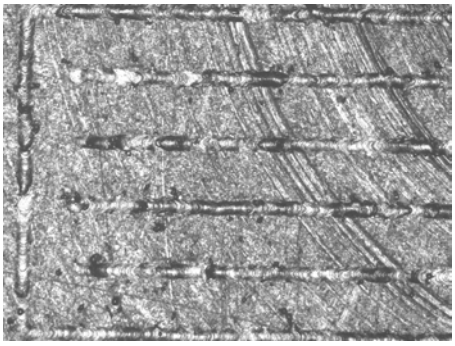

80W 350mm/s

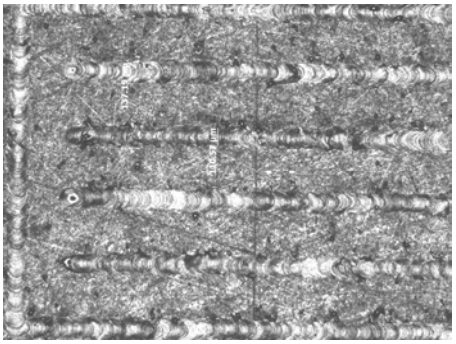

80W 170mm/s

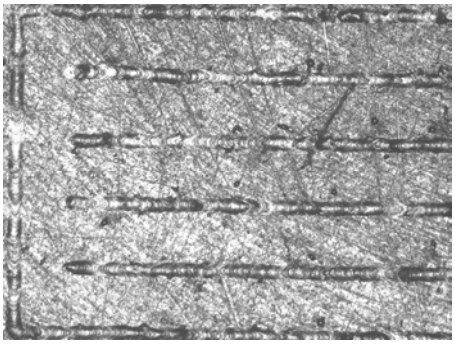

80W 420mm/s

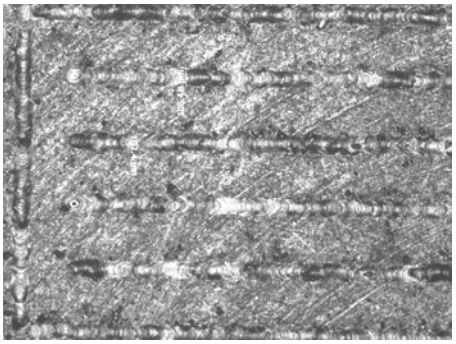

80W 250mm/s

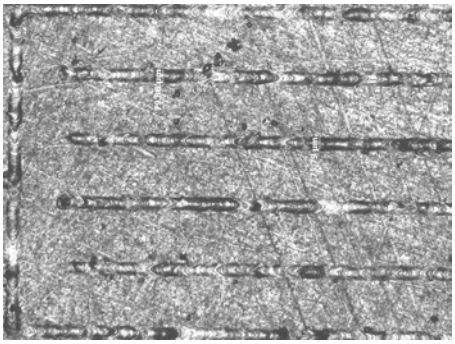

80W 500mm/s

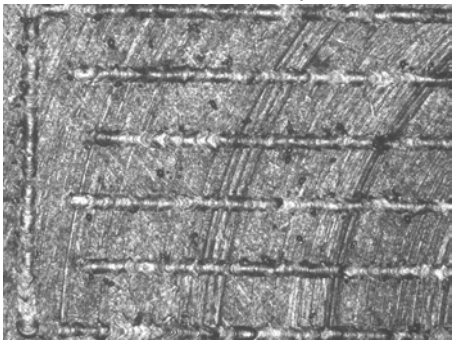

80W 300mm/s

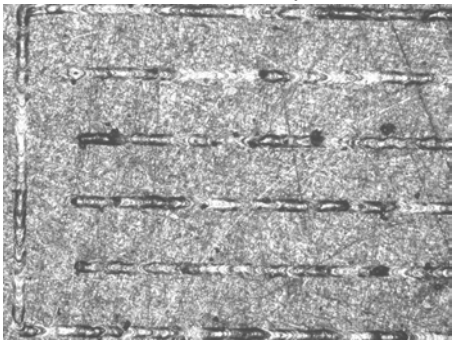

80W 630mm/s

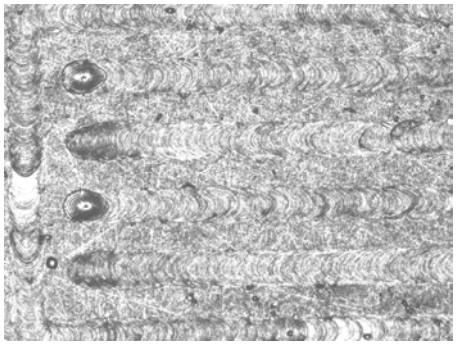

100W 100mm/s

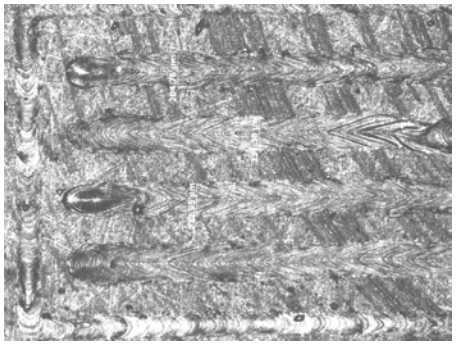

100W 212mm/s (incorrect)

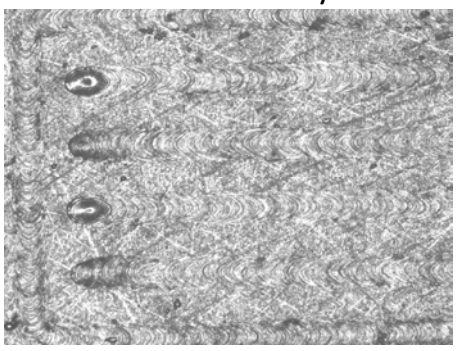

100W 130mm/s

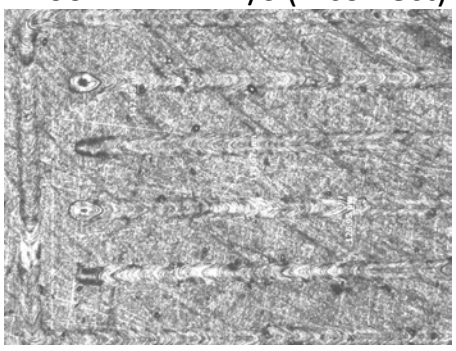

100W 320mm/s

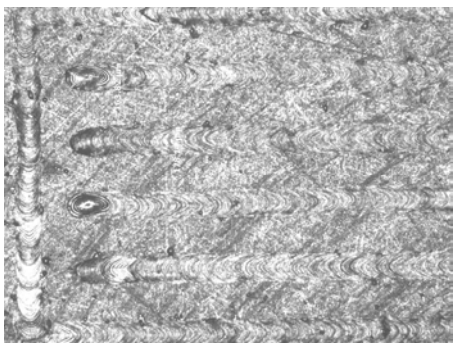

100W 160mm/s

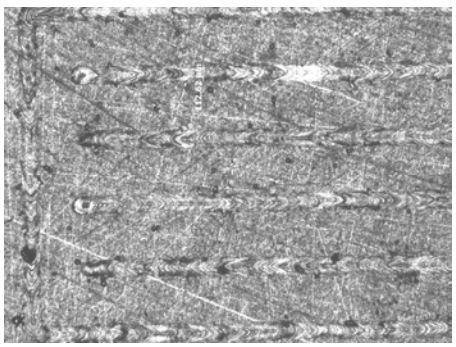

100W 430mm/s

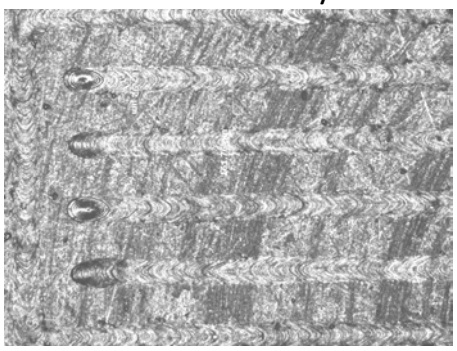

100W 180mm/s

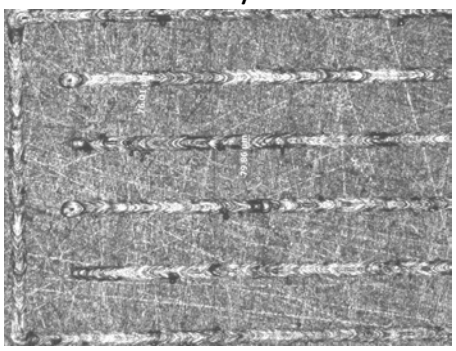

100W 640mm/s

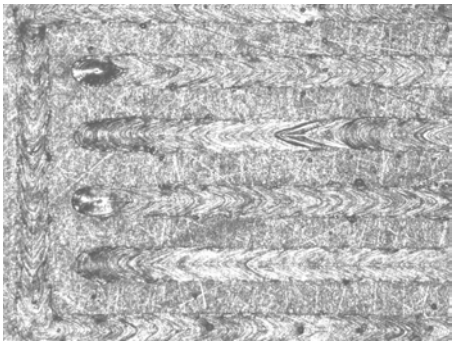

140W 200mm/s

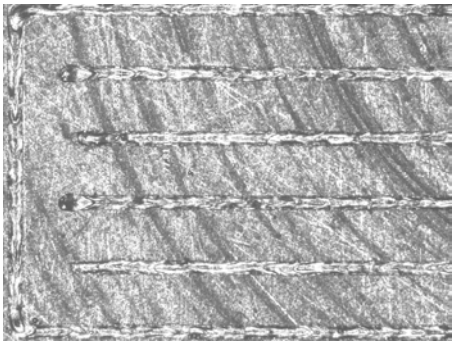

140W 1000mm/s

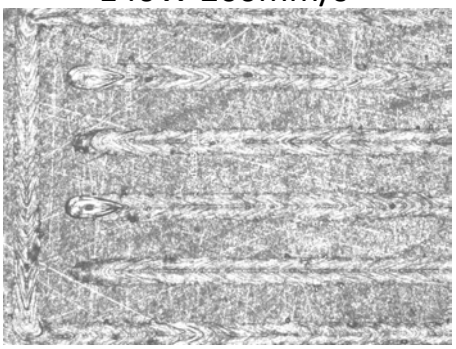

140W 400mm/s

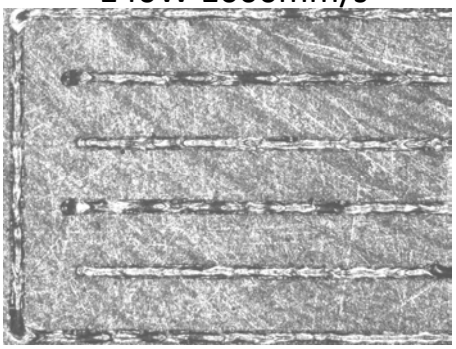

140W 1200mm/s

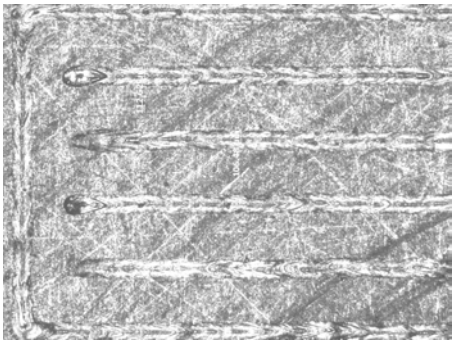

140W 600mm/s

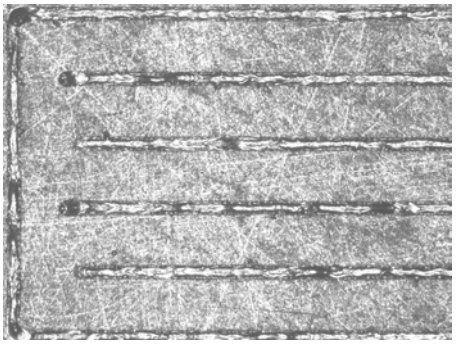

140W 1400mm/s

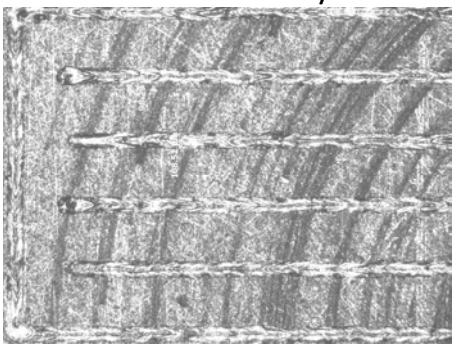

140W 800mm/s

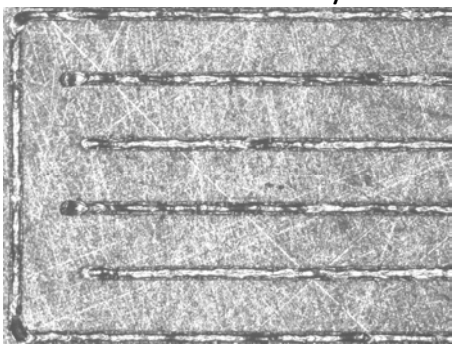

140W 1400mm/s

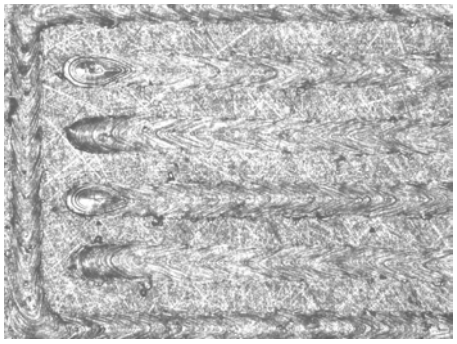

170W 200mm/s

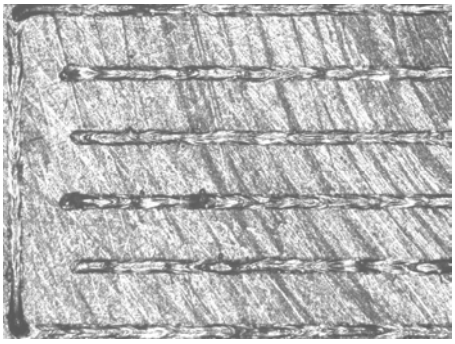

170W 1000mm/s

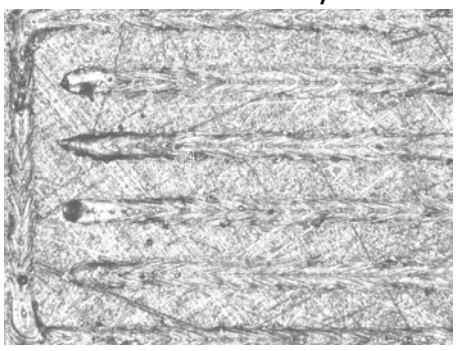

170W 400mm/s

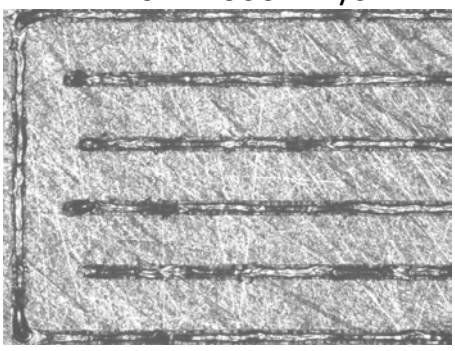

170W 1200mm/s

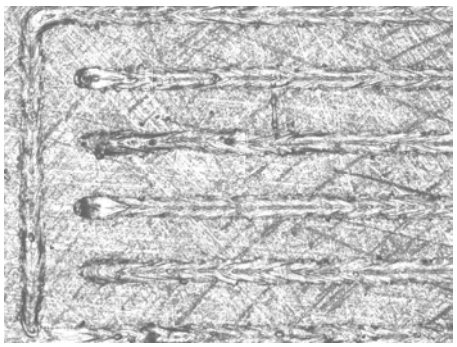

170W 600mm/s

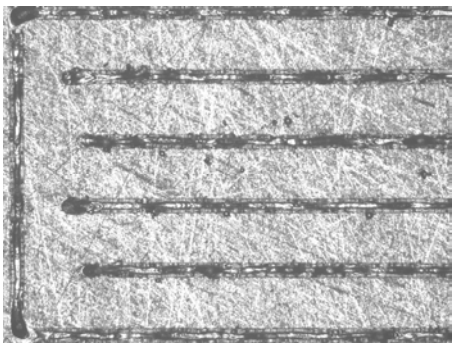

170W 1400mm/s

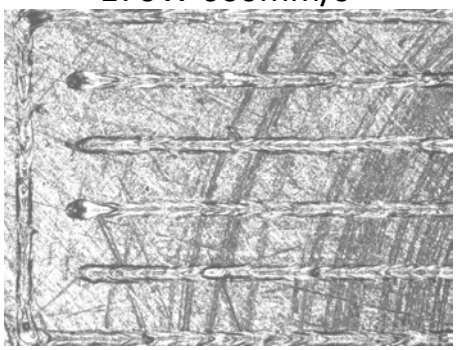

170W 800mm/s

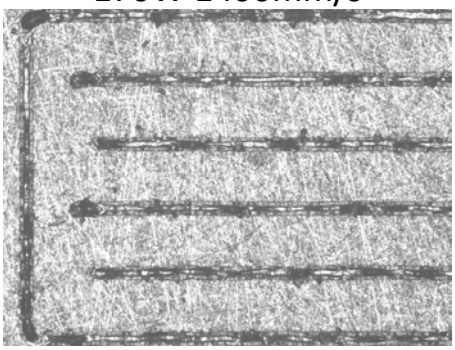

170W 1600mm/s

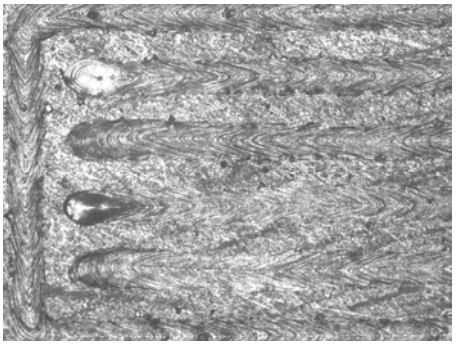

200W 200mm/s

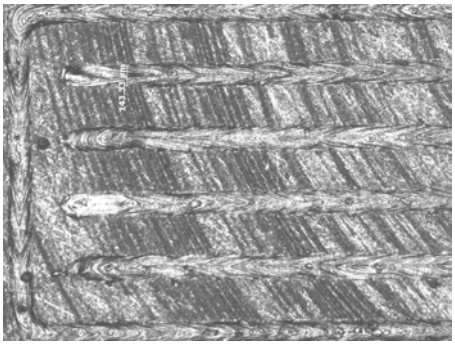

200W 425mm/s

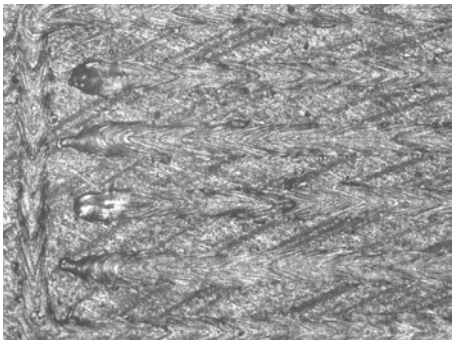

200W 255mm/s

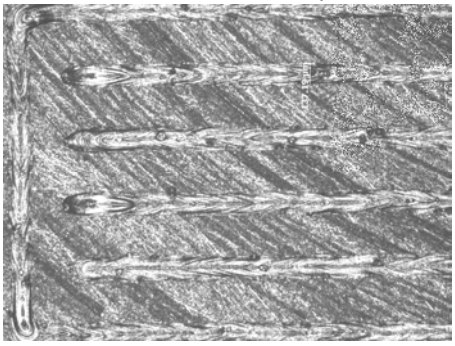

200W 640mm/s

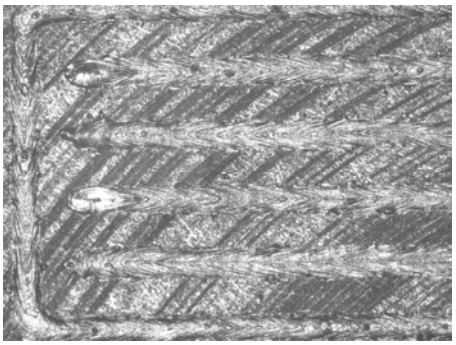

200W 320mm/s

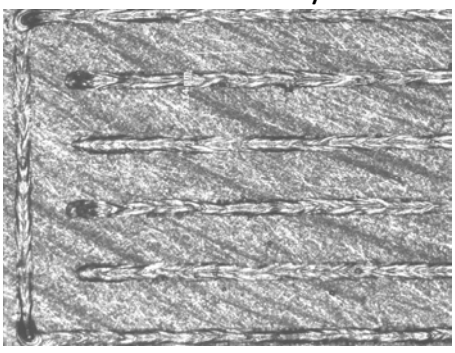

200W 900mm/s

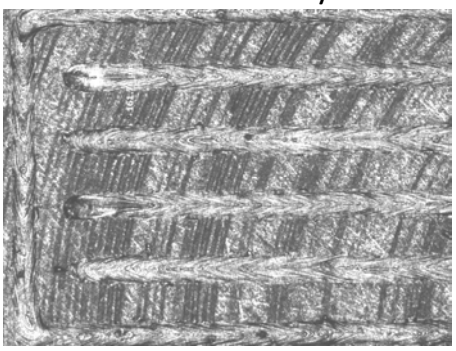

200W 370mm/s

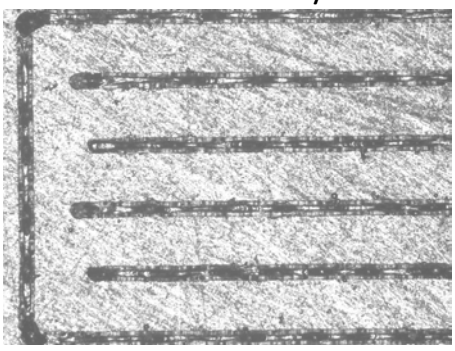

200W 1280mm/s

E.2 MLab Weld Tracks, Sectioned


100W 640mm/s
100W 430mm/s
100W 320mm/s
100W 212mm/s (incorrect)
100W 180mm/s
100W 160mm/s
100W 130mm/s
100W 100mm/s

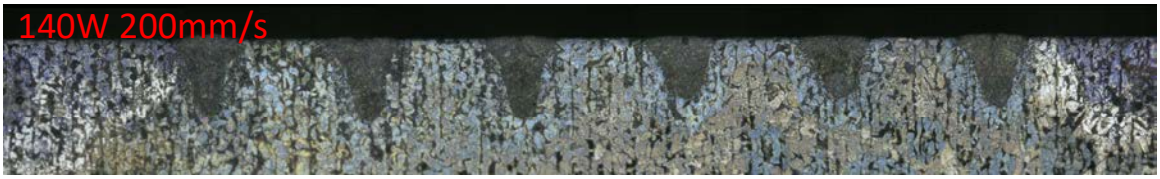
140W 200mm/s

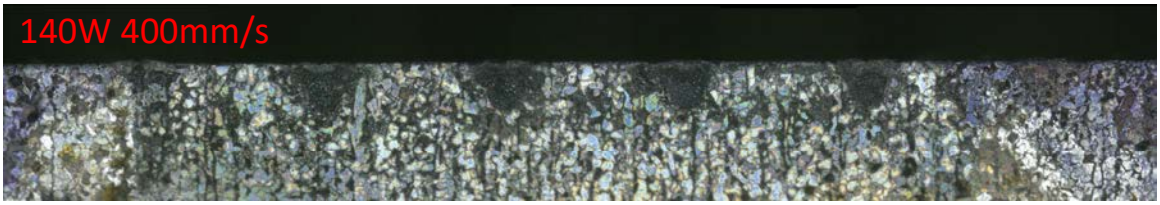
140W 400mm/s

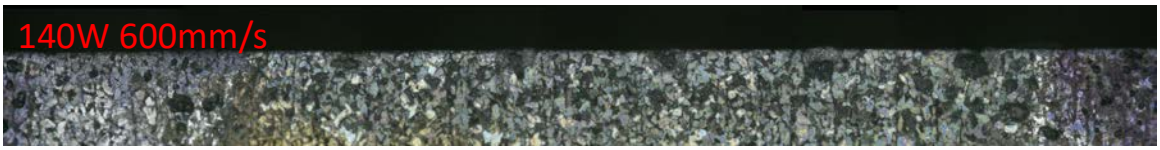
140W 600mm/s

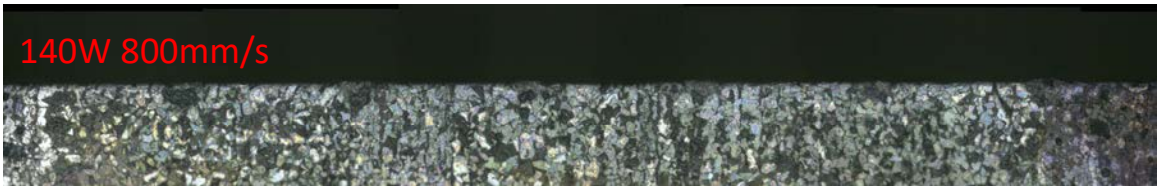
140W 800mm/s

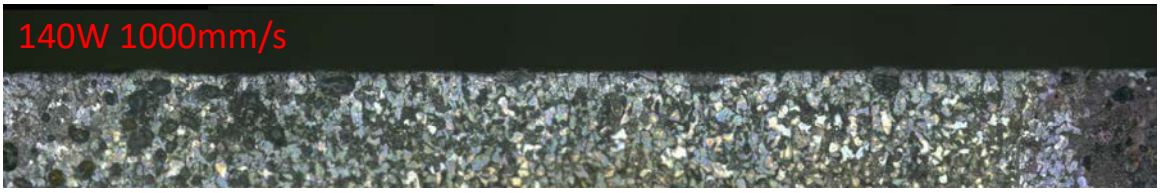
140W 1000mm/s

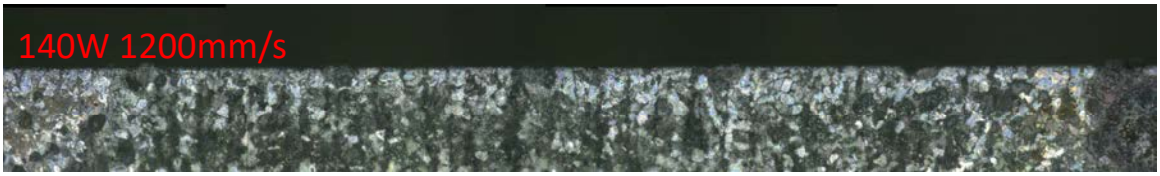
140W 1200mm/s

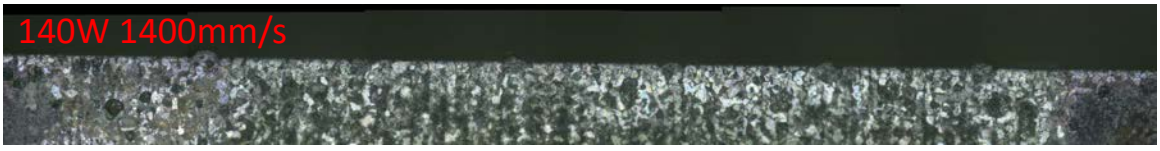
140W 1400mm/s


140W 1600mm/s

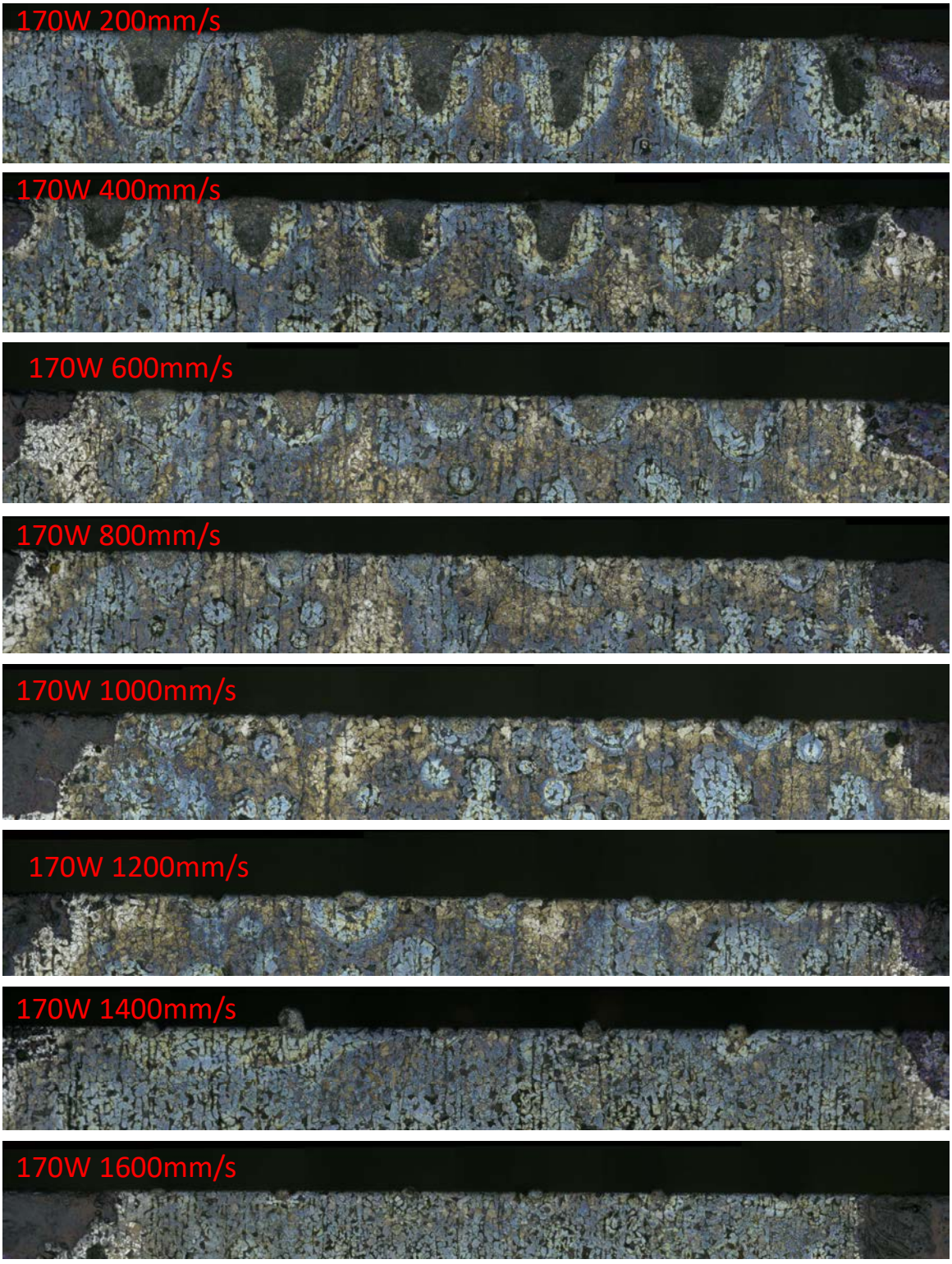
170W 200mm/s
170W 400mm/s
170W 600mm/s
170W 800mm/s
170W 1000mm/s
170W 1200mm/s
170W 1400mm/s
170W 1600mm/s

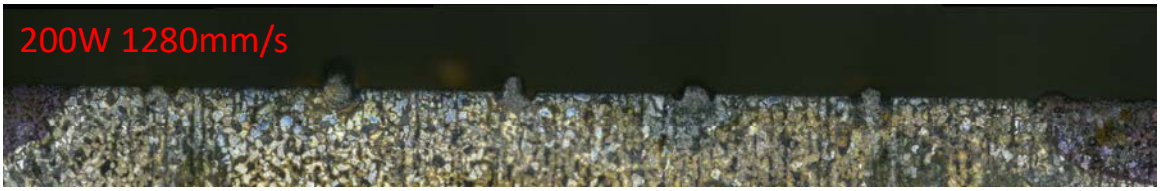
200W 1280mm/s

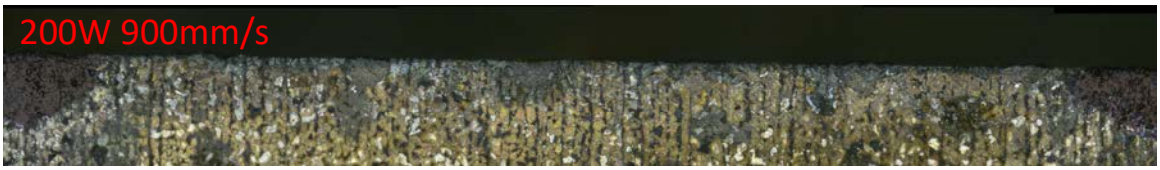
200W 900mm/s

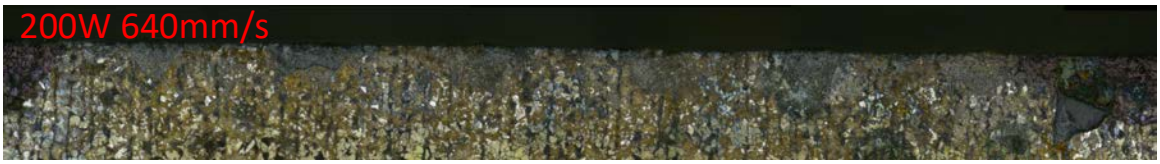
200W 640mm/s

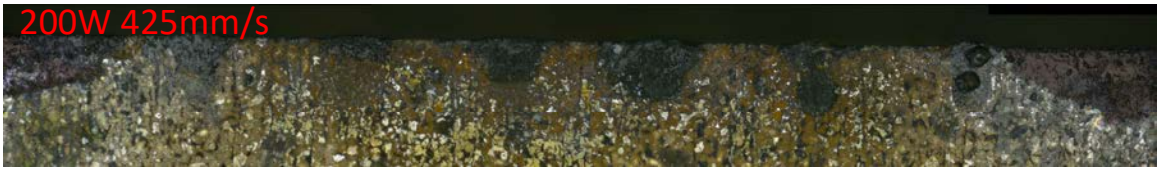
200W 425mm/s


200W 370mm/s

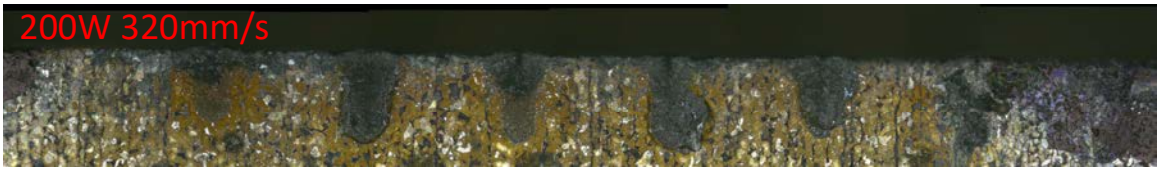
200W 320mm/s

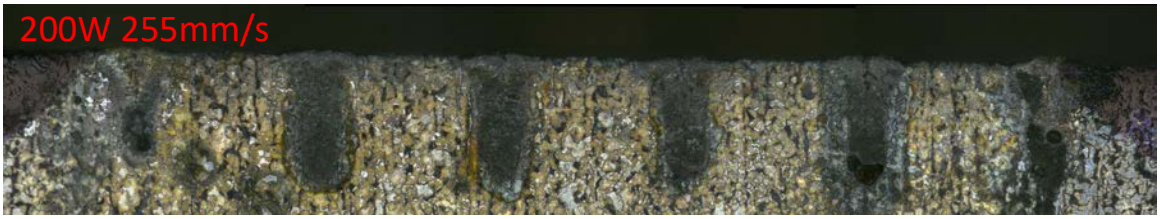
200W 255mm/s


200W 200mm/s

E.3 Laser Scanning Microscope Topology

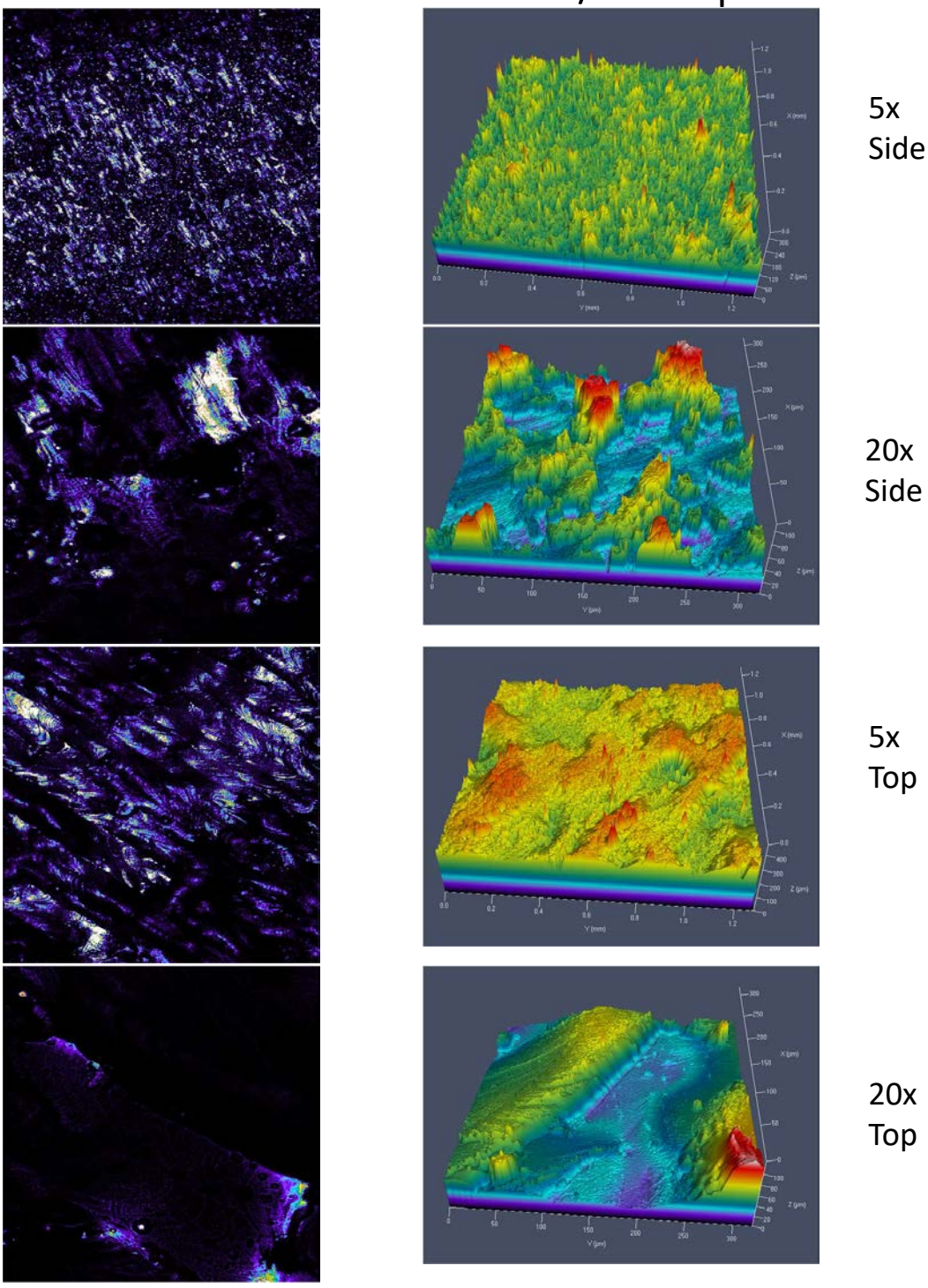

100 W 430 mm/s 85 µm

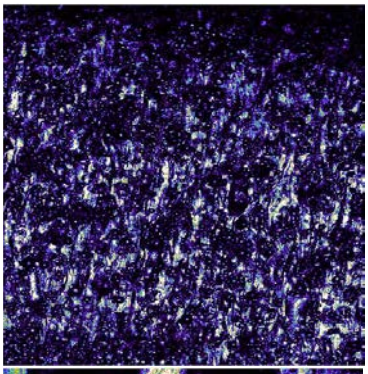

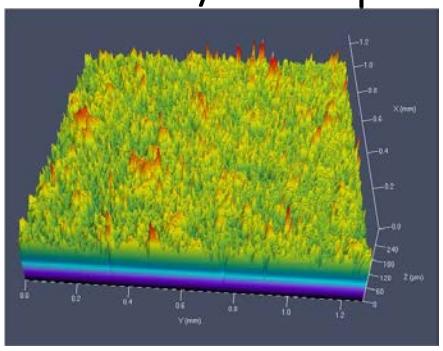

5x
Side

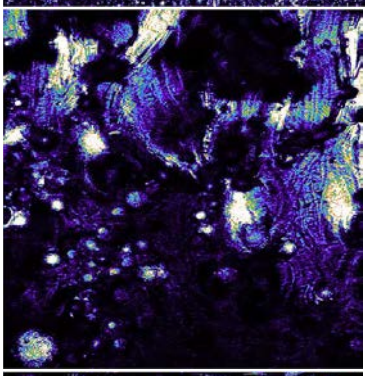

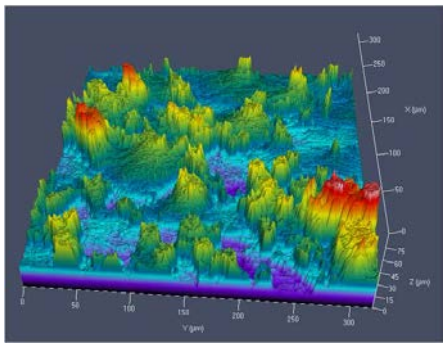

20x
Side

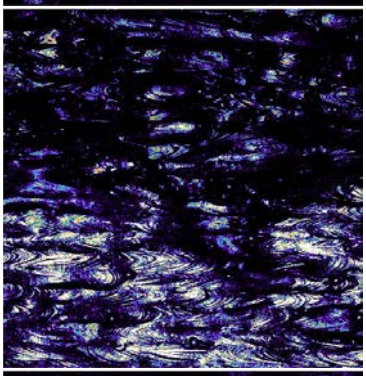

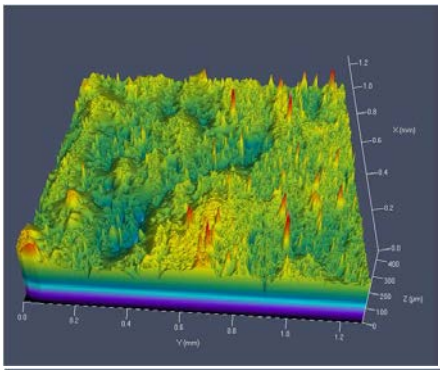

5x
Top

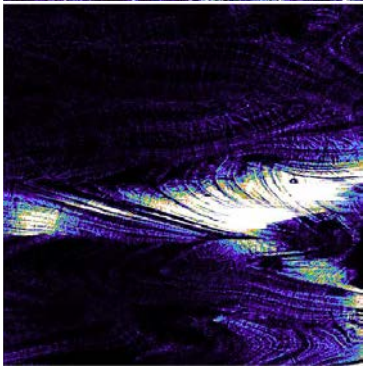

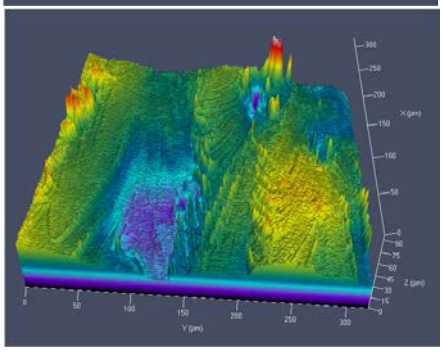

20x
Top

140 W 400 mm/s 119 µm

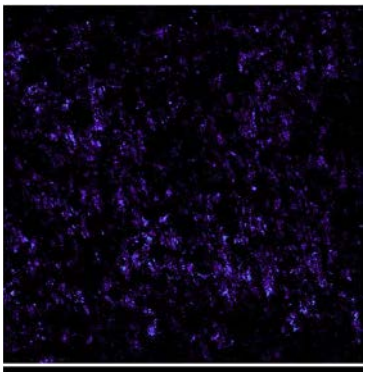

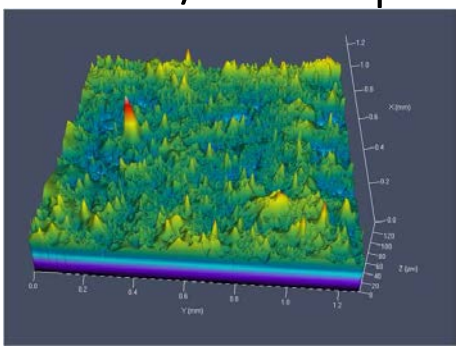

5x
Side

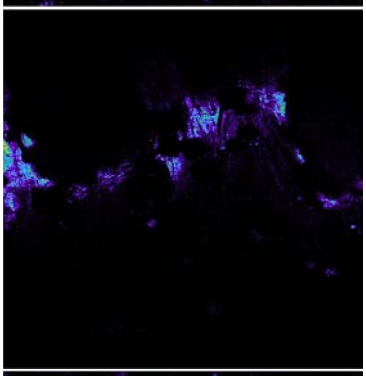

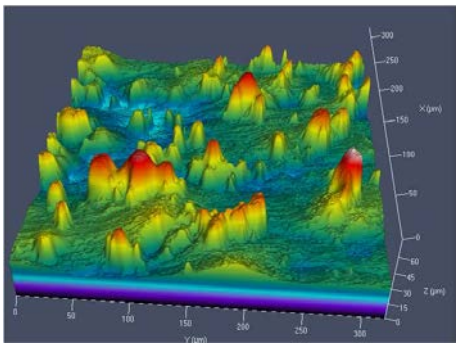

20x
Side

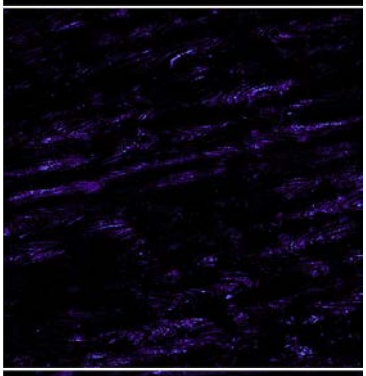

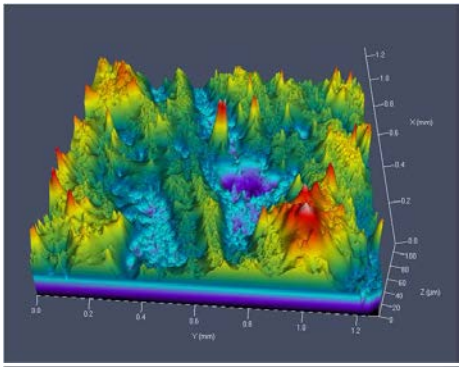

5x
Top

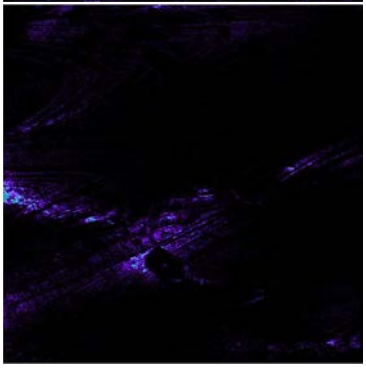

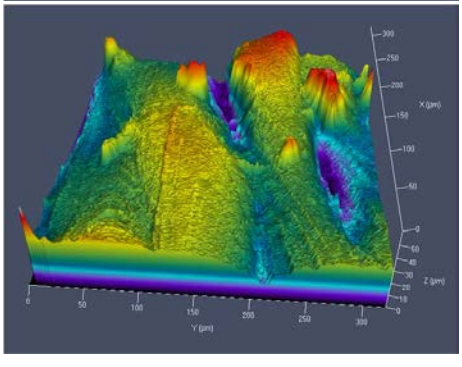

20x
Top

140 W 600 mm/s 86 µm

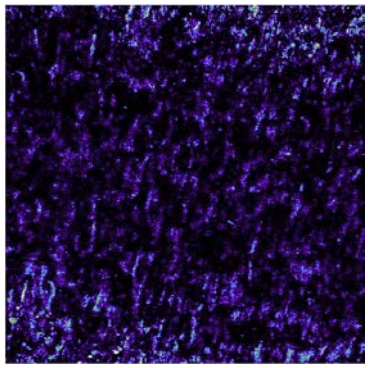

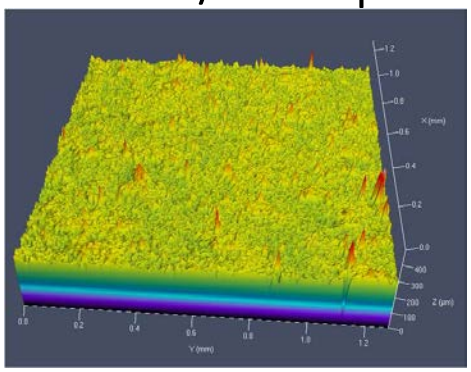

5x
Side

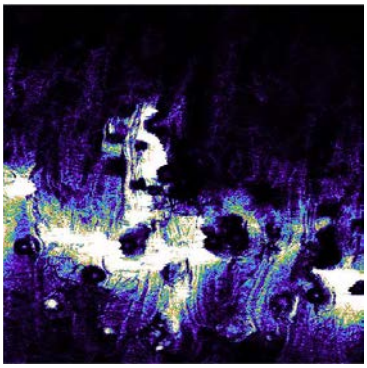

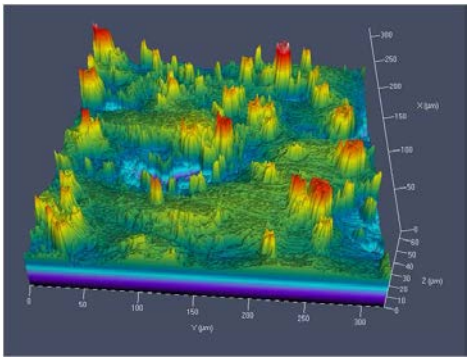

20x
Side

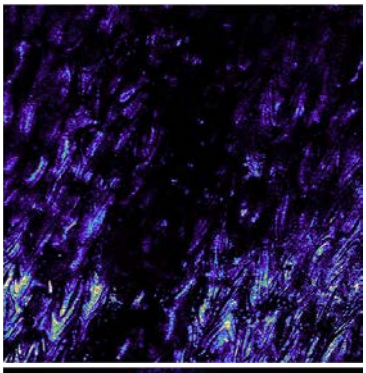

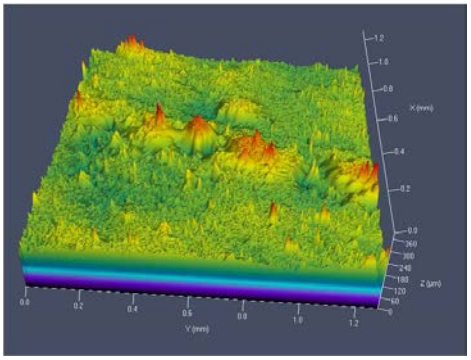

5x
Top

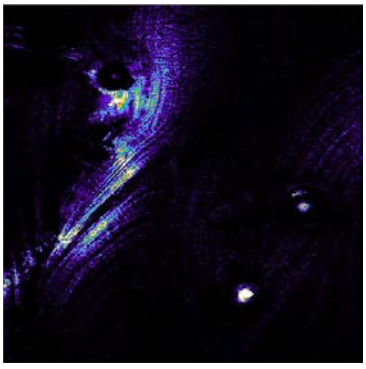

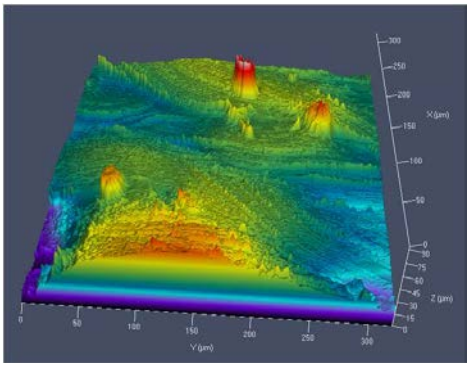

20x
Top

170 W 480 mm/s 137 µm

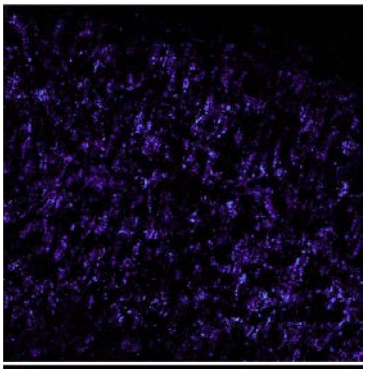

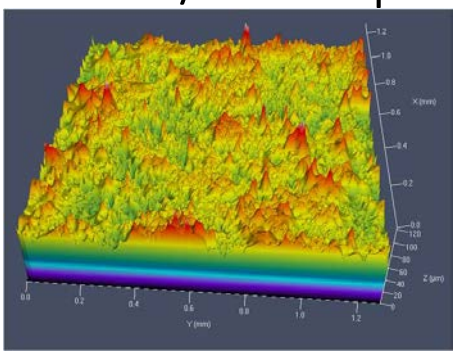

5x
Side

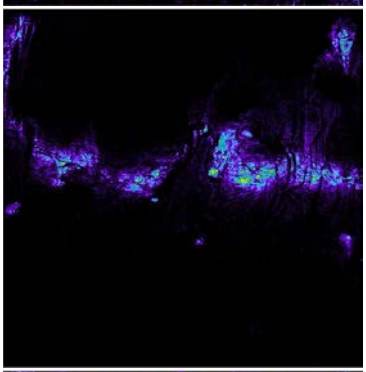

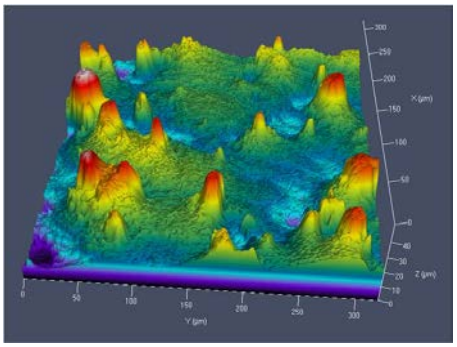

20x
Side

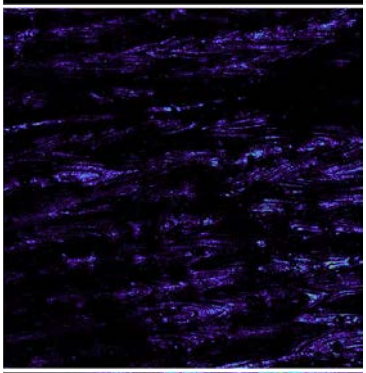

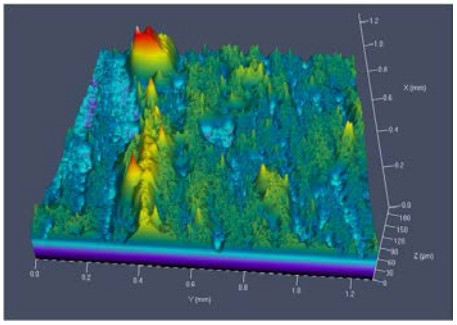

5x
Top

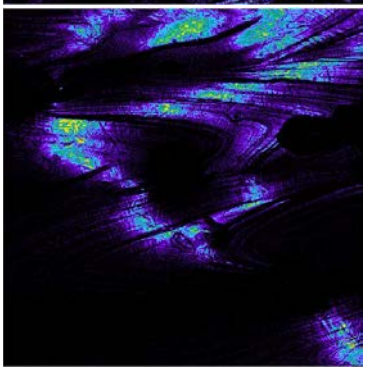

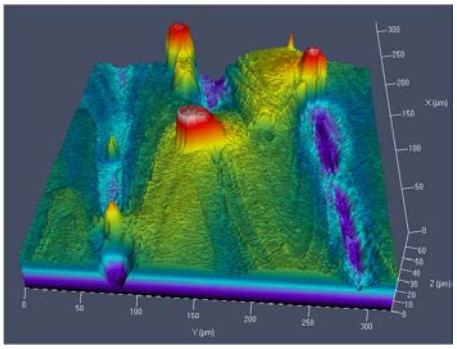

20x
Top

170 W 600 mm/s 110 µm

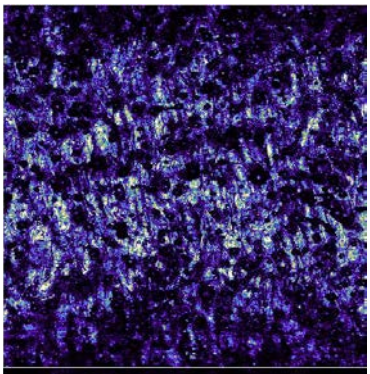

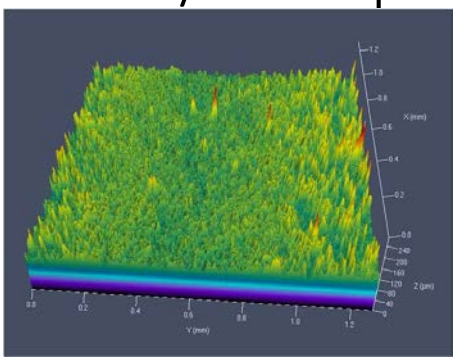

5x
Side

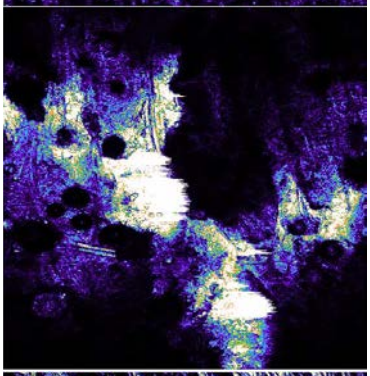

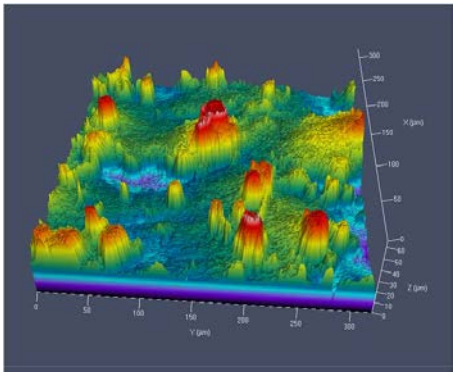

20x
Side

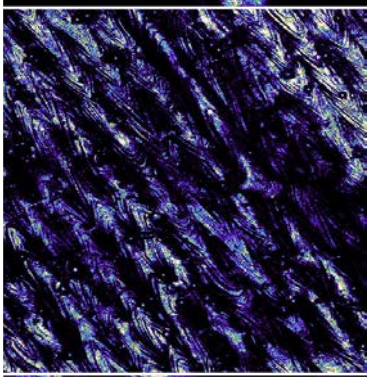

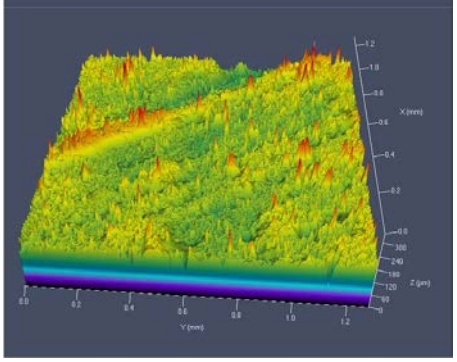

5x
Top

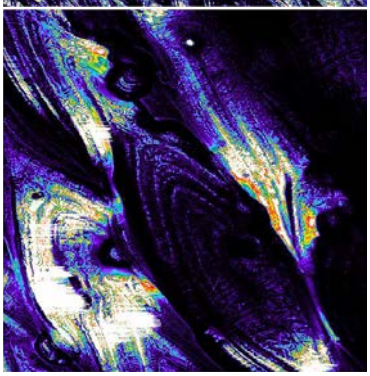

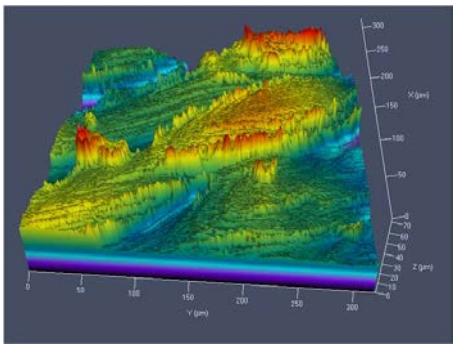

20x
Top

200 W 640 mm/s 93 µm

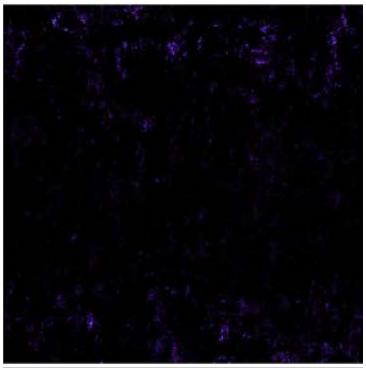

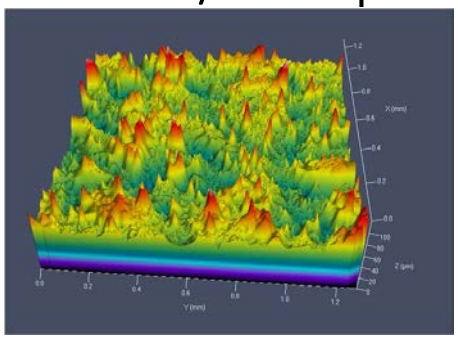

5x
Side

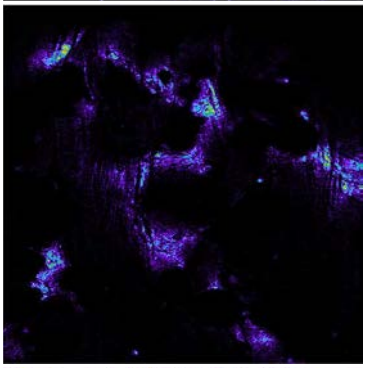

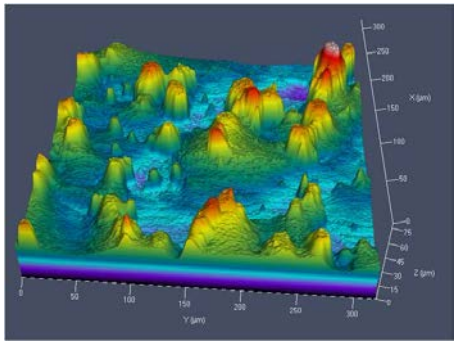

20x
Side

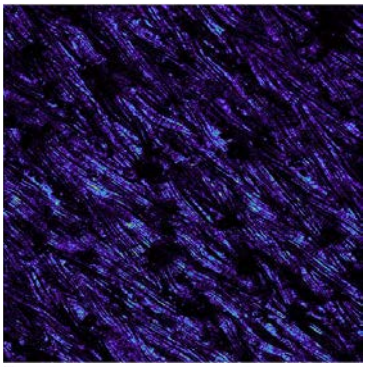

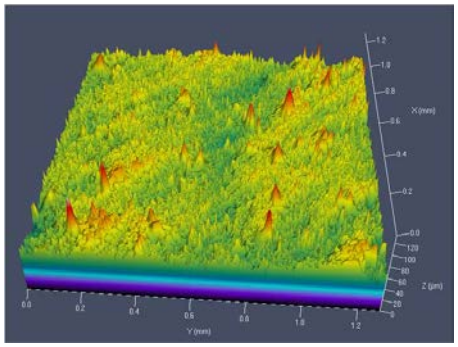

5x
Top

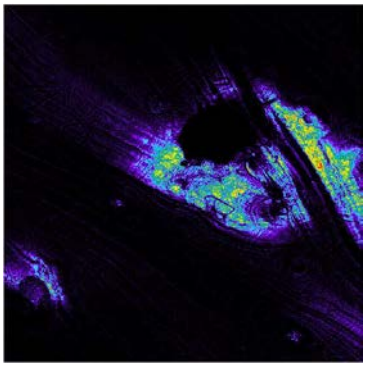

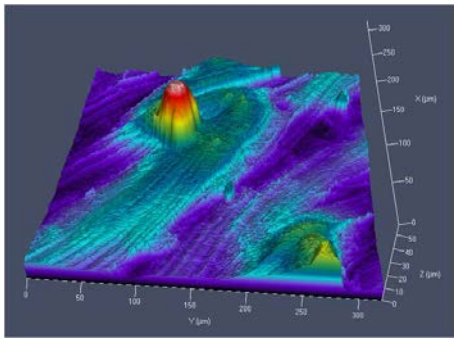

20x
Top

200 W 800 mm/s 94 µm

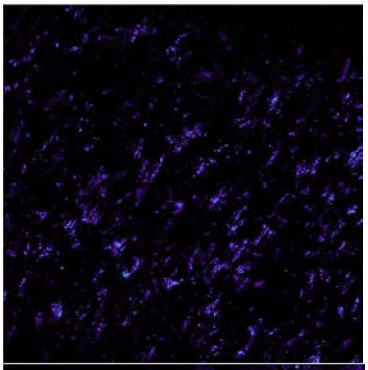

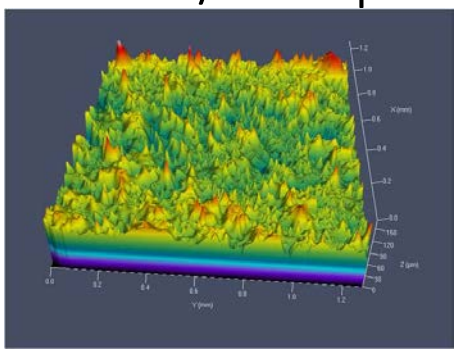

5x
Side

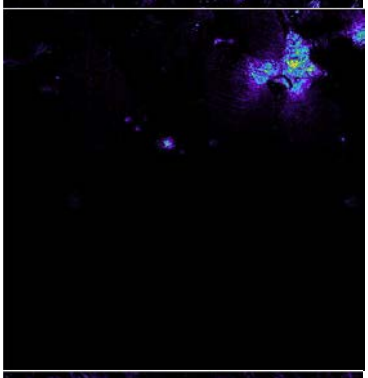

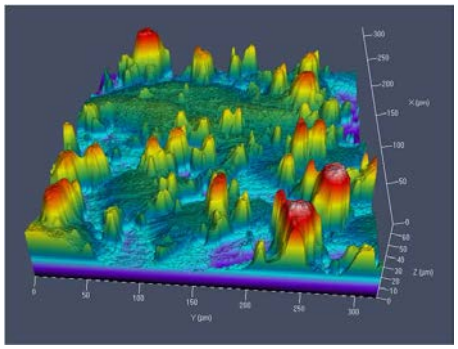

20x
Side

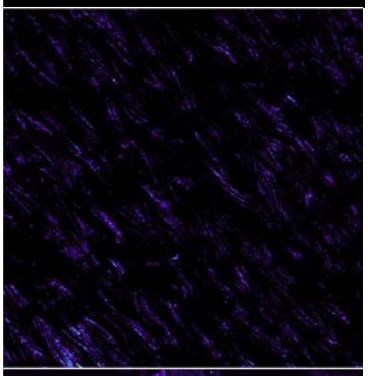

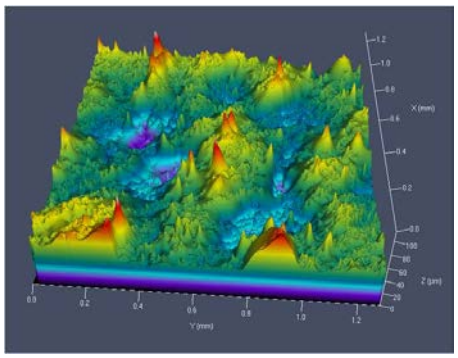

5x
Top

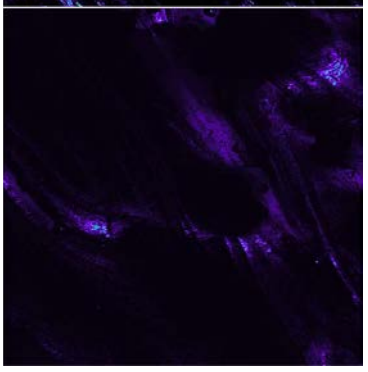

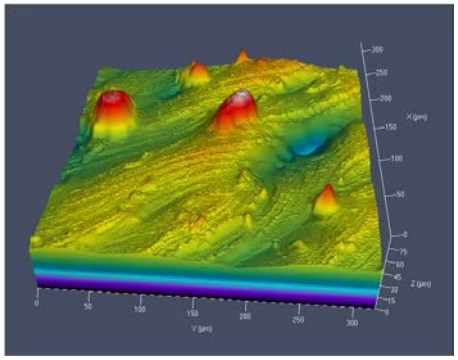

20x
Top

E.4 M2 Weld Tracks, Top

100 μm Spot Size

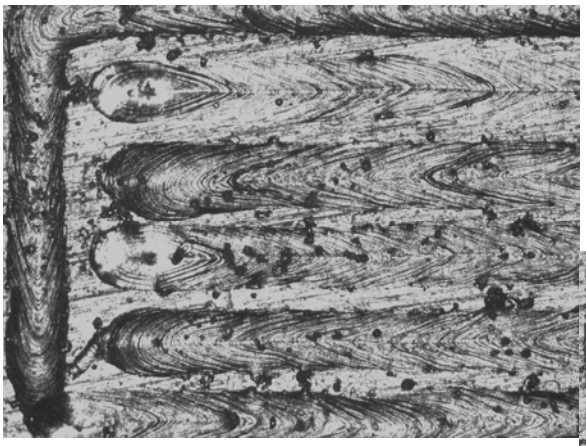

275W 175mm/s

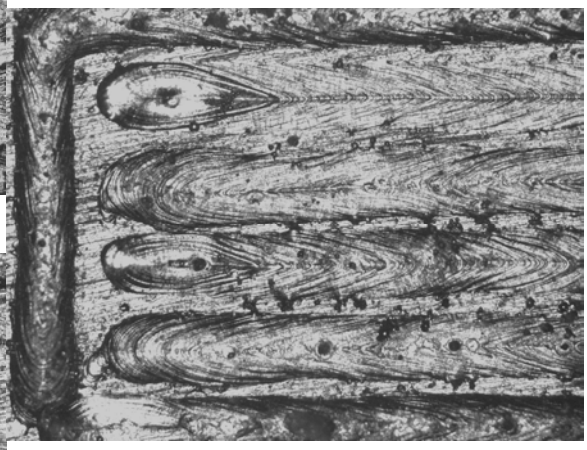

350W 225mm/s

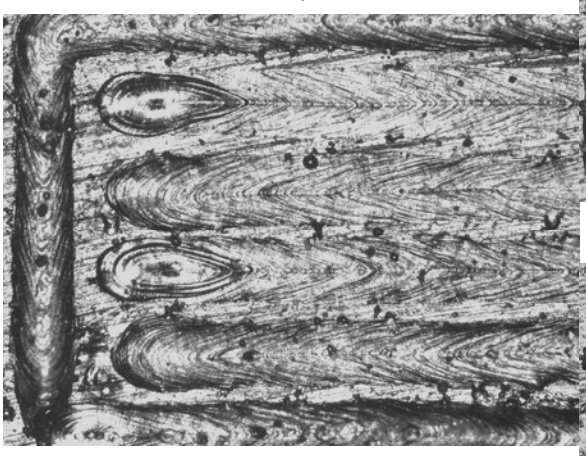

300W 190mm/s

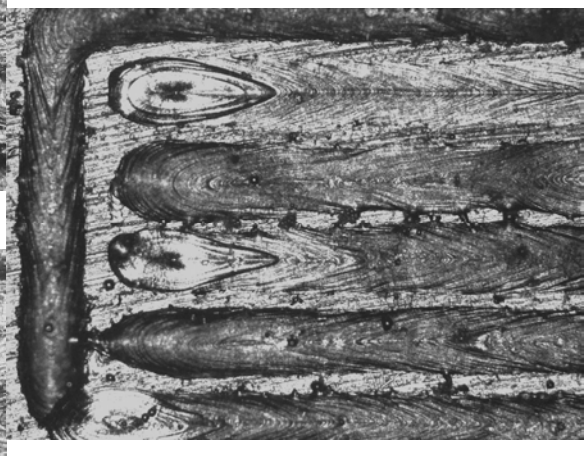

375W 240mm/s

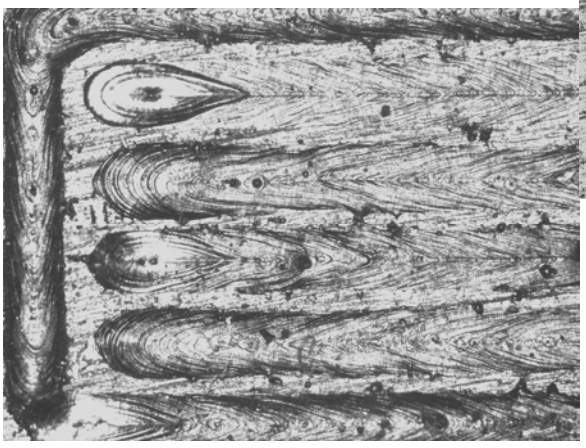

325W 300mm/s

120 μm Spot Size

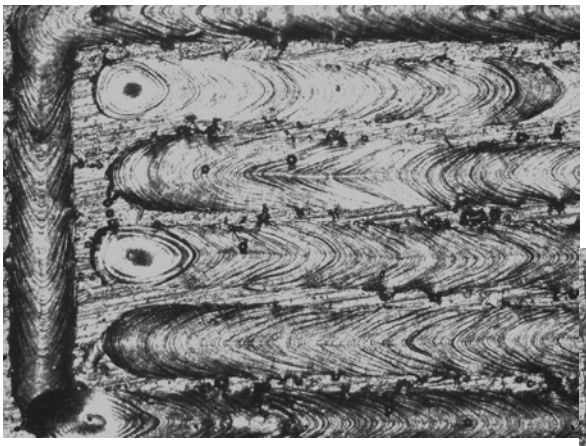

275W 145mm/s

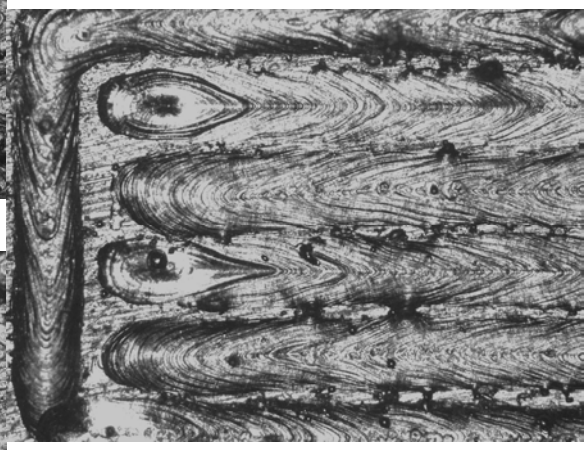

350W 180mm/s

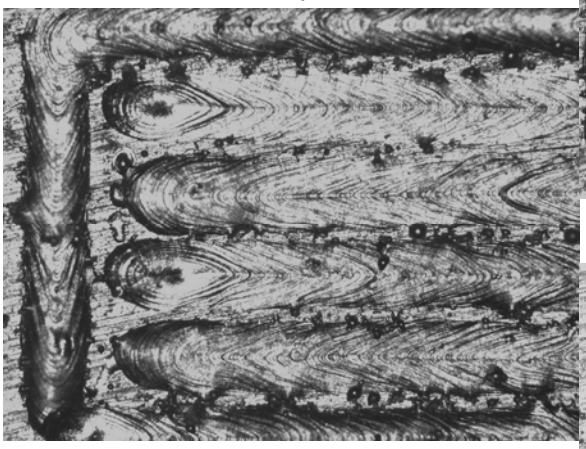

300W 160mm/s

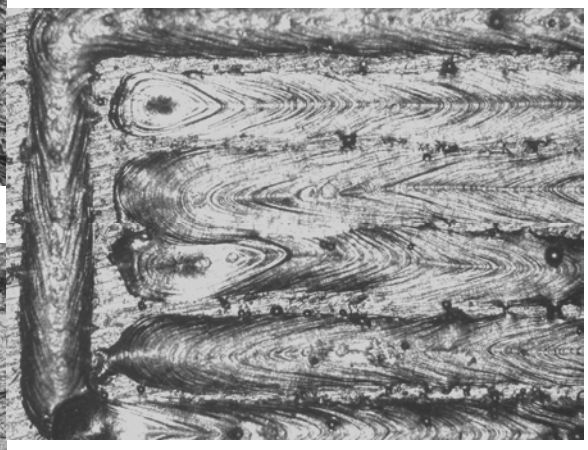

375W 200mm/s

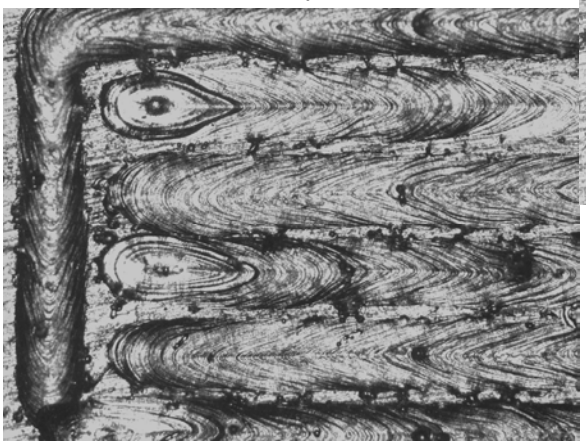

325W 170mm/s

140 μm Spot Size

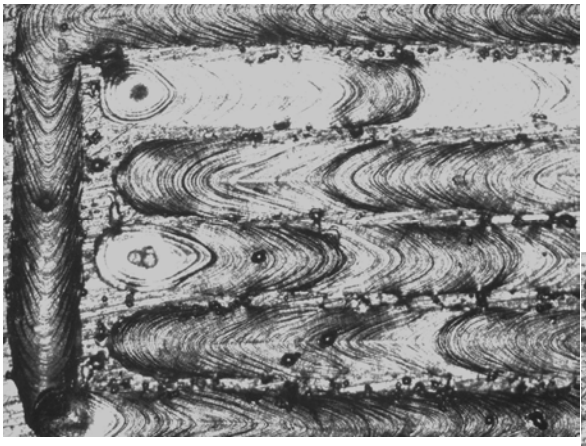

275W 125mm/s

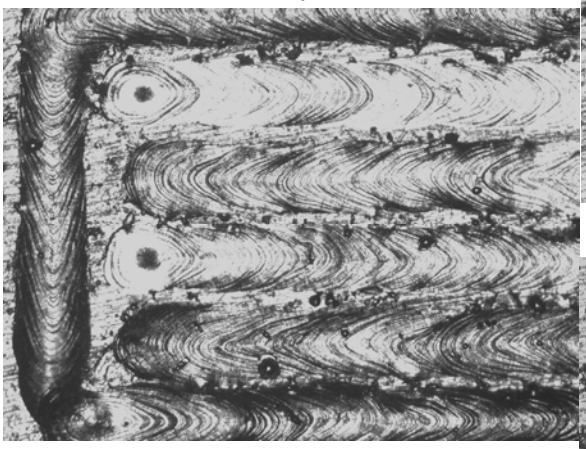

300W 135mm/s

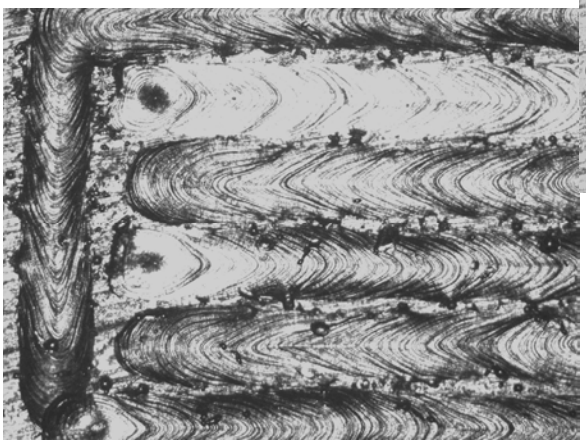

325W 150mm/s

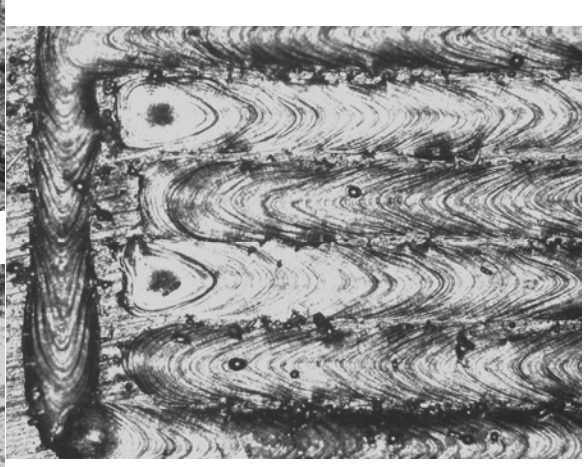

350W 160mm/s

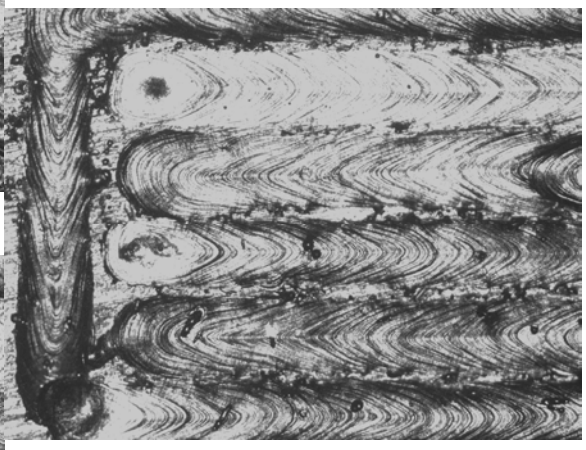

375W 170mm/s

160 μm Spot Size

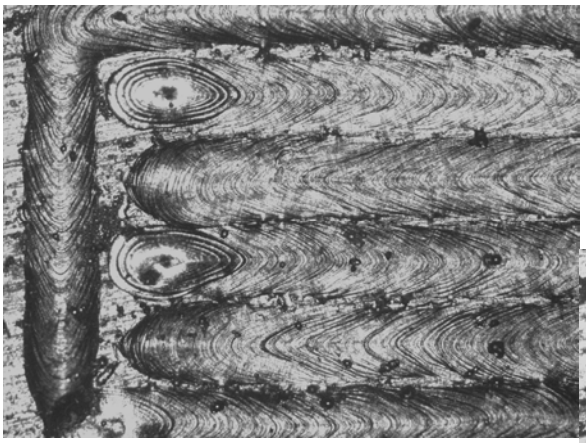

275W 110mm/s

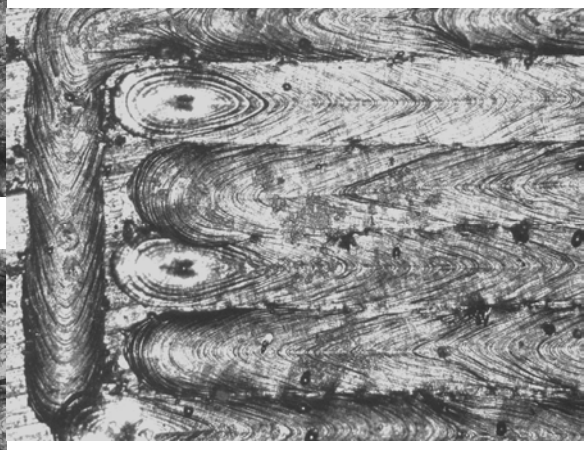

350W 140mm/s

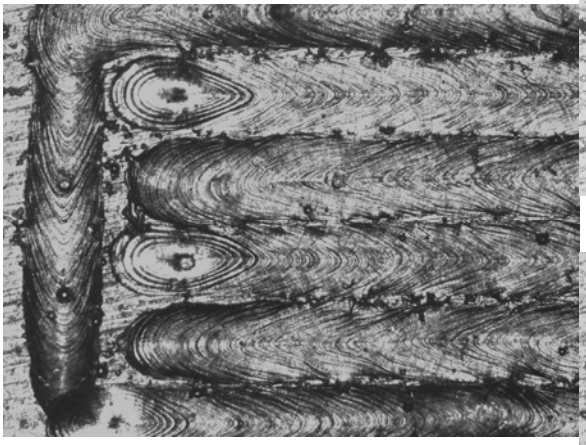

300W 120mm/s

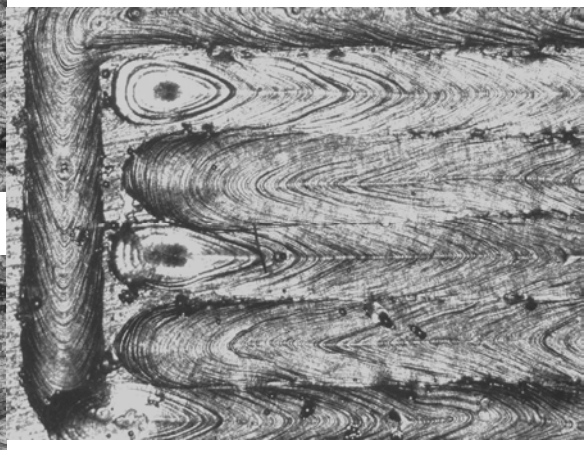

375W 150mm/s

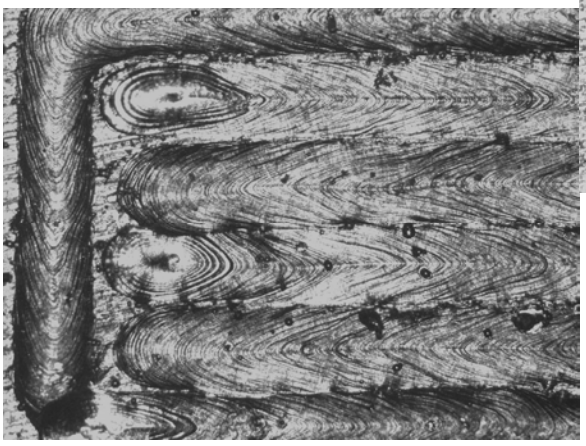

325W 130mm/s

E.5 M2 Weld Tracks, Sectioned

100 μm Spot Size

275W 175mm/s

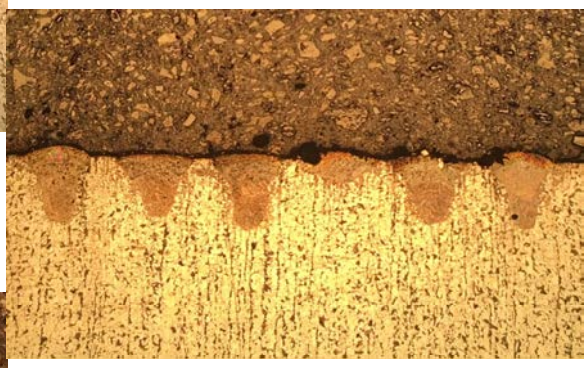

350W 225mm/s

300W 190mm/s

375W 240mm/s

325W 300mm/s

120 μm Spot Size

275W 145mm/s

350W 180mm/s

300W 160mm/s

375W 200mm/s

325W 170mm/s

140 μm Spot Size

275W 125mm/s

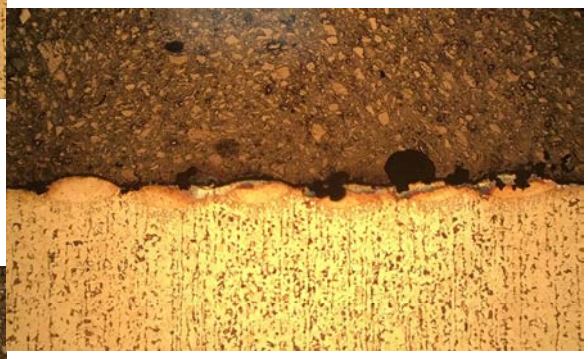

350W 160mm/s

300W 135mm/s

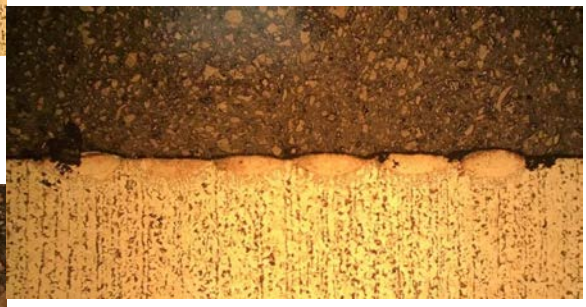

375W 170mm/s

325W 150mm/s

160 μm Spot Size

275W 110mm/s

350W 140mm/s

300W 120mm/s

375W 150mm/s

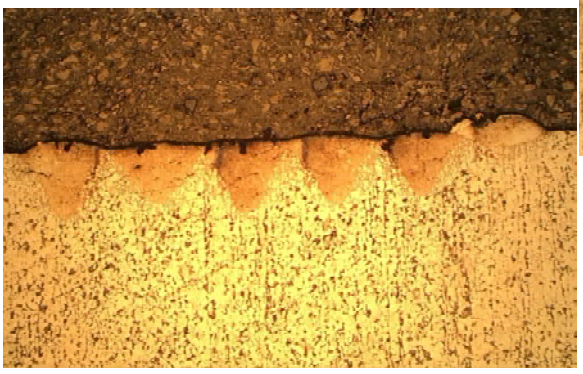

325W 130mm/s

Bibliography

[1] J. Schifman, "The Entire History of Steel," *Popular Mechanics*, 7 2018. [Online]. Available: https://www.popularmechanics.com/technology/infrastructure/a20722505/history-of-steel/

[2] J. Donovan, "Two Sams and Their Six-Shooter," *Texas Monthly*, no. April, 2016.

[3] "Otto Engine, circa 1883." [Online]. Available: https://www.thehenryford.org/collections-and-research/digital-collections/artifact/118195/

[4] J. W. McDaniel, "1903 Wright Flyer I." [Online]. Available: http://www.wright-brothers.org/Information_Desk/Just_the_Facts/Airplanes/Flyer_I.htm

[5] Defense Acquisition University, "Berry Amendment." [Online]. Available: https://www.dau.mil/acquipedia/Pages/ArticleDetails.aspx?aid=be528c25-b648-4797-99b0-ff27ba7ce75b

[6] A. Chaikin, "Why the SR-71 Blackbird is the Epitome of Cold War Spycraft — At the Smithsonian — Smithsonian," *Smithsonian Magazine*, no. December, 2014. [Online]. Available: https://www.smithsonianmag.com/smithsonian-institution/why-sr-71-blackbird-epitome-cold-war-spycraft-180953402/

[7] M. Dilmore and J. D. Ruhlman, "EGLIN STEELA LOW ALLOY HIGH STRENGTH COMPOSITION (75)," 1 2004. [Online]. Available: https://patents.google.com/patent/US7537727B2/en

[8] "Tungsten — Minerals Education Coalition." [Online]. Available: https://mineralseducationcoalition.org/elements/tungsten/

[9] "US Conflict Minerals Law: Section 1502 of U.S. Dodd Frank Act: the landmark US law requiring responsible minerals sourcing," 2017. [Online]. Available: https://www.globalwitness.org/en/campaigns/conflict-minerals/dodd-frank-act-section-1502/

[10] K. Humphrey, "Engineer's discovery could save Air Force millions," 2015.

[11] R. Abrahams, "Low alloy high performance steel," 5 2016. [Online]. Available: https://patents.google.com/patent/US20160369362A1/en

[12] AZoM, "SAE/AISI Carbon Steel Naming Conventions," 2012. [Online]. Available: https://www.azom.com/article.aspx?ArticleID=6151

[13] D. H. Rumsfeld, "Report to Congress on the Defeat of Hard and Deeply Buried Targets," 2001.

[14] F. Murphy and R. Boulton, "Iran sticks to deadline of nuclear deal with centrifuge move :," 1 2016. [Online]. Available: https://www.reuters.com/article/us-iran-nuclear/iran-sticks-to-deadline-of-nuclear-deal-with-centrifuge-move-iaea-idUSKBN1501R5

[15] R. M. German, *Powder metallurgy and particulate materials processing : the processes, materials, products, properties and applications*. [Online]. Available: https://books.google.com/books/about/Powder_Metallurgy_and_Particulate_Materi.html?id=xiUeAgAACAAJ

[16] L. Garwin and T. Lincoln, *A century of nature : twenty-one discoveries that changed science and the world*. University of Chicago Press, 2003.

[17] H. B. Cary, *The History of Welding*, 1998. [Online]. Available: https://www.millerwelds.com/resources/article-library/the-history-of-welding

[18] M. Shellabear and O. Nyrhilä, "DMLS-DEVELOPMENT HISTORY AND STATE OF THE ART," Tech. Rep. [Online]. Available: https://www.i3dmfg.com/wp-content/uploads/2015/07/History-of-DMLS.pdf

[19] T. Kellner, "An Epiphany of Disruption: GE Additive Chief Explains How 3D Printing Will Upend Manufacturing," General Electric, Tech. Rep., 2017. [Online]. Available: https://www.ge.com/reports/epiphany-disruption-ge-additive-chief-explains-3d-printing-will-upend-manufacturing/

[20] E. Jelis, "DEVELOPMENT OF LOW ALLOY STEEL BY DIRECT METAL LASER SINTERING," Ph.D. dissertation, New Jersey Institute of Technology, 2017.

[21] H. Richards and D. Liu, "Topology Optimization of Additively Manufactured Penetrating Warheads," *I3Dmfg.Com*, no. March, 2015. [Online]. Available: http://www.i3dmfg.com/wp-content/uploads/2015/07/DCASS-presentation-V3.pdf

[22] W. T. Graves, "Topology Optimazation of a Penetrating Warhead," Ph.D. dissertation, Air Force Institute of Technology, 2016.

[23] W. E. King *et al.*, "Journal of Materials Processing Technology Observation of keyhole-mode laser melting in laser powder-bed fusion additive manufacturing," *Journal of Materials Processing Tech.*, vol. 214, no. 12, pp. 2915–2925, 2014. [Online]. Available: http://dx.doi.org/10.1016/j.jmatprotec.2014.06.005

[24] P. Yost, "Secrets of the Viking Sword," 2012. [Online]. Available: https://www.pbs.org/wgbh/nova/video/secrets-of-the-viking-sword

[25] W. C. Leslie, *The Physical Metallurgy of Steels*, 1st ed. McGraw-Hill, 1981.

[26] A. C. Reardon, *Metallurgy for the Non-Metallurgist*, 2nd ed. ASM International, 2011.

[27] H. K. D. H. Bhadeshia, "Interpretation of the Microstructure of Steels." [Online]. Available: https://www.phase-trans.msm.cam.ac.uk/2008/Steel_Microstructure/SM.html

[28] R. Abbaschian *et al.*, *Physical Metallurgy Principles, SI Edition*, 4th ed. CENGAGE Learning, 2010.

[29] "Time Temperature Transformation curve — TTT diagram," 2017. [Online]. Available: http://www.mechscience.com/time-temperature-transformation-curve-ttt-diagram/

[30] G. Vander Voort *et al.*, "Martensite and the Control of Retained Austenite Martensite," pp. 4–7, 2015.

[31] M. Maalekian, "Christian Doppler Laboratory for Early Stages of Precipitation: The Effects of Alloying Elements on Steels (I)," Technische Universitat Graz, Tech. Rep., 2007. [Online]. Available: https://online.tugraz.at/tug_online/voe_main2.getvolltext?pCurrPk=32837

[32] T. DebRoy *et al.*, "Additive manufacturing of metallic components Process, structure and properties," 2018.

[33] N. Bailey, *Weldability of ferritic steels*, 1st ed. ASM International, Abington Publishing, 1994.

[34] *Metallographer's Guide: Irons and Steels; Ch. 1 Introduction to Steels and Cast Irons.* Materials Park, Ohio: ASM International, 2002. [Online]. Available: www.asminternational.org

[35] N. Dowling, *Mechanical Behavior of Materials*, 3rd ed. Pearson Prentice Hall, 2007.

[36] E. Payton and V. Sinha, "Effect of Thermal Cycling on AF9628 Steel," 2018.

[37] "Toughness." [Online]. Available: https://www.nde-ed.org/EducationResources/CommunityCollege/Materials/Mechanical/Toughness.htm

[38] Atrona Test Labs, "Charpy Impact Testing and DBTT." [Online]. Available: http://atrona.com/charpy-testing.html

[39] G. F. V. Voort, "Revealing Prior-Austenite Grain Boundaries," vol. 16, no. Suppl 2, pp. 5–6, 2017.

[40] J. Chapman, "DVIDS - Video - AF-96 Metal Alloy," 2017. [Online]. Available: https://www.dvidshub.net/video/569219/af-96-metal-alloy

[41] *Metallic Materials Properties Development and Standardization (MMPDS) Handbook-08.* Battelle Memorial Institute, 2013.

[42] Carpenter Technology Corporation, "CarTech® HY-180 Alloy." [Online]. Available: https://www.cartech.com/en/product-solutions/cartech-hy-180-alloy/#

[43] Latrobe Specialty Steel Co, "LESCALLOY ® HP 9-4-30 VAC-ARC ® Data Sheet," Tech. Rep., 2007. [Online]. Available: www.latrobesteel.com

[44] Service Steel Aerospace Corp, "AerMet 100 Data Sheet," Tech. Rep., 2016. [Online]. Available: https://www.ssa-corp.com/documents/DataSheetAerMet100.pdf

[45] ASTM F3213M, "Standard Specification for Additive Manufacturing Cobalt-28 Chromium-6 Molybdenum Alloy with Powder Bed Fusion," *ASTM Book of Standards*, vol. i, pp. 1–9, 2017.

[46] R. M. German, *Powder Metallurgy Science*, 2nd ed. Metal Powder Industries Federation, 1994.

[47] LPW Carpenter Additive, "Powder production." [Online]. Available: https://www.lpwtechnology.com/technical-library/powder-production/

[48] A. B215-15, "Standard Practices for Sampling Metal Powders," 2015.

[49] A. F3049-14, "Standard Guide for Characterizing Properties of Metal Powders Used fo Additive Manufacturing Processes," 2014.

[50] J. W. Carson and B. H. Pittenger, "Bulk Properties of Powders," 1998. [Online]. Available: www.asminternational.org

[51] ACuPowder International, "Hall Flowmeter Package." [Online]. Available: http://www.mcssl.com/store/ea8c48e7c1884434b664b991d8c792/outdoor-clothing/hall-flowmeter-package

[52] D. Rasmussen, "Undercooling and Nucleation in Rapid Solidification Rate Metal Powders Using Solid in Solid Emulsification," US Army Research Office, Tech. Rep., 1989. [Online]. Available: https://apps.dtic.mil/dtic/tr/fulltext/u2/a218527.pdf

[53] M. R. O. Hara and J. Smith, "AFIT Additive Manufacturing Laboratory Standard Operating Procedures," pp. 1–11.

[54] D. Herzog *et al.*, "Additive manufacturing of metals," *Acta Materialia*, vol. 117, pp. 371–392, 2016. [Online]. Available: http://dx.doi.org/10.1016/j.actamat.2016.07.019

[55] K. Hranka, "Hybrid Printing Could Leave Powder-Bed 3D Printing in the Dust," *Machine Design*, 4 2017.

[56] S. S. Al-bermani, "An Investigation into Microstructure and Microstructural Control of Additive Layer Manufactured Ti-6AI-4V by Electron Beam Melting," no. January, 2011.

[57] W. E. Frazier, "Metal additive manufacturing: A review," *Journal of Materials Engineering and Performance*, vol. 23, no. 6, pp. 1917–1928, 2014.

[58] R. J. Smith *et al.*, "Spatially resolved acoustic spectroscopy for selective laser melting," *Journal of Materials Processing Technology*, vol. 236, pp. 93–102, 10 2016. [Online]. Available: https://linkinghub.elsevier.com/retrieve/pii/S0924013616301352

[59] T. E. Shelton *et al.*, "Surface Roughness of Additively Manufactured Nickel Superalloy," 2018.

[60] K. G. Prashanth *et al.*, "Is the energy density a reliable parameter for materials synthesis by selective laser melting?" *Materials Research Letters*, vol. 5, no. 6, pp. 386–390, 2017. [Online]. Available: https://doi.org/10.1080/21663831.2017.1299808

[61] L. Quintino and E. Assunção, "Conduction laser welding," *Handbook of Laser Welding Technologies*, pp. 139–162, 1 2013. [Online]. Available: https://www.sciencedirect.com/science/article/pii/B9780857092649500064

[62] J. Elmer *et al.*, "Microstructure and mechanical properties of 21-6-9 stainless steel electron beam welds," *Metall Mater Trans A*, pp. 1771–87, 2017.

[63] M. Maguire, "Unpublished work," 2016.

[64] D. Qiao *et al.*, "Modeling of weld residual plastic strain and stress in dissimilar metal butt weld in nuclear reactors," in *ASME pressure vessels and piping conference*, 2014.

[65] D. Day *et al.*, "Development and Material Characterization of an Additively Manufactured Nickel Alloy for Turbine Applications," in *Volume 6: Ceramics; Controls, Diagnostics, and Instrumentation; Education; Manufacturing Materials and Metallurgy*. ASME, 6 2018, p. V006T24A019. [Online]. Available: http://proceedings.asmedigitalcollection.asme.org/proceeding.aspx?doi=10.1115/GT2018-76614

[66] D. Newell, "Solution Anneal Heat Treatments to Enhance Mechanical Performance of Additively Manufactured IN718," 2018.

[67] W. King *et al.*, "Observation of keyhole-mode laser melting in laser powder-bed fusion additive manufacturing," *J Mater Process Technol*, pp. 2915–25, 2014.

[68] W. Sames *et al.*, "Effect of process control and powder quality on Inconel 718 produced using electron beam melting," in *8th international symposium on superalloy 718 and derivatives*, 2014, p. 409.

[69] N. Aboulkhair *et al.*, "Reducing porosity in AlSi10Mg parts processed by selective laser melting," *Addit Manuf*, pp. 77–86, 2014.

[70] A. Bauereiss *et al.*, "Defect generation and propagation mechanism during additive manufacturing by selective beam melting," *J Mater Process Technol*, no. 11, pp. 2522–8, 2014.

[71] K. Mumtaz and N. Hopkinson, "Top surface and side roughness of Inconel 625 parts processed using selective laser melting," *Rapid Prototyping*, pp. 96–103, 2009.

[72] D. Bu and Y. Shen, "Balling phenomena in direct laser sintering of stainless steel powder: metallurgical mechanisms and control methods," *Mater Des*, pp. 2903–10, 2009.

[73] W. King, "Accelerated Certification for Additively Manufactured Metals," *Lawrence Livermore National laboratory LDRD Annual Report*, pp. 1–10, 2015.

[74] K. Roberts, "Design and testing of an additively manufactured cubesat structural bus," Air Force Institute of Technology, Tech. Rep., 2018. [Online]. Available: http://www.dtic.mil/dtic/tr/fulltext/u2/1056620.pdf

[75] M. Mani *et al.*, "Design rules for additive manufacturing: A categorization," National Institute of Standards and Technology, Tech. Rep., 2016. [Online]. Available: https://ws680.nist.gov/publication/get_pdf.cfm?pub_id=921515

[76] M. J. Matthews *et al.*, "Denudation of metal powder layers in laser powder bed fusion processes," *Acta Materialia*, vol. 114, pp. 33–42, 2016. [Online]. Available: http://dx.doi.org/10.1016/j.actamat.2016.05.017

[77] L. Langnau, "What to know about working with steel materials in additive manufacturing," Renishaw, Tech. Rep., 2017. [Online]. Available: https://www.makepartsfast.com/know-working-steel-materials-additive-manufacturing/

[78] S. Ghouse *et al.*, "The influence of laser parameters and scanning strategies on the mechanical properties of a stochastic porous material," *Materials & Design*, vol. 131, pp. 498–508, 10 2017. [Online]. Available: https://www.sciencedirect.com/science/article/pii/S026412751730624X

[79] A. Kirchner *et al.*, "Process window for electron beam melting of Ti-6Al-4V," *Powder Metall*, vol. 58, no. 4, pp. 246–9, 2015.

[80] C. Kamath *et al.*, "Density of additively-manufactured, 316L SS parts using laser powder-bed fusion at powers up to 400 W," *International Journal of Advanced Manufacturing Technology*, vol. 74, no. 1-4, pp. 65–78, 2014.

[81] D. R. Tobergte *et al.*, "Microstructure and Mechanical Properties of Maraging Steel 300 After Selective Laser Melting," *Journal of Chemical Information and Modeling*, vol. 53, no. 9, pp. 1689–1699, 2013.

[82] C. Wang *et al.*, "Process parameter optimization and mechanical properties for additively manufactured stainless steel 316L parts by selective electron beam melting," *Materials and Design*, vol. 147, pp. 157–166, 2018. [Online]. Available: https://doi.org/10.1016/j.matdes.2018.03.035

[83] M. Sadowski *et al.*, "Optimizing quality of additively manufactured Inconel 718 using powder bed laser melting process," *Additive Manufacturing*, vol. 11, pp. 60–70, 2016. [Online]. Available: http://dx.doi.org/10.1016/j.addma.2016.03.006

[84] E. Jelis *et al.*, "DMLS (Direct Metal Laser Sintering) of 4340 Steel : Influence of Starting Particle Size Part 1 Part 1 Recoating Direction Recoating Direction," no. October 2015, 2015.

[85] T. C. Dzogbewu *et al.*, "OPTIMAL PROCESS PARAMETERS FOR IN SITU ALLOYED Ti15Mo STRUCTURES BY LASER POWDER BED FUSION," *Solid Freeform Fabrication 2017 Proceedings*, no. 2014, pp. 75–96, 2017. [Online]. Available: http://www.ncbi.nlm.nih.gov/pubmed/20857278

[86] K. Shahzad *et al.*, "Additive manufacturing of alumina parts by indirect selective laser sintering and post processing," *Journal of Materials Processing Technology*, vol. 213, no. 9, pp. 1484–1494, 2013. [Online]. Available: http://dx.doi.org/10.1016/j.jmatprotec.2013.03.014

[87] I. Yadroitsev and I. Smurov, "Selective laser melting technology: From the single laser melted track stability to 3D parts of complex shape," *Physics Procedia*, vol. 5, no. PART 2, pp. 551–560, 2010. [Online]. Available: http://dx.doi.org/10.1016/j.phpro.2010.08.083

[88] "Thermal Conductivity of Metals." [Online]. Available: https://www.engineeringtoolbox.com/thermal-conductivity-metals-d_858.html

[89] Y. Guo *et al.*, "Single track and single layer formation in selective laser melting of niobium solid solution alloy," *Chinese Journal of Aeronautics*, 2017. [Online]. Available: https://doi.org/10.1016/j.cja.2017.08.019

[90] I. Yadroitsev *et al.*, "Single track formation in selective laser melting of metal powders," *Journal of Materials Processing Technology*, vol. 210, no. 12, pp. 1624–1631, 9 2010. [Online]. Available: https://www.sciencedirect.com/science/article/pii/S0924013610001469

[91] A. B. Anwar and Q. C. Pham, "Selective laser melting of AlSi10Mg: Effects of scan direction, part placement and inert gas flow velocity on tensile strength," *Journal of Materials Processing Technology*, vol. 240, pp. 388–396, 2017. [Online]. Available: http://dx.doi.org/10.1016/j.jmatprotec.2016.10.015

[92] G. Casalino *et al.*, "Experimental investigation and statistical optimisation of the selective laser melting process of a maraging steel," *Optics &*

Laser Technology, vol. 65, pp. 151–158, 1 2015. [Online]. Available: https://www.sciencedirect.com/science/article/pii/S0030399214002011

[93] H. L. Wei *et al.*, "Evolution of solidification texture during additive manufacturing," *Scientific Reports*, vol. 5, pp. 1–7, 2015. [Online]. Available: http://dx.doi.org/10.1038/srep16446

[94] J. A. Slotwinski *et al.*, "Characterization of Metal Powders Used for Additive Manufacturing," *Journal of Research of the National Institute of Standards and Technology*, vol. 119, p. 460, 2014. [Online]. Available: http://nvlpubs.nist.gov/nistpubs/jres/119/jres.119.018.pdfhttp://www.ncbi.nlm.nih.gov/pubmed/26601040http://www.pubmedcentral.nih.gov/articlerender.fcgi?artid=PMC4487284

[95] "Morphologi 4 Range," Tech. Rep., 2017.

[96] V. Fassel *et al.*, "Flame Emission Spectrometric Determination of Aluminum, Cobalt, Chromium, Copper, Manganese, Niobium, and Vanadium in Low and High Alloy Steels," *Analytical Chemistry*, vol. 43, no. 2, 1971.

[97] L. Blaney, "Magnetite (Fe3O4): Properties, Synthesis, and Applications," Lehigh University, Tech. Rep., 2007. [Online]. Available: http://preserve.lehigh.edu/cas-lehighreview-vol-15http://preserve.lehigh.edu/cas-lehighreview-vol-15/5

[98] S. Cacace and Q. Semeraro, "About Fluence and Process Parameters on Maraging Steel Processed by Selective Laser Melting: Do They Convey the Same Information?" *INTERNATIONAL JOURNAL OF PRECISION ENGINEERING AND MANUFACTURING*, vol. 19, no. 12, pp. 1873–1884,

2018. [Online]. Available: https://link.springer.com/content/pdf/10.1007%2Fs12541-018-0204-y.pdf

[99] "Mlab cusing - Concept Laser." [Online]. Available: https://www.concept-laser.de/en/products/machines/mlab-cusing.html

[100] X. Su *et al.*, "Theoretical Study on Overlapping Mechanism in SLM Based on Interlayer-staggered Scan Strategy," vol. 47, pp. 1482–1486, 2011.

[101] J. Schindelin *et al.*, "Fiji: an open-source platform for biological-image analysis," *Nature Methods*, vol. 9, no. 7, pp. 676–682, 7 2012. [Online]. Available: http://www.nature.com/articles/nmeth.2019

[102] "ASTM E92 - 17 Standard Test Methods for Vickers Hardness and Knoop Hardness of Metallic Materials," Tech. Rep., 2017. [Online]. Available: https://www.astm.org/Standards/E92.htm

[103] V. Sinha *et al.*, "Delineation of Prior Austenite Grain Boundaries in a Low-Alloy High-Performance Steel," *Metallography, Microstructure, and Analysis*, vol. 6, no. 6, pp. 610–618, 2017.

[104] "Hardness Conversion Chart," NDT Resource Center, Tech. Rep. [Online]. Available: www.nde-ed.org

[105] K. Kempen *et al.*, "No Title," *Physics Procedia*, vol. 12, pp. 255–263, 1 2011. [Online]. Available: https://ac.els-cdn.com/S187538921100112X/1-s2.0-S187538921100112X-main.pdf?_tid=5a3836d8-97de-4cb8-b7d5-da55b8dd3bc3&acdnat=1540171688_20cd917b3d499eec96c486792c7983f4https://www.sciencedirect.com/science/article/pii/S187538921100112X

[106] E. Yasa *et al.*, "Experimental investigation of charpy impact tests on metallic SLM parts," *4th International Conference on Advanced Research in Virtual and Physical Prototyping, VRAP 2009*, pp. 207–214, 2010. [Online]. Available: http://www.scopus.com/inward/record.url?eid=2-s2.0-78649804117&partnerID=40&md5=488de9247a23510bc2a3a30763b32e5c

[107] J. P. Kruth *et al.*, "Selective laser melting of iron-based powder," *Journal of Materials Processing Technology*, vol. 149, no. 1-3, pp. 616–622, 2004.

[108] ——, "Study of laser-sinterability of ferro-based powders," *Rapid Prototyping Journal*, vol. 11, no. 5, pp. 287–292, 2005.

[109] A. B. Spierings and G. Levy, "Comparison of density of stainless steel 316L parts produced with selective laser melting using different powder grades," Tech. Rep. [Online]. Available: http://sffsymposium.engr.utexas.edu/Manuscripts/2009/2009-30-Spierings.pdf

[110] E. Yasa *et al.*, "INVESTIGATION ON OCCURRENCE OF ELEVATED EDGES IN SELECTIVE LASER MELTING," Tech. Rep. [Online]. Available: http://sffsymposium.engr.utexas.edu/Manuscripts/2009/2009-17-Yasa.pdf

[111] E. Yasa, "Manufacturing by Combining Selective Laser Melting and Selective Laser Erosion / Laser Re-melting (Productie door het combineren van selectief laser smelten en selectief laser eroderen / laser hersmelten)," 2011. [Online]. Available: https://lirias.kuleuven.be/1747902?limo=0

[112] E. Yasa and J.-P. Kruth, "Microstructural investigation of Selective Laser Melting 316L stainless steel parts exposed to laser re-melting," *Procedia Engineering*, vol. 19, pp. 389–395, 2011. [Online]. Available: https://linkinghub.elsevier.com/retrieve/pii/S1877705811029390

[113] B. Liu *et al.*, "INVESTIGATION THE EFFECT OF PARTICLE SIZE DISTRIBUTION ON PROCESSING PARAMETERS OPTIMISATION IN SELECTIVE LASER MELTING PROCESS," Tech. Rep. [Online]. Available: https://s3.amazonaws.com/academia.edu.documents/46314034/INVESTIGATION_THE_EFFECT_OF_PARTICLE_SIZ20160607-28797-1jdrgse.pdf?AWSAccessKeyId=AKIAIWOWYYGZ2Y53UL3A&Expires=1551480109&Signature=KF8KJgTkdTrbLxUoSjfLKWrU6zQ%3D&response-content-disposition=inline%3B%20filename%3DInvestigation_the_effect_of_particle_siz.pdf

[114] A. Laohaprapanon *et al.*, "Optimal Scanning Condition of Selective Laser Melting Processing with Stainless Steel 316L Powder," *Advanced Materials Research*, vol. 341-342, pp. 816–820, 9 2011. [Online]. Available: https://www.scientific.net/AMR.341-342.816

REPORT DOCUMENTATION PAGE

Form Approved
OMB No. 0704–0188

1. REPORT DATE *(DD–MM–YYYY)*	2. REPORT TYPE	3. DATES COVERED *(From — To)*
22-03-2019	Master's Thesis	Sept 2018 — 21 March 2019

4. TITLE AND SUBTITLE

Process Parameter Development of Additively Manufactured AF9628 Weapons Steel

5a. CONTRACT NUMBER

5b. GRANT NUMBER

5c. PROGRAM ELEMENT NUMBER

6. AUTHOR(S)

Hager, Erin M. , Captain

5d. PROJECT NUMBER

5e. TASK NUMBER

5f. WORK UNIT NUMBER

7. PERFORMING ORGANIZATION NAME(S) AND ADDRESS(ES)

Air Force Institute of Technology
Graduate School of Engineering and Management (AFIT/EN)
2950 Hobson Way
WPAFB OH 45433-7765

8. PERFORMING ORGANIZATION REPORT NUMBER

AFIT-ENY-MS-19-M-310

9. SPONSORING / MONITORING AGENCY NAME(S) AND ADDRESS(ES)

AFRL/RX
Att: Dr. Philip Flater
101 W. Eglin Blvd
Eglin AFB FL 32542
philip.flater@us.af.mil

AFRL/RXSA
Att: Dr. Eric Payton
2230 10th Street
WPAFB OH 45433
eric.payton@us.af.mil

10. SPONSOR/MONITOR'S ACRONYM(S)

AFRL/RX

11. SPONSOR/MONITOR'S REPORT NUMBER(S)

12. DISTRIBUTION / AVAILABILITY STATEMENT

DISTRIBUTION STATEMENT A:
APPROVED FOR PUBLIC RELEASE; DISTRIBUTION UNLIMITED.

13. SUPPLEMENTARY NOTES

This material is declared a work of the U.S. Government and is not subject to copyright protection in the United States.

14. ABSTRACT

An approach to selecting power, speed, and hatch spacing values for a newly powderized material, AF9628 weapons steel, is described that results in highly dense (>99.9%) parts on an MLab 200R Cusing. Initial power and speed values used in a weld track study were selected based on a survey of parameters used on similar materials, with a focus on the energy density value known as laser fluence. Shape and penetration depth of the weld tracks were used to select the most promising parameters for generation of solid parts. Solid cylinders were printed with hatch spacing values of 90%, 80%, and 70% of the weld track widths and evaluated for porosity using sectioning and microscopy and CT scanning. Several parameter combinations resulted in parts with >99.9% density, with these parts occurring at a Fluence value of between 200 and 300 J/mm^3, and a volumetric energy density (E_V) value of between 60 and 80 J/mm^3. Initial material characterization of the as-built material was conducted, with strength and hardness values that met or exceeded values taken from the original material patent. Weld track studies at various laser focal diameters were then conducted on the larger, more powerful M2 Cusing by sweeping along a 250 J/mm^3 line of fluence. Additionally, the gas atomized AF9628 powder morphology and chemistry were evaluated in both the virgin and used-sieved conditions.

15. SUBJECT TERMS

Steel; AF9628; Additive Manufacturing; LBPF; Parameter Development

16. SECURITY CLASSIFICATION OF:			17. LIMITATION OF ABSTRACT	18. NUMBER OF PAGES	19a. NAME OF RESPONSIBLE PERSON
a. REPORT	b. ABSTRACT	c. THIS PAGE			Maj Ryan O'Hara, AFIT/ENY
U	U	U	UU	192	19b. TELEPHONE NUMBER *(include area code)* (937)255-3636, x4542; ryan.ohara@afit.edu